THE UNIVERSITY OF HULL

Surfactant Aspects of Corrosion Inhibition

being a Thesis submitted for the Degree of Doctor of Philosophy

in the University of Hull

by

Jake Thomas Hicks, M.Chem.

June 2007

Acknowledgements

I would like to express my gratitude to my supervisors Prof. Bernard P. Binks and Prof. Paul D.I. Fletcher for their support and constant availability throughout this study.

I am also extremely grateful to Nalco for the provision of a studentship and for financing my attendance to international conferences. In particular, I would like to thank Dr. David I. Horsup from Nalco, Sugar Land, USA and Dr. William H. Durnie and Dr. Lax Tiwari from Nalco, Fawley, UK for their guidance and support during this project.

I would like to express my gratitude to all members of the Surfactant and Colloid Group for their help and friendship. I particularly thank Dr. Miles R. Porter and Mr. Tim S. Dunstan for their help and advice throughout my research period.

I also thank Mr. Tony Sinclair for the excellent scanning electron microscopy images and all staff in the glassblowing and mechanical workshops within the Department of Chemistry. In addition, I would like to thank Mr. Garry S. Robinson from the Department of Mechanical Engineering for the mechanical polishing of the steel samples.

Finally, I am indebted to my parents for their support and encouragement throughout my academic life as well as my friends and housemates, Scott and Matt, for their support and friendship.

Publications and Presentations

The work presented in this thesis has given rise to the following presentations and conference proceedings:

Presentation and conference proceeding: **Comparison of the effects of air, carbon dioxide and hydrogen sulphide on corrosion of a low carbon steel under water and its inhibition by a quaternary ammonium salt**, B.P. Binks, P.D.I. Fletcher, J.T. Hicks, W.H. Durnie and D.I. Horsup, Paper No. 05307, NACE Corrosion/2005, Houston, USA (3^{rd} – 7^{th} March 2005).

Presentation: **"Surfactant aspects of corrosion inhibition"** at the 10^{th} European Student Conference, Biezenmortel, The Netherlands (12^{th} – 15^{th} July 2005).

Conference proceeding: **"I put it in, but where does it go? – The fate of corrosion inhibitors in multiphase systems"**, D.I. Horsup, J.C. Clark, B.P. Binks, P.D.I. Fletcher and J.T. Hicks, Paper No. 07617, NACE Corrosion/2007, Nashville, USA (11^{th} – 15^{th} March 2007).

Abstract

This thesis is concerned with investigating the surfactant aspects of corrosion inhibition. Corrosion inhibitors are of great industrial importance because they are a relatively inexpensive and easily applicable method of protecting oil pipelines against internal corrosion. The performance of corrosion inhibitors is known to depend upon the prevailing conditions within the pipeline.

We have used a range of experimental techniques to study corrosion of steel surfaces, adsorption of corrosion inhibitors and the behaviour of inhibitors in mixtures of oil and water in order to understand more about the factors which affect the performance of corrosion inhibitors under oil field conditions. Firstly, electrochemical and weight-loss measurements were used to measure the corrosion rate of steel immersed in aqueous environments under atmospheric conditions and in the presence of dissolved carbon dioxide and hydrogen sulphide. The measurements were repeated in the presence of dodecylbenzyldimethylammonium chloride and 1-aminoethyl-2-(8-heptadecenyl)-2-imidazoline acetate, which are thought of as model corrosion inhibitors. Both surfactants were found to effectively reduce the corrosion rate of steel when the dissolved gas was hydrogen sulphide, but were found to increase the corrosion rate in some aerated and carbonated environments.

The optical technique ellipsometry has been used to study the adsorption of dodecylbenzyldimethylammonium chloride at the steel-water interface. We have determined the thickness of the surfactant film adsorbed from aqueous solution in the absence of electrolyte. The results are consistent with the formation of a monolayer at inhibitor concentrations close to the critical micelle concentration and possible multilayer formation at higher concentrations. Determination of inhibitor film thickness has not been possible in the presence of electrolyte and corrosive dissolved gases which cause rapid corrosion of the steel surface. The technique has been employed subsequently to study the initial stages of corrosion in the presence and absence of dodecylbenzyldimethylammonium chloride. Scanning electron microscopy and elemental analysis have also been used to examine the changes which occur to the steel surface during corrosion. These results show that the optical properties of the steel surface undergo changes as the steel is attacked by corrosive aqueous solutions and that dodecylbenzyldimethylammonium chloride can increase the rate of these changes or completely suppress them, depending on the nature of the dissolved gas present.

Finally, we have investigated the phase behaviour of alkylbenzyldimethylammonium chloride and 1-aminoethyl-2-(8-heptadecenyl)-2-imidazoline acetate using equilibrium partitioning and emulsion phase inversion methods. The results show that variations in common oil field variables, such as temperature, electrolyte concentration and oil type, can lead to the consumption of the aggregated form of water-soluble corrosion inhibitors by partitioning to the oil phase. The results are discussed in terms of the effect of these variables upon the effective geometry of the inhibitor within the monolayer of the aggregates. We have also performed electrochemical corrosion rate measurements in systems containing oil and water, under conditions which cause virtually all of the inhibitor to exist in the oil phase. The results suggest that partitioning of the aggregated form of corrosion inhibitors from water to oil does not adversely affect corrosion inhibition in the aqueous phase.

CONTENTS

CHAPTER 1

Introduction

1.1 Industrial relevance of current research

A report in 2001 estimated that corrosion costs United States industries and government agencies an estimated $276 billion per year[1]. The cost of corrosion in the oil and gas production industry is almost $1.5 billion per year. Research and development of organic corrosion inhibitors serves many purposes within the oil production industry. Primarily, controlling corrosion has economical benefits for oil companies. Corrosion inhibition allows the use of relatively inexpensive materials for constructing pipelines which transport the corrosive and toxic production fluids to oil refineries. As accessible oil fields in shallow water areas become exhausted after many years of drilling, oil prospectors have begun to drill in more remote, deep-water areas, which are extremely corrosive environments[2,3]. Catastrophic failure of oil pipelines caused by corrosion can result in environmental damage and the loss of human life if corrosion inhibition is improperly applied. In 2006, internal corrosion of a pipeline in the Prudhoe Bay oil field in Alaska caused an oil spill which led to the loss of over one million litres of oil[4]. Environmentalists considered the spill to be a catastrophe to the local environment.

Corrosion inhibition can be controlled in a variety of ways; however this work focuses solely on organic corrosion inhibitors, which are surface active agents. Research into corrosion and corrosion inhibitors is generally carried out within the field of electrochemistry. This study aims to investigate the surfactant aspects of corrosion inhibition which are often over-looked during electrochemical studies, including much needed research into the behaviour of corrosion inhibitors added to mixtures of oil and water.

1.2 Surfactants

1.2.1 General surfactant structure

Surface active agents (or surfactants) are amphiphilic molecules. They have a hydrophilic headgroup and a hydrophobic tailgroup (Figure 1.1). Headgroups are polar and can be anionic (negatively charged), cationic (positively charged), zwitterionic (positive and negative charges) or nonionic. Tailgroups are usually nonpolar, straight or branched hydrocarbon chains. Surfactants can be soluble in both water and oil phases depending on the nature of the hydrophilic and hydrophobic groups. The hydrocarbon

moiety favours solubility in oil, whereas the hydrophilic headgroup has a greater affinity for the aqueous environment. Therefore, in two-phase oil and water systems a surfactant may partition itself between the oil and water phases. If the hydrophilicity of the headgroup exceeds the hydrophobicity of the tailgroup the surfactant may be expected to partition in favour of the aqueous phase. When the hydrophobicity of the tailgroup exceeds the hydrophilicity of the tailgroup the surfactant may be expected to partition to a greater extent into the oil phase.

Figure 1.1. The general structure of a surfactant molecule. The example given is the cationic surfactant hexadecyltrimethylammonium bromide (CTAB).

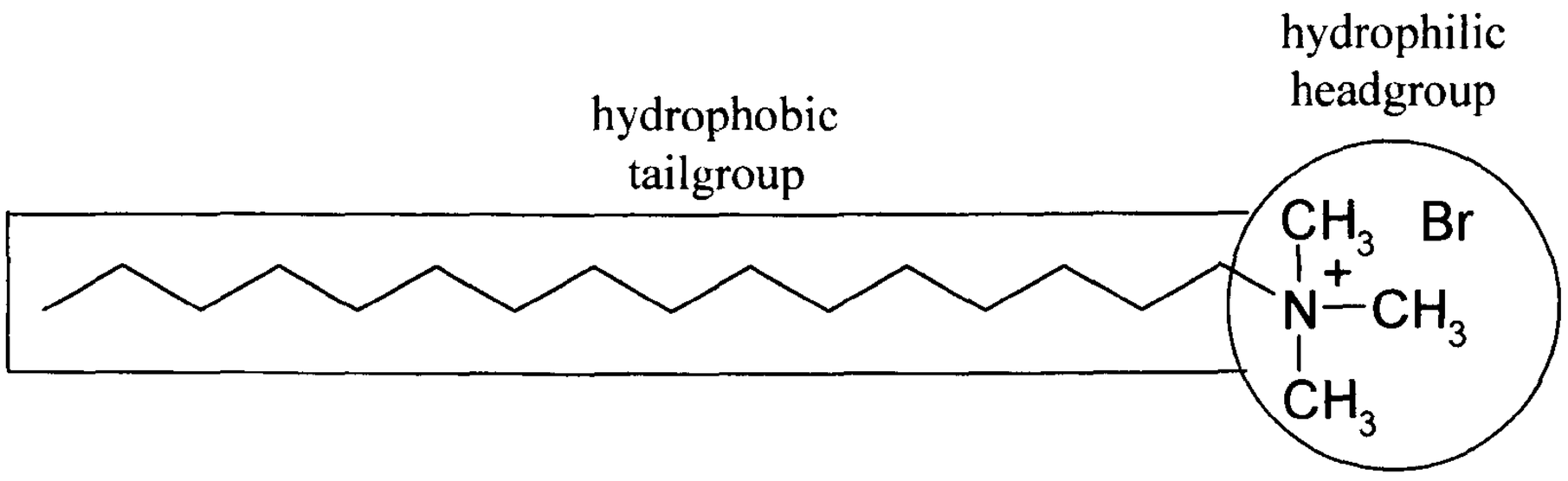

When present at low concentrations in water, surfactants act like normal electrolytes and are also able to adsorb onto various interfaces. Adsorption alters the interfacial free energy per unit area, the minimum work required to create a unit area of the interface. A reduction in the interfacial free energy of an air-water or oil-water interface is generally observed in the presence of a surfactant. This phenomenon is the key to many of the industrial applications of surfactants as detergents and emulsifiers.

At higher concentrations, surfactants can aggregate in aqueous solution to form various structures such as micelles, vesicles and liquid crystalline phases[5]. The aggregation process is driven by the tendency for the hydrophobic chains to minimise their contact with water.

1.2.2 Adsorption of surfactants

Surfactants have a tendency to adsorb at liquid-vapour and liquid-liquid interfaces, leading to a reduction in the surface or interfacial tension, respectively. When a surfactant is dissolved in water, the presence of the hydrophobic moiety causes unfavourable distortion of the liquid structure, which increases the overall free energy

of the system. Water molecules surrounding the hydrophobic tailgroup become ordered which decreases the total entropy of the system[5]. The entropy is increased when a surfactant molecule is transported to an interface. As less work is required to bring a surfactant molecule to an interface compared to solvent molecules the surfactant will preferentially adsorb at the interface in order to lower the free energy of the system. The hydrophilic moiety retains its affinity for the solvent molecules which causes the surfactant to orient itself at the interface with the hydrophilic group in aqueous solution and the hydrophilic group protruding into the vapour or oil phase. The work required to increase the interfacial area decreases, which causes a decrease in the surface or interfacial tension[6]. The amount of surfactant adsorbed at the interface can be calculated by measuring the interfacial tension and applying the Gibbs' adsorption equation[7]. The interfacial tension decreases with increasing surfactant concentration as the amount of adsorbed surfactant increases and reaches a saturation value at a critical concentration (Figure 1.2). The interfacial tension continues to decrease and then reaches a plateau value at the critical micelle concentration of the surfactant[6].

Figure 1.2. The effect of adsorption of surfactant at the liquid-vapour or liquid-liquid interface on the interfacial tension.

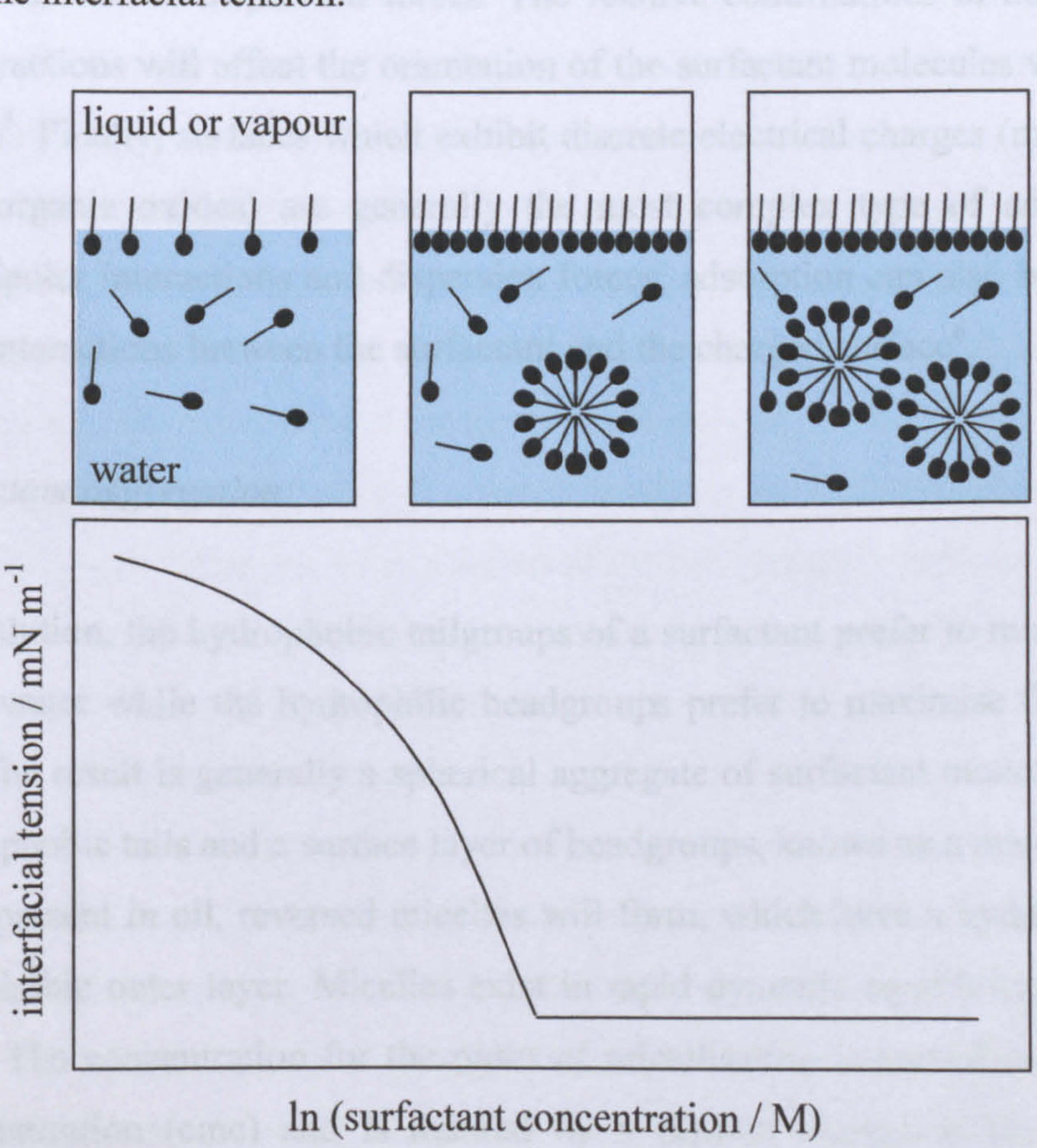

Surfactant molecules can also adsorb at the solid-liquid interface. Adsorption onto solid surfaces is an important process in many applications of surfactants including detergency and waterproofing. Adsorption mechanisms are controlled by interactions between the adsorbing surfactant and the substrate, as well as interactions between adsorbed surfactant molecules. The nature of these interactions is determined by the properties of the solid surface, the nature and concentration of the surfactant and environmental factors such as temperature, pH and the type of the solvent[8]. Generally, adsorption mechanisms are evaluated from an adsorption isotherm, which can be obtained using solution depletion methods or techniques such as ellipsometry[9]. A variety of isotherm shapes have been determined experimentally to describe different mechanisms for the adsorption of surfactants onto solid surfaces from aqueous solution[5].

Adsorption of surfactants onto nonpolar, hydrophobic surfaces such as polyethylene occurs as a result of dispersion force interactions. When adsorbing from aqueous solution, the hydrophobic portion of the surfactant will be associated with the surface with the hydrophilic tailgroups protruding into the aqueous solution. The interaction of surfactants with uncharged, polar surfaces, such as polyester and cotton, is more complex. Dipolar interactions, hydrogen bonding and other acid-base interactions may exist in addition to dispersion forces. The relative contributions of the polar and nonpolar interactions will affect the orientation of the surfactant molecules with respect to the surface[5]. Finally, surfaces which exhibit discrete electrical charges (metals, silica and other inorganic oxides) are generally the most complex type of adsorbent. In addition to dipolar interactions and dispersion forces, adsorption can also be driven by electrostatic interactions between the surfactant and the charged surface[6].

1.2.3 Surfactant aggregation

In aqueous solution, the hydrophobic tailgroups of a surfactant prefer to minimise their contact with water while the hydrophilic headgroups prefer to maximise their contact with water. The result is generally a spherical aggregate of surfactant monomers with a core of hydrophobic tails and a surface layer of headgroups, known as a micelle[10]. If the surfactant is present in oil, reversed micelles will form, which have a hydrophilic core and a hydrophobic outer layer. Micelles exist in rapid dynamic equilibrium with their monomers[11]. The concentration for the onset of micellisation is known as the critical micelle concentration (cmc) and is marked by a distinct change in the colligative properties of the solution. Below the cmc the surfactant exists in its monomeric form.

When the concentration of surfactant is increased above the cmc, the concentration of monomers remains constant and the number of aggregates increases[12].

Normal micelles can solubilise oils and oil-soluble substances that would not otherwise dissolve into aqueous solution in the absence of surfactant, resulting in 'swollen' micelles. Solubilisation occurs because the micelle interiors have the properties of a liquid hydrocarbon due to mixing of the hydrocarbon moieties in the core of the aggregate.

1.3 Emulsions and microemulsions

Emulsions are defined as heterogeneous mixtures of two immiscible liquids (usually oil and water) where one phase is dispersed in the other as drops with a diameter of several microns[13]. Emulsions can be either oil-in-water (o/w) or water-in-oil (w/o); with o/w emulsions oil drops are dispersed in an aqueous continuous phase and in w/o emulsions water drops are dispersed in an oil continuous phase. Preparation of an emulsion requires the formation of a large interfacial area between the two liquids. The work required to disperse one liquid within another remains in the system as potential energy. This means that the system is thermodynamically unstable and must reduce this energy by decreasing the interfacial area. Therefore, an emulsion will eventually separate into the two bulk phases if is not stabilised by an appropriate emulsifier.

Emulsifiers are surfactants which facilitate emulsion formation by reducing the interfacial tension between the two immiscible liquids through adsorption at the oil-water interface. The reduction in interfacial tension reduces the amount of work required to produce the emulsion but the system will only be thermodynamically stable if the interfacial tension can be reduced to zero[5]. However, emulsions can be considered to be kinetically stable if the rate of separation of the two phases is sufficiently slow. In addition to a low interfacial tension, emulsion stability can be favoured by the formation of a mechanically strong and elastic interfacial film and electrostatic repulsion between the dispersed droplets, depending upon the nature of the emulsifier[14].

There are four main processes by which emulsions can destabilise. These are creaming (or sedimentation), flocculation, coalescence and Ostwald ripening[13] (Figure 1.3). In o/w emulsions creaming involves the movement of oil drops to form a concentrated layer at the top of the vessel; however there is no change in the drop size distribution. In w/o emulsions, the equivalent process, in which water drops fall to the

Figure 1.3. Schematic showing the four processes by which emulsions can destabilise: (a) creaming (o/w) or sedimentation (w/o), (b) flocculation, (c) coalescence and (d) Ostwald ripening.

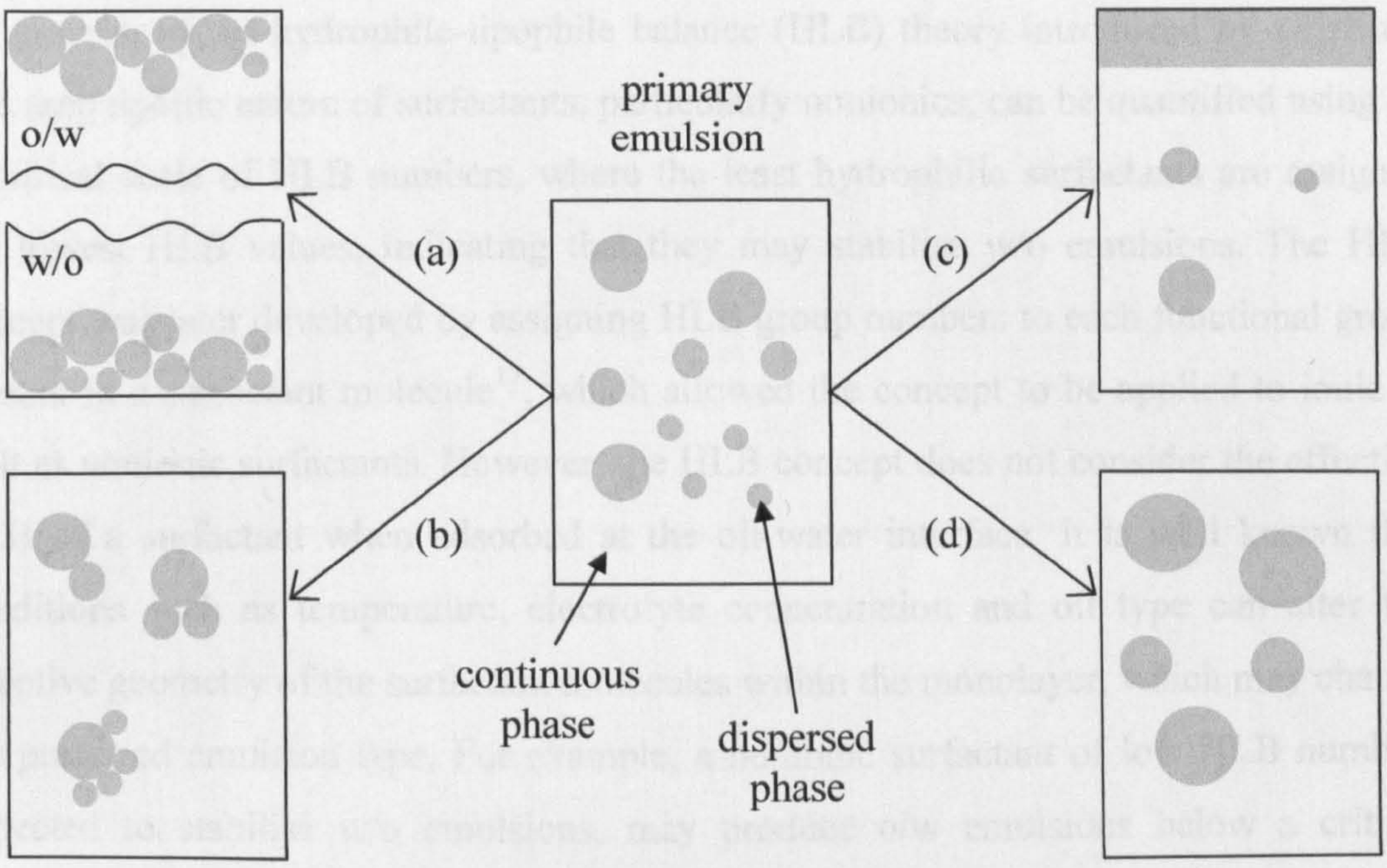

bottom of the vessel, is known as sedimentation. In each case the difference in the densities of the dispersed and continuous phase results in the movement of the emulsion drops under the action of gravity. Flocculation is the aggregation of emulsion drops, without rupture of the surfactant film present at the oil-water interface. Flocculation can enhance creaming because the aggregates (or flocs) effectively have a larger radius compared to a single emulsion drop. Coalescence is the process by which two or more emulsion drops merge together to form a single drop of greater volume, but with a smaller interfacial area[5]. Ostwald ripening is the process by which large drops grow at the expense of smaller ones and is caused by solubility differences of dispersed drops of differing sizes. The solubility of the dispersed oil or water increases with decreasing drop size, therefore material within the drops tends to dissolve and diffuse through the continuous phase before re-condensing onto larger drops. The resulting decrease in interfacial area acts as the driving force for the growth of the emulsion drops.

When oil and water are emulsified in the presence of a surfactant, there are a number of variables which will affect the type of emulsion produced, most notably, the nature of the emulsifier, the relative volumes of the two immiscible phases, the presence of electrolyte and the temperature of the system[13,14]. It is well known that the continuous

phase of an emulsion tends to be the phase in which the surfactant is most soluble. This is known as Bancroft's rule[15].

When selecting a surfactant for a desired application as an emulsifier it is often useful to consider the balance between the hydrophobic and hydrophilic groups. This is the essence of the hydrophile-lipophile balance (HLB) theory introduced by Griffin[16]. The amphiphilic nature of surfactants, particularly nonionics, can be quantified using an empirical scale of HLB numbers, where the least hydrophilic surfactants are assigned the lowest HLB values, indicating that they may stabilise w/o emulsions. The HLB concept was later developed by assigning HLB group numbers to each functional group present in a surfactant molecule[17], which allowed the concept to be applied to ionic as well as nonionic surfactants. However, the HLB concept does not consider the effective HLB of a surfactant when adsorbed at the oil-water interface. It is well known that conditions such as temperature, electrolyte concentration and oil type can alter the effective geometry of the surfactant molecules within the monolayer, which may change the preferred emulsion type. For example, a nonionic surfactant of low HLB number, expected to stabilise w/o emulsions, may produce o/w emulsions below a critical temperature[13].

Microemulsions are thermodynamically stable isotropic dispersions of oil-in-water or water-in-oil stabilised by a surfactant[18]. Microemulsion systems generally appear transparent because the dispersed droplet size is typically 5 – 50 nm which means that they scatter light weakly. When a surfactant is added to a two-phase oil and water system in excess of the critical microemulsion concentration (cμc), one of three possible Winsor systems can be obtained (Figure 1.4). A Winsor I system consists of an o/w microemulsion in existence with an excess oil phase. A Winsor II system consists of a w/o microemulsion with a conjugate aqueous phase. In a Winsor III system, a third phase containing all the surfactant coexists with both excess oil and water phases. The third phase may be bicontinuous microemulsion[19] or a lamellar (L_α) or L_3 liquid crystal phase[20]. The phase system progression Winsor I - III - II can be achieved by changing parameters such as electrolyte concentration, temperature, the nature of the oil and the concentration of a second surface active component (co-surfactant)[18,21]. Such changes can alter the effective geometry of the surfactant within the monolayer coating the microemulsion aggregates. These changes affect the curvature of the monolayer, which is positive in the Winsor I system and negative in the Winsor II system. In the surfactant-rich third phase the monolayer has, on average, zero net curvature.

Figure 1.4. Schematic showing Winsor microemulsion systems.

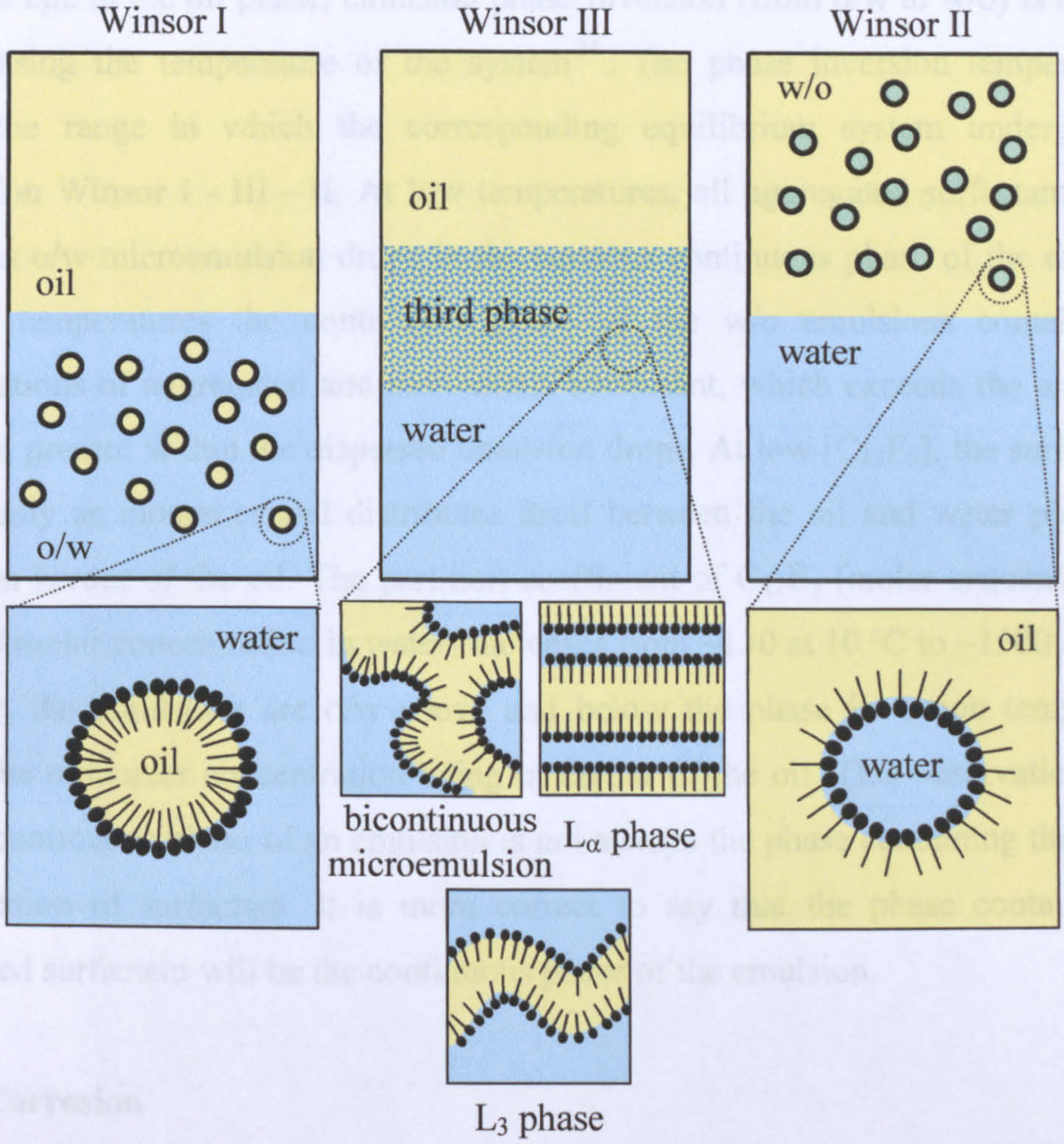

It is frequently observed that in mixtures of equal volumes of water and oil, the type of emulsion formed by the homogenisation of a Winsor system is the same as the equilibrium microemulsion type[22]. For example, emulsification of a Winsor I system generally produces an o/w emulsion, the continuous phase of which is an o/w microemulsion. For the system containing the anionic surfactant sodium bis-2-ethylhexyl sulphosuccinate (AOT), heptane and aqueous sodium chloride at surfactant concentrations above the cmc in the aqueous phase, emulsions phase inversion (from o/w to w/o) occurs at electrolyte concentrations close to the corresponding microemulsion inversion[23]. When the concentration of electrolyte is below the emulsion phase inversion concentration, emulsions are water continuous below and above the cmc in the aqueous phase. In each case, the continuous phase of the emulsion is always the phase which contains the majority of the surfactant, whether it is in the form of monomer or microemulsion aggregates, in accordance with Bancroft's rule.

In the system containing the nonionic surfactant dodecyl pentaoxyethylene glycol ether ($C_{12}E_5$), heptane and 0.01 M aqueous sodium chloride at concentrations above the cμc in the oil phase, emulsion phase inversion (from o/w to w/o) is achieved by increasing the temperature of the system[24]. The phase inversion temperature is around the range in which the corresponding equilibrium system undergoes the progression Winsor I - III - II. At low temperatures, all aggregated surfactant will be present as o/w microemulsion drops in the aqueous continuous phase of the emulsion. At high temperatures the continuous phase of the w/o emulsions contains high concentrations of aggregated and monomeric surfactant, which exceeds the amount of surfactant present within the dispersed emulsion drops. At low [$C_{12}E_5$], the surfactant is present only as monomer and distributes itself between the oil and water phases but heavily in favour of the oil. The partition coefficient of $C_{12}E_5$ (molar concentration in heptane / molar concentration in water) increases from ~130 at 10 °C to ~1500 at 50 °C. However, the emulsions are o/w above and below the phase inversion temperature, despite the monomer concentration being in favour of the oil. This observation shows that the continuous phase of an emulsion is not always the phase containing the highest concentration of surfactant. It is more correct to say that the phase containing the aggregated surfactant will be the continuous phase of the emulsion.

1.4 Corrosion

Corrosion is the destructive result of chemical reactions between a metal (or metal alloy) and its environment[25]. Corrosion is a process which has an impact on many aspects of human life, from the occurrence of rust on buildings and automobiles to tarnishing of jewellery. Almost all metallic corrosion processes involve transfer of electronic charge in aqueous solution. The electrochemistry of iron corrosion in acidic solutions can be summarized by a series of half-equations:

$$Fe \rightarrow Fe^{2+} + 2e^- \qquad \text{(anodic reaction)} \qquad (1.1)$$

$$2H^+ + 2e^- \rightarrow H_2 \qquad \text{(cathodic reaction)} \qquad (1.2)$$

In the anodic reaction (equation (1.1)) iron is oxidised liberating two electrons, while hydrogen is reduced in the cathodic reaction (equation (1.2))[26]. In the overall reaction (equation (1.3)), ferrous ions dissolve into solution liberating electrons into the bulk

metal, the electrons migrate to the surface of the metal where they reduce aqueous hydrogen ions (Figure 1.5) to molecular hydrogen.

$$Fe + 2H^+ \rightarrow Fe^{2+} + H_2 \quad (1.3)$$

Figure 1.5. Schematic diagram showing dissolution of iron metal in acidic solution, liberating an Fe^{2+} ion plus two electrons which are consumed in the reduction of hydrogen ions to molecular hydrogen.

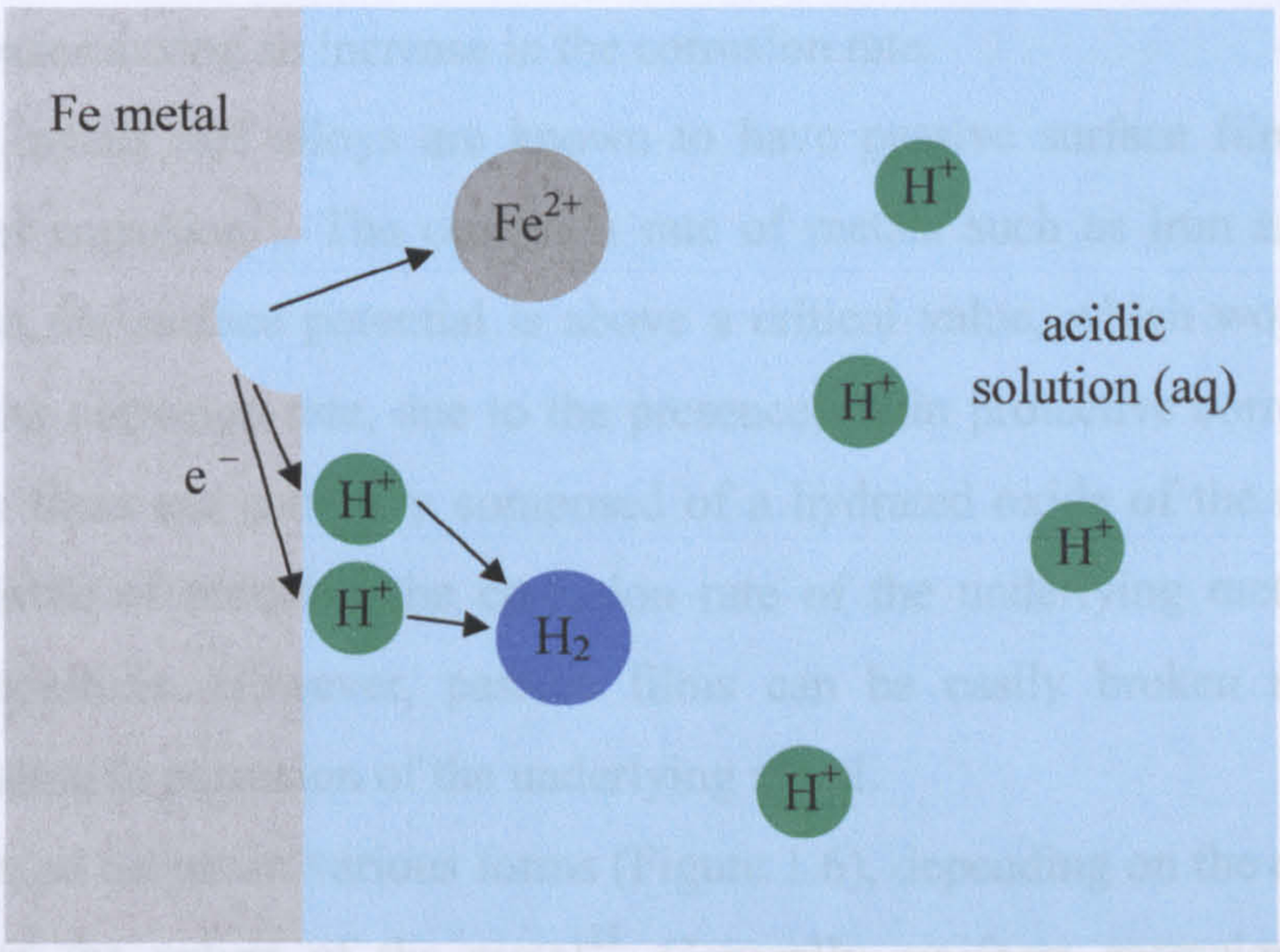

The reduction of dissolved oxygen is observed in neutral and acidic solutions exposed to the atmosphere (equations (1.4) and (1.5)). The overall corrosion reaction produces ferrous hydroxide (equation (1.6)).

$$\tfrac{1}{2}O_2 + H_2O + 2e^- \rightarrow 2OH^- \quad (1.4)$$

$$\tfrac{1}{2}O_2 + 2H^+ + 2e^- \rightarrow H_2O \quad (1.5)$$

$$Fe + H_2O + \tfrac{1}{2}O_2 \rightarrow Fe(OH)_2 \quad (1.6)$$

Ferrous hydroxide acts as a diffusion barrier layer; oxygen must diffuse through this layer to continue corrosion of the underlying iron surface. Exposure of the ferrous layer to dissolved oxygen produces ferric hydroxide, which is main constituent of common rust:

$$Fe(OH)_2 + \tfrac{1}{2}H_2O + \tfrac{1}{4}O_2 \rightarrow Fe(OH)_3 \quad (1.7)$$

Electrochemical reactions proceed at finite rates. When electrons are supplied as in equation (1.2) the potential at the surface becomes more negative; this is known as cathodic polarization. The negative potential suggests that the reaction is not fast enough to accommodate all the available electrons, causing excess electrons to accumulate at the metal-solution interface to await reaction. A shortage of electrons liberated by equation (1.1) would produce a positive potential at the metal surface; this is known as anodic polarization. Here, there is a greater tendency for the metal to dissolve into solution. In an aqueous electrolyte solution, a metal surface will reach a steady state potential. If the potential is shifted to a higher potential the anodic reaction rate will increase causing an increase in the corrosion rate.

Many metals and alloys are known to have passive surface films which can protect against corrosion[25]. The corrosion rate of metals such as iron and chromium decrease when the surface potential is above a critical value, which would otherwise lead to a higher corrosion rate, due to the presence a thin protective corrosion product layer. Passive films are generally composed of a hydrated oxide of the metal and are generally capable of reducing the corrosion rate of the underlying metal by several orders of magnitude. However, passive films can be easily broken and scratched ultimately leading to corrosion of the underlying metal.

Corrosion occurs in various forms (Figure 1.6), depending on the environmental conditions and the nature of the metal[25]. Generally, uniform corrosion is the most common form of corrosion, involving uniform removal of the metal under conditions where the corrosive liquid can access the entire metal surface.

Figure 1.6. Schematic showing different types of corrosion.

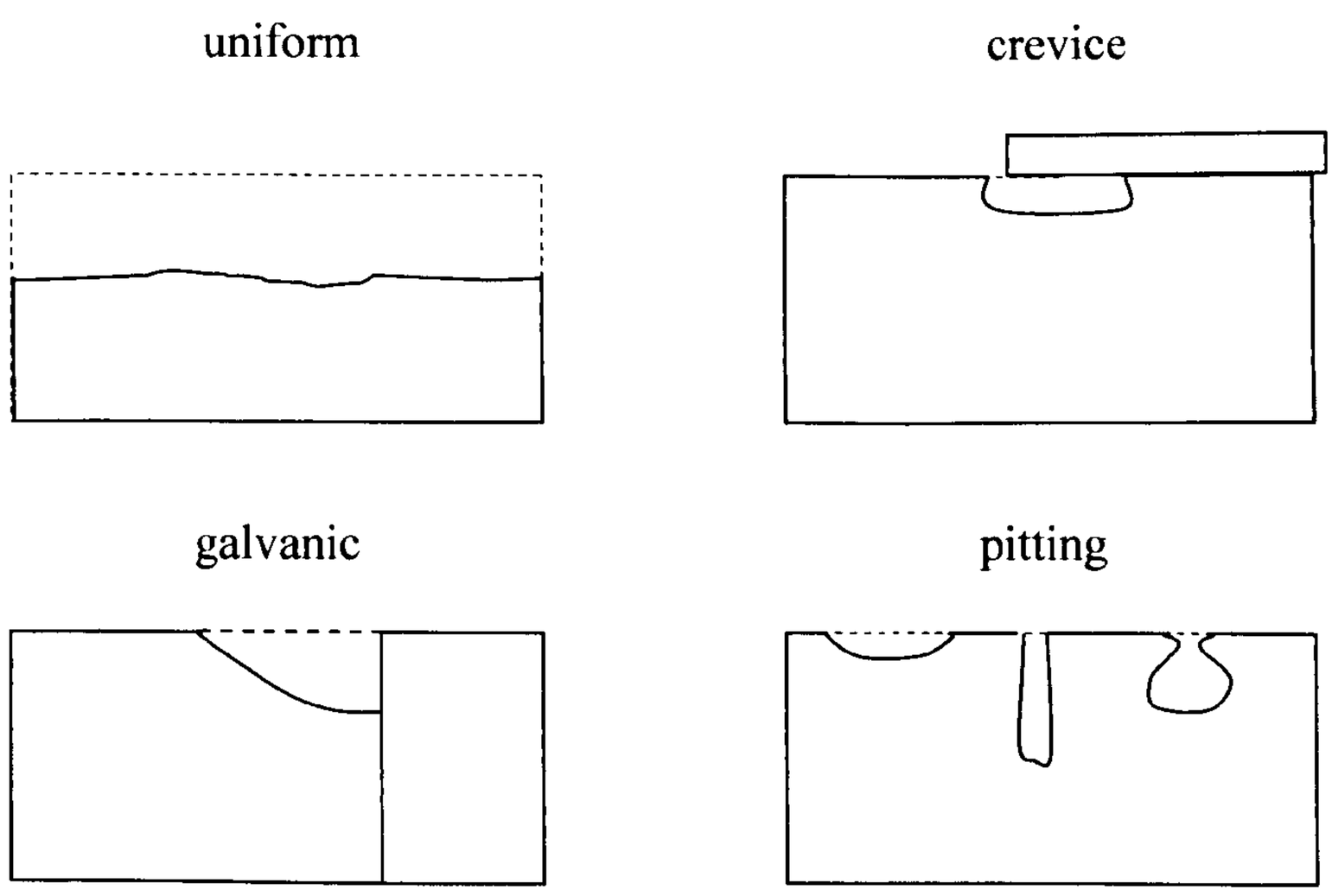

Galvanic corrosion results when two different alloys are coupled in the presence of a corrosive liquid. This situation is commonly encountered when dissimilar metals are welded together. A difference in the corrosion potentials of the two alloys causes preferential corrosion of one alloy while the other is protected from corrosion. The alloy which is protected from corrosion is the metal which has the more positive potential in the Galvanic Series. This principle is the basis for methods of sacrificial protection of metals, such as galvanised zinc coatings on steel surfaces. Crevice corrosion is induced by a greater extent of corrosion in a small volume of a crevice created by another material, such as a washer or bolt. Pitting corrosion is localised attack of a metal surface, generally caused by a failure of the protective passive film. The corrosion rate in a pit is several orders of magnitude greater than the rate of uniform corrosion. Pitting and crevice corrosion have similar mechanisms in that a small sheltered volume restricts transport between the bulk solution and the corroding anodic site within the pit or crevice. Although uniform corrosion causes the greatest loss of metal, high pitting corrosion rates can lead to rapid failure of metal structures. Other forms of corrosion include environmentally induced cracking, dealloying and erosion-corrosion.

1.5 Oil field corrosion

Crude oil is composed of aliphatic and aromatic hydrocarbons of different chain lengths. Oil is extracted from wells in oil fields in three main stages. In the primary recovery stage, the natural pressure of the reservoir is used to drive the transport of oil to the surface. During secondary recovery, techniques such as gas re-injection and water flooding are used to extract more of the oil. Finally, tertiary recovery uses the injection of gases such as CO_2 or steam to enhance the flow of oil which has not been recovered during the primary and secondary recovery stages. The produced fluids are transported through pipelines to oil refineries which are often located hundreds of miles away from the source.

An oil pipeline is a complex multiphase system consisting of a mixture of crude oil and water, containing many soluble and insoluble materials, flowing turbulently through a complex network of steel pipes. Carbon steels are the most common material used for the construction of pipelines. These grades of steel contain approximately 0.05 – 1 % carbon, which is added to improve the mechanical properties of the steel[25,27] and have relatively low corrosion resistance. Despite the highly corrosive conditions encountered in oil production, the use of more expensive corrosion-resistant alloys is

seen only as a last resort and other preventative measures are required to control corrosion of carbon steel oil pipelines.

The major cause of corrosion in oil pipelines is the highly corrosive water extracted with the crude oil. Water is frequently re-injected into reservoirs to maintain the pressure and stability of the reservoir as well as to drive oil out of the rock formation[28]. As the oil field ages, the volume ratio of oil and water phases will alter as water is re-injected to remove the remaining oil. The resulting increase in the water content will generally increase the corrosivity of the production fluid. Although the presence of water alone causes corrosion of the steel pipes, corrosion rates increase dramatically in the presence of dissolved salts[29], organic acids[25] and dissolved gases such as carbon dioxide (CO_2) and hydrogen sulphide (H_2S).

Corrosion in the presence of dissolved carbon dioxide gas is often termed 'sweet' corrosion. Carbon dioxide gas forms carbonic acid when dissolved in water, which decreases the pH of the solution and is mildly corrosive (equation (1.8)). The main corrosion processes are summarised by one anodic reaction (equation (1.1)) and three cathodic reactions (equations (1.2), (1.9) and (1.10))[28].

$$CO_{2\,(g)} + H_2O_{\,(l)} \rightarrow H_2CO_{3\,(aq)} \quad (1.8)$$

$$2H_2CO_3 + 2e^- \rightarrow H_2 + 2HCO_3^- \quad (1.9)$$

$$2HCO_3^- + 2e^- \rightarrow H_2 + 2CO_3^{2-} \quad (1.10)$$

Carbonic acid reacts with iron in carbon steel to form an iron carbonate ($FeCO_3$) layer next to the steel surface, which can act as a barrier to corrosion (equations (1.11) – (1.13)).

$$Fe^{2+} + CO_3^{2-} \rightarrow FeCO_3 \quad (1.11)$$

$$Fe^{2+} + 2HCO_3^- \rightarrow Fe(HCO_3)_2 \quad (1.12)$$

$$Fe(HCO_3)_2 \rightarrow FeCO_3 + CO_2 + H_2O \quad (1.13)$$

'Sour' corrosion is caused by the presence of dissolved hydrogen sulphide (equation (1.14)), which also lowers the pH of the solution to approximately 4 in saturated systems due its dissociation in water (equations (1.15) and (1.16)). A 'sour' pipeline will generally contain dissolved CO_2 and H_2S. However, the presence of only 3 – 5 parts per million of H_2S can significantly increase the corrosion rate of steel and causes

the formation of iron sulphide (FeS) corrosion products and increased localised (or pitting) corrosion.

$$Fe + H_2S \rightarrow FeS + 2H \quad (1.14)$$

$$H_2S \rightarrow HS^- + H^+ \quad (1.15)$$

$$HS^- \rightarrow S^{2-} + H^+ \quad (1.16)$$

The sulphide ion acts as a poison, which retards the recombination of nascent hydrogen atoms at the iron surface. This increases the amount of time that hydrogen atoms spend at the surface, increasing hydrogen penetration into the metal lattice. When the atomic hydrogen combines to form molecular hydrogen within the metal structure, the resulting increase in gas volume can lead to hydrogen blistering or hydrogen induced cracking of the metal[25].

1.6 Corrosion inhibitors

A corrosion inhibitor is defined as a substance which, when added at a low concentration to an environment, effectively reduces the corrosion rate of a metal exposed to that environment. The main industries using corrosion inhibitors are oil and gas exploration and production, petroleum refining, heavy industrial manufacturing and water treatment facilities. The greatest utilization of corrosion inhibitors is within the oil industry, particularly in the petroleum refining industry. The total consumption of corrosion inhibitors in the United States was nearly $1.1 billion in 1998[1]. Corrosion inhibition is used internally with carbon steel pipelines and storage vessels as a cost effective alternative to stainless steels and other alloys, organic coatings, and non-metallic composites. The particular advantage of corrosion inhibition is that it can be implemented easily.

Organic inhibitors are surfactants. Their surface activity is the key to their transport to the pipeline surface, where they may reduce the corrosion rate of the metal. Many types of surfactant have been used as corrosion inhibitors including quaternary ammonium salts[30], alkylpyridinium salts[31], alkylamines[32] and imidazolines[33]. Figure 1.7 shows some examples of common organic corrosion inhibitors. The choice of inhibitor should be one which provides the maximum level of corrosion protection at the lowest possible concentration. The concentration of inhibitor present in the production fluids is

typically between 10 – 100 parts per million, depending upon the nature of the inhibitor and the prevailing conditions of the oil field.

Figure 1.7. Schematic structures of some typical organic corrosion inhibitor molecules.

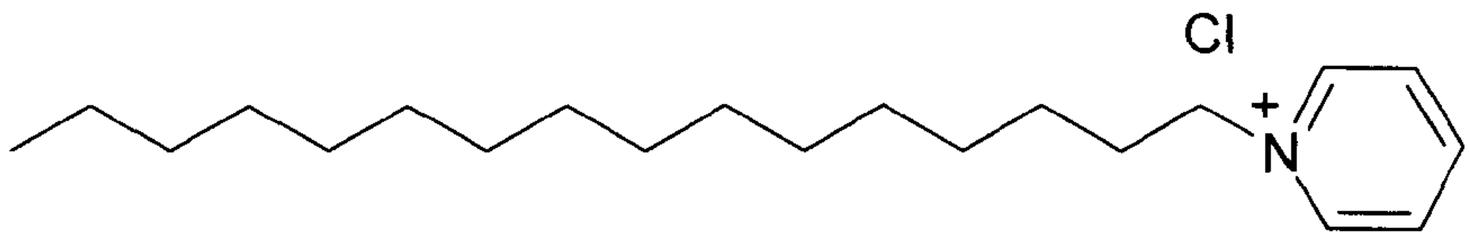

hexadecylpyridinium chloride

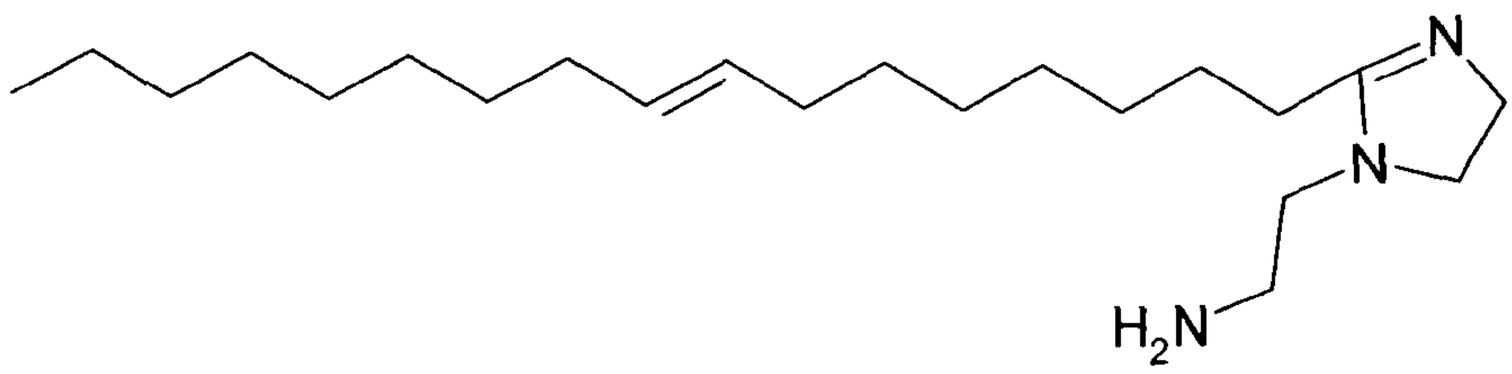

1-aminoethyl-2-(8-heptadecenyl)-2-imidazoline acetate

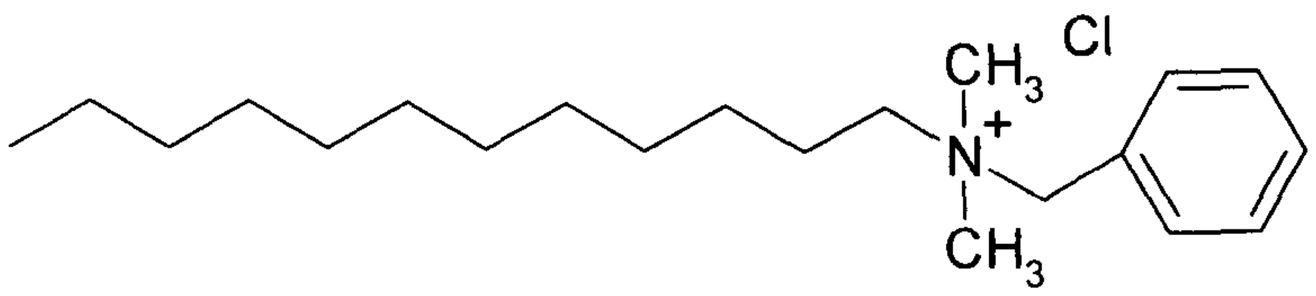

dodecylbenzyldimethylammonium chloride

Oil companies will generally produce formulations of different types of corrosion inhibitor plus other additives such as anti-fouling agents[34] and scale inhibitors. Inhibitor formulations can be supplied as liquids, emulsions or in the solid state[35]. The inhibitor formulation can be applied either in an intermittent batch process or continuously into the pipeline[35]. Batch applications can be applied using concentrated 'slugs', which form thick films on the pipe surface, or using a liquid flush to transport the inhibitor down the pipeline. The chosen method of application should ensure that the inhibitor is transported to the metal surface, especially at distances far from the point of addition.

The production of oil takes place throughout the world and the environmental conditions of pipelines can differ greatly, depending on the composition of the oil recovered. Production fluids will generally contain dissolved CO_2 gas, but parameters such as the oil to water volume ratio, the salinity of the aqueous phase and the concentration of dissolved H_2S and other sulphur species can vary greatly depending upon the location of the oil field. In order to control corrosion within a pipeline correct

assessment of the oil field conditions must be carried out in order to choose the most suitable formulation to provide corrosion inhibition.

Corrosion occurs primarily when the steel surface is in contact with the aqueous phase of the production fluids. It is for this reason that the many inhibitors are developed for addition to the aqueous phase. In many offshore oil drilling operations water from the produced fluids is often discharged into the sea. High concentrations of corrosion inhibitor may still remain in the water that is discharged. In recent years, there has been increasing concern about the toxicity and biodegradability of these discharged chemicals, therefore the choice of inhibitor should be one which does not pose any threat to the marine environment once discharged[36].

Research and testing of corrosion inhibitors is generally carried out with studies under laboratory conditions followed by testing in the field. Weight-loss and electrochemical measurements are used to determine the corrosion rate of a metal surface in an aqueous environment in the presence and absence of a potential corrosion inhibitor. These experiments are generally conducted in acidic solutions or under conditions which model the aqueous phase of a particular oil field, by sparging the aqueous phase with corrosive gases such as CO_2 and H_2S and also by varying the concentration and composition of the brine phase. Larger scale laboratory investigations aim to replicate closely conditions encountered in pipeline systems, studying the effects of high temperatures and pressures and turbulent multiphase liquid flow on corrosion and its inhibition by surfactants[37,38].

The concentration of inhibitor has a profound effect upon corrosion inhibition. For surfactants which act as corrosion inhibitors, the level of inhibition increases with concentration up to a maximum level, close to the critical micelle concentration of the surfactant[39,40]. The extent of adsorption of inhibitor will depend upon the activity of the inhibitor (as opposed to the concentration), which may be reduced by precipitation or aggregation into micelles[41]. Above the cmc or solubility limit, monomer activity remains virtually constant and equal to the cmc or solubility.

Several studies have suggested that at low concentrations the inhibitor adsorbs parallel to the steel surface[42,43]. As the bulk concentration increases the hydrophobic tail groups begin to protrude into the aqueous phase to accommodate more surfactant molecules, increasing the surface coverage (Figure 1.8). At the cmc, monolayer coverage is achieved and the tailgroups are parallel to each other and perpendicular to the metal surface[44]. The surface becomes hydrophobic due to the orientation of the surfactant molecules, which is characterised by an increase in the contact angle (θ) of a

Figure 1.8. Schematic showing monolayer and bilayer adsorption of corrosion inhibitor from aqueous solution onto iron.

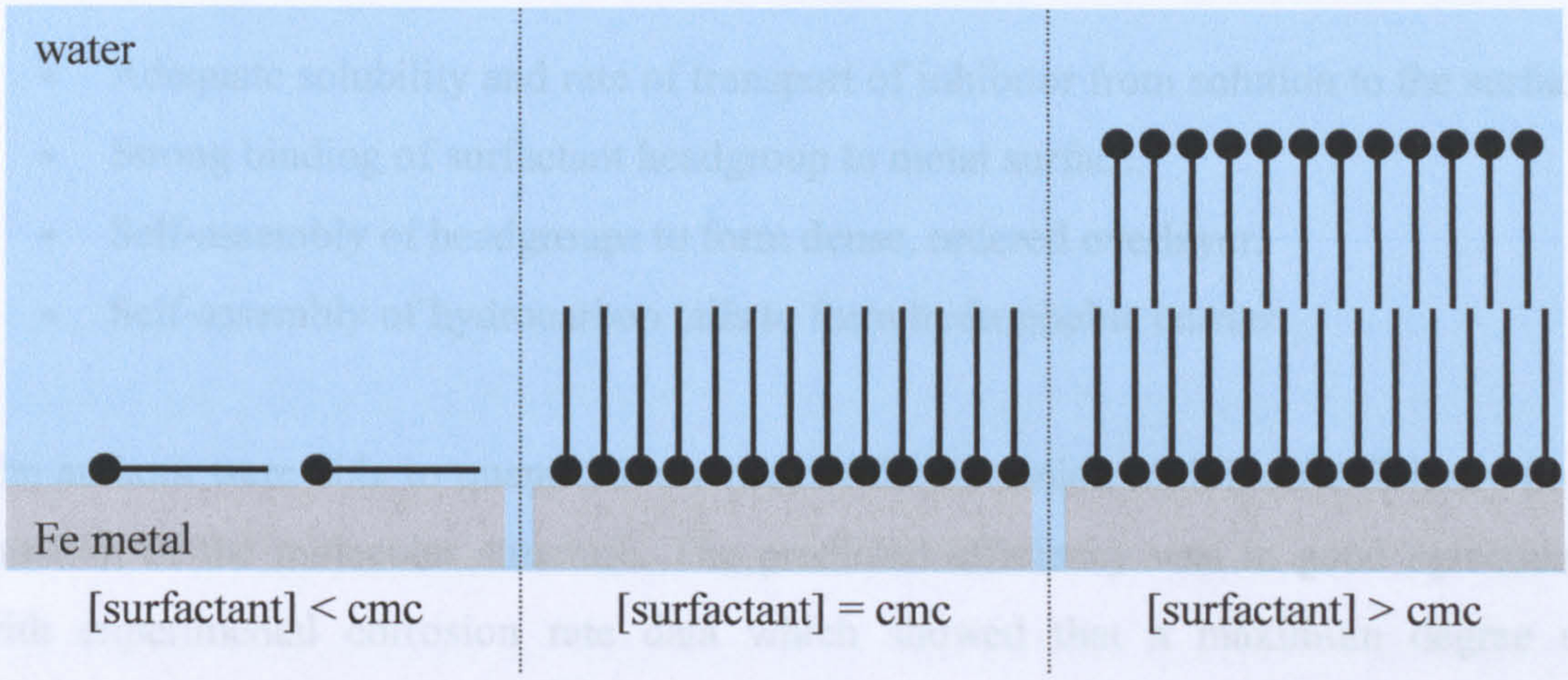

sessile water drop placed on the treated surface. McMahon has shown that the adsorption of oleic imidazoline onto steel produces a completely hydrophobic surface[33]. After adsorption of the inhibitor onto the steel surface, spherical sessile water drops (θ = 180 º) were observed to roll across the surface indicating that the surface has no affinity for water. Therefore, adsorbed corrosion inhibitor films are believed to act as a waterproof barrier between the corrosive aqueous phase and the steel pipeline. Increasing the inhibitor concentration can lead to bilayer adsorption due to hydrophobic interactions between the tailgroups of the primary monolayer and the additional adsorbing monomers, which may render the surface hydrophilic.

Adsorption of surfactants onto metal surfaces has a strong dependency on the length of the surfactant tailgroup. Generally, corrosion inhibition increases with hydrocarbon chain length up to about C_{18}. Longer hydrocarbon chains increase the van der Waals forces of attraction between the hydrophobic tailgroups, contributing to the tightly bound surface layer. Depending upon the nature of the surfactant, corrosion inhibition can increase continuously[45], increase and then remain constant[46] or pass through as maximum[47] as the tail group length is increased. For a series of alkyltrimethylammonium bromide surfactants ($C_{10} - C_{16}$), the concentration of inhibitor required to achieve the highest level of corrosion inhibition decreases as the alkyl chain length increases[45]. This effect is thought to be related to the decrease in the cmc of the inhibitor as the hydrophobicity of the tail group increases.

An investigation into the inhibition of corrosion of iron by a series of imidazoline derivatives by Ramachandran *et al*. suggests a self-assembled monolayer

mechanism for corrosion inhibition. The model suggests the following criteria for efficient corrosion inhibitors[48,49].

- Adequate solubility and rate of transport of inhibitor from solution to the surface.
- Strong binding of surfactant headgroup to metal surface.
- Self-assembly of headgroups to form dense, ordered overlayer.
- Self-assembly of hydrocarbon tails to form hydrophobic barrier.

The authors were able to quantitatively predict the corrosion inhibition efficiency as a function of the molecular structure. The predicted efficiency was in good agreement with experimental corrosion rate data which showed that a maximum degree of inhibition was achieved for inhibitors with intermediate chain lengths (C_{12} – C_{18}). The results suggest that inhibitors with short hydrocarbon chains exhibit poor corrosion inhibition due to incomplete hydrophobic film coverage. The decrease in efficiency at long chain lengths is thought to be due to the very low monomer solubility of the inhibitor which causes their rate of adsorption to be extremely slow.

Although laboratory corrosion studies may suggest that a particular inhibitor must be applied at a given concentration (in water) to provide corrosion inhibition, subsequent tests under oil field conditions may indicate that a higher concentration of inhibitor is required to provide the same level of inhibition. This suggests that not all of the inhibitor added to the pipeline has the ability to reach the metal surface. Although the surface activity of corrosion inhibitors is the key to inhibition by adsorption at the steel-liquid interface, this property also has the possibility to reduce the effectiveness of corrosion inhibitors in actual pipeline systems in the presence of a hydrocarbon phase. In addition to adsorption at the steel-liquid interface, corrosion inhibitors are also able to aggregate in solution, stabilise emulsions of oil and water, distribute or partition themselves between oil and water phases and may also adsorb onto solid surfaces other than the steel pipeline. Parasitic consumption of the inhibitor caused by these processes may reduce the activity of the monomeric form of the inhibitor which is available to provide corrosion inhibition[34,41,50]. Gulbrandsen and Kvarekval have shown that the performance of corrosion inhibitors is dramatically reduced in the presence of dispersed oil drops[51]. Adsorption of the corrosion inhibitor molecules onto the oil-water interface of dispersed oil drops decreases the activity of the inhibitor therefore less inhibitor is available to adsorb onto the pipe surface to inhibit corrosion. The inhibitor activity can also be reduced by adsorption onto dispersed solid particles such as sand and silt

particles[52]. The concentration of inhibitor adsorbed onto dispersed solid particles (or oil drops) is given by:

$$[\text{ads.inhibitor}] = \frac{3\phi_{\text{particles}}}{rAN_{Av}} \qquad (1.17)$$

where $\phi_{particles}$ is the volume fraction of particles, r is the particle radius, A is the area occupied per inhibitor molecule and N_{Av} is the Avogadro constant. The inhibitor is assumed to adsorb onto the particles with monolayer coverage. Figure 1.9 shows the effect of varying the particle radius and $\phi_{particles}$ on the concentration of inhibitor adsorbed onto the dispersed particles. This shows that particles or oil drops of radius 0.1 μm at a volume fraction of 0.001 have the ability to consume approximately 40 ppm of inhibitor.

Figure 1.9. Variation of concentration of corrosion inhibitor (in parts per million) adsorbed on particles as a function of particle radius for $\phi_{particles}$ values of 0.001 (black), 0.01 (red) and 0.1 (blue). The molecular weight of the inhibitor was taken to be 400 and the solvent was water.

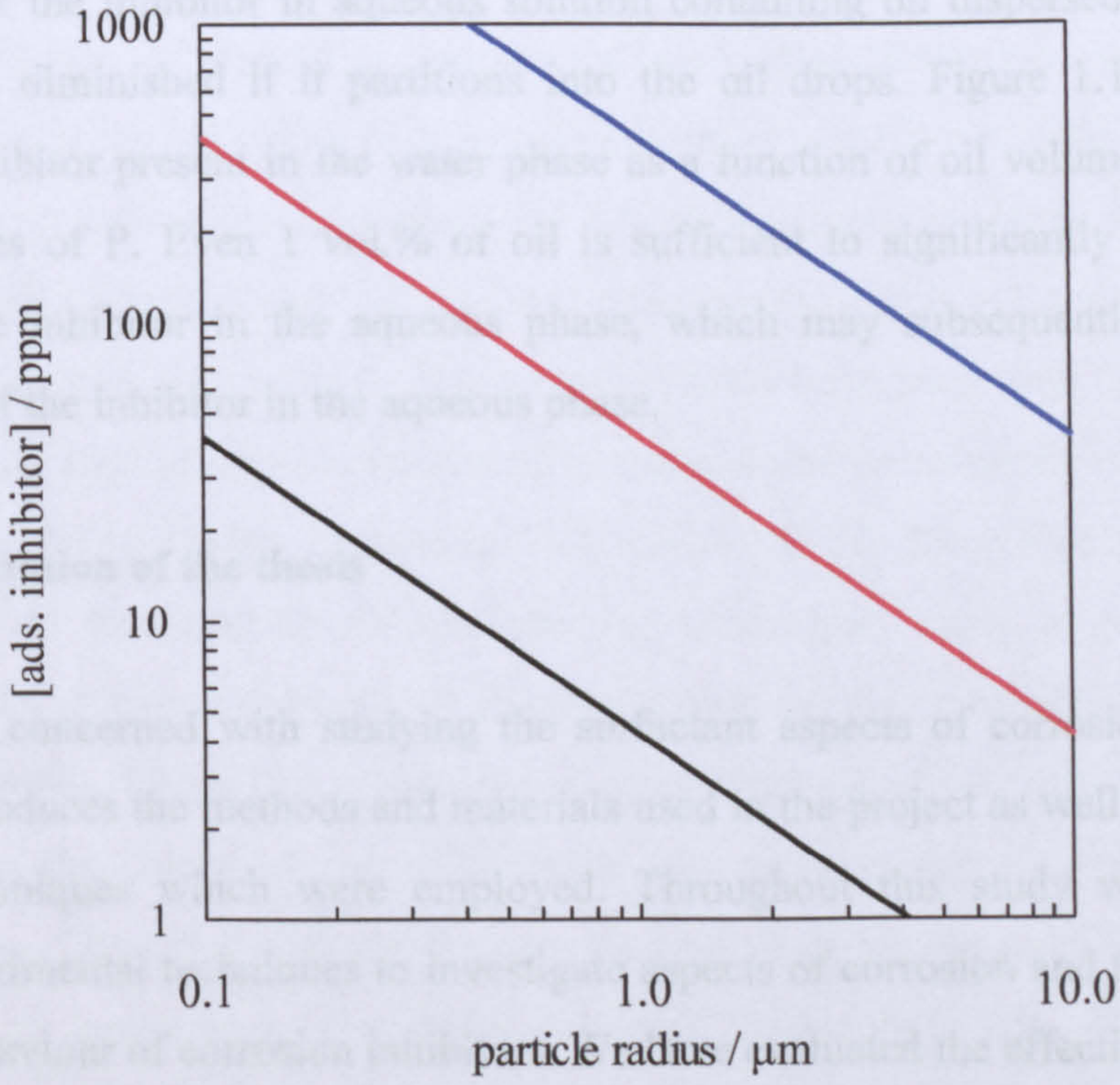

Corrosion inhibitors are amphiphilic and therefore they can often be soluble in both the oil and water phases of the produced fluids. The degree of solubility in each

phase depends upon the molecular structure of the surfactant. The partition coefficient of a corrosion inhibitor, X, is defined as by equation (1.18).

$$P = \frac{[X]_{oil}}{[X]_{water}} \tag{1.18}$$

When the corrosion inhibitor is distributed between the oil and water phases the total concentration of inhibitor is given by:

$$[X]_{total} = [X]_{water}\phi_{water} + [X]_{oil}\phi_{oil} \tag{1.19}$$

where ϕ_{oil} and ϕ_{water} are the volume fractions of oil and water, respectively. The fraction of corrosion inhibitor present in the water phase can be written as a function of the oil volume fraction:

$$\frac{[X]_{water}}{[X]_{total}} = \frac{1}{(1-\phi_{oil})+P\phi_{oil}} \tag{1.20}$$

The activity of the inhibitor in aqueous solution containing oil dispersed as emulsion drops may be diminished if it partitions into the oil drops. Figure 1.10 shows the fraction of inhibitor present in the water phase as a function of oil volume fraction for different values of P. Even 1 vol.% of oil is sufficient to significantly decrease the activity of the inhibitor in the aqueous phase, which may subsequently reduce the performance of the inhibitor in the aqueous phase.

1.7 Presentation of the thesis

This thesis is concerned with studying the surfactant aspects of corrosion inhibition. Chapter 2 introduces the methods and materials used in the project as well as describing the main techniques which were employed. Throughout this study we have used different experimental techniques to investigate aspects of corrosion and the adsorption and phase behaviour of corrosion inhibitors. We have evaluated the effectiveness of two corrosion inhibitors using some electrochemical and weight-loss methods. The optical technique ellipsometry has been employed to determine the thickness of corrosion inhibitor films adsorbed onto steel surfaces. This technique has also been used, in

Figure 1.10. Fraction of total inhibitor present in the water phase vs. volume fraction of oil for P values of 10 (black), 100 (red) and 1000 (blue).

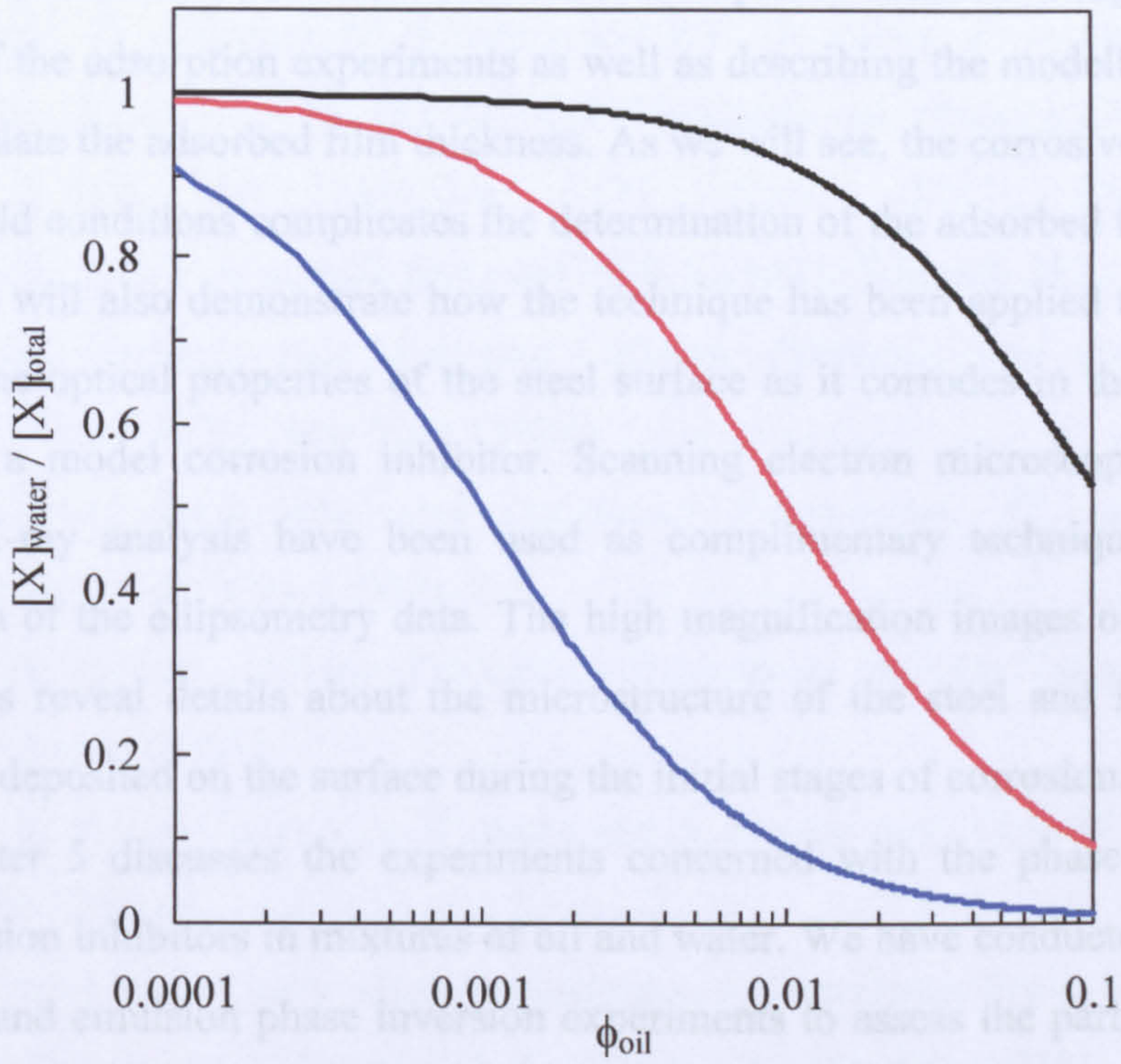

conjunction with scanning electron microscopy and elemental analysis, to study the corrosion of steel surfaces in different aqueous environments. Finally, we have used traditional methods of emulsion preparation and characterisation and analytical techniques to study the behaviour of corrosion inhibitors in mixtures of oil and water.

In order to assess the corrosivity of different aqueous environments, we have conducted electrochemical and weight-loss experiments which are used extensively within corrosion inhibitor research. These two methods have been used to measure the corrosion rate of steel specimens immersed in water under atmospheric conditions and two model oil field systems containing CO_2 and H_2S. We have also measured the corrosion rate of the steel in the presence of electrolyte, using a synthetic brine formulation. The steel is a carbon steel frequently used for the construction of pipelines and storage vessels. The effect of increasing concentrations of two different corrosion inhibitors upon the corrosion rate of the steel was subsequently determined in each aqueous system. Chapter 3 presents the corrosion rate data for the steel in the presence and absence of quaternary ammonium salt and imidazoline salt compounds and demonstrates that the effectiveness of surfactants as corrosion inhibitors depends upon the type of dissolved gas present and the concentration of electrolyte.

In order to understand more about the effects of corrosion inhibitors under different gas conditions we decided to use ellipsometry to determine the thickness of surfactant films adsorbed onto steel surfaces from aqueous solution. Chapter 4 presents the results of the adsorption experiments as well as describing the modelling procedure used to calculate the adsorbed film thickness. As we will see, the corrosive nature of the model oil field conditions complicates the determination of the adsorbed film thickness. However we will also demonstrate how the technique has been applied to monitor the changes in the optical properties of the steel surface as it corrodes in the absence and presence of a model corrosion inhibitor. Scanning electron microscopy and energy dispersive X-ray analysis have been used as complimentary techniques to aid the interpretation of the ellipsometry data. The high magnification images of the corroded steel surfaces reveal details about the microstructure of the steel and how corrosion products are deposited on the surface during the initial stages of corrosion.

Chapter 5 discusses the experiments concerned with the phase behaviour of model corrosion inhibitors in mixtures of oil and water. We have conducted equilibrium partitioning and emulsion phase inversion experiments to assess the partitioning of the inhibitors under different conditions. After establishing the effects of variables such as oil type and electrolyte concentration on the partitioning of the model corrosion inhibitors we also discuss the effect of partitioning from water to oil upon corrosion inhibition in the aqueous phase. We will present the results of electrochemical measurements used to monitor the corrosion rate of steel immersed in aqueous environments in the presence of the model corrosion inhibitors before and after the addition of an oil phase under conditions which cause virtually all of the corrosion inhibitor to favour the oil phase.

Finally, Chapter 6 summarises the main conclusions on all of the experimental results performed in this study of the surfactant aspects of corrosion inhibition together with a discussion of possibilities for future work.

1.8 References

1. G. H. Koch, M.P.H. Brongers, N.G. Thompson, Y.P. Virmani and J.H. Payer, *Corrosion Costs and Preventive Strategies in the United States*, Federal Highway Administration, Office of Infrastructure Research and Development, Report FHWA-RD-01-156 (30th September 2001).

2. K. Bilkova, N. Hackerman and M. Bartos, *Proceedings of NACE Corrosion/2002*, Paper No. 02284, NACE International, Houston (2002).

3. T.H. Bieri, D.I. Horsup, M. Reading and R.C. Woollam, *Proceedings of NACE Corrosion/2006*, Paper No. 06692, NACE International, Houston (2006).

4. *Alaska Hit by 'Massive' Oil Spill*, *BBC News Online*, news.bbc.co.uk/1/hi/world/americas/4795866.stm (11th March 2006).

5. D. Myers, *Surfaces, Interfaces and Colloids: Principles and Applications, 2nd edition*, Wiley-VCH, New York (1999).

6. M.J. Rosen, *Surfactants and Interfacial Phenomena, 2nd edition*, Wiley-Interscience, New York (1989).

7. K. Tsujii, *Surface Activity: Principles, Phenomena and Applications*, Academic Press, London (1998).

8. R. Atkin, V.S.J. Craig, E.J. Wanless and S. Biggs, *Adv. Colloid Interface Sci.*, **103**, 219 (2003).

9. H.G. Tompkins, *A Users' Guide to Ellipsometry*, Academic Press, London (1993).

10. J.W. McBain and C.S. Salmon, *J. Am. Chem. Soc.*, **43**, 426 (1920).

11. Y. Moroi, *Micelles: Theoretical and Applied Aspects*, Plenum Press, New York (1992).

12. J.H. Clint, *Surfactant Aggregation*, Blackie, London (1992).

13. B.P. Binks, in *Modern Aspects of Emulsion Science*, ed. B.P. Binks, Royal Society of Chemistry, Cambridge, p.1 (1998).

14. D.J. Shaw, *Introduction to Colloid and Interface Science, 4th edition*, Butterworth-Heinemann, Oxford (1991).

15. W.D Bancroft, *J. Phys. Chem.*, **17**, 501 (1913).

16. W.C. Griffin, *J. Soc. Cosmet. Chem.*, **1**, 311 (1949).

17. J.T. Davies and E.K. Rideal, *Interfacial Phenomena*, Academic Press, New York (1991).

18. R. Aveyard, B.P. Binks and P.D.I. Fletcher, in *The Structure, Dynamics and Equilibrium Properties of Colloidal Systems*, eds. D.M. Bloor and E. Wyn-Jones, Kluwer Academic, Amsterdam, p.557 (1990).

19. O. Abillon, B.P. Binks, C. Otero, D. Langevin and R. Ober, *J. Phys. Chem.*, **92**, 4411 (1988).

20. B.P. Binks, *Chem. Ind. (London)*, **14**, 537 (1993).

21. R. Aveyard, *Chem. Ind. (London)*, **14**, 474 (1987).

22. H. Kunieda and K. Shinoda, *J. Colloid Interface Sci.*, **106**, 107 (1985).

23. B.P. Binks, *Colloids Surf. A*, **71**, 167 (1993).

24. B.P. Binks, *Langmuir*, **9**, 25 (1993).

25. D.A. Jones, *Principles and Prevention of Corrosion, 2nd Edition*, Prentice-Hall, New Jersey (1996).

26. D. Pletcher, R. Greef, R. Peat, L.M. Peter and J. Robinson, *Instrumental Methods in Electrochemistry*, Horwood Publishing, Chichester (2001).

27. L.M. Gourd, *An Introduction to Engineering Materials*, Edward Arnold, London (1982).

28. D.A. López, T. Pérez and S.N. Simison, *Mater. Des.*, **24**, 561 (2003).

29. H. Fang, S. Nesic, B. Brown and S. Wang, *Proceedings of NACE Corrosion/2006*, Paper No. 06372, NACE International, Houston (2006).

30. T.Y. Soror and M.A. El-Ziady, *Mater. Chem. Phys.*, **77**, 697 (2002).

31. M.L. Free, *Corrosion Sci.*, **44**, 2865 (2002).

32. H. Luo, Y.C. Guan and K.N. Han, *Corrosion*, **54**, 721 (1998).

33. A.J. McMahon, *Colloids Surf.*, **59**, 187 (1991).

34. D.I. Horsup, D. Lewis, K. Sprague, J.H. Clint and T.S. Dunstan, *Proceedings of NACE Corrosion/2007*, Paper No. 07690, NACE International, Houston (2007).

35. S.E. Campbell, K. Bartrip, F. Civan, G. Sanghvi and D. Garcia, *Proceedings of NACE Corrosion/2003*, No. 03337, NACE International, Houston (2003).

36. W.M. Hedges and S.P. Lockledge, *Proceedings of NACE Corrosion/96*, Paper No. 151, NACE International, Houston (1996).

37. J. Kvarekval, R. Nyborg and H. Choi, *Proceedings of NACE Corrosion/2003*, Paper No. 03339, NACE International, Houston (2003).

38. B. Brown, S.R. Parakala and S. Nesic, *Proceedings of NACE Corrosion/2004*, Paper No. 04736, NACE International, Houston (2004).

39. N. Pebre, M. Duprat, F. Dabosi, A. Lattes and A. de Savignac, *J. Appl. Electrochem.*, **18**, 225 (1988).

40. G.T. Hefter, N.A. North and S. H. Tan, *Corrosion*, **53**, 6 (1997).

41. B.P. Binks and P.D.I. Fletcher, *Corrosion Inhibition: A Consultancy Report prepared for Nalco/Exxon Energy Chemicals Ltd.* (2000).

42. N. Hajjaji, I. Rico, A. Srhiri, A. Lattes, M. Soufiaoui and A. Ben Bachir, *Corrosion*, **49**, 326 (1993).

43. M. Elachouri, M.S. Hajji, M. Salem, S. Kertit, J. Aride, R. Coudert and E. Essassi, *Corrosion*, **52**, 103 (1996).

44. B.P. Binks, P.D.I. Fletcher, J.T. Hicks, D.I. Horsup and W.H. Durnie, *Proceedings of NACE Corrosion/2005*, Paper No. 05307, NACE International, Houston (2005).

45. E. Khamis, H.A. Al-Lohedan, A. Al-Mayouf and Z.A. Issa, *Mat.-wiss. U. Werkstofftech*, **28**, 46 (1997).

46. R.D. Braun, E.E. Lopez and D.P. Vollmer, *Corrosion Sci.*, **34**, 1251 (1993).

47. Z. Abdel-Hamid, T.Y. Soror, H.A. El-Dahan and A.M.A. Omar, *Anti-Corrosion Methods and Mat.*, **45**, 306 (1998).

48. S. Ramachandran, B-L. Tsai, M. Blanco, H. Chen, Y. Tang and W.A. Goddard III, *Langmuir*, **12**, 6419 (1996).

49. S. Ramachandran, B-L. Tsai, M. Blanco, H. Chen, Y. Tang and W.A. Goddard III, *J. Phys. Chem. A*, **101**, 83 (1997).

50. D.I. Horsup, J. Caleb, B.P. Binks, P.D.I. Fletcher and J.T. Hicks, *Proceedings of NACE Corrosion/2007*, Paper No. 07617, NACE International, Houston (2007).

51. E. Gulbrandsen and J. Kvarekval, *Proceedings of NACE Corrosion/2004*, Paper No. 04365, NACE International, Houston (2004).

52. T. Moon and D.I. Horsup, *Proceedings of NACE Corrosion/2002*, Paper No. 02298, NACE International, Houston (2002).

CHAPTER 2

Experimental

2.1 Materials

2.1.1 Water

Water was purified by an Elga Prima reverse osmosis unit, and then treated with a Milli-Q reagent water system. Experiments carried out at Nalco (Fawley, UK) used deionised water obtained from a Millipore filtration unit. In both cases the water produced had a resistivity of 18 mΩ cm^{-1} or greater.

2.1.2 Oils

Table 2.1 lists the oils used in this project. Prudhoe Bay crude oil was used as received and all other oils were purified by column chromatography using activated basic alumina (BDH, UK) to remove polar, surface-active impurities. Heptol was made by mixing 70 vol.% heptane and 30 vol.% toluene.

Table 2.1. Supplier and purity of oils.

Name	Purity / %	Supplier
Heptane	> 99	Fisher, UK
Toluene	> 99	Fisher, UK
Prudhoe Bay crude oil (inhibitor free)	n/a	Nalco, USA

2.1.3 Surfactants

Table 2.2 lists the purity and suppliers of surfactants used in this work. All surfactants were used as received except for 1-aminoethyl-2-(8-heptadecenyl)-2-imidazoline, which was acidified with glacial acetic acid (Fisher, UK, purity 99 %) to produce water-soluble 1-aminoethyl-2-(8-heptadecenyl)-2-imidazoline acetate.

2.1.4 Inorganic solids

Table 2.3 lists the purity and suppliers of inorganic solids used in this project. All inorganic solids were used as received except for the mineral samples.

Table 2.2. Supplier and purity of surfactants.

Name	Abbreviation	Purity / %	Supplier
Dodecylbenzyldimethylammonium chloride	C12BDMAC	> 99	Fluka , UK
Tetradecylbenzyldimethylammonium chloride	C14BDMAC	> 99	Fluka , UK
Hexadecylbenzyldimethylammonium chloride	C16BDMAC	> 99	Fluka , UK
1-aminoethyl-2-(8-heptadecenyl)-2-imidazoline acetate	IA	> 60	Nalco, UK
Sodium dodecylsulphate	SDS	> 99	Fluka, UK

Table 2.3. Supplier and purity of inorganic solids.

Name	Formula	Purity / %	Supplier
Boric acid	H_3BO_3	> 99	Fisher, UK
Calcium chloride	$CaCl_2$	> 99	Fisher, UK
Iron (single crystal)	Fe	> 99	MaTech, Germany
Magnesium chloride	$MgCl_2$	> 99	Fisher, UK
Magnetite (iron oxide)	Fe_3O_4	> 90	Ward's, USA
Potassium bromide	KBr	> 99	Fisher, UK
Potassium chloride	KCl	> 99	Fisher, UK
Potassium hydroxide	KOH	≥ 85	BDH, UK
Pyrite (iron sulphide)	FeS_2	> 90	Ward's, USA
Pyrrhotite (iron sulphide)	$Fe_{(1-x)}S$ x = 0 - 0.17	> 90	Ward's, USA
Siderite (iron carbonate)	$FeCO_3$	> 90	Ward's, USA
Sodium chloride	NaCl	≥ 99.5	BDH, UK
Sodium fluoride	NaF	> 99	Fisher, UK
Sodium hydrogen carbonate	$NaHCO_3$	≥ 99.5	BDH, UK
Sodium sulphate	Na_2SO_4	> 99	Fisher, UK
Sodium sulphide	Na_2S	37	Fluka, UK
Strontium chloride	$SrCl_2$	≥ 98	BDH, UK

Table 2.4. Composition of ASTM D1141-90 synthetic brine mixture.

Name	Formula	Composition / wt.%
Sodium chloride	NaCl	68.07
Magnesium chloride	$MgCl_2$	14.43
Sodium sulphate	Na_2SO_4	11.35
Calcium chloride	$CaCl_2$	3.22
Potassium chloride	KCl	1.93
Sodium hydrogen carbonate	$NaHCO_3$	0.56
Potassium bromide	KBr	0.28
Boric acid	H_3BO_3	0.075
Strontium chloride	$SrCl_2$	0.069
Sodium fluoride	NaF	0.008

Mineral samples were polished for use in ellipsometry measurements using a using a Motopol grinder/polisher (Buehler, UK); grains of each mineral were mounted in trans-optic mounts made from Lucite (Leco, UK) using a Simplimet mounting press (Beuhler) before planar grinding with a Metlap 10 ceramic grinding platen (Buehler) with a 45 μm colloidal diamond aerosol abrasive. Following planar grinding, a Metlap 4 iron composite grinding platen (Buehler) was used with 14 μm colloidal diamond aerosol followed by a Pan-W chemotextile cloth (Leco) with 3 μm diamond polishing compound (Kemet, UK). The final polishing stage used an Imperial napped cloth (Leco) with 1 μm diamond polishing compound (Kemet), and then the samples were cleaned by ultrasonic cleaning in methanol followed by drying with a hair dryer.

Synthetic brine mixture was prepared according to ASTM D1141-90[1]; the composition of this salt mixture is given in Table 2.4.

2.1.5 Gases

Carbon dioxide gas cylinders (purity 99 %) were purchased from Energas, UK and were used as received. Gas sparging was performed using a gas dispersion tube (VWR, UK).

2.1.6 Steel

There are many different types of steel available and these are designated to a specific

grade, type or class of steel by a number, letter, symbol or name. Within the steel industry they have very specific uses. Grade is used to denote chemical composition; type is used to indicate deoxidation practice, and class is used to describe some other attribute, such as mechanical strength or surface finish. In this study we have used AISI / SAE C1018 steel, a carbon steel whose composition is given in Table 2.5. Steel specimens with different dimensions and surface finishes were used depending on the type of experiment in which they were used.

Table 2.5. Composition of 1018 carbon steel[2].

Element	Fe	Mn	Si	C	P	N
Composition (%)	98.898	0.72	0.19	0.18	0.009	0.003

1018 carbon steel discs (diameter 35 mm, thickness 3 mm) purchased from European Corrosion Supplies, UK were used in ellipsometry measurements. The 1018 steel discs were first cut into quarters and then polished to a mirror-like finish using a five-step procedure using a Motopol grinder/polisher (Buehler, UK). Before polishing, the steel quadrants were mounted in Lucite (Leco, UK) or Bakelite (Kemet, UK) using a hot mounting procedure. The first two grinding steps used 240 and 600 grit silicon carbide papers (Buehler) respectively, with water as a lubricant to achieve a level surface. The coarse polishing step used a Pan-W chemotextile polishing cloth (Leco) with a small amount of 6 μm diamond polishing compound (Kemet) with OS (oil soluble) type lubricant. The fine polishing step used an Imperial short nap polishing cloth (Leco) with a small amount of 1 μm diamond polishing compound plus OS type lubricant. The final step used an Imperial napped polishing cloth (Leco) with 0.1 μm colloidal silica dispersion (Buehler) as an abrasive to achieve a level, highly reflective surface. The steel discs were cleaned following polishing and before each experimental run by ultrasonic cleaning in methanol followed by drying with a hair dryer.

1018 carbon steel electrodes (diameter 4 mm, length 30 mm) for linear polarization resistance measurements were supplied by European Corrosion Supplies, UK. The electrodes were received in vapour corrosion inhibitor (VCI) impregnated envelopes. They were washed in acetone to remove the VCI and then dried in an oven at 60 °C prior to use.

1018 carbon steel coupons (width 6.35 mm, length 187.33 mm, thickness 1.58 mm) with a sandblast finish were used for weight-loss corrosion rate measurements.

2.1.7 Glassware

All glassware was cleaned in a solution of 10 wt.% KOH in ethanol to remove any surfactant residues. The clean glassware was rinsed with copious amounts of Milli-Q water and then dried in an oven at 45 °C.

2.2 Methods

2.2.1 Ellipsometry

Ellipsometry is the measurement of the effect of reflection on the state of polarization of light[3,4]. These measurements can be used to determine the optical constants of a reflecting surface, or the thickness and optical constants of thin films adsorbed onto a reflecting substrate. Ellipsometry can be applied to adsorbed films ranging from nanometre (partial atomic coverage) to micrometer (polymer films) thickness. This makes ellipsometry extremely useful for studying surfactant adsorption at solid-liquid interfaces[5].

A monochromatic light source, such as a laser, consists of an alternating electric and magnetic field, which are perpendicular to one another and orthogonal to the direction of propagation. The state of polarization is defined by the phase and amplitude relationships between the two component plane waves of the electric field. One component is parallel to the plane of incidence (p-wave), the other component is normal to the plane of incidence (s-wave). There are three types of polarization: linearly, circularly and elliptically polarized (Figure 2.1). In general, reflection causes a change in the relative phases (δ_p-δ_s) of the s- and p-waves and the ratio of their amplitudes (A_p/A_s) such that:

$$\tan\Psi = \frac{A_p^r / A_s^r}{A_p^i / A_s^i} \tag{2.1}$$

and

$$\Delta = \left(\delta_p^r - \delta_s^r\right) - \left(\delta_p^i - \delta_s^i\right) \tag{2.2}$$

where i and r denote incident and reflected beams, respectively. Ψ, the amplitude component, and Δ, the phase component, are the parameters measured by an

Figure 2.1. Schematic drawing showing the three polarization states of light.

(a) Linearly polarized: the s- and p-waves propagate in the same direction, orthogonal and in phase with each other.

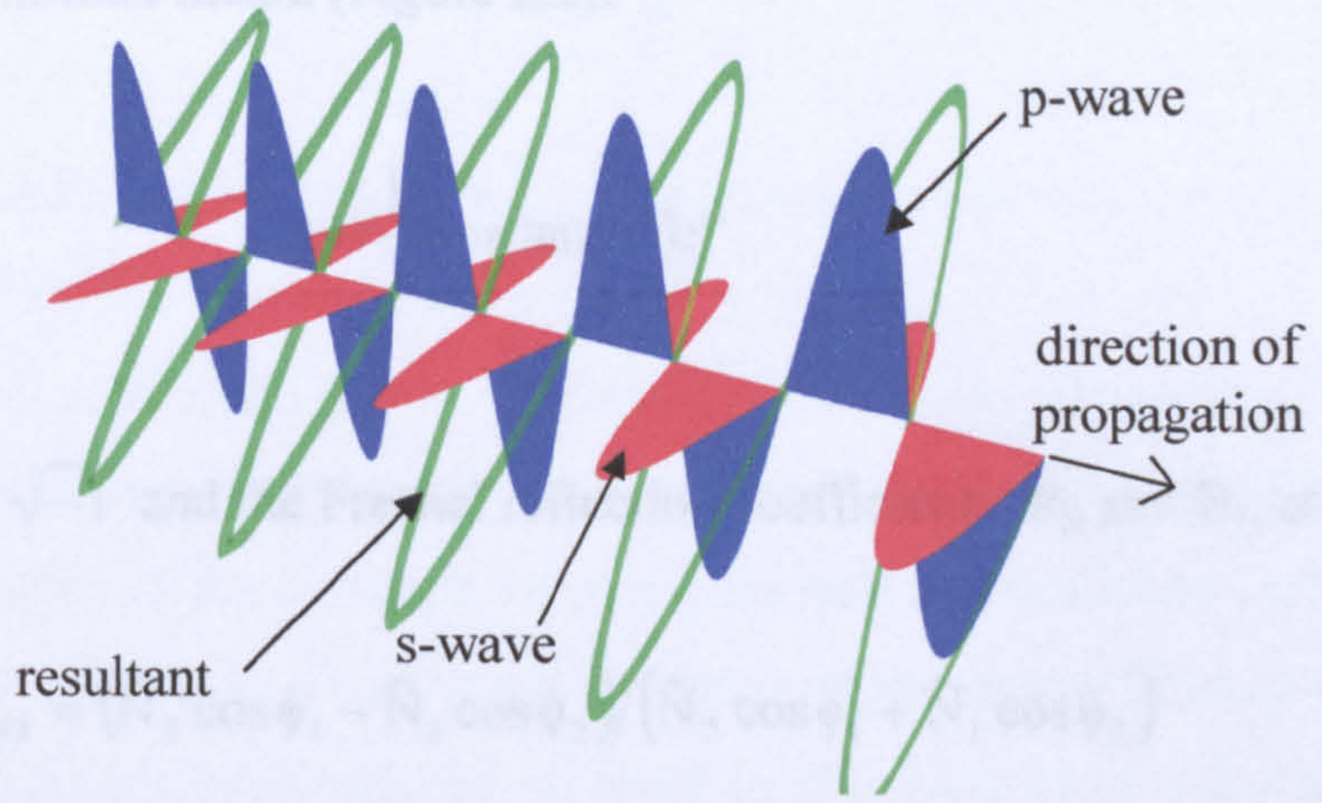

(b) Circularly polarized: the two component waves are equal in amplitude and 90° out of phase (one reaches a maximum as the other is at a minimum).

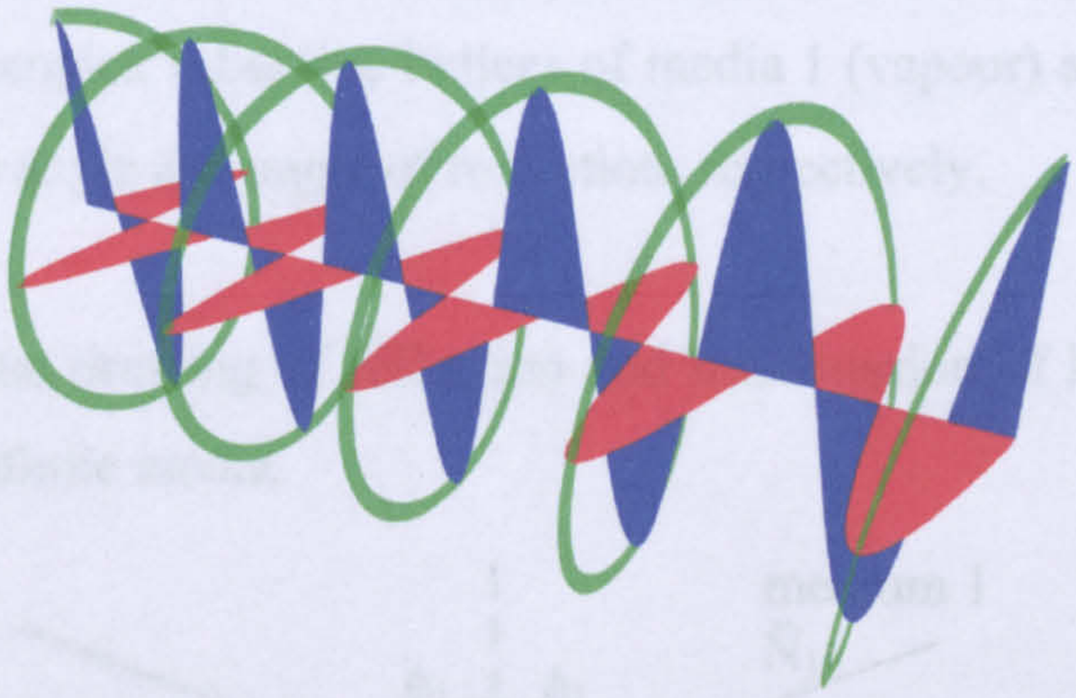

c) Elliptically polarized: the s- and p-waves take on arbitrary phase and amplitudes.

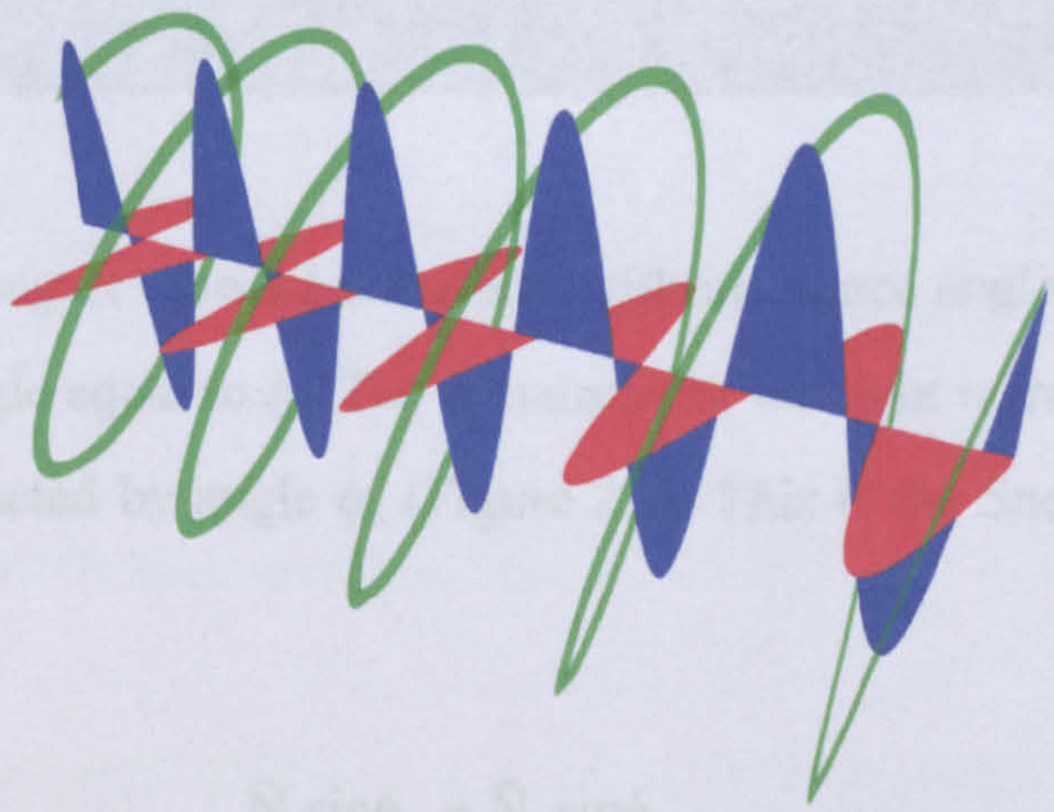

ellipsometer (in units of degrees). Ψ and Δ are related to the ratio (ρ) of Fresnel reflection coefficients R_p and R_s (equation (2.3)) for the p-and s-waves, which are derived from the oblique reflection and transmission of a plane wave at the interface between two semi-infinite media (Figure 2.2):

$$\rho = \frac{R_p}{R_s} = \tan(\Psi)e^{i\Delta} \tag{2.3}$$

where i is equal to $\sqrt{-1}$ and the Fresnel reflection coefficients, R_p and R_s, are given by:

$$R_{p12} = \left(\tilde{N}_2 \cos\phi_1 - \tilde{N}_1 \cos\phi_2\right)/\left(\tilde{N}_2 \cos\phi_1 + \tilde{N}_1 \cos\phi_2\right) \tag{2.4}$$

and

$$R_{s12} = \left(\tilde{N}_1 \cos\phi_1 - \tilde{N}_2 \cos\phi_2\right)/\left(\tilde{N}_1 \cos\phi_1 + \tilde{N}_2 \cos\phi_2\right) \tag{2.5}$$

where $\tilde{N}_{1,2}$ are the complex refractive indices of media 1 (vapour) and 2 (substrate) and $\phi_{1,2}$ are the incidence angle and angle of refraction, respectively.

Figure 2.2. Schematic drawing of reflection and transmission of light at the interface between two semi-infinite media.

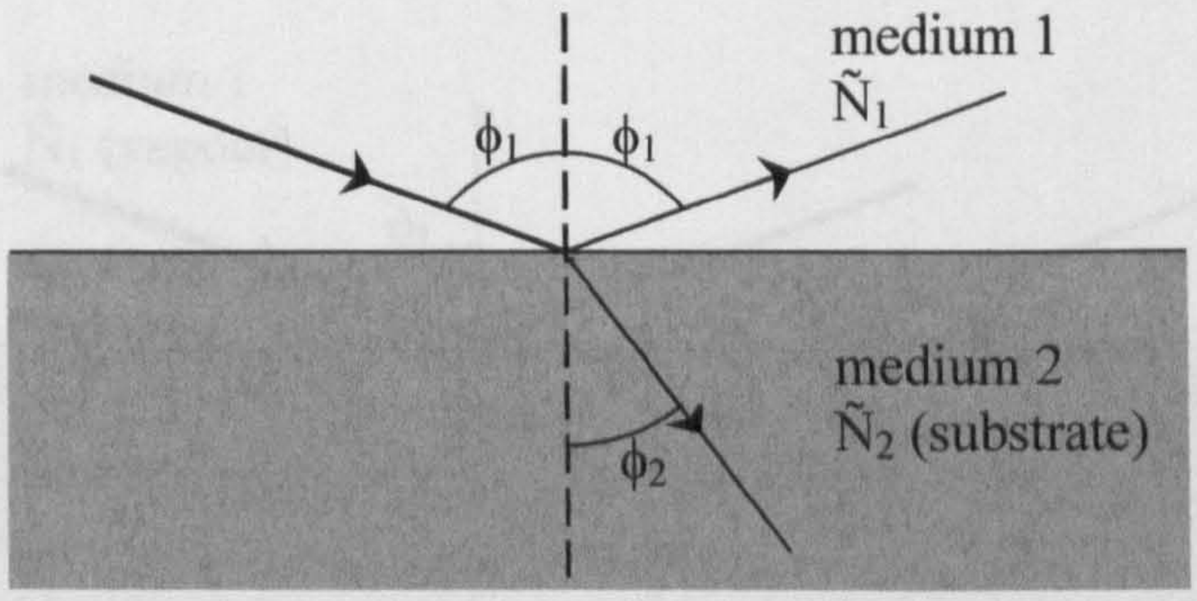

As a light beam propagates toward a surface, with incidence angle ϕ_1, some of the light is reflected, at an angle equal to ϕ_1. The remainder of the light is transmitted through the substrate and is refracted by angle ϕ_2 (Figure 2.2). This is the Snell's law of refraction and is given by:

$$\tilde{N}_1 \sin\phi_1 = \tilde{N}_2 \sin\phi_2 \tag{2.6}$$

The complex refractive index, $\tilde{N}$, of a material describes the interaction of light with the material:

$$\tilde{N} = n - ik \tag{2.7}$$

where n is the real index of refraction and k is the imaginary part of the refractive index (or extinction coefficient).

When unpolarized light makes a reflection with a specific angle of incidence, none of the light polarized parallel to the plane of incidence is reflected. It is completely transmitted, and therefore the reflected light is polarized perpendicular to the plane of incidence. This specific angle is called the Brewster angle, and is used as the angle of incidence in ellipsometry measurements in order to give maximum polarization of the light reflected from an interface and minimise the intensity of reflected parallel polarization. If a reflecting surface is covered with a film, or multiple films, the resultant reflected light returning to the ambient consists of light reflected directly from the first interface plus all transmissions from light approaching the interface from the film (Figure 2.3).

Figure 2.3. Schematic diagram showing reflection and transmission with multiple interfaces.

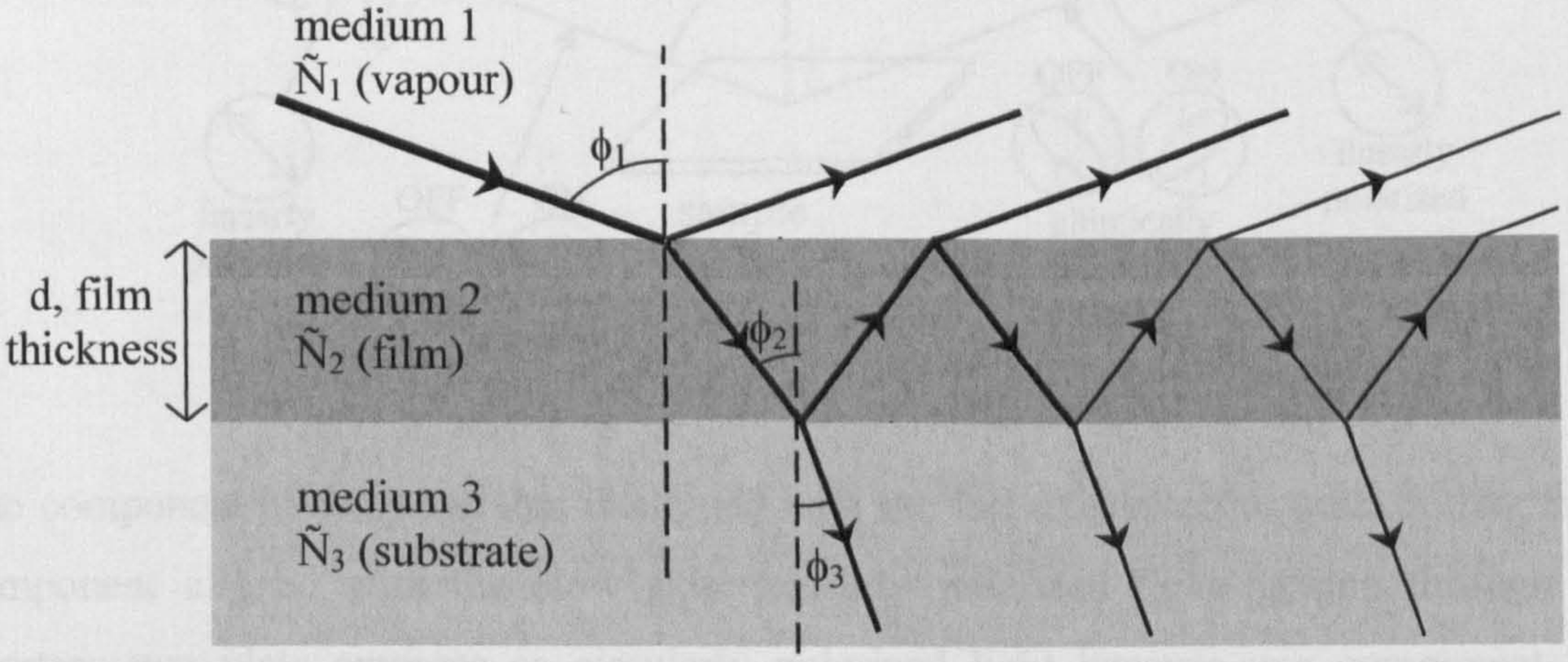

The total reflection coefficients are given by:

$$R^p = \frac{r_{12}^p + r_{23}^p \exp(-j2\beta)}{1 + r_{12}^p + r_{23}^p \exp(-j2\beta)} \qquad R^s = \frac{r_{12}^s + r_{23}^s \exp(-j2\beta)}{1 + r_{12}^s + r_{23}^s \exp(-j2\beta)} \tag{2.8}$$

where the subscript "12" denotes the Fresnel reflection coefficients for the interface between medium 1 and medium 2. β is the film phase thickness given by:

$$\beta = 2\pi\left(\frac{d}{\lambda}\right)\tilde{N}_2 \cos\phi_2 \tag{2.9}$$

where d is the film thickness and λ is the wavelength of the incident radiation.

Figure 2.4 shows a schematic of a typical ellipsometer. An unpolarized, monochromatic light source is polarized by a calcite Glan-Thompson polarizer to produce linearly polarized light. The linearly polarized light then passes through a compensator or quarter-wave plate, an anisotropic optical element, which has a fast and a slow axis, both perpendicular to one another and to the direction of propagation.

Figure 2.4. Schematic drawing of a typical ellipsometer.

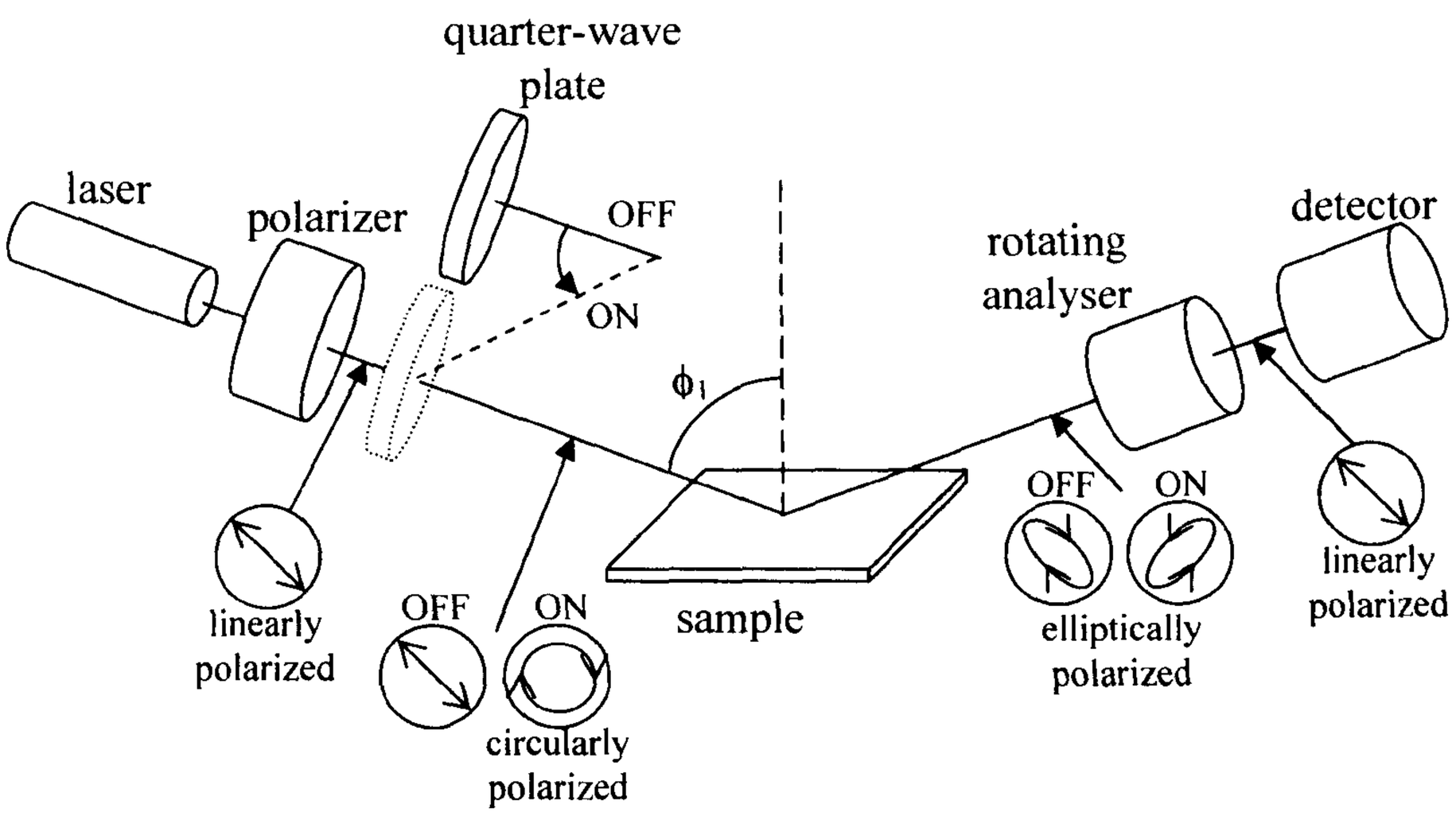

The component of the wave that is aligned with the fast axis emerges quicker than the component aligned with the slow axis. Linearly polarized light passing through a quarter-wave plate emerges as circularly polarized light because one component is retarded by a quarter of a wavelength such that the phase difference between the two components of the electrical field vector is 90°. Reflection of circularly polarized light from the substrate causes a phase shift, affecting one or both of the components of the electric field vector producing elliptically polarized light. A second Glan-Thompson prism acts as the analyser, which determines the state of polarization of the reflected, elliptically polarized light while a photodetector determines the amplitude.

Ellipsometers measure Ψ and Δ; they do not measure film thicknesses directly. The quantities Ψ and Δ are used with an assumed model to calculate the thickness and complex refractive index of adsorbing films. Correct Ψ and Δ values can produce unfeasible optical parameters and film thicknesses if an inappropriate model is used. In the majority of ellipsometric investigations, a film adsorbed on top of a substrate will be of interest. A material is a substrate if its thickness and extinction coefficient are such that light entering the material is totally absorbed. If the substrate is a dielectric (k = 0), its lower boundary should be far enough away or rough enough that reflected light does not contribute to the total reflections entering the analyser. A material is considered a film if it is transparent enough that the underlying interface must be considered.

The optical constants of the substrate must be known in order to determine the properties of the film so ellipsometry is used to determine n and k for the substrate. Optical parameters for many materials have been measured and tabulated in the literature; however, unless a material is extremely reproducible, its optical constants will vary. Therefore it is important to measure the optical constants of the particular sample being studied. For a substrate covered by a film (Figure 2.3), values of n_2, k_2, n_3, k_3 and thickness, d, can be used with equations (2.3) – (2.6), (2.8) and (2.9) to calculate expected values of Ψ and Δ. In 1969 McCrackin produced a FORTRAN program to perform ellipsometry calculations including calculation of Ψ and Δ values for various film thicknesses, called Ψ/Δ trajectories[6]. For the determination of substrate parameters the program requires experimental values along with initial approximations for the real and imaginary parts of the complex refractive index. The program calculates Ψ and Δ values based on the approximations and then adjusts, or floats, these parameters until the difference between the measured and calculated values, the sum difference, is minimised. For the determination of the refractive index and thickness of adsorbed films, the McCrackin program uses the complex refractive index of the substrate and experimental Ψ and Δ values; there are two different methods that can be used from this point. The first involves estimating the thickness and refractive index of the film and simultaneously floating these variables until agreement is reached between the measured and calculated values of Ψ and Δ. The second method involves fixing the refractive index of the film whilst floating the thickness. The fixed value of the refractive index of the film can be obtained from literature values or determined by refractometry.

In this study, all ellipsometry measurements were performed using a Plasmos SD2300 instrument (Philips), which is equipped with a 632.8 nm wavelength HeNe

laser. The incidence angle used was 70°, close to the Brewster angle for pure iron substrates. The 1018 low carbon steel disc was placed within a quartz sample cell, with transmitting sidewalls angled at 70° (Hellma, Germany). Measurements of the ellipsometric angles Δ and Ψ were carried out at 25 ± 0.1 °C, using an Air Therm thermostat (World Precision Instruments, USA) to maintain the temperature of the system in the cell, which was enclosed within a polythene tent. The experimental values were analysed using an in-house version of the original McCrackin program.

2.2.1.1 Equilibrium inhibitor film thickness measurements

Measurement of Ψ and Δ values for the polished 1018 steel was first carried out in air. Following this, 40 ml of Milli-Q water was added to the cell, and the Ψ and Δ values were re-measured. The steel disc was not moved so that the incident laser beam probed the same region of the surface as in air. One hundred Ψ and Δ measurements were recorded in each medium, taking approximately 4 min. The mean of the final ten measurements was used for calculation of the complex refractive index of the steel in each medium.

A batch method was used for the adsorption experiments. Firstly the Milli-Q water was removed from the cell using a Pasteur pipette to avoid disturbing the steel disc. Then 40 ml of 0.01 mM dodecylbenzyldimethylammonium chloride solution was added to the cell, and then one hundred Ψ and Δ measurements were recorded. The mean of the final ten measurements was used in subsequent calculations. This method was repeated using 0.1 – 100 mM aqueous solutions of C12BDMAC.

The refractive index of C12BDMAC was determined with an Abbé refractometer (Hilger, UK) which was thermostatted at 25 ± 0.1 °C using a Grant LTD6G water bath. The refractive index and optical dispersion were measured for aqueous solutions of C12BDMAC from 1 – 10 wt.% using incident light from a sodium vapour lamp (λ = 589 nm). These values were used to determine the refractive index of pure C12BDMAC at a wavelength of 632.8 nm.

2.2.1.2 Dynamic corrosion measurements

Dynamic ellipsometry measurements were performed in brine solutions under three different gas conditions; aerated, CO_2 or H_2S conditions at atmospheric pressure. 40 ml of 4.7 wt.% brine, under the relevant gas condition, was prepared prior to the

ellipsometric measurement. CO_2 gas conditions were established by sparging brine with CO_2 gas using a gas dispersion tube for 30 min. H_2S gas conditions were produced by sparging brine with CO_2 gas for 30 min. Then sodium sulphide (Na_2S) was added to the acidic brine to generate 18 ppm H_2S in solution. Under CO_2 and H_2S conditions, plastic tubing fed CO_2 gas into the headspace above the solution, through a Plexiglas lid, to maintain the gas saturation. Measurement of Δ and Ψ was started as soon as the liquid had been added to the cell. Dodecylbenzyldimethylammonium chloride or imidazoline acetate was added to the cell after 30 min. of pre-corrosion, apart from the control experiments in the absence of surfactant. Following each experiment the discs were quickly washed with Milli-Q water, then acetone, dried and stored under vacuum in a desiccator.

2.2.1.3 Determination of optical constants of iron and minerals

Measurement of Δ and Ψ for an iron single crystal and mineral samples were performed under air. The polished mineral grains were kept in the trans-optic mounts so that they could easily be placed level on the ellipsometer stage. One hundred Δ and Ψ measurements were recorded under air for samples of magnetite, pyrite, pyrrhotite and siderite. The same protocol was also used for the polished single crystal of iron. The mean of the final ten Δ and Ψ values was used in subsequent calculations to determine the complex refractive index.

2.2.2 Corrosion rate measurements

2.2.2.1 Linear polarization resistance method

The 'bubble test' is a cheap and extremely effective method of screening corrosion inhibitors. The test simulates pipeline corrosion conditions using aqueous and hydrocarbon phases in aerated, CO_2 and H_2S environments. Linear polarization resistance (LPR) continually measures the corrosion rate of steel electrodes over a period of 15 – 20 hr.

The LPR technique involves applying a potential to a freely corroding steel specimen and measuring the resultant current response. The potential is generally applied step-wise, beginning below the free corrosion potential and terminating above it. The polarization resistance (R_p) is defined as the ratio of the applied potential to the current response and is inversely proportional to the corrosion current density and

therefore the corrosion rate (equation (2.10))[7]. R_p is obtained from the gradient of a measured potential versus current curve. The corrosion current density (i_{corr}) is calculated from R_p.

$$R_p = \frac{\Delta\varepsilon}{\Delta i} = \frac{B}{i_{corr}} \tag{2.10}$$

where ε is the overvoltage impressed on the corroding electrode and B is an empirically determined proportionality constant for the system:

$$B = \frac{\beta_a \beta_c}{2.3(\beta_a + \beta_c)} \tag{2.11}$$

where β_a and β_c represent the Tafel constants for the anodic and cathodic half-cell reactions, respectively.

The corrosion rate is calculated using Faraday's law of electrolysis, which defines the proportionality between the current and mass reacted in an electrochemical reaction (equation (2.11)):

$$m = \frac{I_{corr} t a}{nF} \tag{2.12}$$

where m is the mass reacted, I_{corr} is the corrosion current, t is the time, a is the atomic weight, n is the number of equivalents (electrons) exchanged and F is Faraday's constant. In the oxidation of iron (equation (1.1)) two equivalents are transferred for each atomic weight reacted, so n = 2. Dividing equation (2.12) by time and the surface area gives the corrosion rate:

$$r = \frac{m}{tA} = \frac{i_{corr} a}{nF} \tag{2.13}$$

where r is the corrosion rate, A is the surface area and i is the current density, which equals I/A. Equation (2.12) shows a proportionality between mass lost per unit area per unit time and current density. The proportionality constant includes a/nF and any unit conversion factors. It is the current density that is proportional to the corrosion rate

rather than current because the same current concentrated into a smaller area results in a higher corrosion rate. Units of corrosion rate are obtained by dividing equation (2.13) by the density of the metal. To obtain the corrosion rate in units of millimetres per year, equation (2.13) becomes:

$$r = 3.27 \times 10^{-3} \frac{i_{corr} a}{n\rho} \qquad (2.14)$$

for units of i, $\mu A\ cm^{-2}$, and ρ, $g\ cm^{-3}$ where ρ is the density of the metal.

In this project the 'bubble test' method was used to determine the corrosion inhibition efficiency of dodecylbenzyldimethylammonium chloride (C12BDMAC) and 1-aminoethyl-2-(8-heptadecenyl)-2-imidazoline acetate (IA) on the corrosion of 1018 steel in aqueous solution under aerated, CO_2 and H_2S conditions, in the presence and absence of electrolyte at 25 °C. In a separate line of study, corrosion rate measurements were carried out with hexadecylbenzyldimethylammonium chloride (C16BDMAC) and IA in the presence of oil. All bubble test measurements were carried out at Nalco, Fawley, UK.

800 ml of the relevant aqueous phase (deionised water or 4.7 wt.% brine) was added to a flange cell and a black nitrile O-ring was placed on the flange of the cell. Then the lids were placed on top and secured with bulldog clips to prevent ingress of air into the cell. The temperature probes, gas dispersion tubes, condensers and air traps were then fitted to the lid as required (Figure 2.5). The system was thermostatted at 25 ± 0.2 °C by a hotplate and stirred at a speed of 200 rpm with a magnetic stirrer. For aerated conditions the cell was open to the atmosphere, so there was no need to fit spargers, condensers or gas bubblers to the cell. For CO_2 conditions the aqueous phase in the cell was sparged with CO_2 for 2 hr. prior to the start of the experiment to ensure CO_2 saturation. For H_2S conditions the aqueous phase was sparged with CO_2 for 2 hr., then aqueous sodium sulphide (Na_2S) was added to generate 18 ppm of H_2S in solution.

The probe consists of a stainless steel rod fitted with three 1018 steel electrodes; the working, counter and reference electrodes. The electrodes were screwed onto the stainless steel rod along with small nitrile O-rings to prevent contact between the electrodes and the stainless steel rod, and then the probes were immediately added to the pre-heated and sparged cells. The reference electrode measures the rest potential, the natural potential that exists in the system. The GillAC 12 potentiostat (ACM Instruments, UK) applies a potential from –10 mV through to 10 mV to the working

electrode, forcing a current to flow between the working and counter electrodes. The current is measured by the zero resistance ammeter in the potentiostat and the corrosion rate is calculated by the computer software.

Figure 2.5. The 'bubble test' setup.

(a) Schematic representation

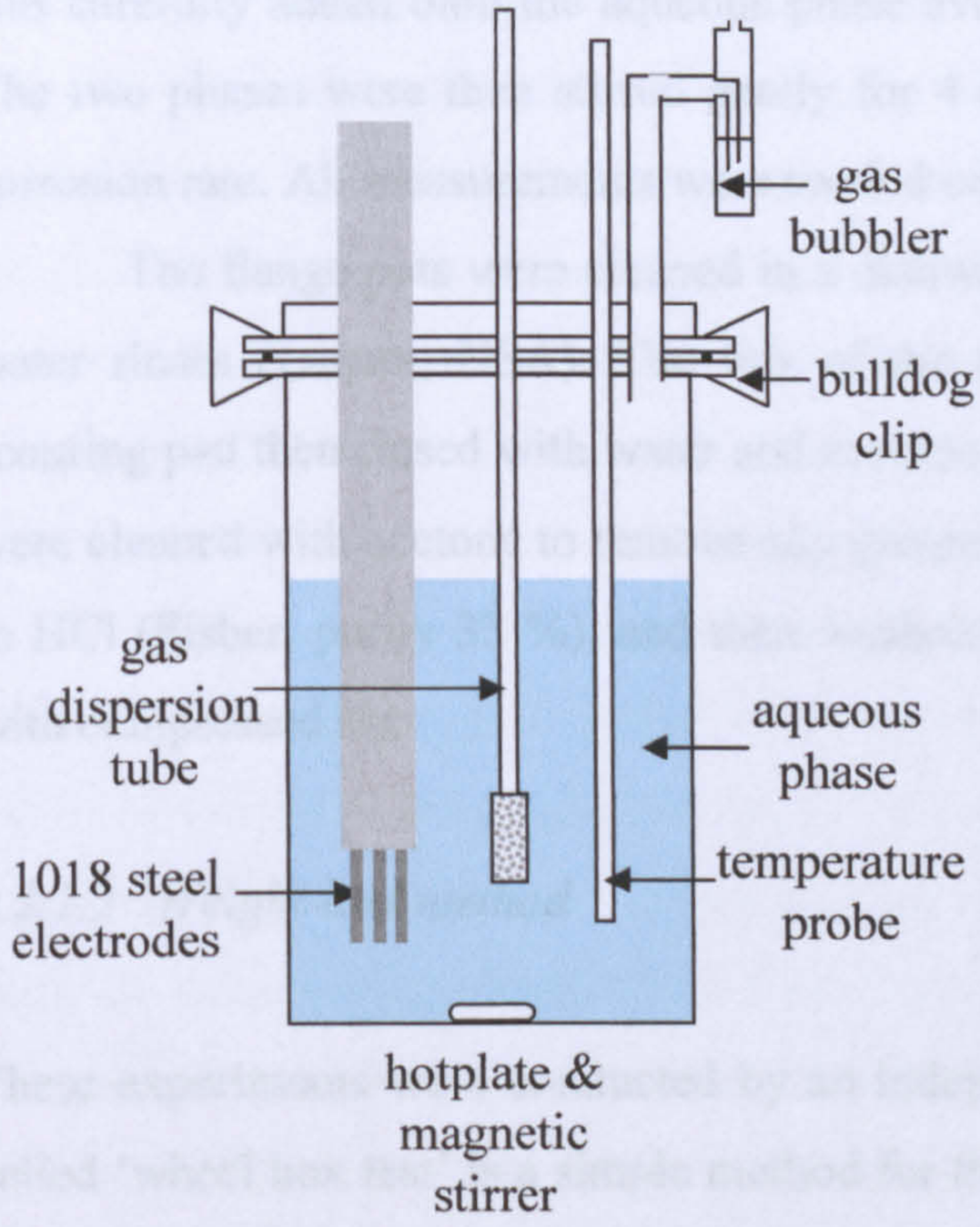

(b) Photograph of the cell

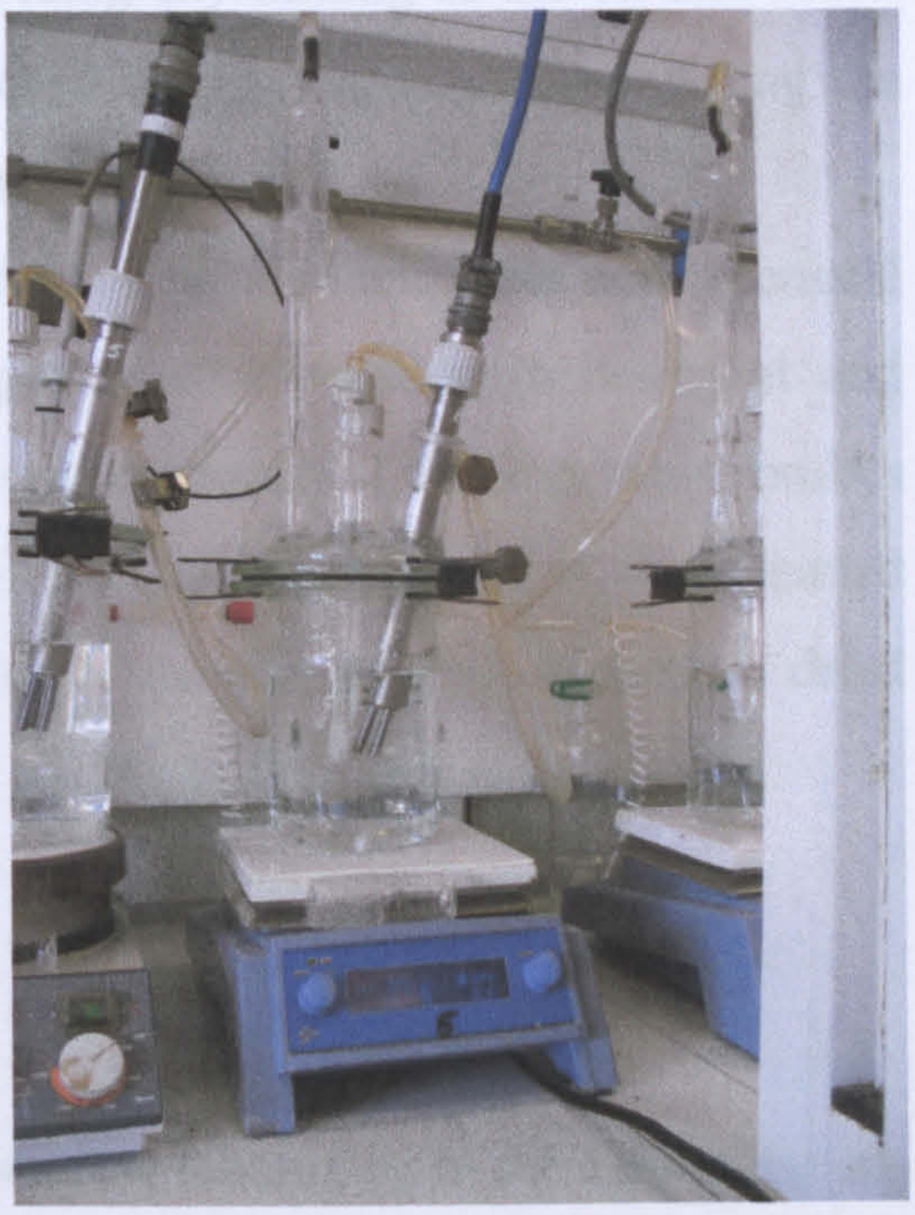

For each gas system under investigation, the corrosion rate in the presence of surfactant, at concentrations of 0.01 - 100 mM, was monitored with time. In addition, control experiments were carried out in the absence of corrosion inhibitor. Once the cells were prepared and the probes were added, the electrodes were allowed to corrode in the absence of any surfactant for 30 min. before the addition of the surfactant. The measurement continued for 15 – 20 hr. or until there was no significant change in the corrosion rate. All measurements were made in duplicate. The bubble test apparatus allows twelve cells to be studied simultaneously. However, the measurements do not take place continuously; the corrosion rate of each cell is measured in sequence at ten minute intervals. All the electrochemical probes were added to the cells at the same time and were allowed to pre-corrode for 30 min. The frequency of the measurements means that the corrosion rate of some cells are not measured during the pre-corrosion period, therefore the effect of addition of surfactant on the corrosion rate is not

immediately obvious. The performance of the surfactants as corrosion inhibitors was determined by comparing the long-time corrosion rates of 1018 in the presence and absence of surfactant.

Experiments carried out in the presence of oil were carried out using a similar protocol. Firstly, the corrosion rate of 1018 steel electrodes was measured in 500 ml of the relevant aqueous phase under H_2S conditions, with addition of the surfactants after 30 min. of pre-corrosion. 24 hr. after the addition of the surfactant, 500 ml of toluene was carefully added onto the aqueous phase avoiding any mixing of the oil and brine. The two phases were then stirred gently for 4 days whilst continually monitoring the corrosion rate. All measurements were carried out in duplicate.

The flange pots were cleaned in a dishwasher equipped with acid and deionised water rinses (Lancer, USA). The lids of the pots were cleaned with detergent and scouring pad then rinsed with water and acetone and left to dry. The temperature probes were cleaned with acetone to remove any grease. The gas dispersion tubes were cleaned in HCl (Fisher, purity 33 %), and then washed with water and then acetone and dried with compressed air.

2.2.2.2 Weight-loss method

These experiments were conducted by an independent laboratory in the USA. The so-called 'wheel box test' is a simple method for the determination of the corrosion rate of steel by weight-loss. Experiments were conducted in the presence and absence of an oil phase. Either 200 ml of the relevant aqueous phase (deionised water or 4.7 wt.% brine) or 180 ml of the relevant aqueous phase plus 20 ml of depolarized kerosene was siphoned into beverage-type bottles with a flow of the prescribed gas (CO_2 and H_2S), except for those under aerated conditions which were under normal atmospheric conditions. Then the inhibitor was added to the bottles, except the uninhibited control experiments. Weighed 1018 steel coupons were fitted into the bottles, which were placed on a wheel rotating at 26 rpm for 24 hr. The bottles are capped under a blanket of prescribed gas to displace air in the vapour phase of the test bottle. The coupon fits top to bottom in the bottle and remains stationary throughout the duration of the test allowing for consistent flow of the corrosive fluids over the coupon. After 24 hr. the coupons were removed from the bottles, cleaned, weighed and the weight loss used to calculate the corrosion rate. All wheelbox measurements were made in triplicate.

2.2.3 Scanning Electron Microscopy and Energy Dispersive X-Ray Analysis

A scanning electron microscope (SEM) is a type of electron microscope capable of producing high resolution images of a sample surface. In a typical SEM, electrons are emitted from a cathode (typically tungsten or lanthanum hexaboride) and are accelerated towards an anode. The electron beam is focused by one or two condenser lenses into a beam with a very fine focal spot (approximately 1 - 5 nm in diameter). The beam passes through pairs of scanning coils in the objective lens, which deflect the beam in a raster fashion over a rectangular area of the sample surface. Images are produced by monitoring low energy secondary electrons. The brightness of the signal depends on the number of secondary electrons reaching the detector; the resulting signal is rendered into a two-dimensional intensity distribution that can be viewed as a digital image. The SEM is also fitted with a backscattered electron detector, which is used to detect contrast between areas with different chemical compositions.

Energy dispersive X-ray analysis (EDX) is an elemental analysis technique, which is commonly used in conjunction with SEM. When the primary electron beam of the SEM interacts with an atom of the sample, an electron from the inner electron shell may be ejected resulting in a vacancy, leaving the atom in an excited state[8]. An electron from an outer valence shell can fill this vacancy, de-exciting the atom. The energy released upon de-excitation can be released by emission of an X-ray photon. EDX uses a silicon-lithium detector. When an X-ray photon strikes the detector it generates a photoelectron within the body of the Si. As this photoelectron travels through the Si, it generates electron-hole pairs. The electrons and holes are attracted to opposite ends of the detector with the aid of a strong electric field. The size of the current pulse generated depends on the number of electron-hole pairs created, which depends on the energy of the incoming X-ray. The composition of the material is determined by the detection of chemical elements' characteristic X-ray emission lines.

In this study SEM and EDX were used to view the changes occurring on the surface of 1018 steel when corroded under different gas conditions in the presence and absence of surfactants. Images of the polished and corroded 1018 steel samples were captured using two different scanning electron microscopes. A LEO Stereo Scan 360 SEM (Zeiss-Bragg, formerly Cambridge Instruments, UK) was initially used. Prior to the imaging process the discs were coated with a ~10 nm thin film of carbon (spectrally pure graphite) using a high vacuum evaporator (Edwards, USA). This was later replaced

by an EVO 60 SEM (Carl Zeiss SMT AG, Germany) equipped with an INCAEnergy 350 EDX detector (Oxford Instruments, UK).

2.2.4 Phase behaviour of corrosion inhibitors

2.2.4.1 Air-water surface tension measurements

Surface tension measurements are commonly determined using the du Noüy ring method. When the ring is pulled through the air-liquid interface a meniscus forms (Figure 2.6). Harkins and Jordan[9] have shown that the surface tension of a liquid, γ, is given by:

$$\gamma = \frac{mgF}{4\pi R} = \frac{\Delta\rho VgF}{4\pi R} \qquad (2.15)$$

where R is the radius of the ring, g is the acceleration due to gravity and m is the mass of solution raised my the ring. F is a correction factor, which is a function of R^3/V and R/r, where V is the volume of liquid pulled through the surface by the maximum pull of the ring and r is the radius of the wire from which the ring is constructed. The correction factors are applied by measuring the radii of the ring and the wire, and the density difference between the liquid and air.

Figure 2.6. Schematic representation of the du Noüy ring used for the determination of surface tensions of liquids.

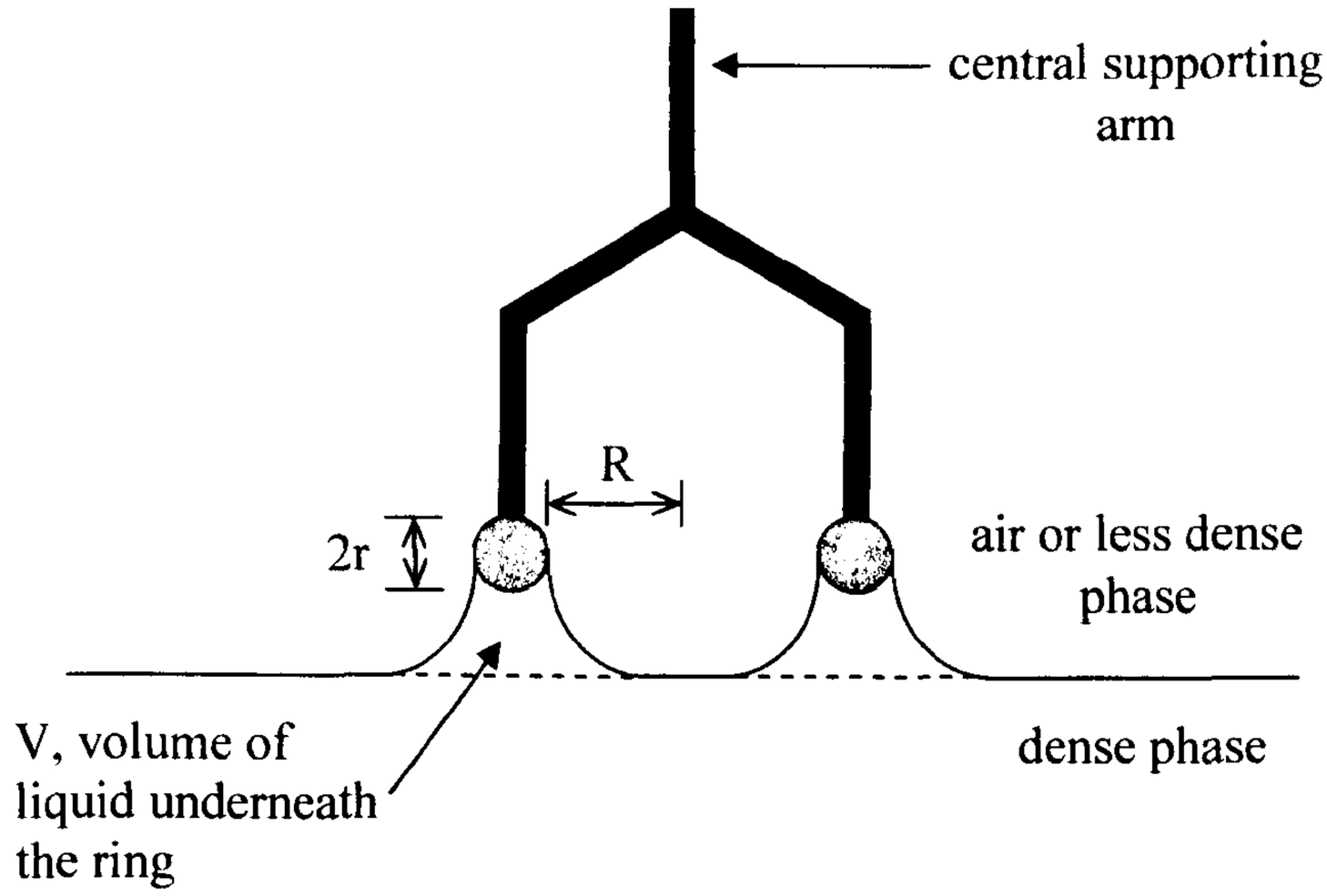

In this study air-water surface tension measurements were used to determine the critical micelle concentration of surfactants in aqueous solution, in the presence and absence of electrolyte. The measurements were performed using the du Noüy ring method on a K12 processor tensiometer (Krüss, Germany) thermostatted by an LTD6G water bath (Grant, UK). The tensiometer automatically applies the equation of Zuidema and Waters[10] (equation (2.16)), which corrects the measured values for the weight of the liquid meniscus:

$$F = 0.725 + \sqrt{\frac{0.01452\gamma}{U^2/4 \cdot \Delta\rho} + 0.04534 - \frac{1.679}{R/r}} \qquad (2.16)$$

where U is the wetted length (equal to two times the circumference of the ring) and $\Delta\rho$ is the density difference between the two phases.

The platinum/iridium du Noüy ring (R = 9.545 mm, r = 0.185 mm) was placed in the apparatus, then the liquid was added to a glass vessel within a thermostatted cell and left to equilibrate. Using the fully automatic measurement method, the tensiometer dips the ring into the liquid and then pulls it out automatically by raising and lowering the height of the thermostatted cell. As the ring is pulled from the liquid surface a meniscus forms. The force required to raise the meniscus reaches a maximum when the tangent at the point of wetting is perpendicular to the liquid surface. At least three measurements were recorded for each liquid; the reproducibility was within ± 0.1 mN m^{-1}. Prior to each measurement, the ring was cleaned in a solution of 10 wt.% KOH in ethanol then rinsed with Milli-Q water and finally heated in a blue Bunsen burner until the ring glowed white.

2.2.4.2 Determination of partition coefficient of surfactant between oil and water

Partitioning of alkylbenzyldimethylammonium chlorides between aqueous and oil phases was investigated at equal volume ratios of oil and water and 1:10 in favour of oil. For 1:1 volume ratio, 50 ml of aqueous surfactant solution (with or without 4.7 wt.% brine) was placed in a specially designed cell containing a magnetic stirrer bar (Figure 2.7). Then 50 ml of the relevant oil was added very gently down the side of the cell so as not to cause any mixing of the two phases.

Figure 2.7. Schematic representation of the cell used in the determination of the partition coefficient for equal volume ratios of oil and water.

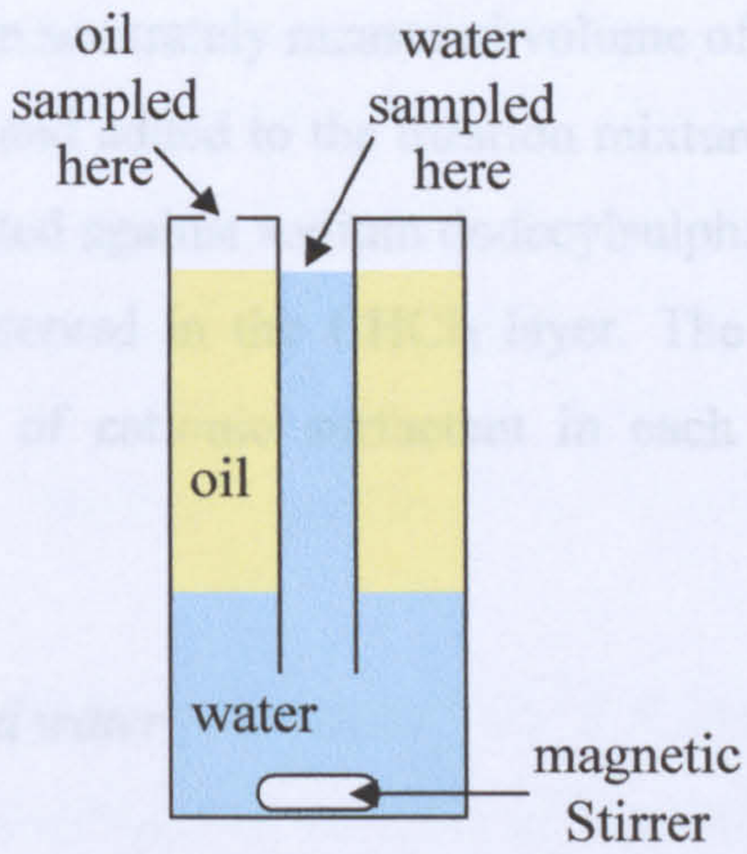

For 1:10 volume ratio 5 ml of aqueous surfactant solution (with or without 4.7 wt.% brine) was placed in a large test tube with a magnetic stirrer bar, then 50 ml of the relevant oil was added, avoiding any mixing of the two phases. The cells or test tubes were placed in a double-walled water bath thermostatted by an LTD6G water bath (Grant, UK) positioned above a Multipoint magnetic stirrer (Variomag, Germany) and left to equilibrate for 7 days. The stirring speed was 150 rpm. However in some cases this was reduced to 100 rpm to prevent mixing of the two phases.

In order to determine the concentration of surfactant in each phase a two-phase titration[11] was used, which is based on the method of Epton[12,13]. The two phases are chloroform (CH_3Cl) (Fisher, UK, purity > 99 %) and water plus the indicator solution, which is a mixture of two ionic dyes in an acidic aqueous solution: anionic disulphine blue (Sigma, UK, purity 95 %) and cationic dimidium bromide (Sigma, UK, purity 70 %). A colour change is observed in the chloroform layer which is pink with excess anionic surfactant and blue with excess cationic surfactant:

start of titration						end of titration				
AD/CS	+	**CD**	+	**AT**	⟶	**CD/AT**	+	**AD**	+	**CS/AT**
blue salt soluble in $CHCl_3$		*yellow* present in aqueous phase				*pink salt* soluble in $CHCl_3$		*green/yellow* present in aqueous phase		*colourless salt* soluble in $CHCl_3$

where AD = anionic dye, CD = cationic dye, AT = anionic titrant, CS = cationic sample.

The amount of cationic surfactant in a sample of water or oil can be determined by titrating against an anionic surfactant.

10 ml of $CHCl_3$, 5 ml of Milli-Q water and 5 ml of mixed indicator solution were placed in a large test tube. An accurately measured volume of the equilibrium phase was withdrawn from the sample and added to the titration mixture. The mixture was shaken thoroughly by hand and titrated against sodium dodecylsulphate of known concentration until a pink colour was observed in the $CHCl_3$ layer. The titre values were used to calculate the concentration of cationic surfactant in each phase of the equilibrium system.

2.2.4.3 Emulsions of oil and water

2.2.4.3.1 Preparation

5 ml of the relevant aqueous surfactant solution and 5 ml of the relevant oil were added to a sample tube (length 75 mm, diameter 25 mm). The mixture was homogenised using an Ultra-Turrax T25 homogeniser (IKA-Werke, Germany), equipped with an 18 mm diameter dispersion head rotating at 13,000 rpm for 2 min.

2.2.4.3.2 Characterisation

After homogenisation the conductivity of the emulsions was measured using a Jenway 4510 conductivity meter (Jenway, UK) equipped with a glass bodied Pt-Pt black electrode. The drop test is a simple method for distinguishing between oil-in-water and water-in-oil emulsions. A droplet of emulsion is added into a small sample tube containing either the relevant oil or water. If the droplet immediately disperses in the liquid that the droplet is added to, then it is very likely that the liquid is the continuous phase of the emulsion. If the droplet remains intact in the liquid then it is likely that the liquid is the dispersed phase of the emulsion.

Emulsions containing dodecylbenzyldimethylammonium chloride or imidazoline acetate were stored at ambient temperature (20 ± 2 °C), and those containing hexadecylbenzyldimethylammonium chloride were stored in a water bath at 40 ± 0.1 °C. The stability of o/w emulsions to creaming and coalescence was assessed by monitoring the change of the height of the water-emulsion and oil-emulsion interfaces, respectively. The stability of w/o emulsions to sedimentation and coalescence was assessed by monitoring the change of the height of the oil-emulsion and water-interfaces,

respectively. The percentages of resolved aqueous and oil phase were calculated using equations (2.17) and (2.18), where h_w is the height of the water-emulsion interface 24 hr. after emulsification, h_o is the height of the of the oil resolved 24 hr. after emulsification and h_t is the total height of the emulsion plus the height of oil and/or water resolved (Figure 2.8).

$$\% \text{ water} = \frac{h_w}{h_t} \times 100 \tag{2.17}$$

$$\%\text{oil} = \frac{h_o}{h_t} \times 100 \tag{2.18}$$

Photographs of the vessels were taken with a Kodak CX7530 digital camera (Kodak, USA). Optical micrographs of samples of emulsions were obtained using a Nikon Labophot microscope (Nikon, Japan) fitted with a QICam Fast CCD camera (Q-Imaging, UK) linked to a PC equipped with Image-Pro Plus software (Media Cybernetics, UK), which was used to add scale bars to the images. A small sample of the emulsion was placed onto a glass slide (Menzel-Gläser, Germany) with a Pasteur pipette and covered with a glass cover slip (Scientific Laboratory Supplies, UK), which was raised at one edge by a second cover slip.

Figure 2.8. Schematic of types of emulsion breakdown.

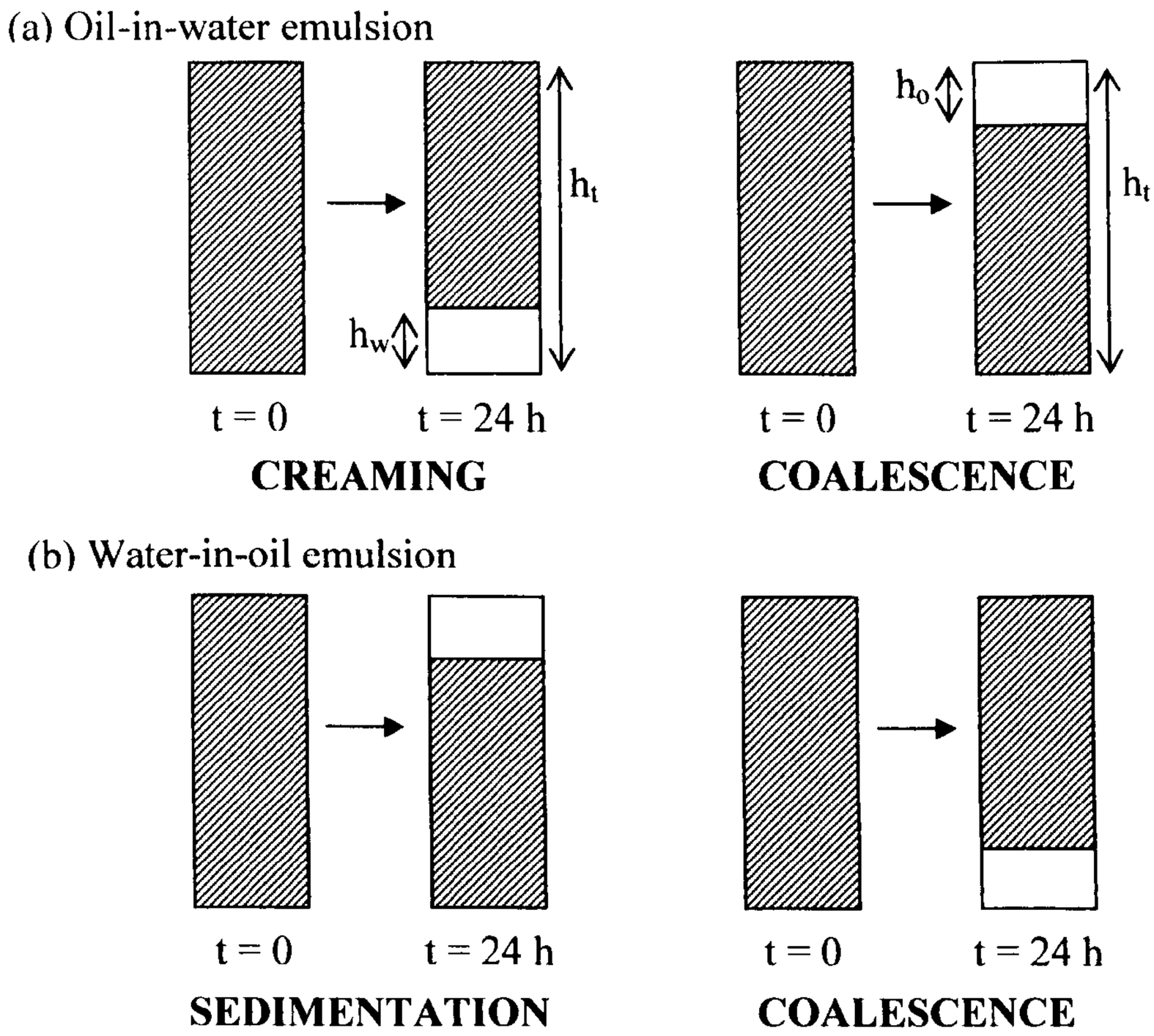

2.3 References

1. *ASTM D1141-90 - Standard Specification for Substitute Ocean Water*, ASTM International (1990).
2. *Certificate of Compliance for Material: Mild Steel C1018, Specification AISI / SAE C1018*, European Corrosion Supplies Ltd., Kidderminster, UK.
3. H.G. Tompkins, *A Users' Guide to Ellipsometry*, Academic Press, London (1993).
4. R.J. Archer, *Ellipsometry*, Gaertner Scientific Corp., Chicago (1968).
5. T. Arnebrant, K. Bäckström, B. Jönsson and T. Nylander, *J. Colloid. Interf. Sci.*, **128**, 303 (1989).
6. F.L. McCrackin, *Natl. Bur. Stand. (U.S.) Tech Note,* 479 (1969).
7. M. Stern and L. Geary, *J. Electrochem. Soc.*, **104**, 56 (1957).
8. D.F. Shriver and P.W. Atkins, *Inorganic Chemistry, 3rd edition*, Oxford University Press, Oxford (1999).
9. W.D. Harkins and H.F. Jordan, *J. Am. Chem. Soc.*, **52**, 1751 (1930).
10. H.H. Zuidema and G.W. Waters, *Ind. Eng. Chem.*, **13**, 312 (1941).
11. V.W. Reid, G.F. Longman and E. Heinerth, *Tenside*, **4**, 292 (1967).
12. S.R.Epton, *Nature (London)*, **160**, 795 (1947).
13. S.R.Epton, *Trans. Faraday Soc.*, **44**, 226 (1948).

CHAPTER 3

Corrosion inhibition by surfactants

3.1 Introduction

The environmental conditions of an oil pipeline system and the type of the steel used in its construction determine the corrosion rate of the steel. The nature of the dissolved gases present in the production fluid affects the rate of penetration into the steel and the type of corrosion products which form at the steel surface. The corrosion rate of steel is increased by the presence of electrolyte in the aqueous phase which facilitates the electrochemical corrosion process. As many oilfields have unique environmental conditions, corrosion inhibitor formulations are generally produced for application into specific oilfields. We have conducted bubble test and weight-loss measurements to determine the corrosion rate of 1018 steel in aqueous solutions containing different dissolved gases in the absence and presence of electrolyte. The measurements were subsequently repeated in the presence of two commonly used corrosion inhibitors to assess their corrosion inhibition performance in each system.

3.2 Comparison of electrochemical and weight-loss methods

The corrosion rate of 1018 steel in aqueous media was measured using electrochemical and weight-loss methods. Figure 3.1 shows the corrosion rate of 1018 steel in deionised water and 4.7 wt.% brine solutions under aerated, CO_2 and H_2S conditions at 25 °C in the absence of corrosion inhibitor. The bubble and wheel box tests are the most common methods for corrosion monitoring within industry. The advantage of the electrochemical technique is that the current (and therefore the corrosion rate) is continuously monitored throughout the experiment. This is a more powerful tool than the wheel box test where the fundamental measurement is weight-loss and where some period of exposure is required to determine the corrosion rate. The zero resistance ammeter which measures the current response can measure a minimum of 10 picoamperes, therefore the lowest detectable corrosion rate is approximately 1×10^{-7} mm y^{-1}.[1]

Corrosion rates measured in brine solutions using the bubble test method are generally two to four times lower than those determined by the wheel box test. In deionised water the corrosion rates differ by more than one order of magnitude. The bubble test data

Figure 3.1. Corrosion rates of 1018 steel in deionised water and 4.7 wt.% brine under aerated, CO_2 and H_2S conditions at 25 °C measured by the bubble test (unshaded) and wheel box test (shaded).

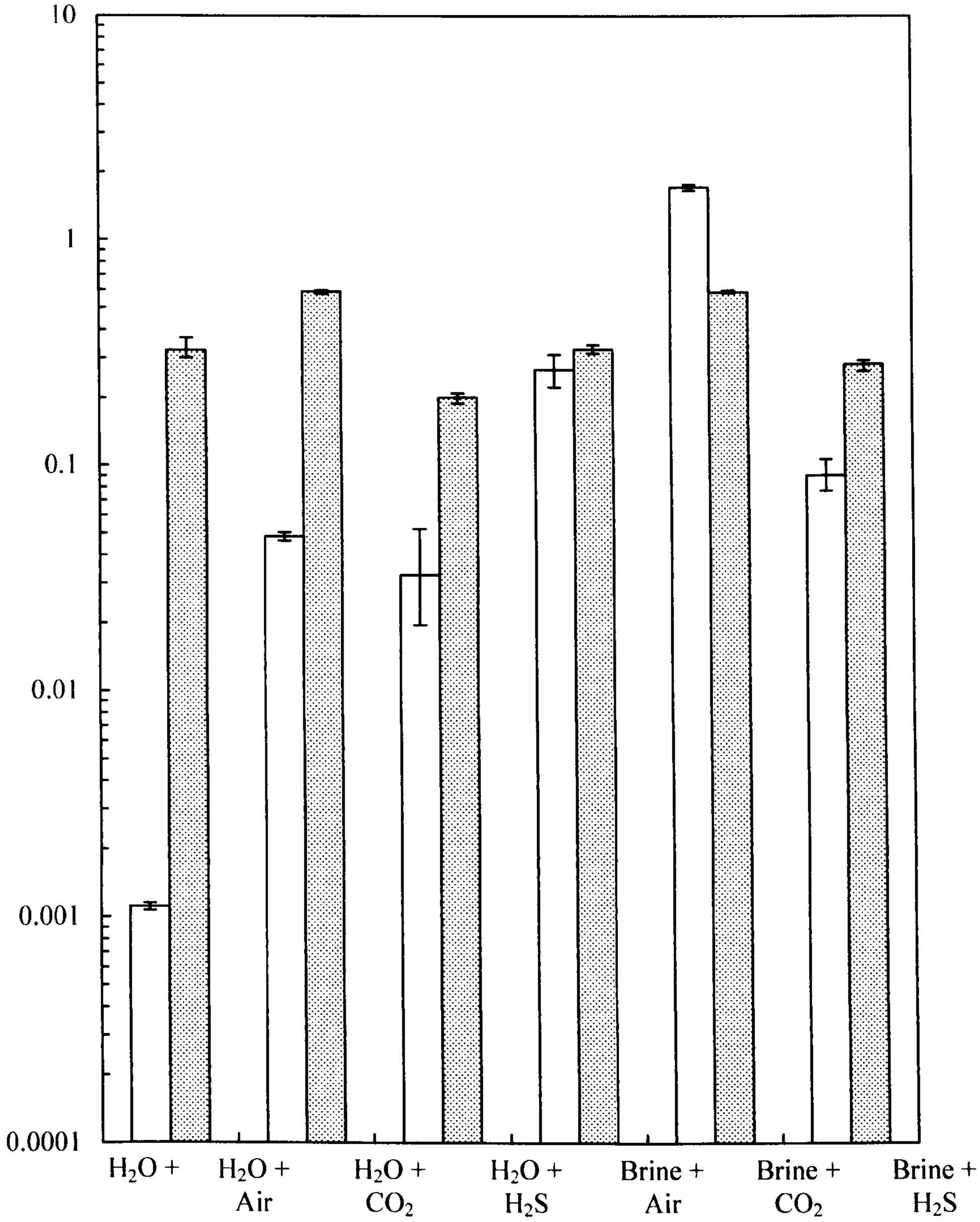

sho

shows that there is no significant difference between the corrosion rates of deionised water and brine solutions. There are several possible explanations for the differences in the measured corrosion rates. Firstly, the two techniques determine the corrosion rate in different ways. In the bubble test, the mean of the final ten measurements (those taken within the last 1.5 hr. of the experiment) was recorded as the corrosion rate. The measured corrosion rate is determined from the current response when a potential is applied between the working and counter electrodes. In the wheel box test, the corrosion rate is calculated from the total weight-loss over the 24 hr. test period. The different surface finishes of the 1018 steel electrodes and weight-loss coupons can also contribute to the difference in corrosion rates. The electrodes used in the bubble test experiments are polished, whereas the wheel box coupons have a sandblasted finish with a rougher surface that can cause aggressive chloride ions and corrosive species to collect and concentrate within the deeper surface cavities[2]. It is also possible that mechanical polishing of the bubble test electrodes may have induced metallurgical changes upon the steel surface[3,4].

In the bubble test method the steel electrodes are immersed in the corrosive fluid, which is magnetically stirred but in the wheel box test the coupons are fixed within a bottle and the fluids flow over the surface as the bottle rotates on the wheel. In the latter case, the corrosion products on the surface of the steel can be removed more easily, exposing the underlying steel surface leading to further corrosion. The ratio of the volume of liquid to the surface area of the steel is also different in these two methods; 684.54 L m^{-2} in the wheel box test and 66.86 L m^{-2} in the bubble test. Weight-loss measurements often have difficulty in determining the corrosion rates of metals because only very small mass changes occur over substantial time periods[3,5]. Overall, we believe that the electrochemical method gives the most credible corrosion rate measurements over 24hr.

3.3 Effect of dissolved gas on the corrosion of steel

3.3.1 Influence of air

In deionised water under aerated conditions the corrosion rate of 1018 steel determined by the bubble test method was 0.0011 mm y^{-1}. Figure 3.2 shows the variation in the corrosion rate with time, which shows that the corrosion rate does not change significantly over the 20 hr. test period. Using the weight-loss method the corrosion rate was 0.32 mm y^{-1}. After corrosion, the steel surfaces were covered with reddish brown and black coloured corrosion

Figure 3.2. Corrosion rate vs time for 1018 steel in deionised water under aerated conditions at 25 °C, determined by bubble test.

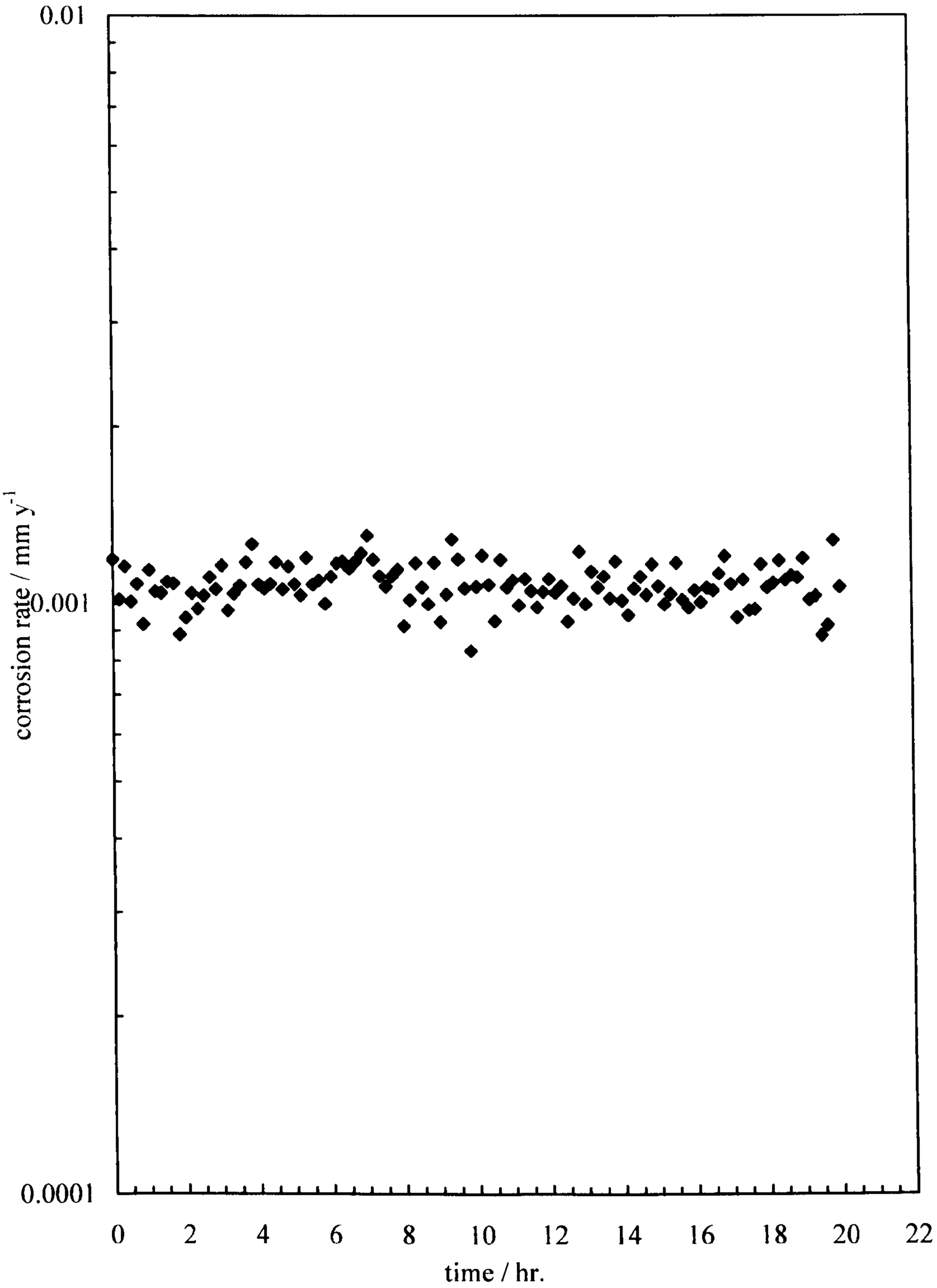

products. The aqueous phase was reddish brown in colour and contained a considerable amount of dispersed corrosion products. The bubble test corrosion rate of the steel in aerated brine was 0.27 mm y^{-1}. Figure 3.3 shows that the corrosion rate at the start of the measurement is approximately 0.90 mm y^{-1} and then decreases with time, reaching a plateau value after 10 hr. The corrosion rate determined by weight-loss was 0.33 mm y^{-1}. The brine solutions were reddish brown coloured at the end of the experiment. The surface of the steel was covered with reddish brown products which were also dispersed in the brine solution.

The corrosion rate of 1018 steel in brine is over 200 times greater than in deionised water when measured with the bubble test. The brine solution facilitates corrosion because the dissolved ions enhance the solution conductivity which allows electrons to move between the working and counter electrodes of the electrochemical probe. The composition of the brine mixture can also affect the corrosion rate. The ASTM brine mixture contains five chloride salts; the chloride ion is known to be an aggressive ion that can cause depassivation and localized pitting corrosion of steels[6,7] and other alloys[8,9]. Carbon steels such as 1018 steel are composed of ferrite (α-Fe) and pearlite. Pearlite is a two-phased, lamellar structure consisting of alternate layers of ferrite and cementite (Fe_3C)[10]. The steel is also covered with a thin iron (III) oxide (hematite) passive film. Ferrite is anodic towards its oxide and therefore it will tend to dissolve into solution if the passive film is broken (Figure 3.4). Ferrite dissolves into solution at the anode (equation (1.1)) and hydroxide ions

Figure 3.4. Schematic diagram showing corrosion of ferrite due to the presence of a film of iron oxide.

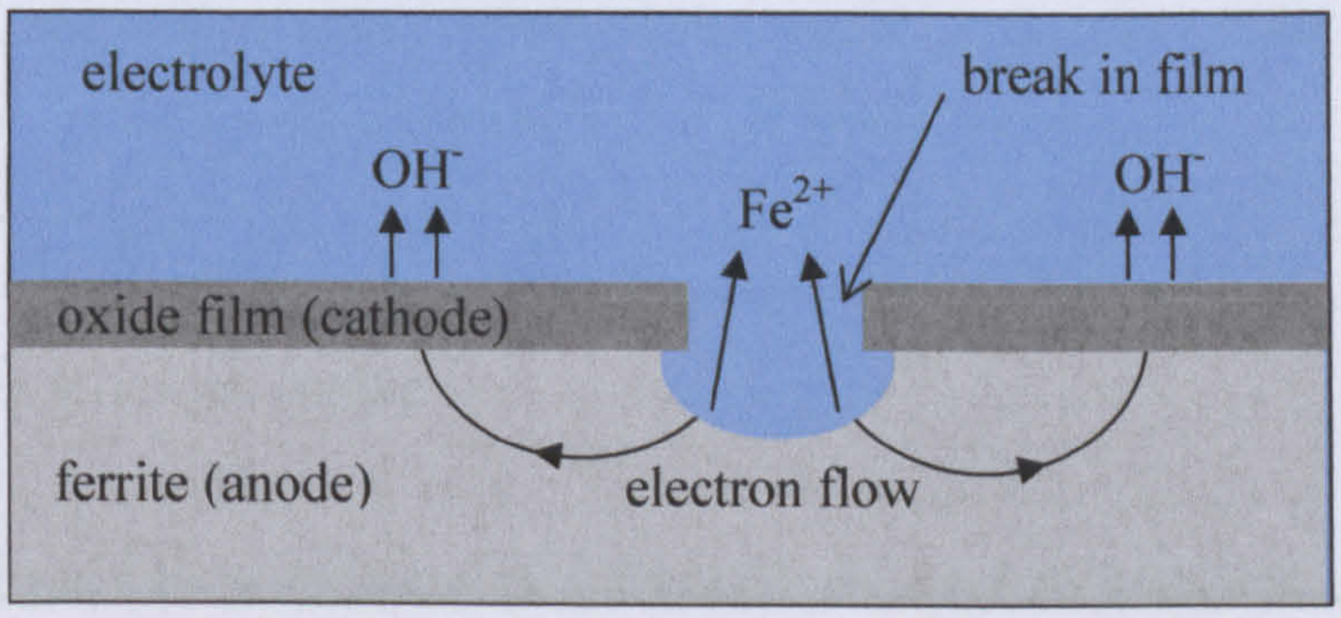

form at the cathode (equation (1.4)); when these ions meet away from the region of electrolytic action iron (II) hydroxide ($Fe(OH)_2$) forms. The iron hydroxide is quickly

Figure 3.3. Corrosion rate vs time for 1018 steel in 4.7 wt.% brine under aerated conditions at 25 °C, determined by bubble test.

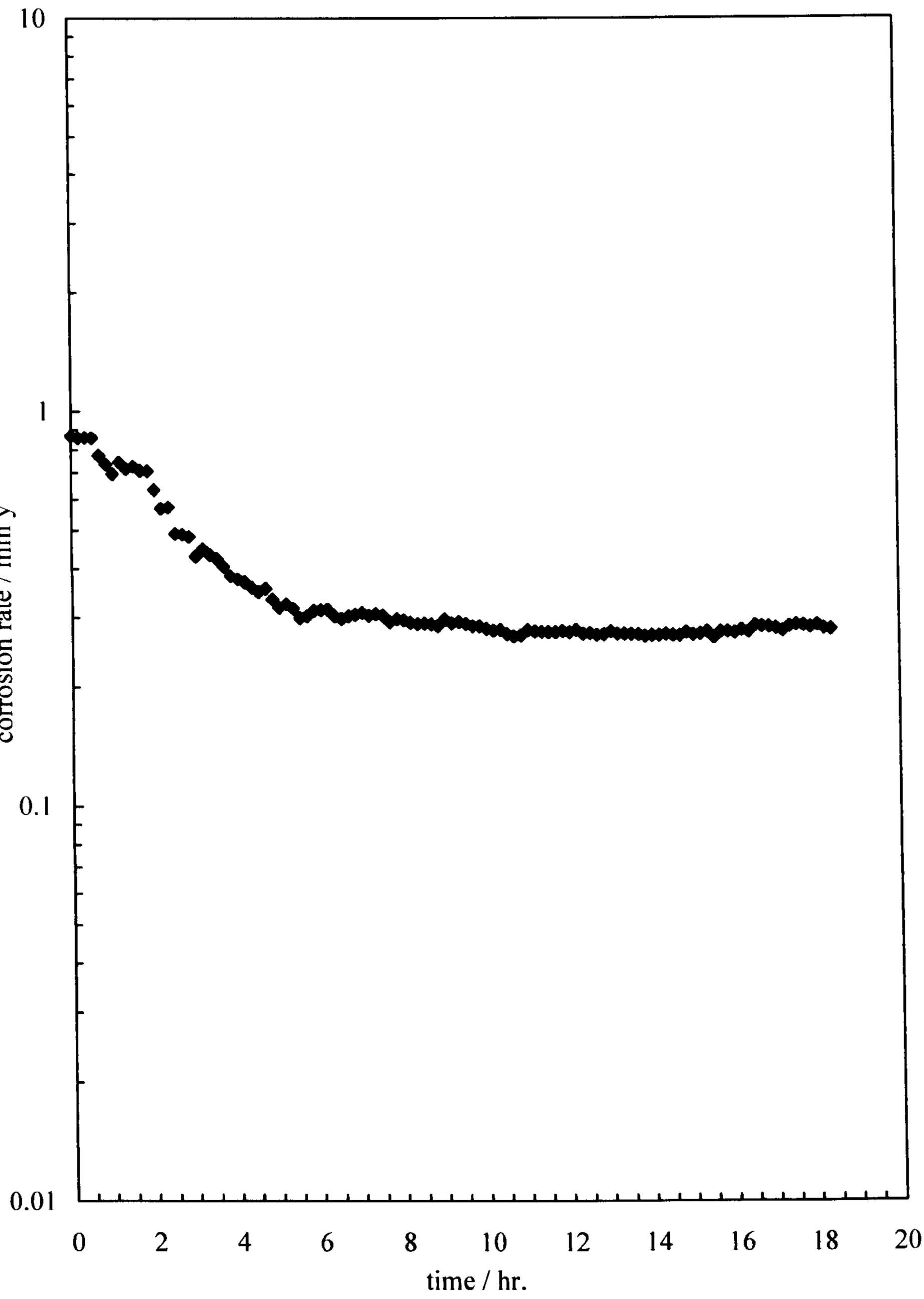

oxidised by dissolved oxygen to give hydrated iron (III) oxide (hematite) or an iron (III) oxide-hydroxide, both of which have an orange to reddish brown colour. The corrosion product covering the 1018 steel after corrosion in the aerated solutions is hydrated hematite or an iron (III) oxide-hydroxide such as goethite (α-FeO(OH)) or lepidocrocite (γ-FeO(OH))[11,12], or a mixture of these compounds. The black corrosion product which forms in deionised water is iron (II,III) oxide (Fe_3O_4, often called magnetite). After corrosion in aerated water, one set of 1018 steel electrodes was wiped with tissue paper to remove some of the black corrosion products. The tissue paper could be attracted to a magnet, suggesting that the black corrosion product was Fe_3O_4 because this is the only naturally occurring magnetic iron oxide[11]. Ferrite dissolution also occurs in the pearlite phase. Ferrite is anodic with respect to cementite which causes ferrite to dissolve preferentially when wetted by a suitable electrolyte[13], leaving the cementite layers intact (Figure 3.5).

Figure 3.5. Schematic diagram showing corrosion of ferrite in pearlite due to the presence of cementite.

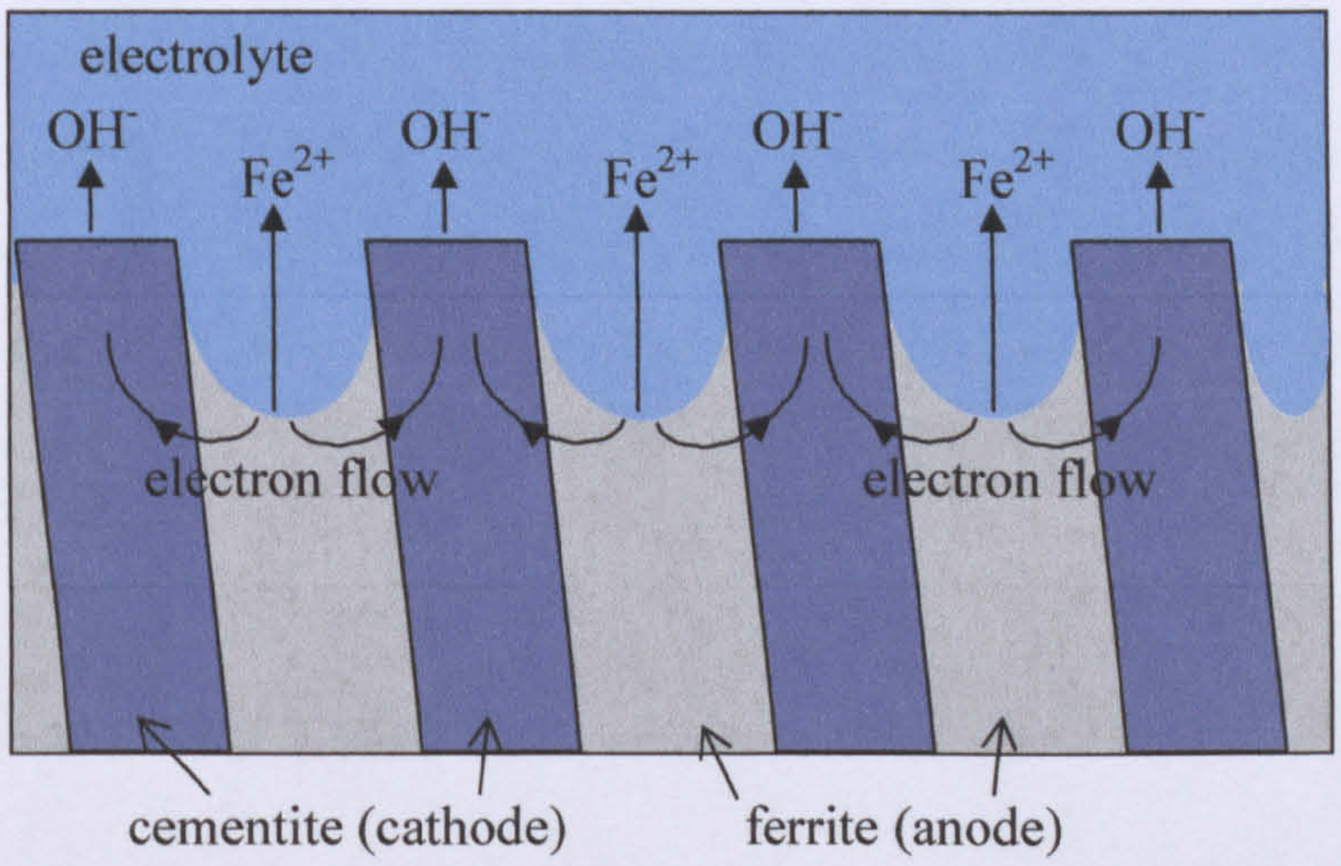

3.3.2 Influence of carbon dioxide

In deionised water containing CO_2 the corrosion rate of 1018 steel was 0.048 mm y^{-1} using the bubble test method. Figure 3.6 shows that the corrosion rate does not change significantly over the test period. Using the wheel box method the corrosion rate was

Figure 3.6. Corrosion rate vs time for 1018 steel in deionised water under CO_2 conditions at 25 °C, determined by bubble test.

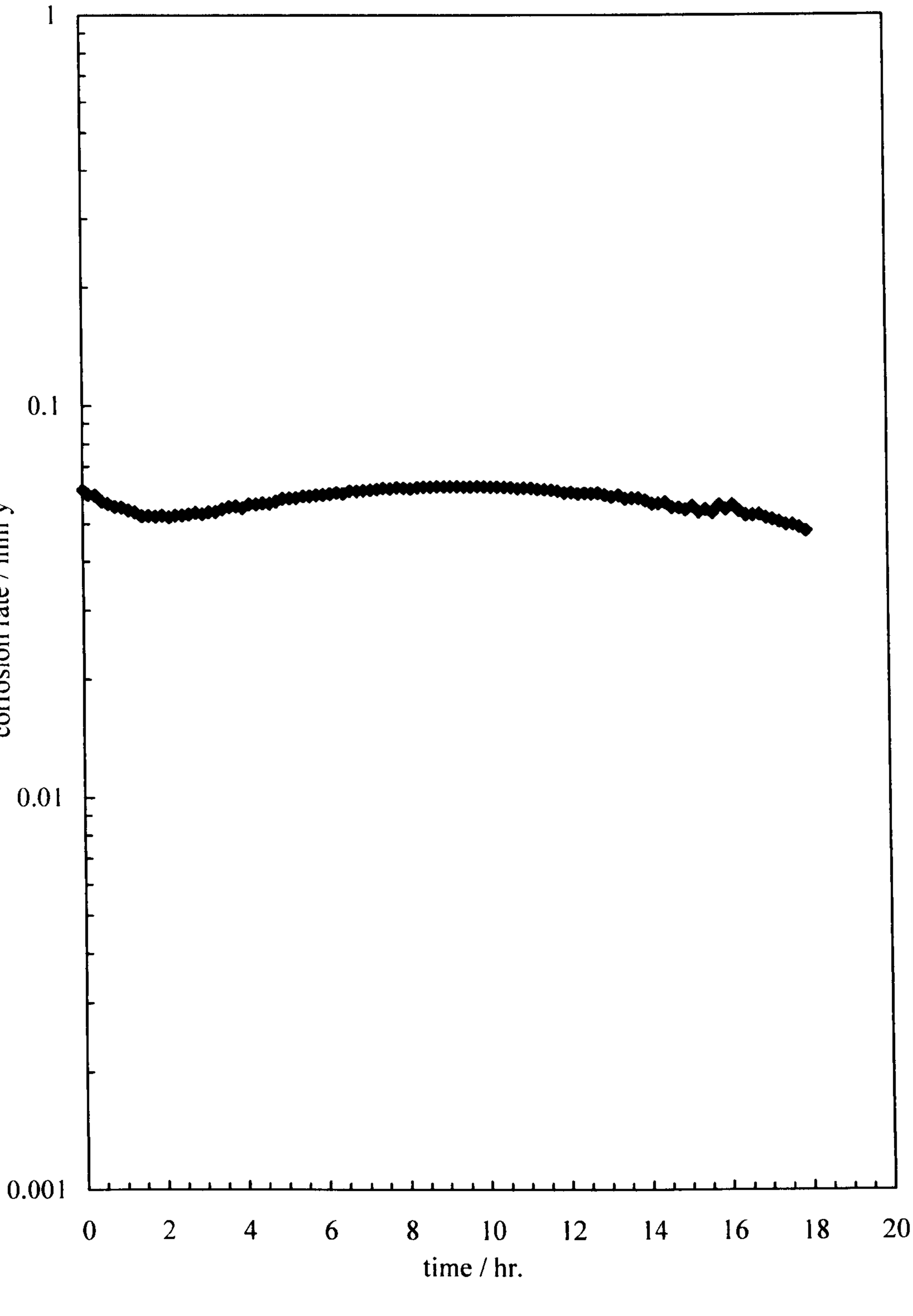

0.57 mm y^{-1}. Following the experiment, the steel was covered with a grey corrosion product.

In brine under CO_2 conditions the corrosion rate measured with the bubble test was 1.71 mm y^{-1}. Figure 3.7 shows the variation of the corrosion rate with time. The initial corrosion rate is 1.5 mm y^{-1} and increases slightly over 18 hr. For the same system the corrosion rate determined by weight-loss was 0.64 mm y^{-1}. Using the bubble test method, the corrosion rate in the presence of electrolyte is much greater than in the absence of electrolyte because the presence of ions in solution facilitates the transport of charge through solution. A grey corrosion product had covered the surface of the steel electrodes by the end of the experiment.

When carbon dioxide is present in aqueous environments, carbonic acid (H_2CO_3) forms in solution which is corrosive to carbon steels (equation (1.8)). The grey corrosion product which forms on the surface of the 1018 steel samples is probably iron carbonate, which can be explained by equations (1.11), (1.12) and (1.13). $FeCO_3$ is precipitated due to its low solubility in water (pK_{sp} = 10.54 at 25 °C)[14] when ferrous cations interact with carbonate and bicarbonate anions. The resultant corrosion product film will also contain cementite which accumulates after the preferential dissolution of the ferrite in the pearlite phase of carbon steels[15]. There is evidence to suggest that the remaining cementite layers can strengthen the carbonate film, anchoring it to the steel. Ueda and Takabe proposed that laminar cementite acts cathodically to the ferrite phase, accelerating the dissolution of iron and causing higher concentrations of ferrous ions in the cavities between the cementite layers[16].

3.3.3 Influence of hydrogen sulphide

In deionised water containing hydrogen sulphide the corrosion rate of 1018 steel determined using the bubble test was 0.033 mm y^{-1}. Figure 3.8 is an example of the corrosion rate versus time profile for steel electrodes in water containing hydrogen sulphide. The corrosion rate is approximately 0.06 mm y^{-1} at the start of the experiment then steadily decreases to a plateau value of 0.02 mm y^{-1} over 15 hr. The mean corrosion rate determined by weight-loss was 0.25 mm y^{-1}. The bubble test electrodes retained their metallic appearance throughout the experiment but the wheel box coupons were covered with a dark grey corrosion product film after 24 hr. of corrosion.

Figure 3.7. Corrosion rate vs time for 1018 steel in 4.7 wt.% brine under CO_2 conditions at 25 °C, determined by bubble test.

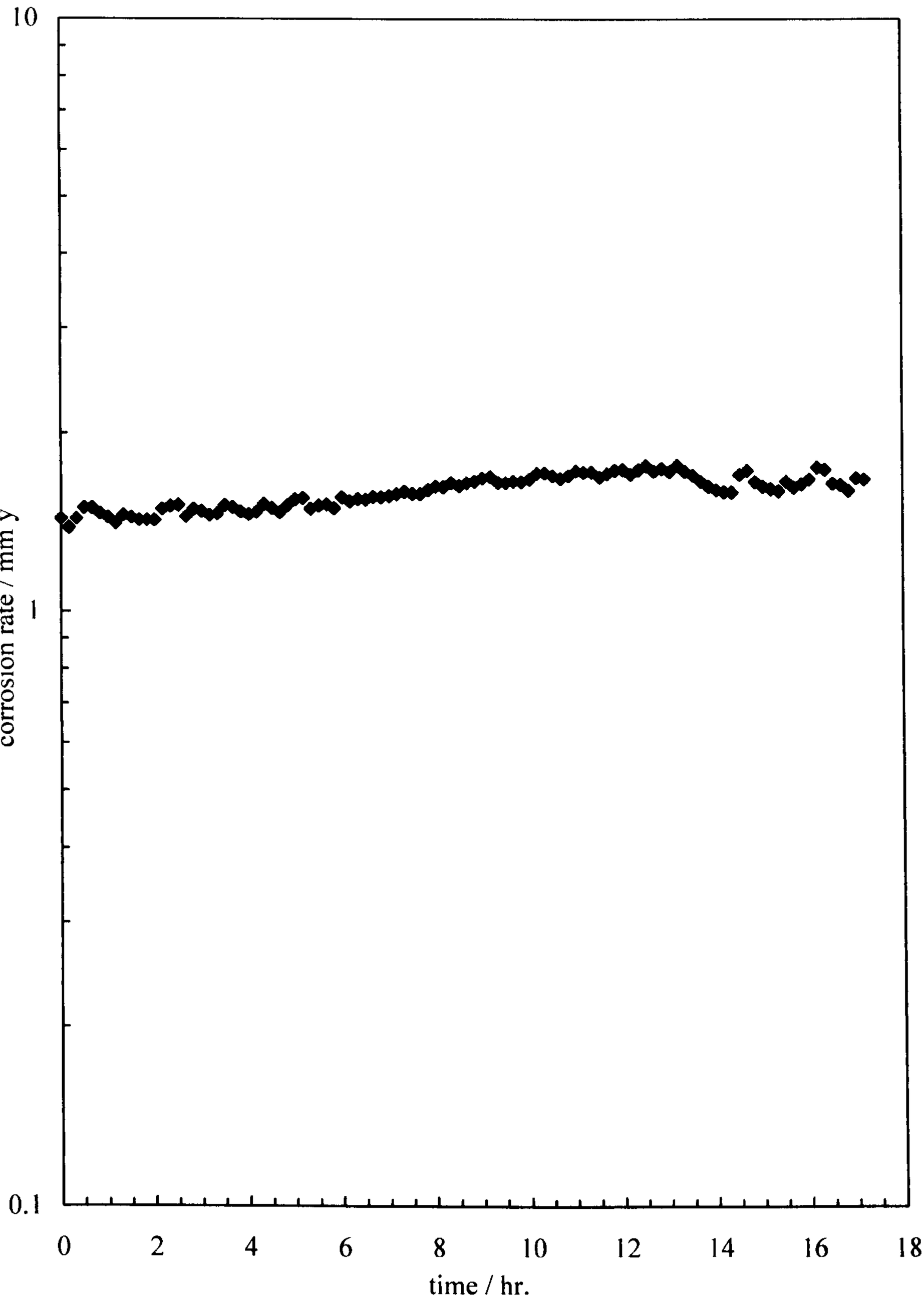

Figure 3.8. Corrosion rate vs time for 1018 steel in deionised water under H_2S conditions at 25 °C, determined by bubble test.

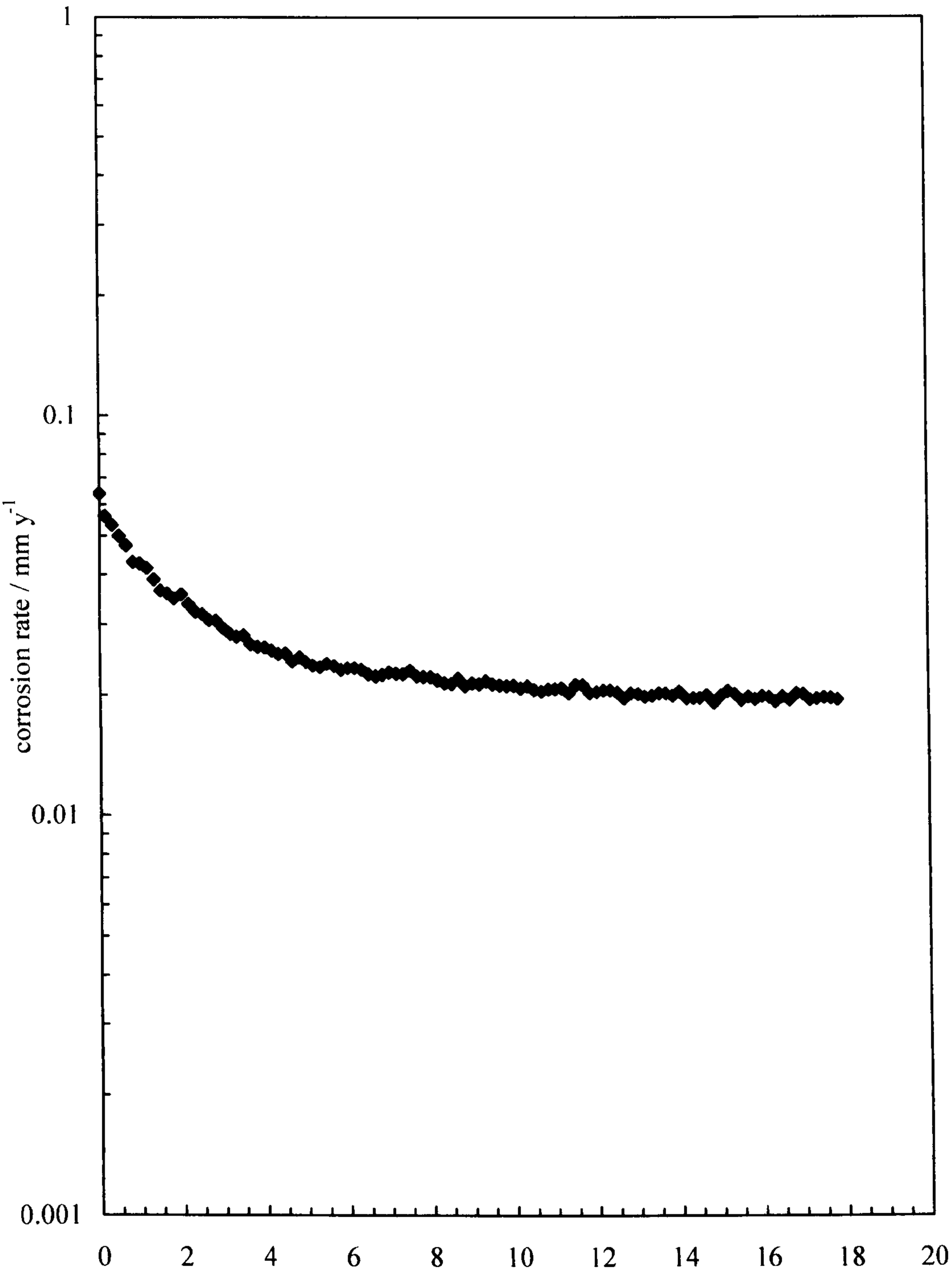

1018 steel immersed in brine containing H_2S was found to corrode at a rate of 0.090 mm y^{-1} using the bubble test method. Figure 3.9 shows the variation in the corrosion rate of steel electrodes with time in H_2S brine; the corrosion rate is approximately 0.15 mm y^{-1} at the start of the measurement, this slowly decreases with time reaching a value of 0.07 mm y^{-1} after 18 hours of corrosion. The corrosion rate of steel in brine containing H_2S was 0.31 mm y^{-1} using the wheel box test. The wheel box coupons were covered with a dark grey film, but the bubble test electrodes kept their metallic appearance throughout the experiment with no visible signs of corrosion.

The appearance of the steel electrodes and weight-loss coupons was visibly different after 24 hr. of corrosion in the H_2S-containing systems. The weight-loss coupons were covered with a dark grey film, in agreement with earlier observations[17,18]. In contrast, the bubble test electrodes retained their metallic appearance. This may be related to the differences between the two experimental methods. The weight-loss experiment is performed in a sealed bottle using a gaseous mixture of CO_2 and H_2S to sparge the water or brine solution. The bubble test apparatus is not as well sealed as the weight-loss experiment and the gas conditions were established by adding Na_2S to CO_2-containing solutions in order to produce H_2S in solution, rather than a mixture of CO_2 and H_2S.

The solution chemistry of H_2S is quite complex. The stability of sulphur species such as H_2S, HS^- and S^{2-} depends on the solution pH and redox potential[19]. These sulphur species combine with ferrous ions to form different iron sulphide species[20] (Table 3.1) which may or may not be protective depending on conditions such as pH, H_2S

Table 3.1. Naturally occurring forms of iron sulphide[20].

Sulphide	**Chemical Formula**	**Stoichiometry**	**Crystal Structure**
Greigite	Fe_3S_4	-	Cubic
Mackinawite	$Fe_{1+x}S$	$x = 0.057 - 0.064$	Tetragonal
Marcasite	FeS_2	-	Orthorhombic
Pyrite	FeS_2	-	Cubic
Pyrrhotite	$Fe_{1-x}S$	$x = 0 - 0.14$	Monoclinic
Smythite	$Fe_{3+x}S_4$	$x = 0 - 0.25$	Hexagonal

Figure 3.9. Corrosion rate vs time for 1018 steel in 4.7 wt.% brine under H_2S conditions at 25 °C, determined by bubble test.

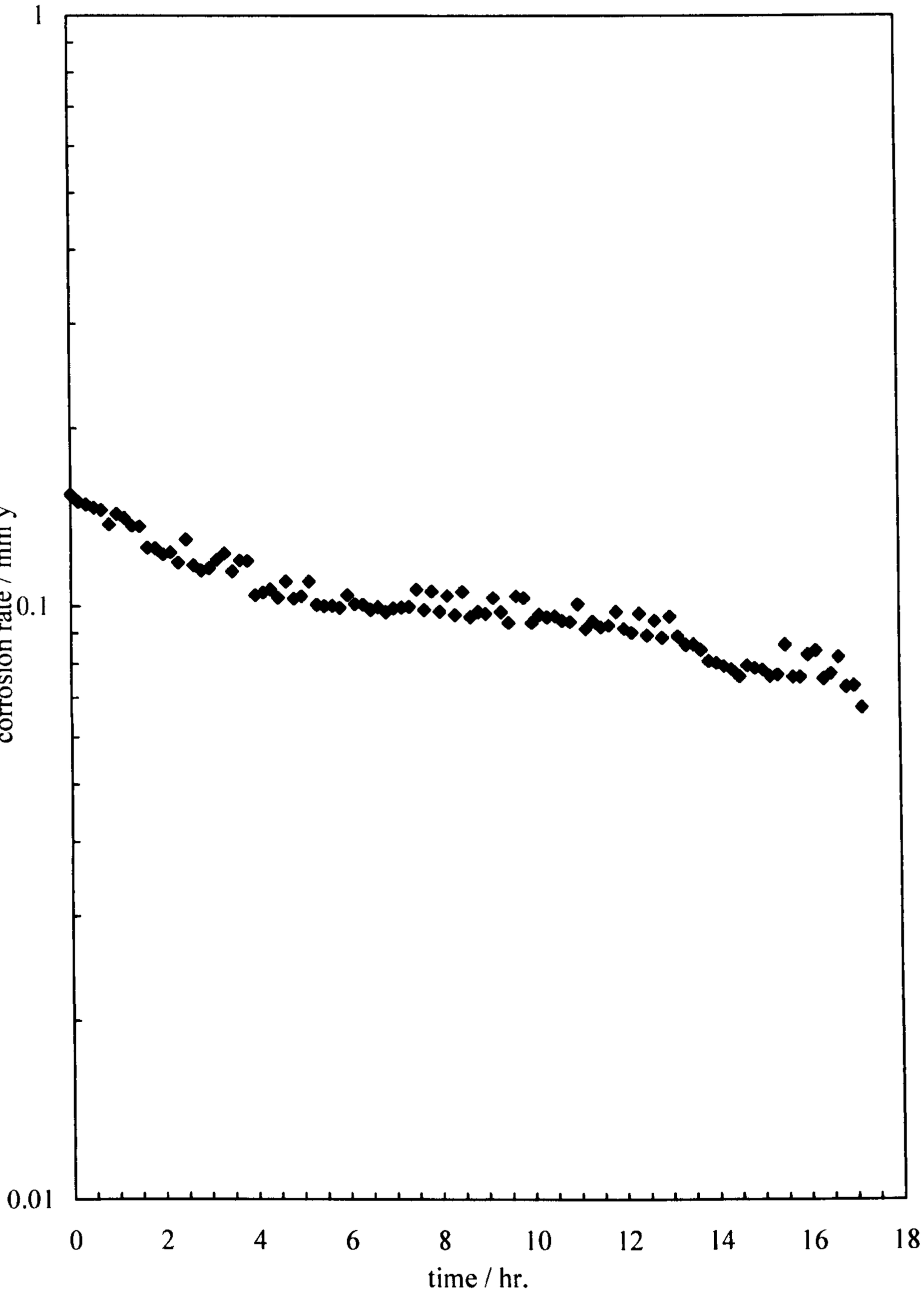

concentration and temperature. The iron sulphide corrosion product films that form in the presence of H_2S control the uniform and localised corrosion rates. The corrosion product films can be very protective, but localised corrosion can occur at high concentrations of chloride ions. Kvarekval has shown that low concentrations of H_2S can increase corrosion rates in CO_2 saturated systems[21]. The effect of H_2S diminishes at higher concentrations and at high temperatures, when protective iron sulphide films form on the steel surface. In other studies[22], trace amounts of H_2S were shown to rapidly reduce the corrosion rate of 1018 steel under CO_2 conditions in both single and multi-phase flow. Figure 3.1 shows that the presence of H_2S in CO_2 saturated deionised water causes the corrosion rate of 1018 steel to decrease, suggesting that the corrosion product film is more protective under these conditions than in the absence of H_2S, where the corrosion product is $FeCO_3$. In CO_2 saturated brine solutions the presence of H_2S causes the corrosion rate to increase, suggesting that the corrosion product film is less protective than in the absence of H_2S.

3.4 Effect of inhibitor addition on the corrosion of steel

In this study we have investigated the effect of two model corrosion inhibitors on the corrosion rate of 1018 steel in deionised water and brine solutions under three different gas conditions. Dodecylbenzyldimethylammonium chloride (C12BDMAC) is a quaternary ammonium salt which was obtained in high purity and 1-aminoethyl-2-(8-heptadecenyl)-2-imidazoline acetate (IA) is a commercial imidazoline-based inhibitor synthesised at Nalco, Fawley. The bubble test method was used to determine the corrosion rate of 1018 steel in the presence of each surfactant. The wheel box method was also used to determine the corrosion rate in the presence of C12BDMAC.

3.4.1 Effect of dodecylbenzyldimethylammonium chloride

3.4.1.1 Atmospheric conditions

Figure 3.10 shows the variation of the corrosion rate with time for 1018 steel electrodes in deionised water under atmospheric conditions. During the first 30 min. of the experiment, the electrodes are corroding in the absence of any C12BDMAC and the corrosion rate is 0.002 mm y^{-1}. After the addition of 0.1 mM C12BDMAC the corrosion rate rapidly

Figure 3.10. Corrosion rate vs time for 1018 steel in deionised water under aerated conditions at 25 °C with 0.1 mM C12BDMAC, determied by bubble test. Dashed vertical line indicates the point at which C12BDMAC was added.

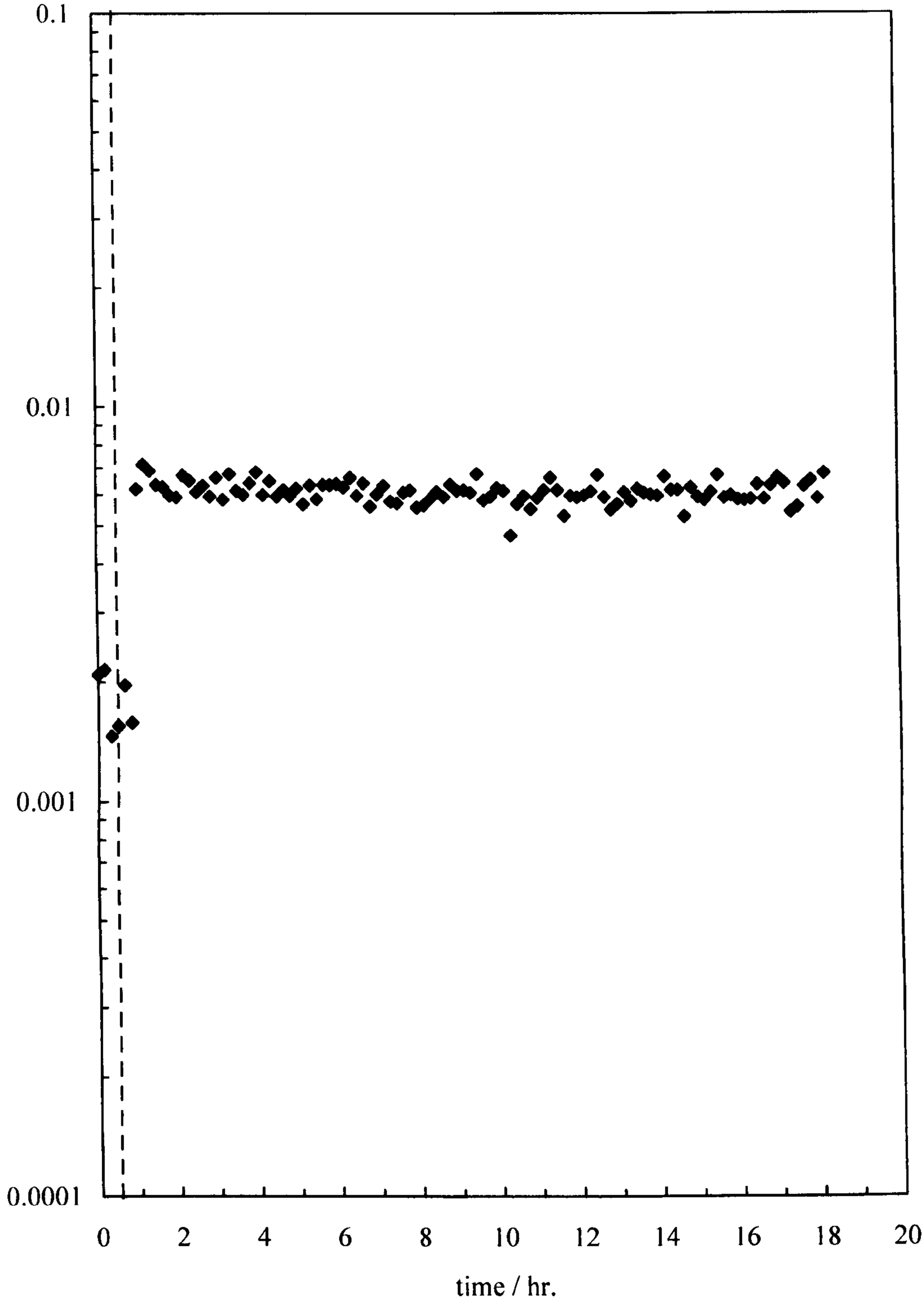

increases to 0.006 mm y^{-1} due to the dissociation of the surfactant which increases the conductivity of the solution. The corrosion rate does not change significantly throughout the rest of the measurement. Figure 3.11 shows the effect of the concentration of C12BDMAC on the corrosion rate of 1018 steel in deionised water under aerated conditions determined using the bubble test. The corrosion rate of the steel increases as the concentration of C12BDMAC increases. At concentrations greater than the cmc, the corrosion rate increases further and then begins to decrease. The increase in corrosion rate can be explained by the ionic nature of the surfactant. On addition to water, the surfactant dissociates into positive and negatively charged ions, which are capable of facilitating the flow of electrons through solution leading to higher corrosion rates than those seen in the absence of surfactant. In this system, the addition of surfactant has a similar effect as adding an electrolyte such as sodium chloride. This observation was confirmed by performing corrosion rate measurements in the absence of C12BDMAC in aqueous solutions of NaCl of equivalent ionic strength which resulted in a similar corrosion rate. Figure 3.12 shows the effect of the concentration of C12BDMAC on the corrosion rate of 1018 steel determined using the wheel box method for the same system. In contrast with the bubble test results, these measurements show that C12BDMAC has no significant effect upon the corrosion rate of 1018 steel at any concentration.

Figure 3.13 shows the corrosion rate versus time profile for 1018 steel electrodes in aerated brine with addition of 0.1 mM C12BDMAC. During the first 30 min., the corrosion rate of 1018 steel in the absence of the surfactant is approximately 1 mm y^{-1}. After the addition of C12BDMAC the corrosion rate slowly decreases to a value of 0.3 mm y^{-1}. If we compare Figure 3.13 with Figure 3.3 it is clear that C12BDMAC has no effect on the corrosion rate because the initial and long-time corrosion rates and the profile of the graph are very similar to those seen in the absence of C12BDMAC. In brine under aerated conditions, bubble test measurements show that there was no effect of surfactant concentration upon the corrosion rate of 1018 steel in the presence of C12BDMAC (Figure 3.14). In deionised water, we saw that the ionic nature of the surfactant caused an increase in the corrosion rate. The addition of the surfactant to the brine solution does not increase the conductivity of the solution significantly; therefore the corrosion rate does not increase. Figure 3.15 shows the effect of the concentration of C12BDMAC on the corrosion rate of 1018 steel determined using the wheel box method. These results are in good agreement with the corresponding bubble test data and show that C12BDMAC does not significantly

Figure 3.11. Corrosion rate vs [C12BDMAC] for 1018 steel in deionised water under aerated conditions at 25 °C, determined by bubble test. Red horizontal line indicates the baseline corrosion rate. Dashed vertical line indicates the cmc of C12BDMAC.

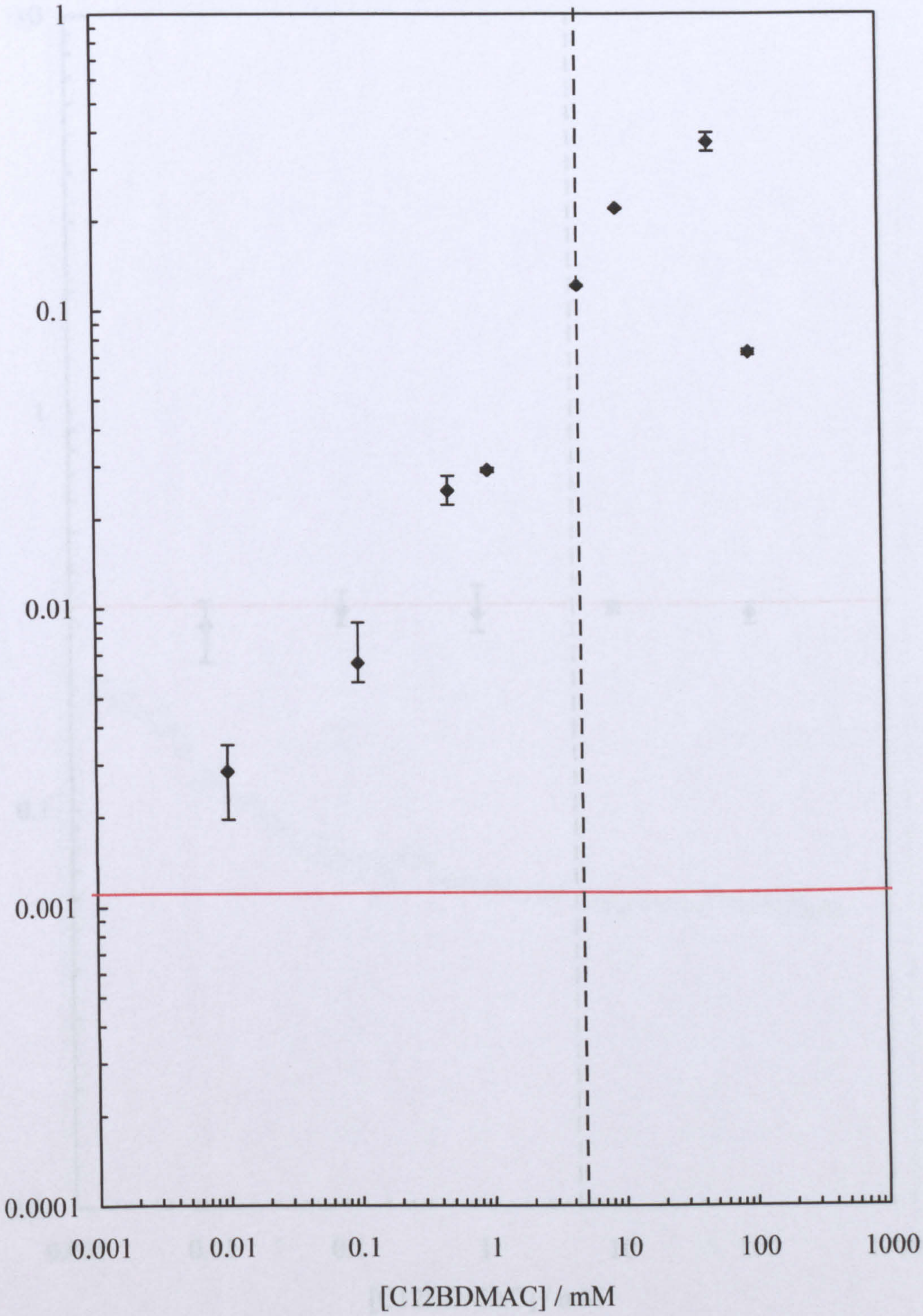

Figure 3.12. Corrosion rate vs [C12BDMAC] for 1018 steel in deionised water under aerated conditions at 25 °C, determined by wheel box test. Red horizontal line indicates the baseline corrosion rate. Dashed vertical line indicates the cmc of C12BDMAC.

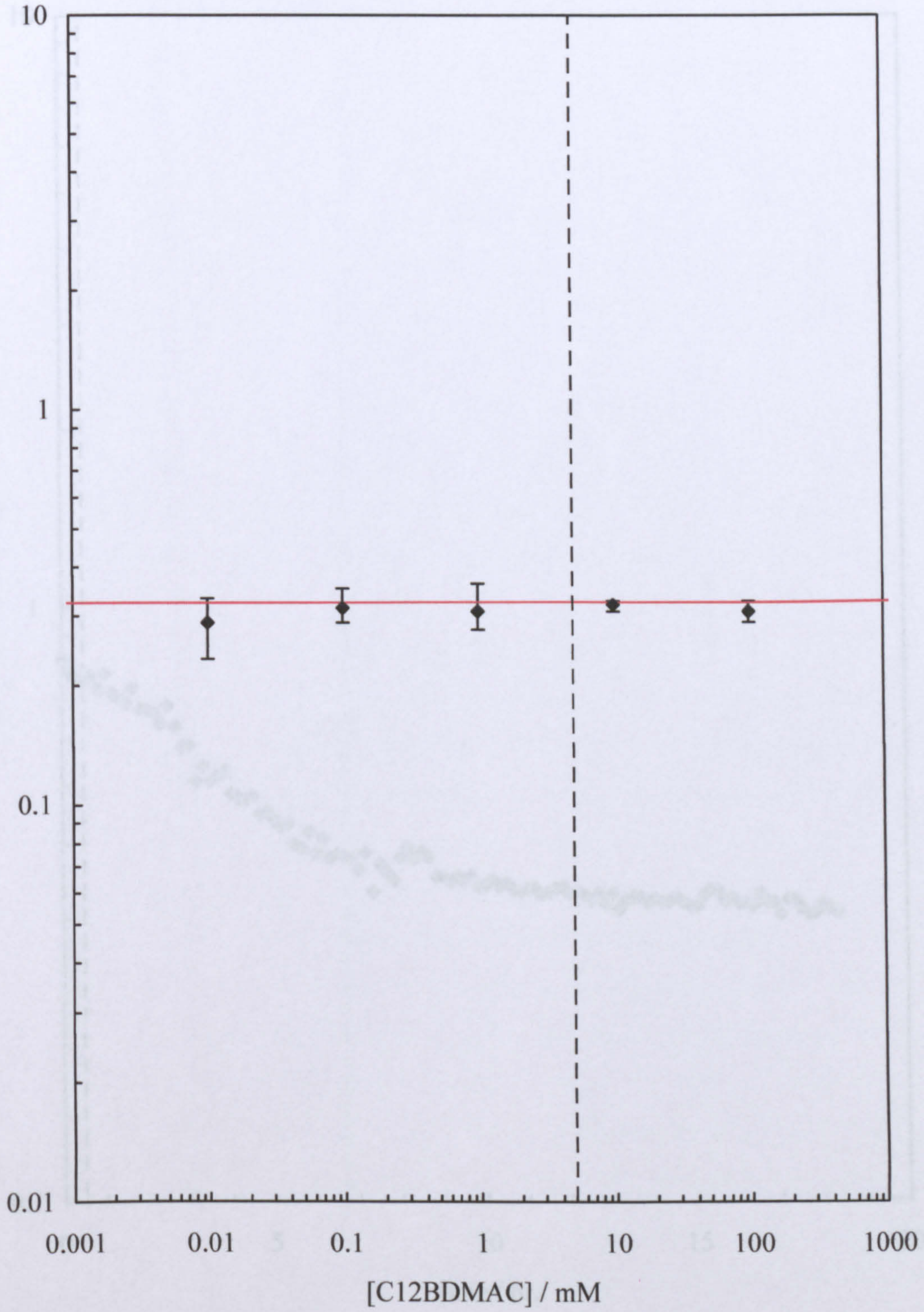

Figure 3.13. Corrosion rate vs time for 1018 steel in 4.7 wt.% brine under aerated conditions at 25 °C with 0.1 mM C12BDMAC, determined by bubble test. Dashed vertical line indicates the point at which C12BDMAC was added.

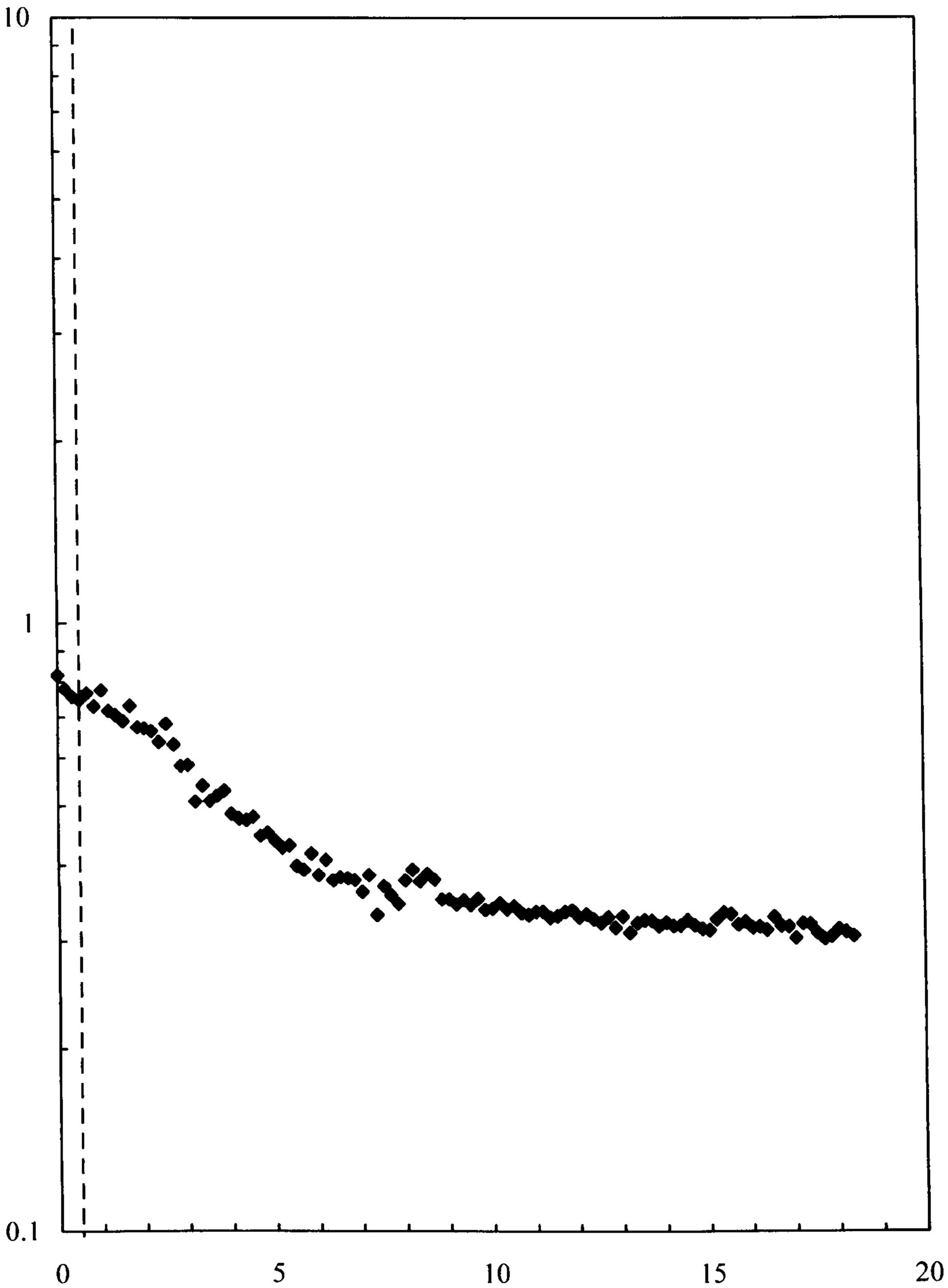

Figure 3.14. Corrosion rate vs [C12BDMAC] for 1018 steel in 4.7 wt.% brine under aerated conditions at 25 °C, determined by bubble test. Red horizontal line indicates the baseline corrosion rate. Dashed vertical line indicates the cmc of C12BDMAC.

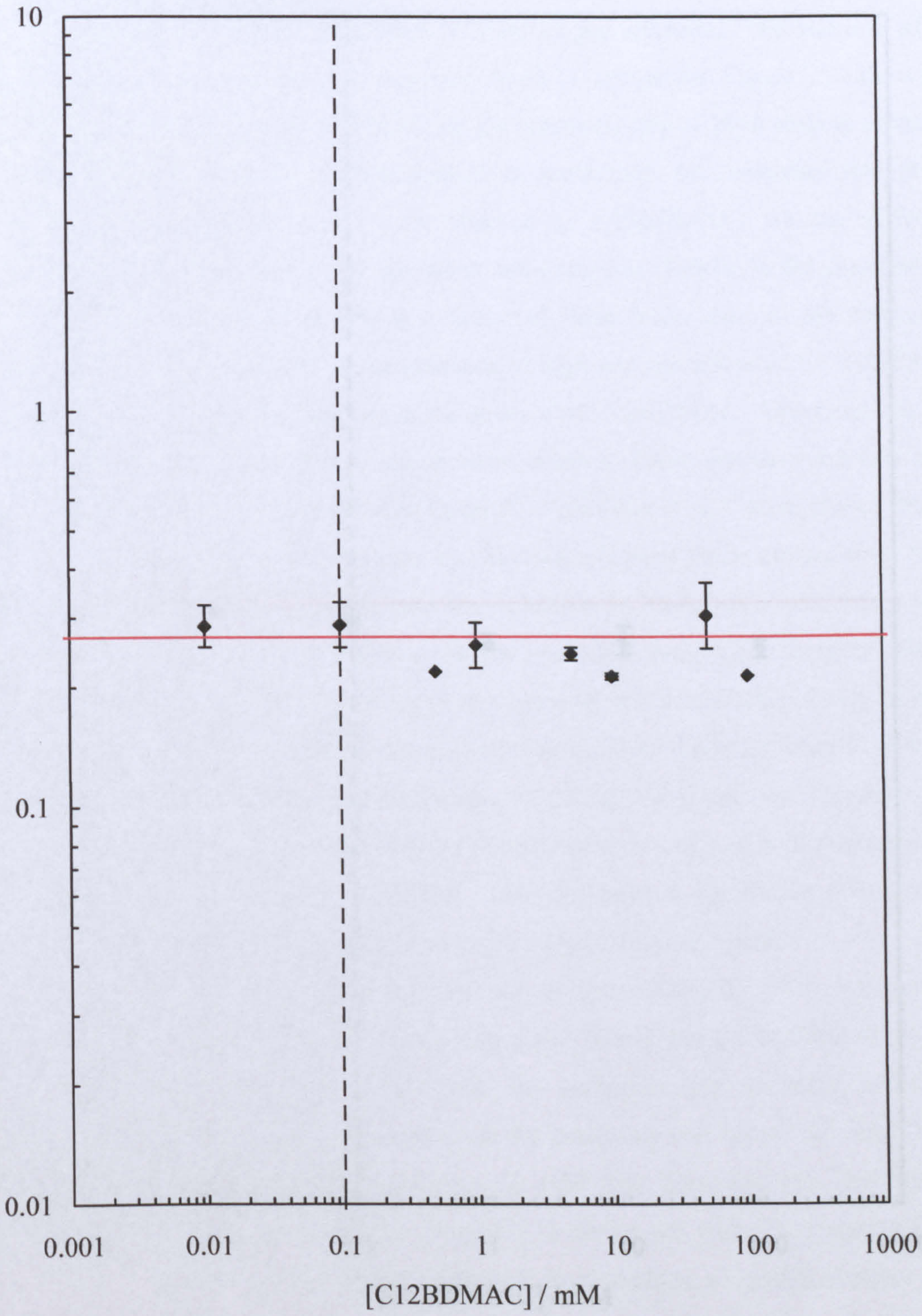

Figure 3.15. Corrosion rate vs [C12BDMAC] for 1018 steel in 4.7 wt.% brine under aerated conditions at 25 °C, determined by wheel box test. Red horizontal line indicates the baseline corrosion rate. Dashed vertical line indicates the cmc of C12BDMAC.

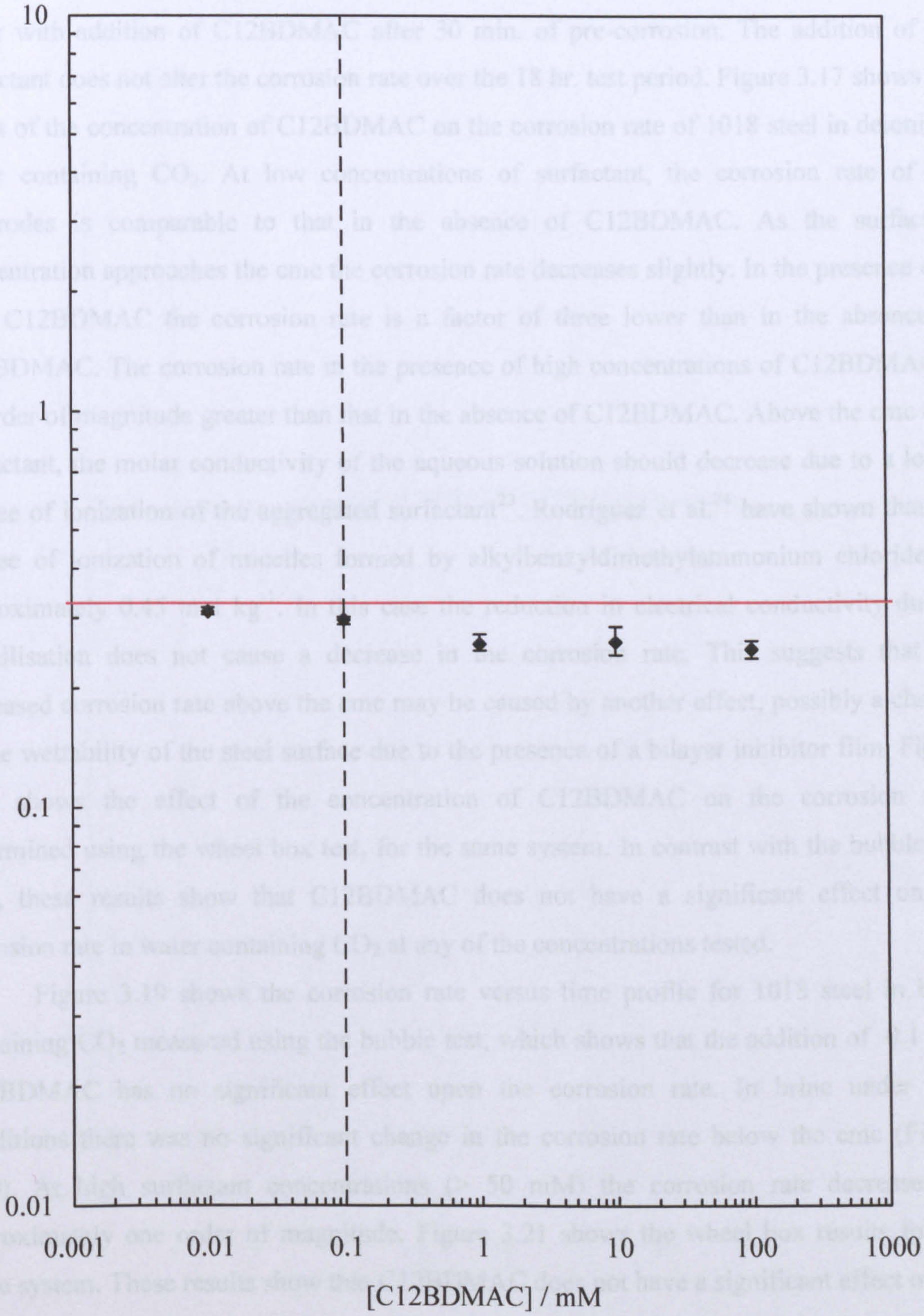

affect the corrosion rate of 1018 steel.

3.4.1.2 Carbon dioxide conditions

Figure 3.16 shows the variation in corrosion rate with time for 1018 steel in carbonated water with addition of C12BDMAC after 30 min. of pre-corrosion. The addition of the surfactant does not alter the corrosion rate over the 18 hr. test period. Figure 3.17 shows the effect of the concentration of C12BDMAC on the corrosion rate of 1018 steel in deionised water containing CO_2. At low concentrations of surfactant, the corrosion rate of the electrodes is comparable to that in the absence of C12BDMAC. As the surfactant concentration approaches the cmc the corrosion rate decreases slightly. In the presence of 1 mM C12BDMAC the corrosion rate is a factor of three lower than in the absence of C12BDMAC. The corrosion rate in the presence of high concentrations of C12BDMAC is an order of magnitude greater than that in the absence of C12BDMAC. Above the cmc of a surfactant, the molar conductivity of the aqueous solution should decrease due to a lower degree of ionization of the aggregated surfactant[23]. Rodríguez et al.[24] have shown that the degree of ionization of micelles formed by alkylbenzyldimethylammonium chlorides is approximately 0.45 mol kg^{-1}. In this case the reduction in electrical conductivity due to micellisation does not cause a decrease in the corrosion rate. This suggests that the increased corrosion rate above the cmc may be caused by another effect, possibly a change in the wettability of the steel surface due to the presence of a bilayer inhibitor film. Figure 3.18 shows the effect of the concentration of C12BDMAC on the corrosion rate, determined using the wheel box test, for the same system. In contrast with the bubble test data, these results show that C12BDMAC does not have a significant effect on the corrosion rate in water containing CO_2 at any of the concentrations tested.

Figure 3.19 shows the corrosion rate versus time profile for 1018 steel in brine containing CO_2 measured using the bubble test, which shows that the addition of 0.1 mM C12BDMAC has no significant effect upon the corrosion rate. In brine under CO_2 conditions there was no significant change in the corrosion rate below the cmc (Figure 3.20). At high surfactant concentrations (> 50 mM) the corrosion rate decreases by approximately one order of magnitude. Figure 3.21 shows the wheel box results for the same system. These results show that C12BDMAC does not have a significant effect on the corrosion rate of 1018 steel in brine below the cmc and only slightly reduces the corrosion

Figure 3.16. Corrosion rate vs time for 1018 steel in deionised water under CO_2 conditions at 25 °C with 0.1 mM C12BDMAC, determined by bubble test. Dashed vertical line indicates the point at which C12BDMAC was added.

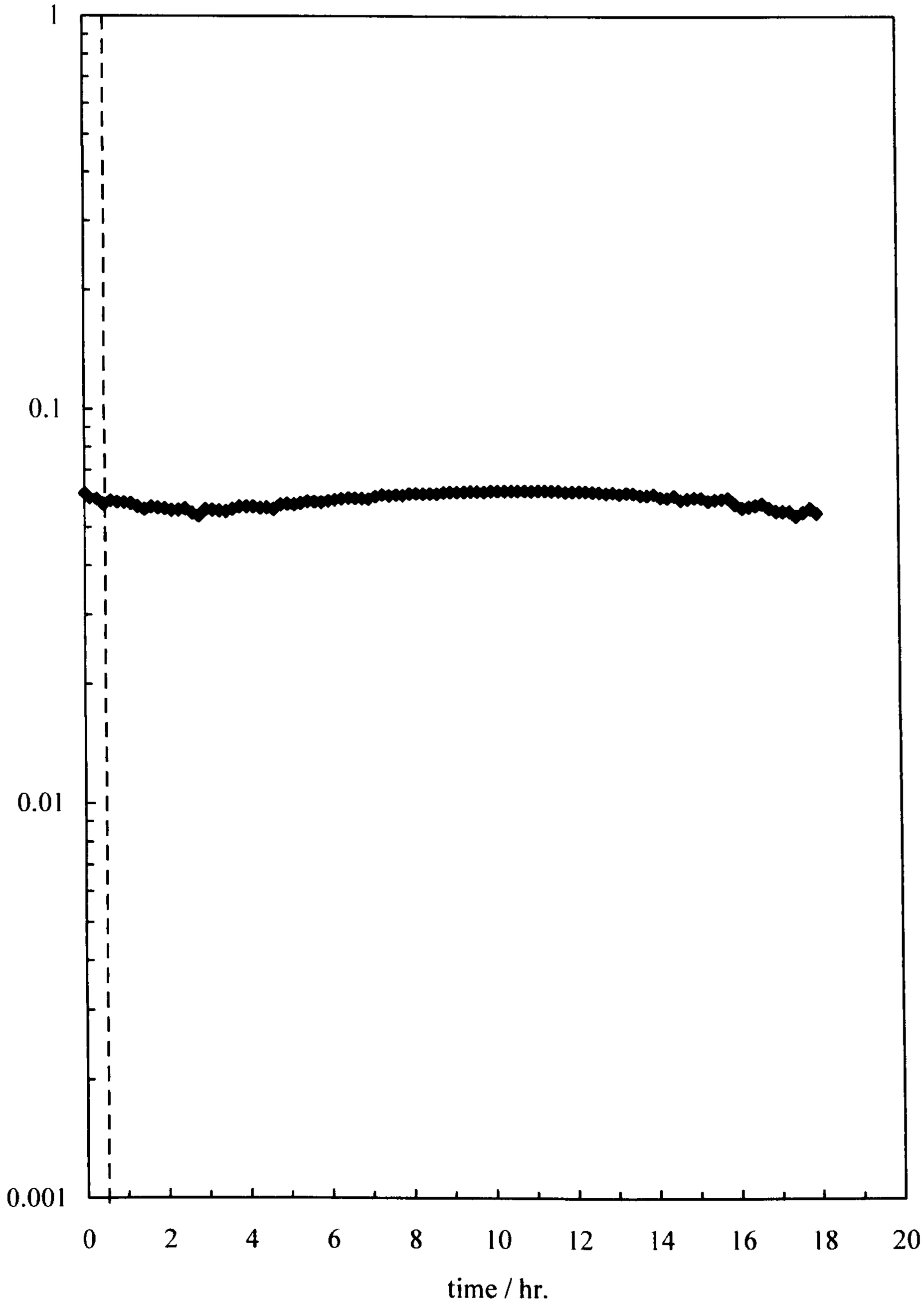

Figure 3.17. Corrosion rate vs [C12BDMAC] for 1018 steel in deionised water under CO_2 conditions at 25 °C, determined by bubble test. Red horizontal line indicates the baseline corrosion rate. Dashed vertical line indicates the cmc of C12BDMAC.

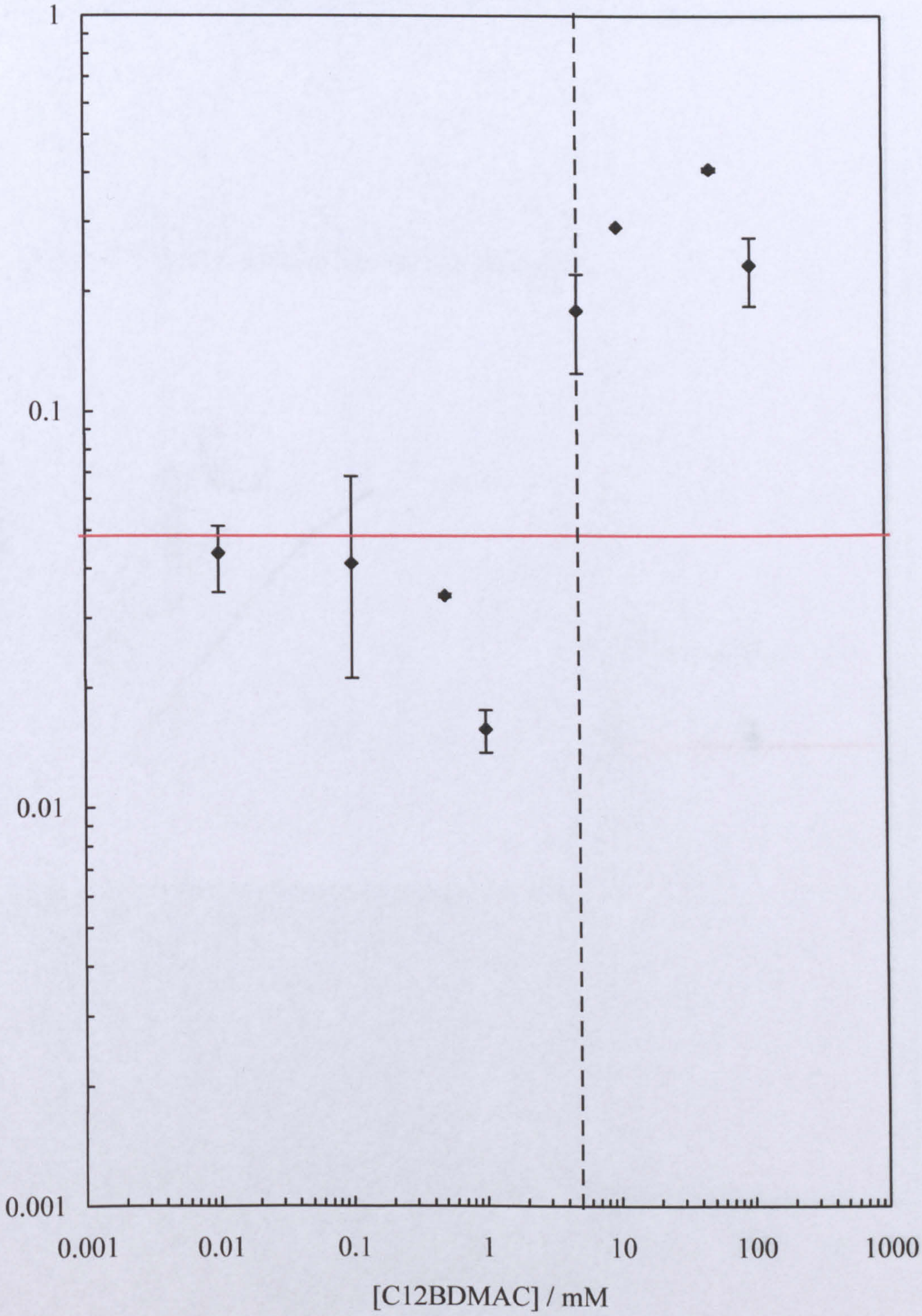

Figure 3.18. Corrosion rate vs [C12BDMAC] for 1018 steel in deionised water under CO_2 conditions at 25 °C, determined by wheel box test. Red horizontal line indicates the baseline corrosion rate. Dashed vertical line indicates the cmc of C12BDMAC.

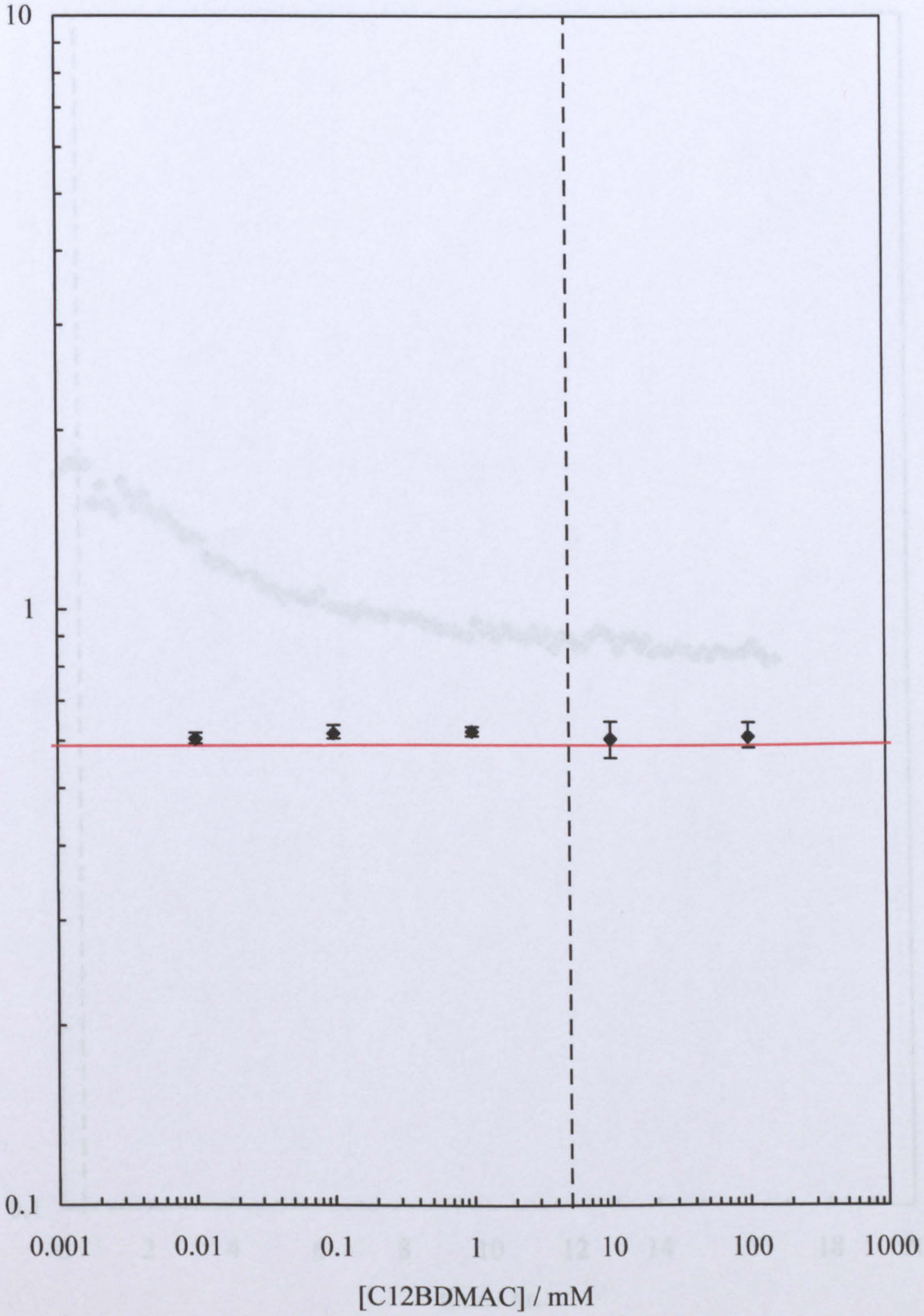

Figure 3.19. Corrosion rate vs time for 1018 steel in 4.7 wt.% brine under CO_2 conditions at 25 °C with 0.1 mM C12BDMAC, determined by bubble test. Dashed vertical line indicates the point at which C12BDMAC was added.

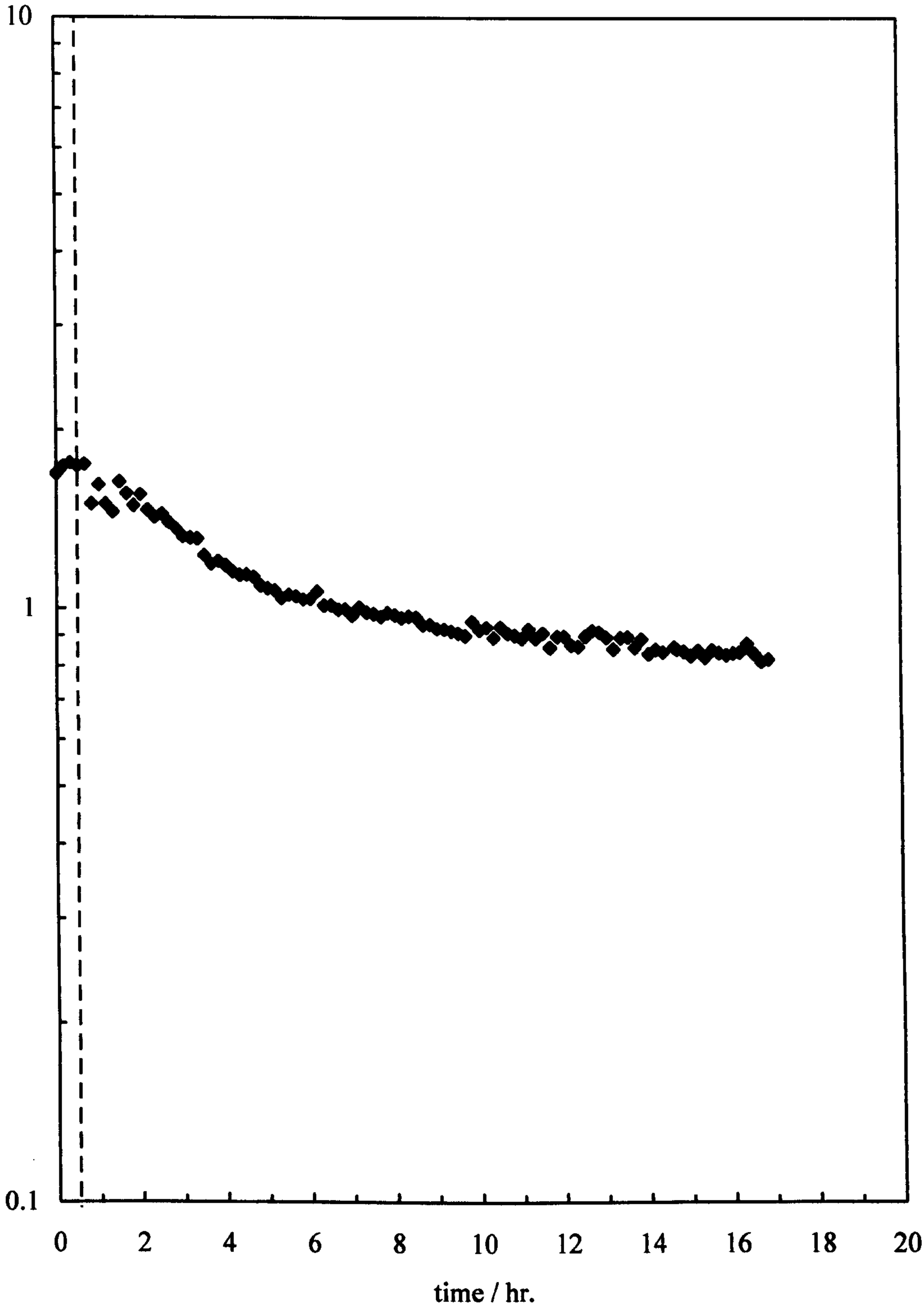

Figure 3.20. Corrosion rate vs [C12BDMAC] for 1018 steel in 4.7 wt.% brine under CO_2 conditions at 25 °C, determined by bubble test. Red horizontal line indicates the baseline corrosion rate. Dashed vertical line indicates the cmc of C12BDMAC.

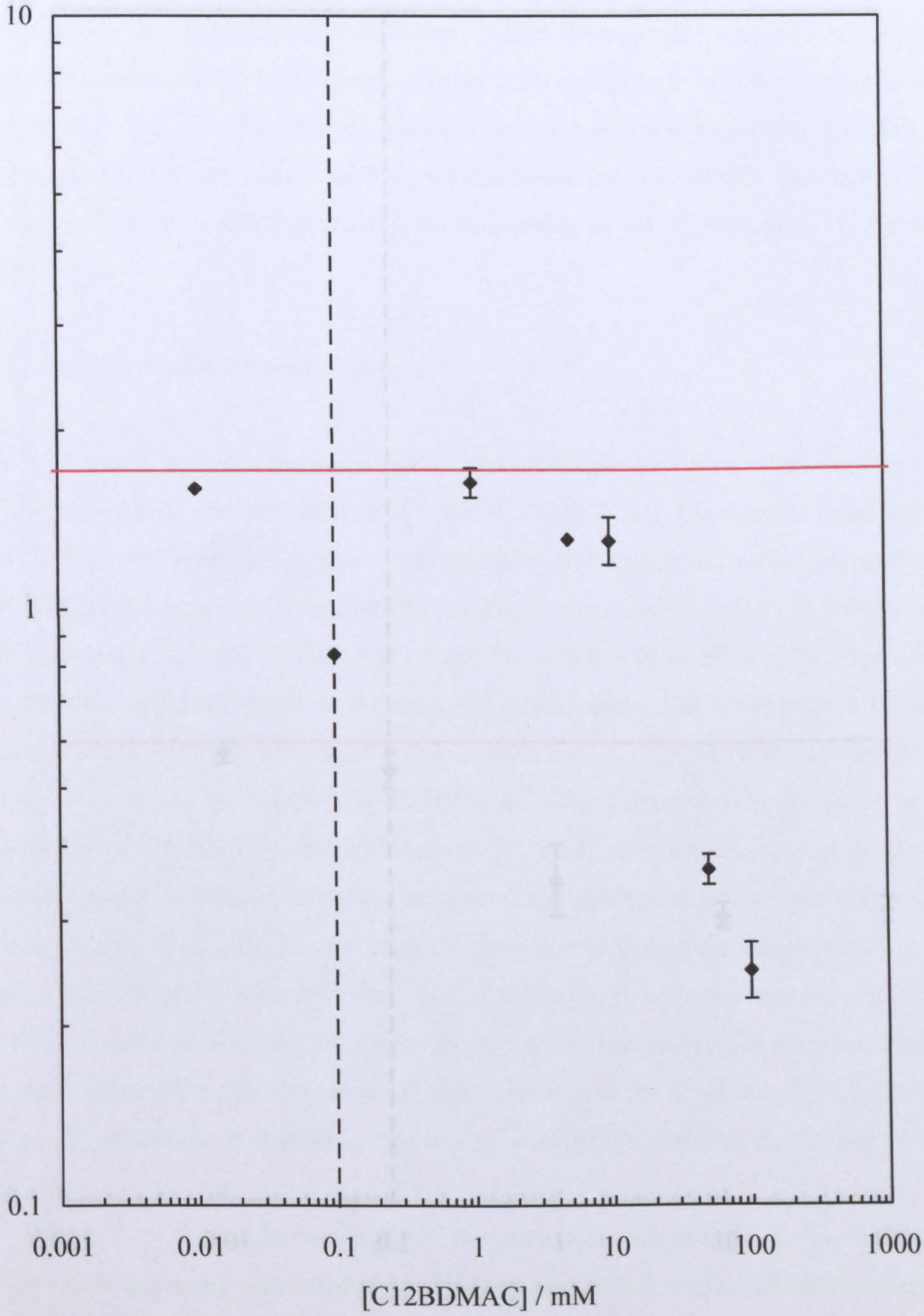

Figure 3.21. Corrosion rate vs [C12BDMAC] for 1018 steel in 4.7 wt.% brine under CO_2 conditions at 25 °C, determied by wheel box test. Red horizontal line indicates the baseline corrosion rate. Dashed vertical line indicates the cmc of C12BDMAC.

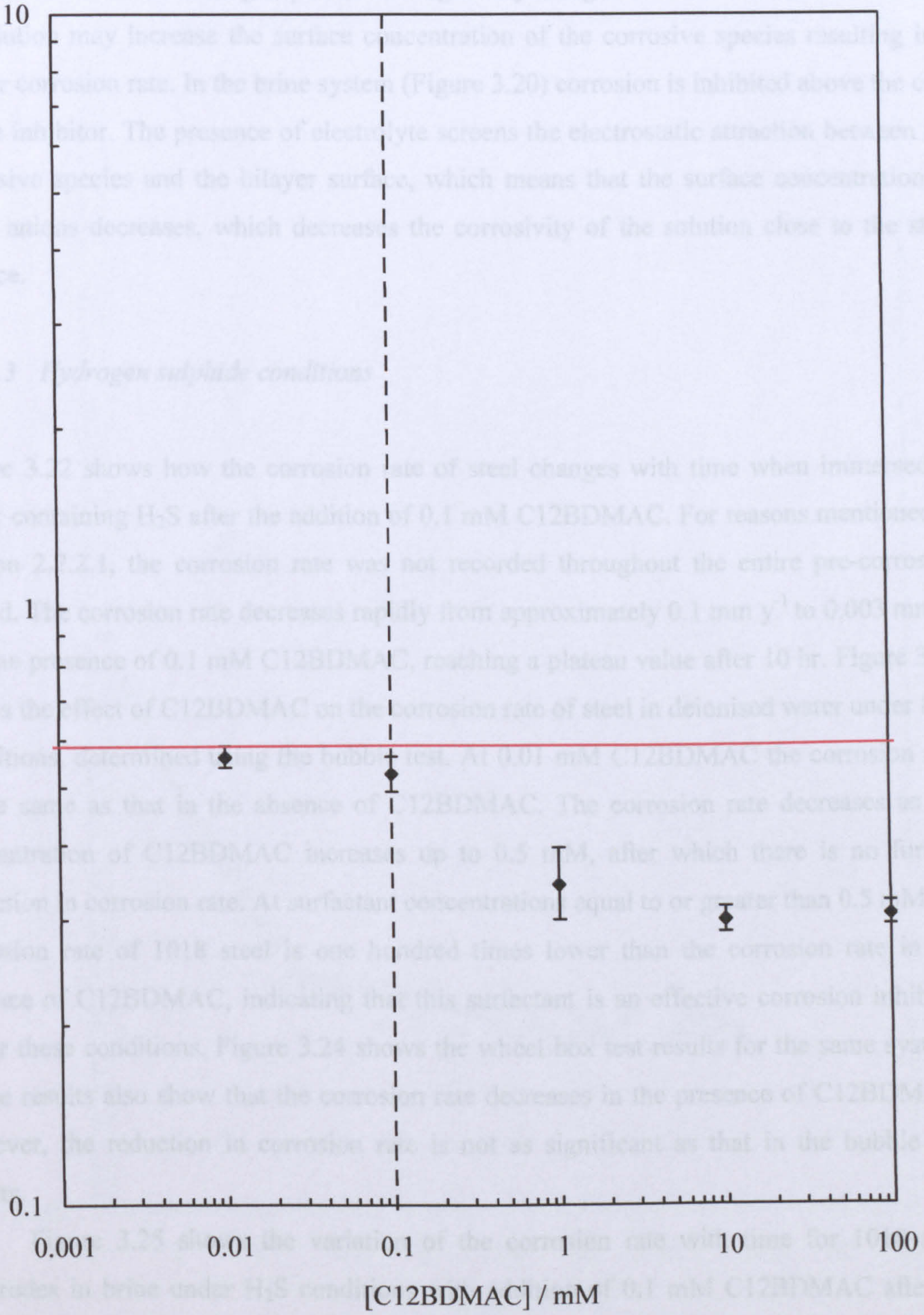

rate above the cmc.

Figure 3.17 shows that the corrosion rate in deionised water increases above the cmc of C12BDMAC, where a bilayer structure may form at the metal surface. The surface of the bilayer is composed of positively charged head groups. Electrostatic attraction between the inhibitor head groups and the negatively charged carbonate or bicarbonate ions in solution may increase the surface concentration of the corrosive species resulting in a higher corrosion rate. In the brine system (Figure 3.20) corrosion is inhibited above the cmc of the inhibitor. The presence of electrolyte screens the electrostatic attraction between the corrosive species and the bilayer surface, which means that the surface concentration of these anions decreases, which decreases the corrosivity of the solution close to the steel surface.

3.4.1.3 Hydrogen sulphide conditions

Figure 3.22 shows how the corrosion rate of steel changes with time when immersed in water containing H_2S after the addition of 0.1 mM C12BDMAC. For reasons mentioned in section 2.2.2.1, the corrosion rate was not recorded throughout the entire pre-corrosion period. The corrosion rate decreases rapidly from approximately 0.1 mm y^{-1} to 0.003 mm y^{-1} in the presence of 0.1 mM C12BDMAC, reaching a plateau value after 10 hr. Figure 3.23 shows the effect of C12BDMAC on the corrosion rate of steel in deionised water under H_2S conditions, determined using the bubble test. At 0.01 mM C12BDMAC the corrosion rate is the same as that in the absence of C12BDMAC. The corrosion rate decreases as the concentration of C12BDMAC increases up to 0.5 mM, after which there is no further reduction in corrosion rate. At surfactant concentrations equal to or greater than 0.5 mM the corrosion rate of 1018 steel is one hundred times lower than the corrosion rate in the absence of C12BDMAC, indicating that this surfactant is an effective corrosion inhibitor under these conditions. Figure 3.24 shows the wheel box test results for the same system. These results also show that the corrosion rate decreases in the presence of C12BDMAC; however, the reduction in corrosion rate is not as significant as that in the bubble test results.

Figure 3.25 shows the variation of the corrosion rate with time for 1018 steel electrodes in brine under H_2S conditions with addition of 0.1 mM C12BDMAC after 30 min. Again, some of the pre-corrosion measurements are absent; the decrease in corrosion

Figure 3.22. Corrosion rate vs time for 1018 steel in deionised water under H_2S conditions at 25 °C with 0.1 mM C12BDMAC, determined by bubble test. Dashed vertical line indicates the point at which C12BDMAC was added.

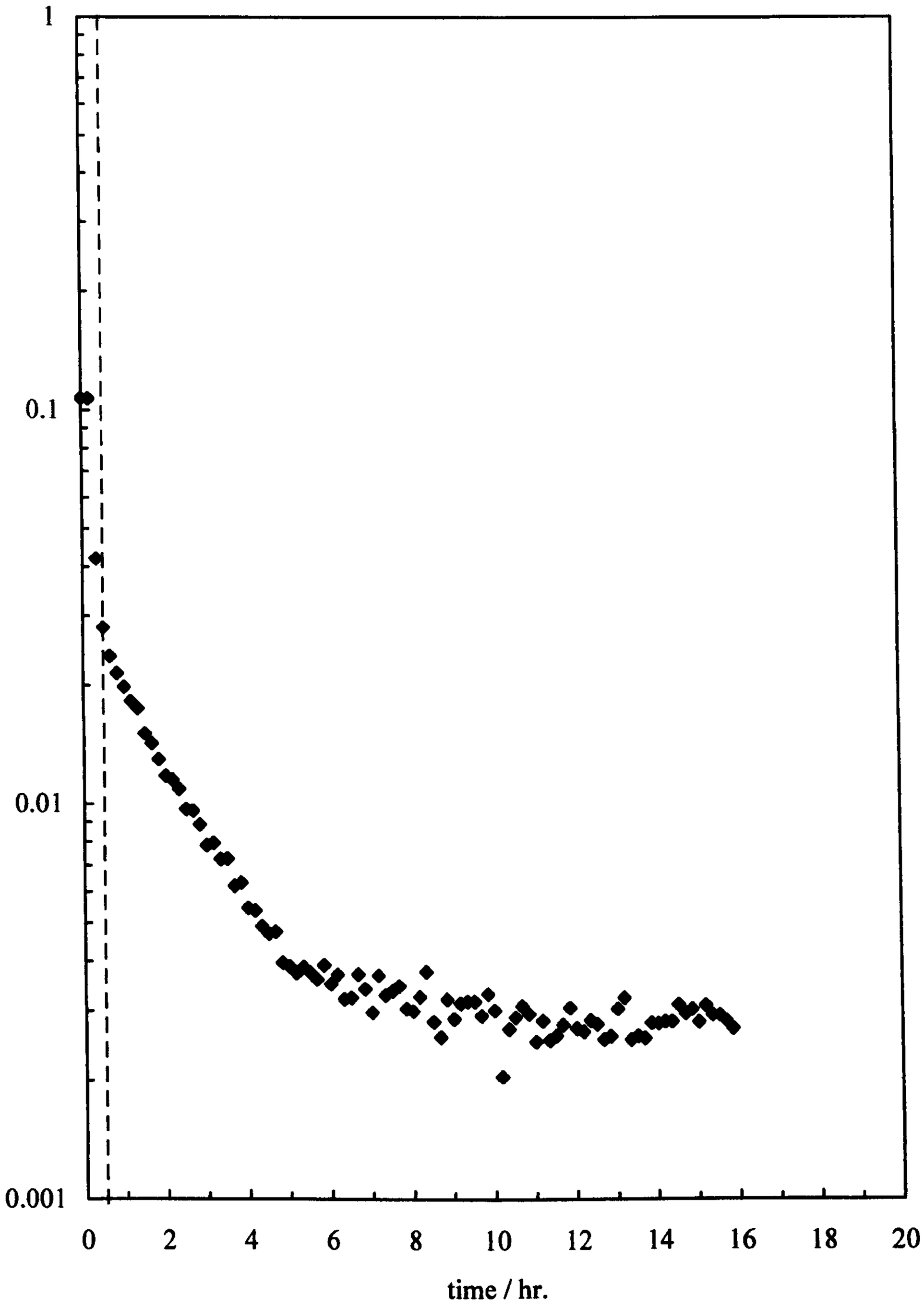

Figure 3.23. Corrosion rate vs [C12BDMAC] for 1018 steel in deionised water under H_2S conditions at 25 °C, determined by bubble test. Red horizontal line indicates the baseline corrosion rate. Dashed vertical line indicates the cmc of C12BDMAC.

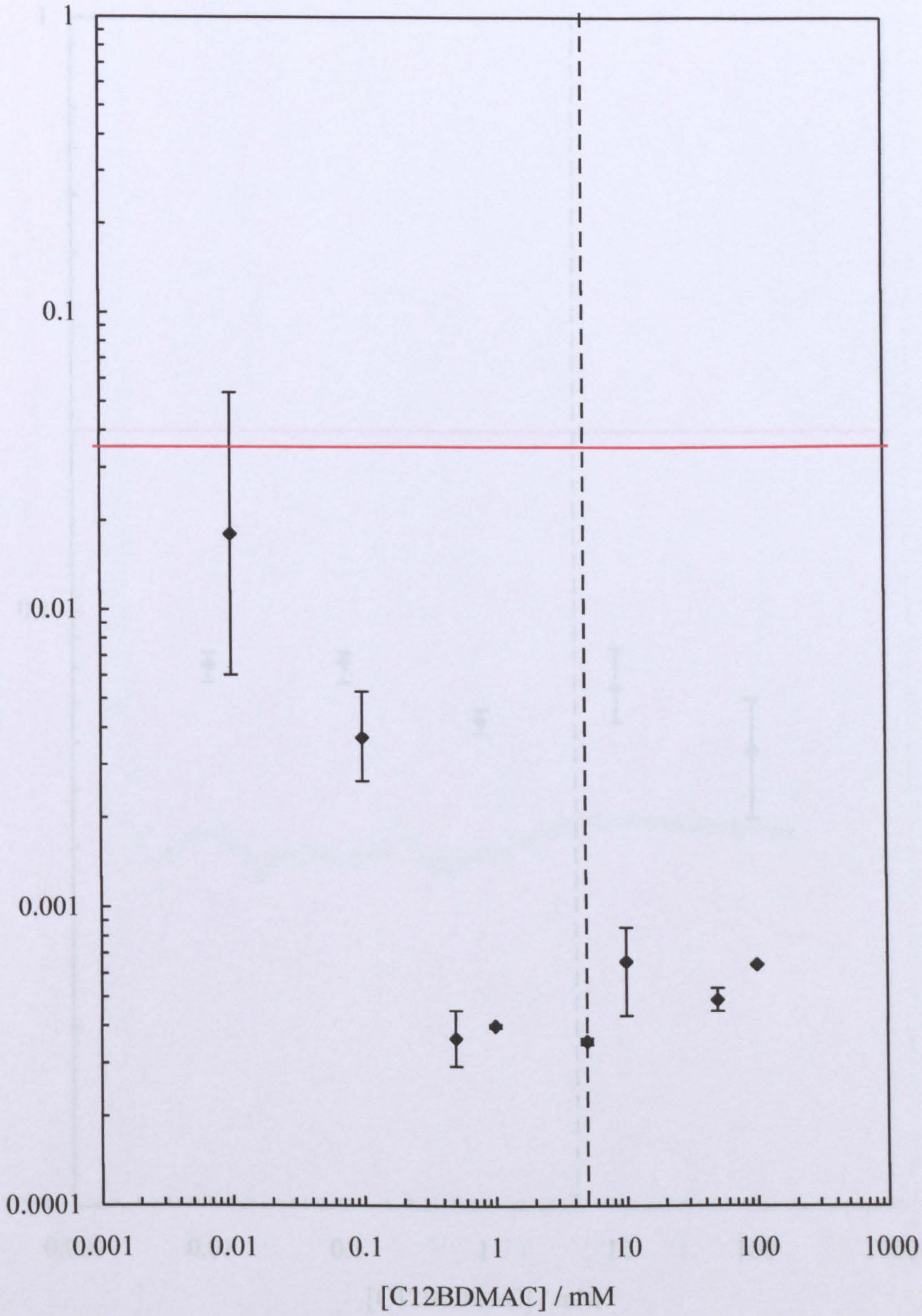

Figure 3.24. Corrosion rate vs [C12BDMAC] for 1018 steel in deionised water under H_2S conditions at 25 °C, determined by wheel box test. Red horizontal line indicates the baseline corrosion rate. Dashed vertical line indicates the cmc of C12BDMAC.

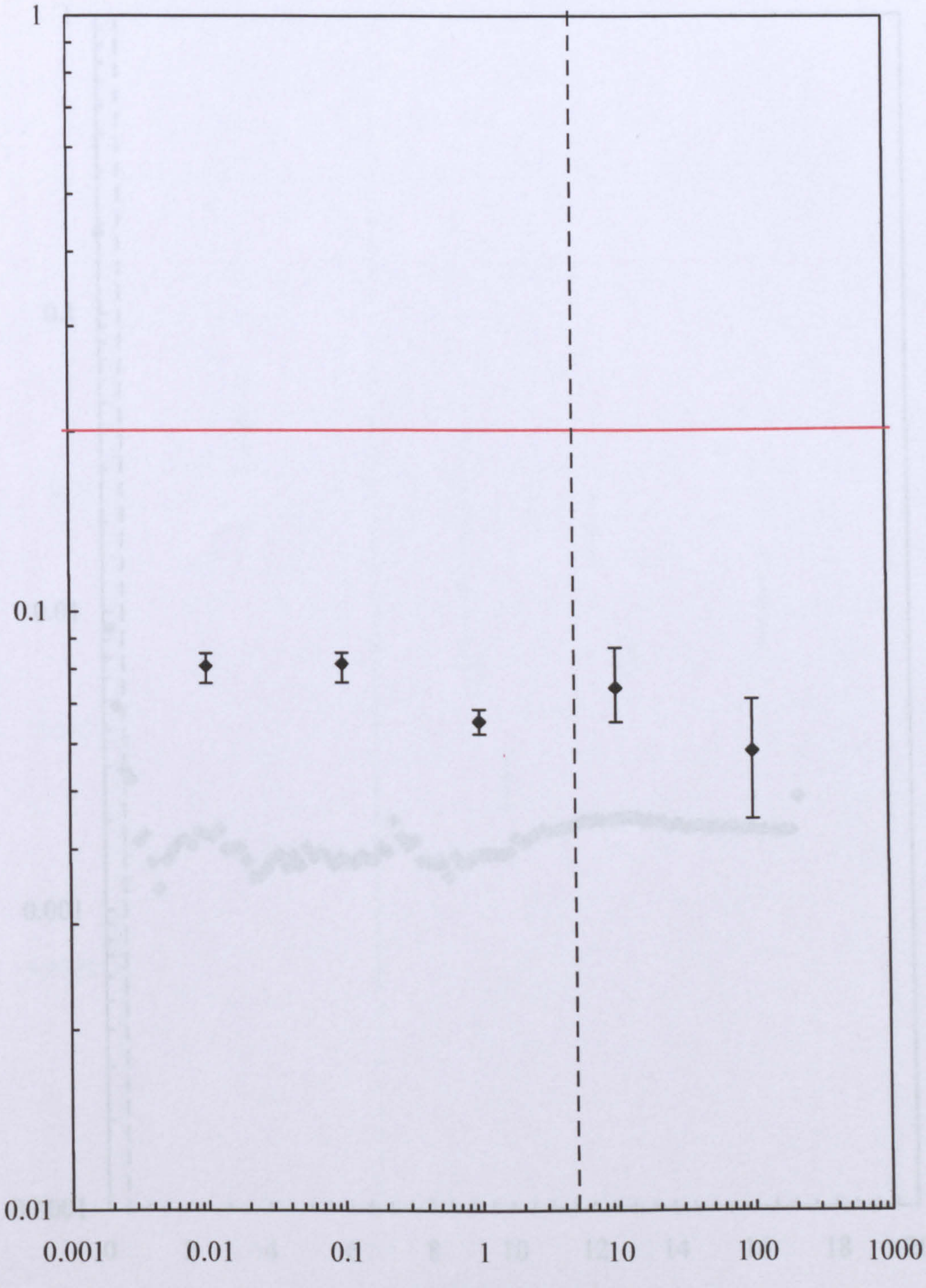

Figure 3.25. Corrosion rate vs time for 1018 steel in 4.7 wt.% brine under H_2S conditions at 25 °C with 0.1 mM C12BDMAC, determined by bubble test. Dashed vertical line indicates the point at which C12BDMAC was added..

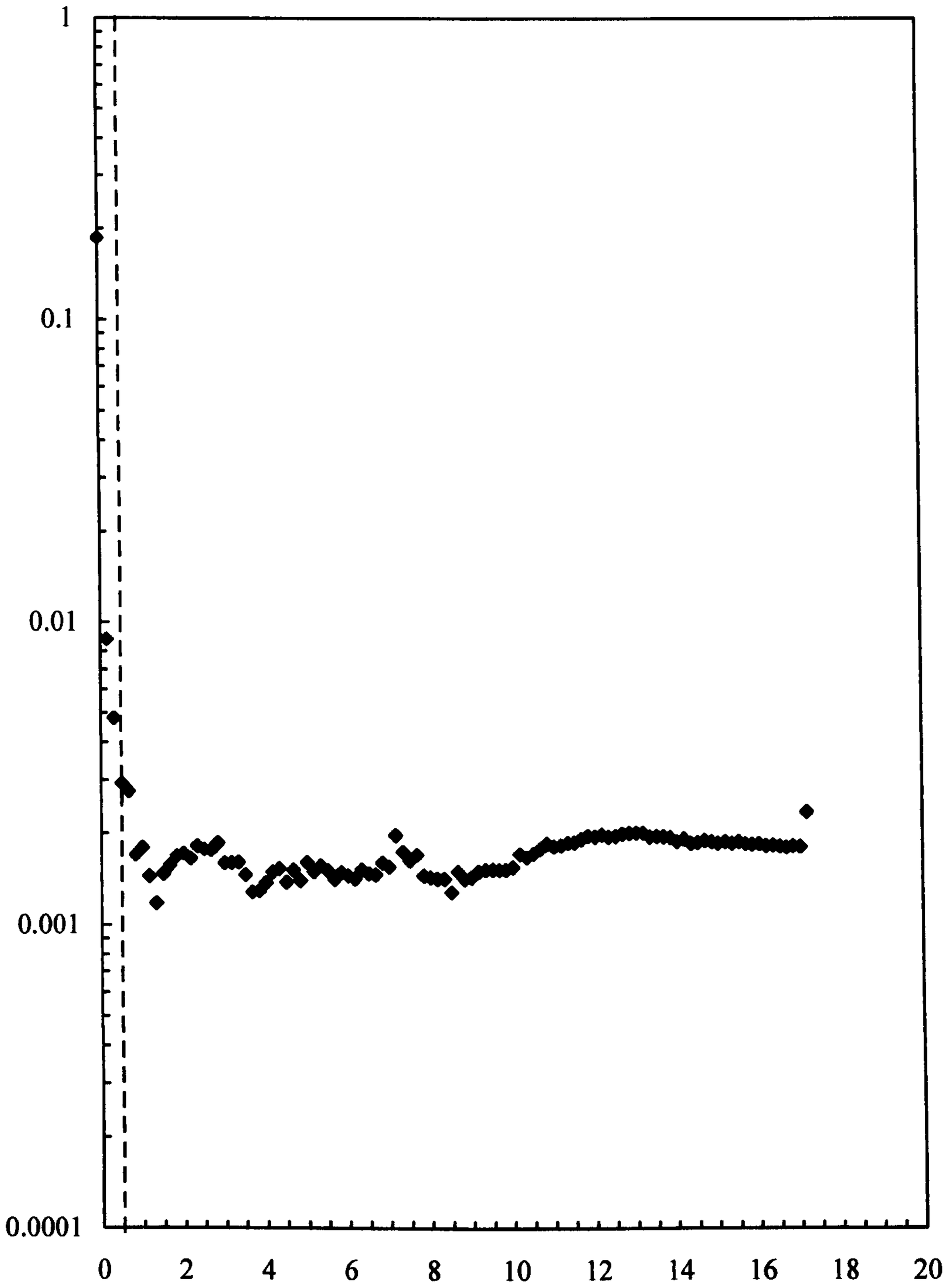

Figure 3.26. Corrosion rate vs [C12BDMAC] for 1018 steel in 4.7 wt.% brine under H_2S conditions at 25 °C, determined by bubble test. Red horizontal line indicates the baseline corrosion rate. Dashed vertical line indicates the cmc of C12BDMAC.

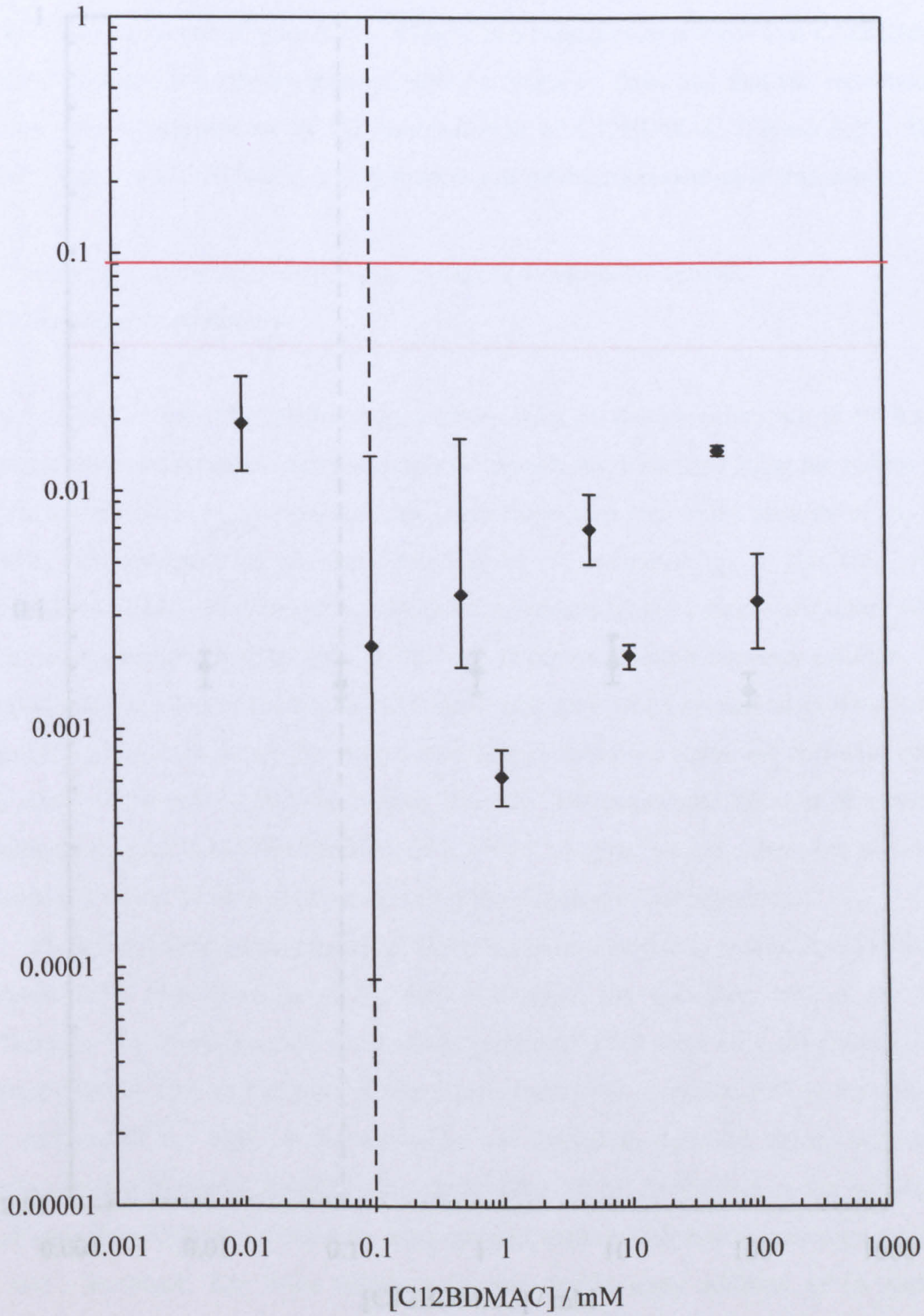

Figure 3.27. Corrosion rate vs [C12BDMAC] for 1018 steel in 4.7 wt.% brine under H_2S conditions at 25 °C, determied by wheel box test. Red horizontal line indicates the baseline corrosion rate. Dashed vertical line indicates the cmc of C12BDMAC in water.

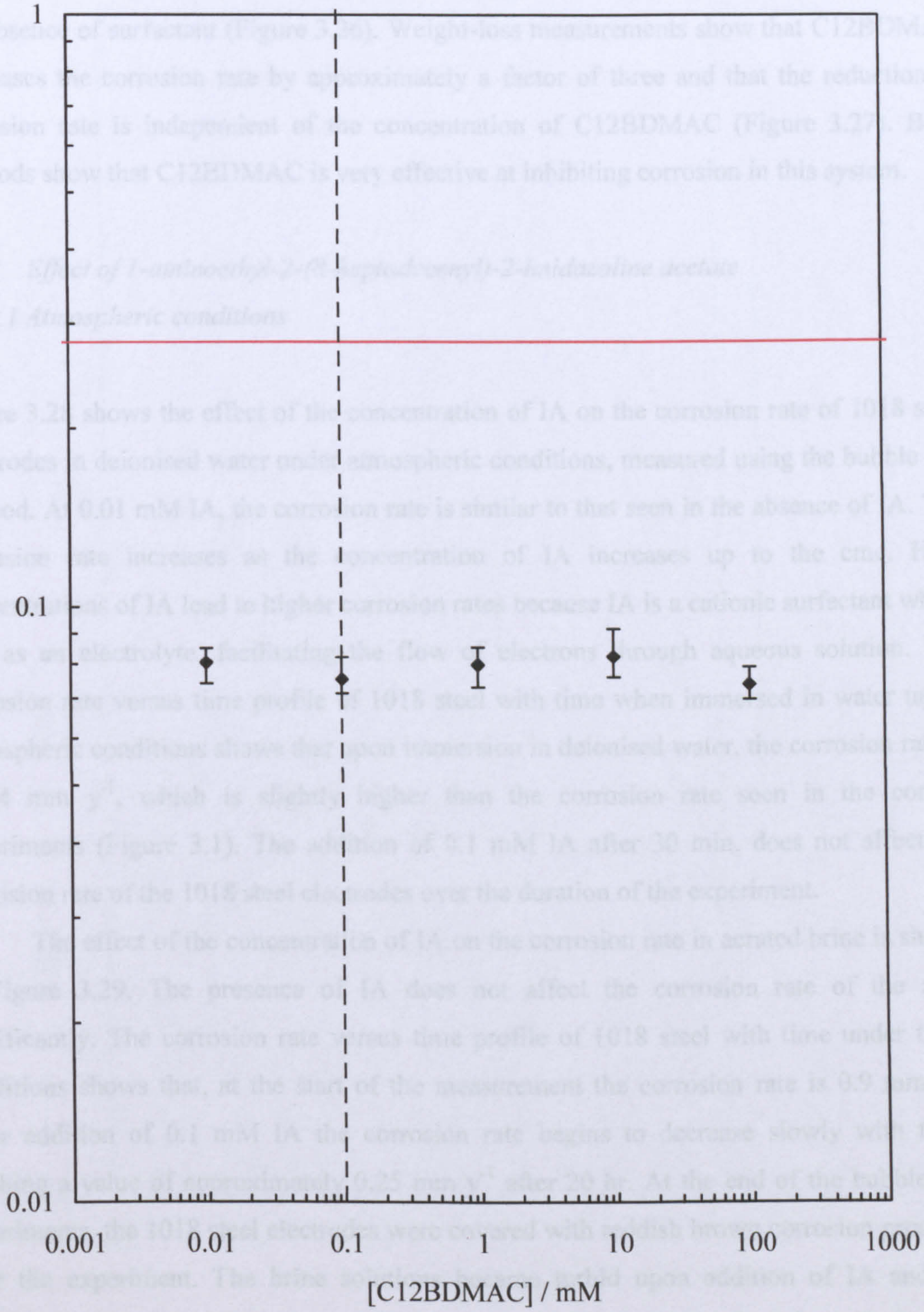

rate in the first 30 min. is due to the presence of C12BDMAC. The corrosion rate decreases from 0.1 mm y^{-1} to approximately 0.001 mm y^{-1} in the presence of 0.1 mM C12BDMAC and remains constant for the duration of the experiment. In brine containing H_2S, the corrosion rate of the 1018 steel in the presence of C12BDMAC, determined using the bubble test, was generally one to two orders of magnitude lower than the corrosion rate in the absence of surfactant (Figure 3.26). Weight-loss measurements show that C12BDMAC decreases the corrosion rate by approximately a factor of three and that the reduction in corrosion rate is independent of the concentration of C12BDMAC (Figure 3.27). Both methods show that C12BDMAC is very effective at inhibiting corrosion in this system.

3.4.2 Effect of 1-aminoethyl-2-(8-heptadecenyl)-2-imidazoline acetate

3.4.2.1 Atmospheric conditions

Figure 3.28 shows the effect of the concentration of IA on the corrosion rate of 1018 steel electrodes in deionised water under atmospheric conditions, measured using the bubble test method. At 0.01 mM IA, the corrosion rate is similar to that seen in the absence of IA. The corrosion rate increases as the concentration of IA increases up to the cmc. High concentrations of IA lead to higher corrosion rates because IA is a cationic surfactant which acts as an electrolyte, facilitating the flow of electrons through aqueous solution. The corrosion rate versus time profile of 1018 steel with time when immersed in water under atmospheric conditions shows that upon immersion in deionised water, the corrosion rate is 0.004 mm y^{-1}, which is slightly higher than the corrosion rate seen in the control experiments (Figure 3.1). The addition of 0.1 mM IA after 30 min. does not affect the corrosion rate of the 1018 steel electrodes over the duration of the experiment.

The effect of the concentration of IA on the corrosion rate in aerated brine is shown in Figure 3.29. The presence of IA does not affect the corrosion rate of the steel significantly. The corrosion rate versus time profile of 1018 steel with time under these conditions shows that, at the start of the measurement the corrosion rate is 0.9 mm y^{-1}. After addition of 0.1 mM IA the corrosion rate begins to decrease slowly with time, reaching a value of approximately 0.25 mm y^{-1} after 20 hr. At the end of the bubble test experiments, the 1018 steel electrodes were covered with reddish brown corrosion products after the experiment. The brine solutions became turbid upon addition of IA and the turbidity increased as the IA concentration increased; at 100 mM IA the brine solution was

Figure 3.28. Corrosion rate vs [IA] for 1018 steel in deionised water under aerated conditions at 25 °C, determined by bubble test. Red horizontal line indicates the baseline corrosion rate. Dashed vertical line indicates the cmc of IA.

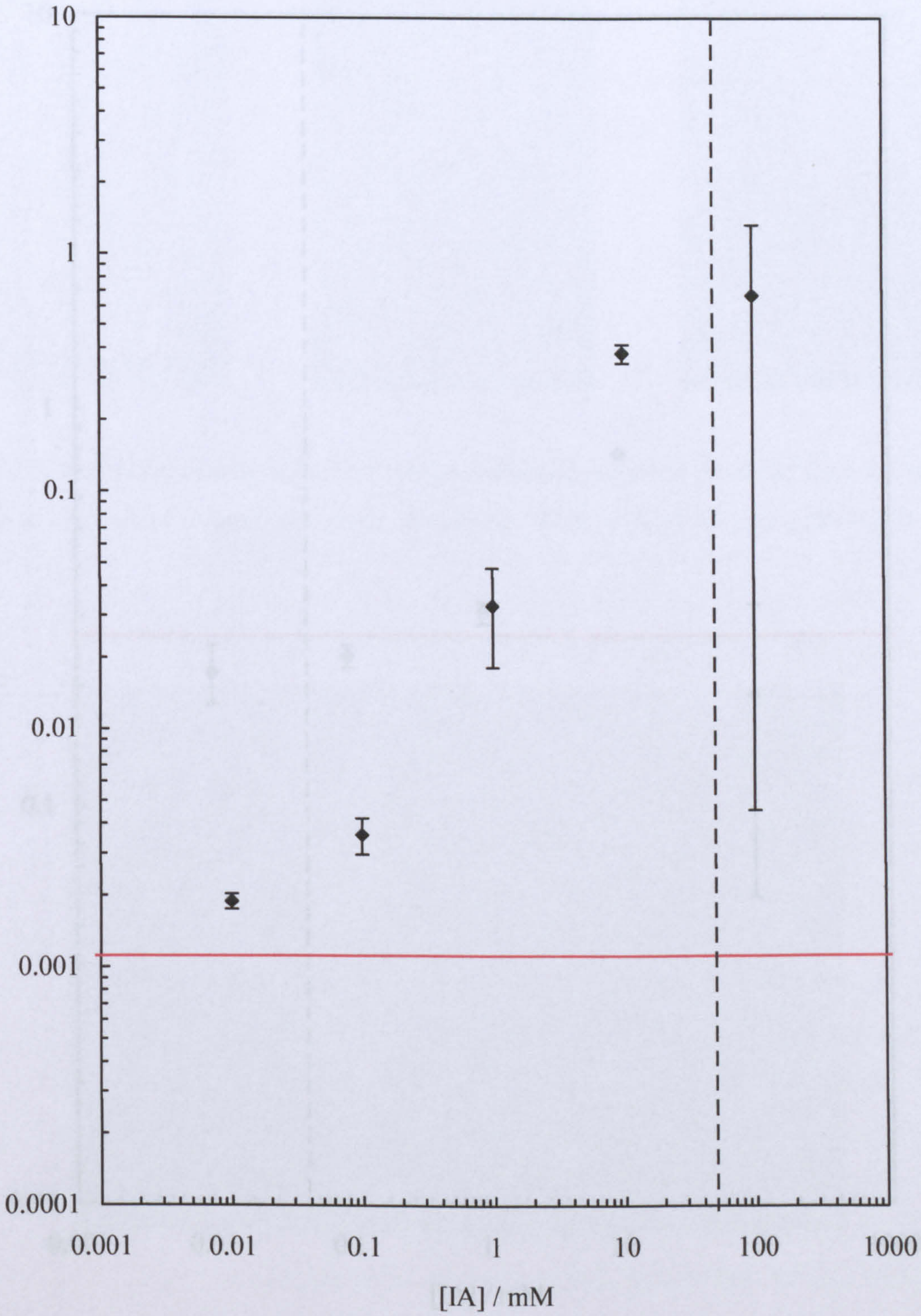

Figure 3.29. Corrosion rate vs [IA] for 1018 steel in 4.7 wt.% brine under aerated conditions at 25 °C, determined by bubble test. Red horizontal line indicates the baseline corrosion rate. Dashed vertical line indicates the cmc of IA.

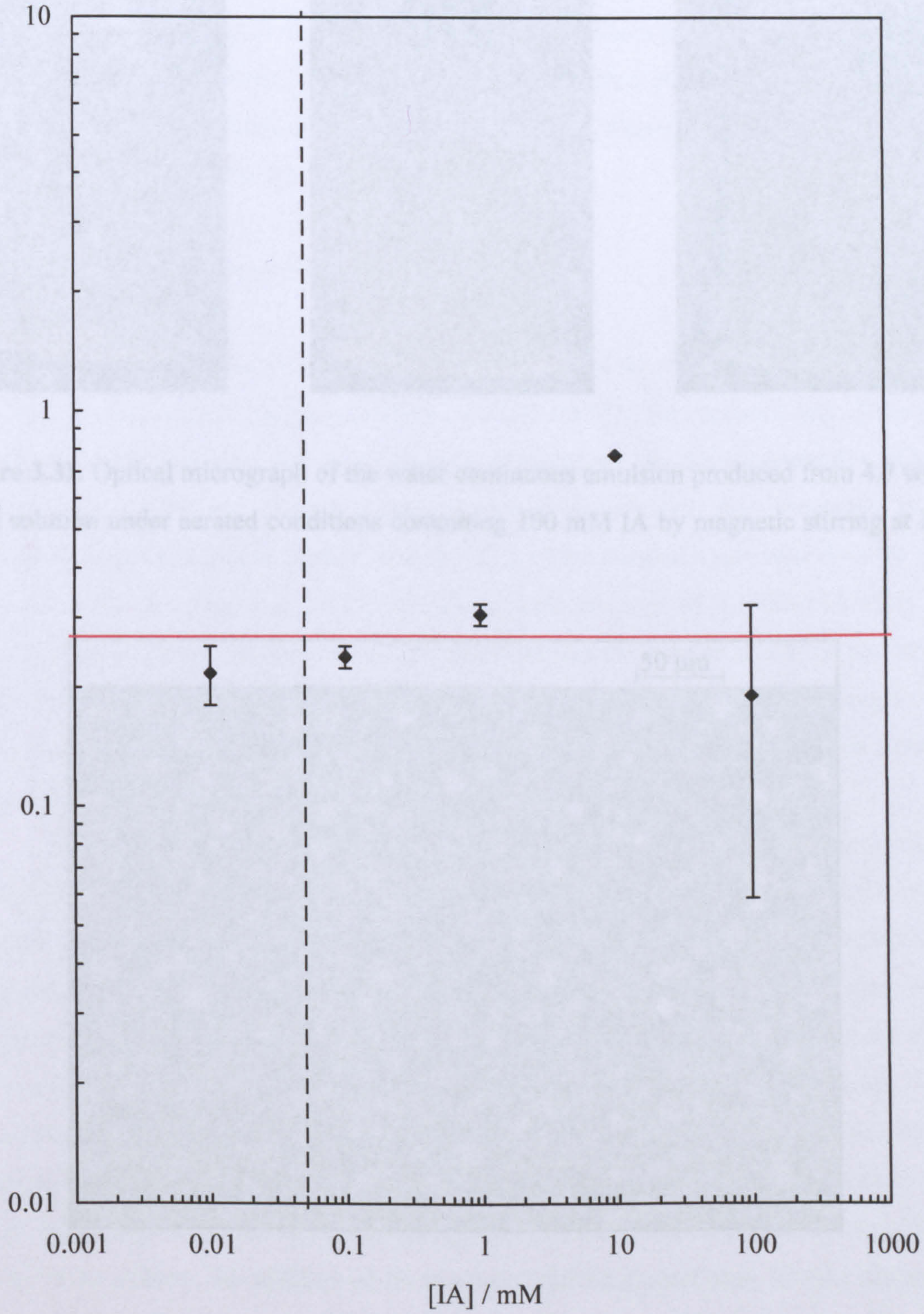

Figure 3.30. Photographs of bubble test cells containing brine under aerated conditions and imidazoline acetate after 24 hr.

(a) 0.01 mM IA

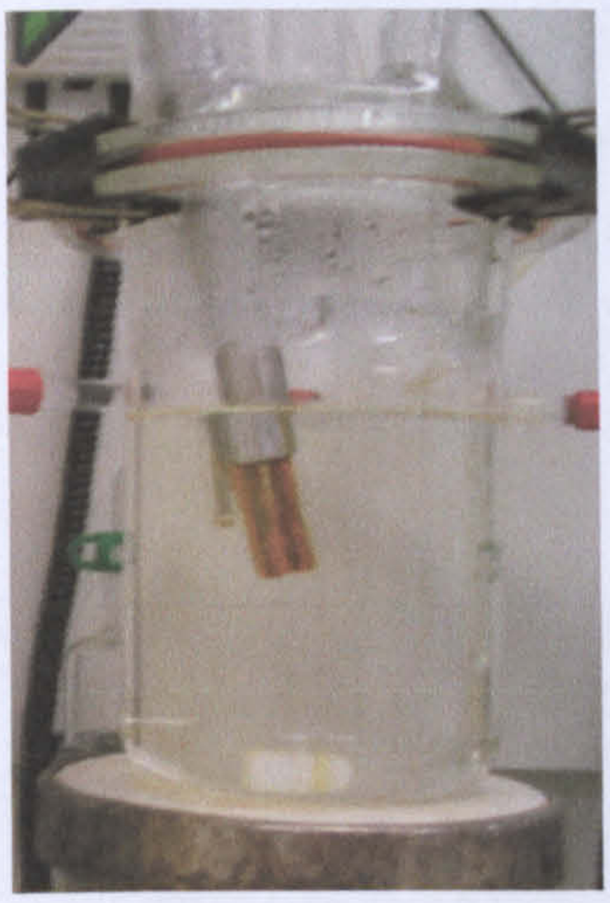

(b) 1 mM IA

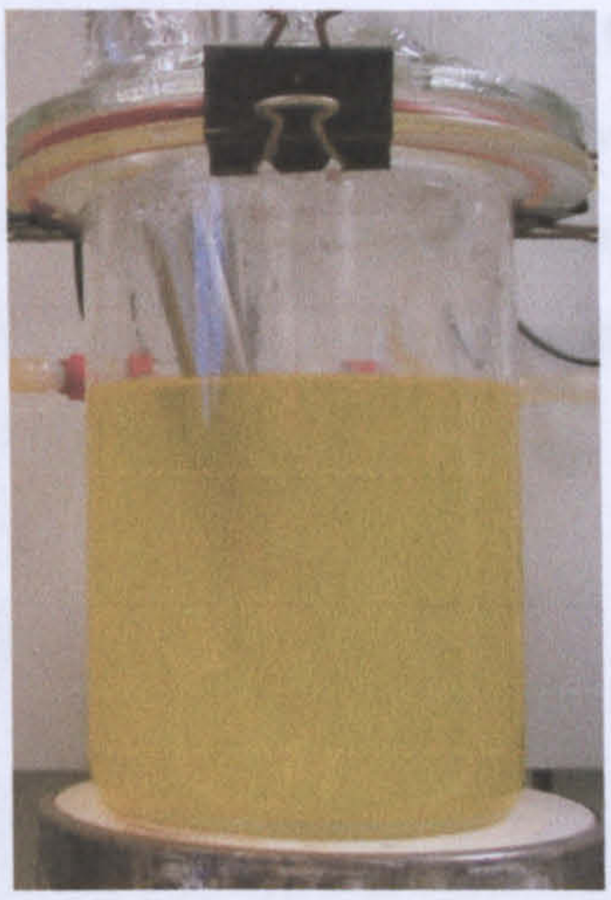

(c) 100 mM IA

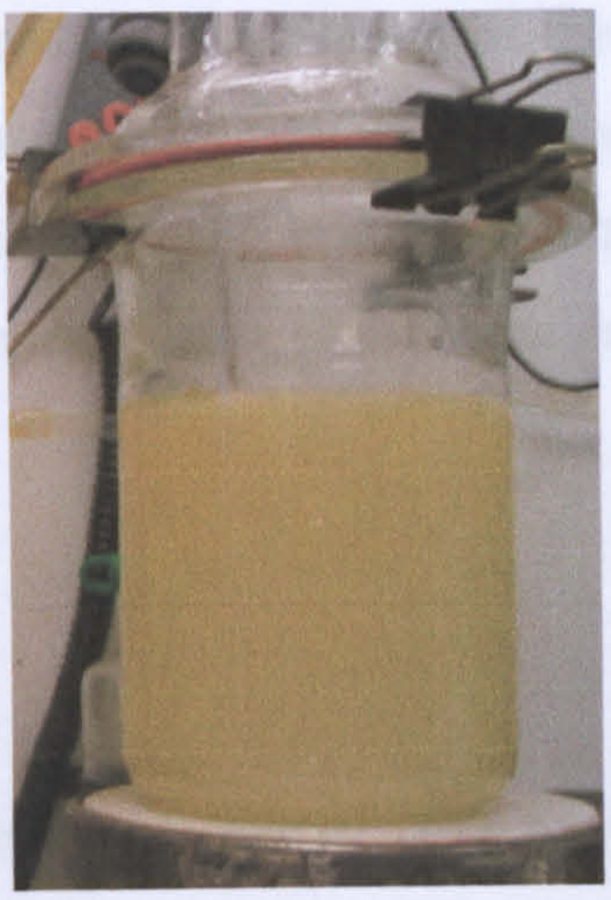

Figure 3.31. Optical micrograph of the water continuous emulsion produced from 4.7 wt.% brine solution under aerated conditions containing 100 mM IA by magnetic stirring at 200 rpm.

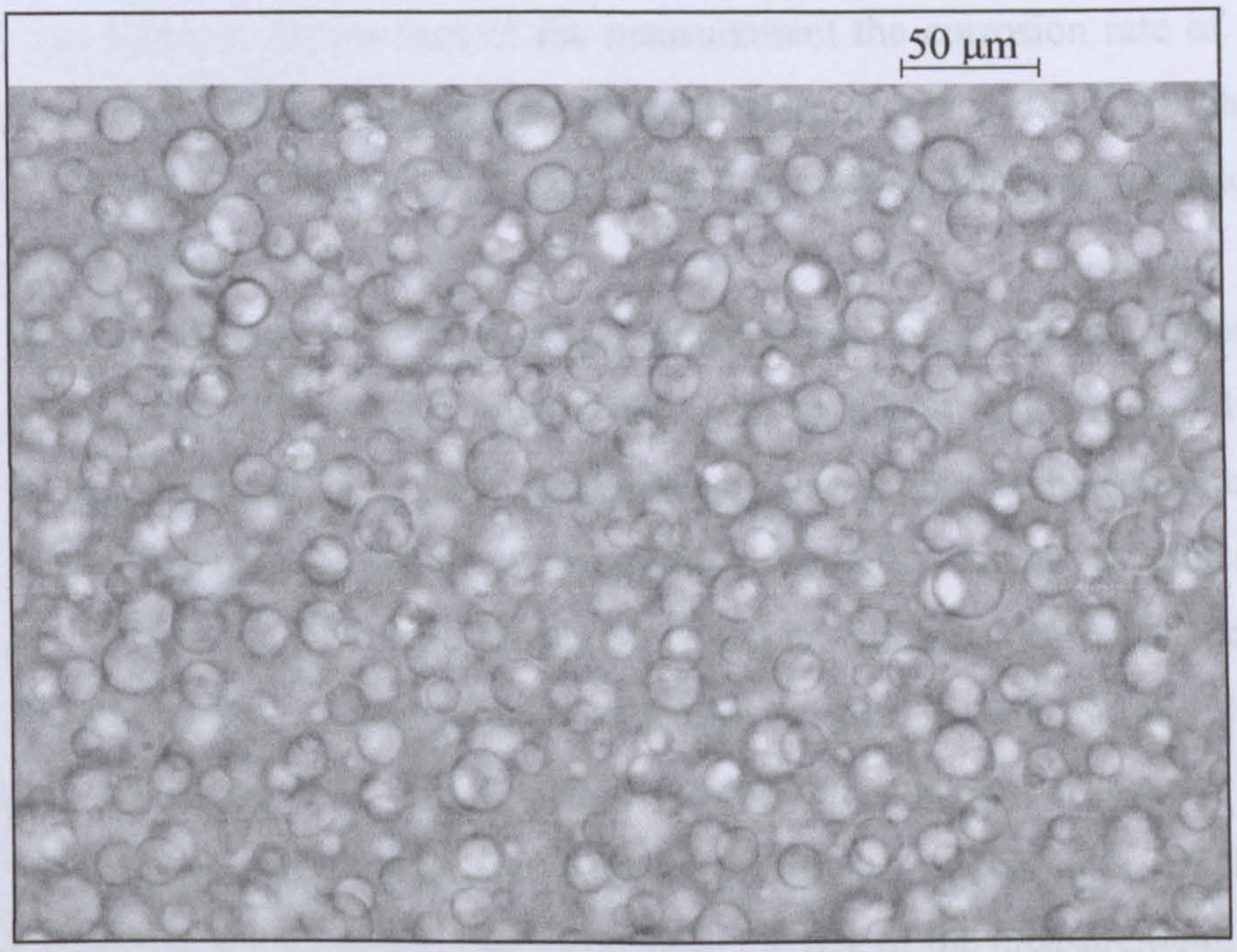

opaque (Figure 3.30). Optical microscopy (Figure 3.31) and drop tests later confirmed that a water continuous emulsion had formed. The presence of a second liquid phase in the system can be explained due to the impurity of the surfactant. The imidazoline was produced by a commercial synthetic route from diethylenetriamine (bis(2-aminoethyl)amine) and oleic acid and consequently the final product is a mixture of the imidazoline plus an amide of oleic acid and some amide which has not been ring-closed as side products[25]. The amount of immiscible organic material added to the brine solution increases as the concentration of surfactant increases and magnetic stirring offers enough energy input to emulsify the two phases.

3.4.2.2 Carbon dioxide conditions

Figure 3.32 shows the effect of the concentration of IA on the corrosion rate of 1018 steel in deionised water under CO_2 gas conditions. At 0.01 mM IA, the corrosion rate of the steel is higher than the corrosion rate in the absence of surfactant. As the concentration of IA is increased to 1 mM, the corrosion rate decreases slightly but then increases as the concentration of IA increases further. The variation of the corrosion rate with time for 1018 steel electrodes in water under CO_2 conditions with addition of 0.1 mM IA after pre-corrosion is as follows. At the start of the measurement the corrosion rate of the steel is 0.065 mm y^{-1}. Addition of IA causes the corrosion rate to increase slowly, reaching a value of 0.1 mm y^{-1} after 20 h. These results show that IA is not an effective corrosion inhibitor under these conditions.

Figure 3.33 shows the effect of the concentration of IA on the corrosion rate in brine under CO_2 conditions. At low concentrations of IA the corrosion rate of 1018 steel is an order of magnitude lower than in the absence of surfactant but as the concentration of IA increases the corrosion rate increases, returning to a value similar to that seen in the absence of surfactant. The variation of the corrosion rate with time for 1018 steel electrodes in CO_2-containing brine with addition of 0.1 mM IA after 30 min. is as follows. Upon immersion of steel in the brine solution the corrosion rate is about 0.5 mm y^{-1}. Addition of IA causes the corrosion rate to decrease to approximately 0.1 mm y^{-1} after which there is no significant change in the corrosion rate throughout the rest of the measurement. As with the aerated brine system, the addition of IA at concentrations greater than 10 mM caused the brine to become an opaque emulsion.

Figure 3.32. Corrosion rate vs [IA] for 1018 steel in deionised water under CO_2 conditions at 25 °C, determined by bubble test. Red horizontal line indicates the baseline corrosion rate. Dashed vertical line indicates the cmc of IA.

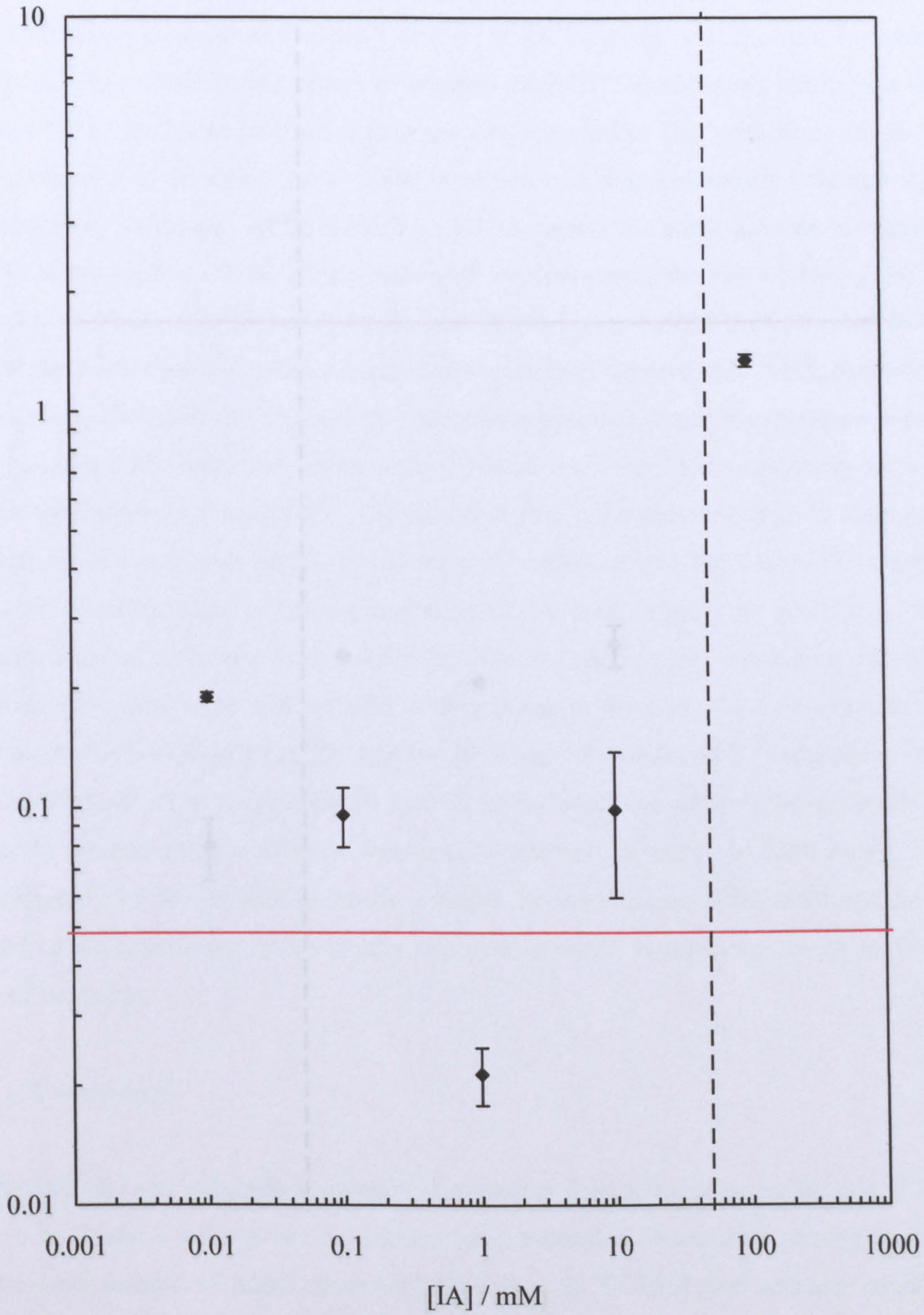

Figure 3.33. Corrosion rate vs [IA] for 1018 steel in 4.7 wt.% brine under CO_2 conditions at 25 °C, determined by bubble test. Red horizontal line indicates the baseline corrosion rate. Dashed vertical line indicates the cmc of IA.

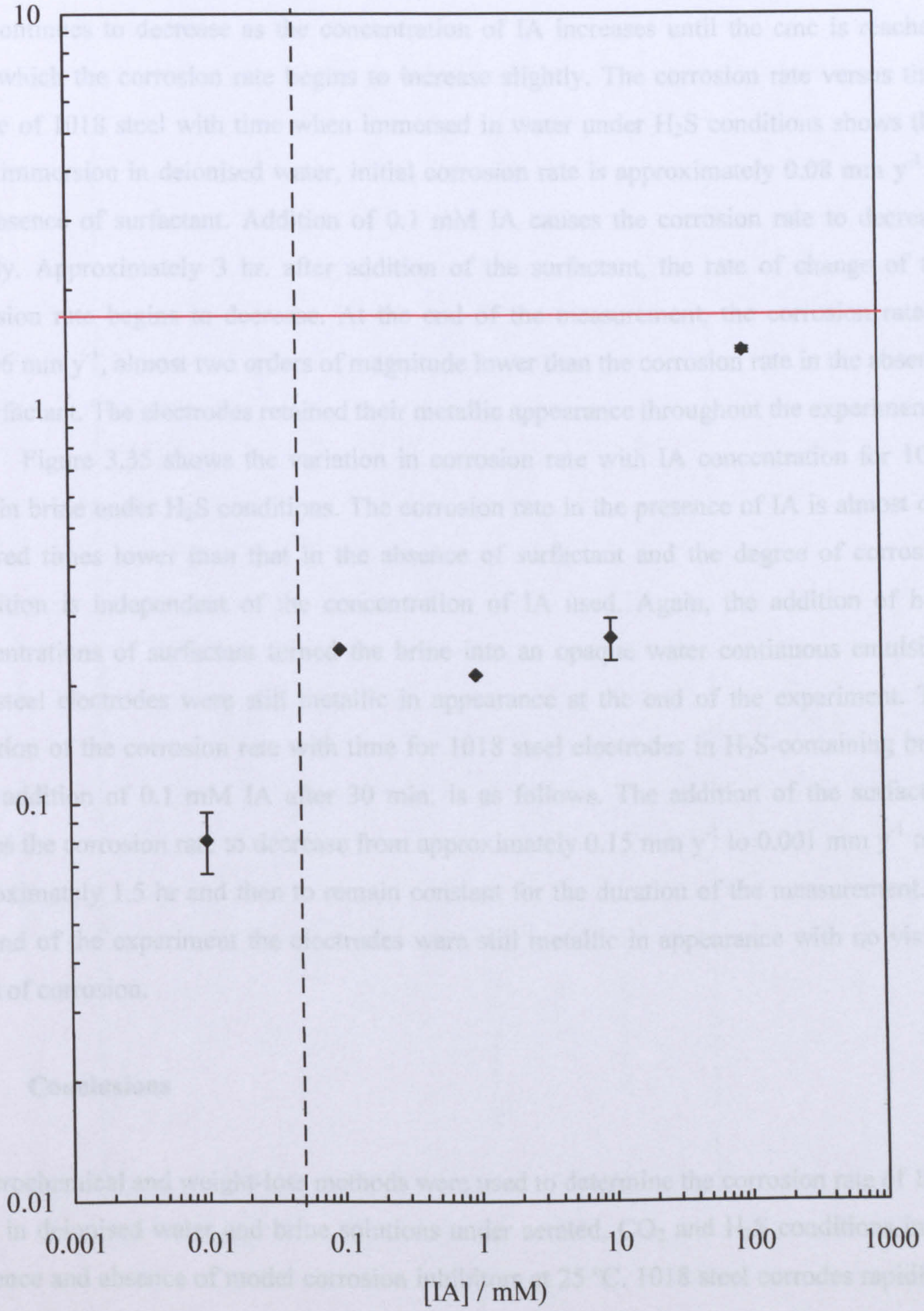

3.4.2.3 Hydrogen sulphide conditions

Figure 3.34 shows the effect of the concentration of IA on the corrosion rate of 1018 steel in deionised water under H_2S gas conditions. At 0.01 mM IA the corrosion rate is almost one order of magnitude lower that the corrosion rate in the absence of IA. The corrosion rate continues to decrease as the concentration of IA increases until the cmc is reached, after which the corrosion rate begins to increase slightly. The corrosion rate versus time profile of 1018 steel with time when immersed in water under H_2S conditions shows that upon immersion in deionised water, initial corrosion rate is approximately 0.08 mm y^{-1} in the absence of surfactant. Addition of 0.1 mM IA causes the corrosion rate to decrease rapidly. Approximately 3 hr. after addition of the surfactant, the rate of change of the corrosion rate begins to decrease. At the end of the measurement, the corrosion rate is 0.0006 mm y^{-1}, almost two orders of magnitude lower than the corrosion rate in the absence of surfactant. The electrodes retained their metallic appearance throughout the experiment.

Figure 3.35 shows the variation in corrosion rate with IA concentration for 1018 steel in brine under H_2S conditions. The corrosion rate in the presence of IA is almost one hundred times lower than that in the absence of surfactant and the degree of corrosion inhibition is independent of the concentration of IA used. Again, the addition of high concentrations of surfactant turned the brine into an opaque water continuous emulsion. The steel electrodes were still metallic in appearance at the end of the experiment. The variation of the corrosion rate with time for 1018 steel electrodes in H_2S-containing brine with addition of 0.1 mM IA after 30 min. is as follows. The addition of the surfactant causes the corrosion rate to decrease from approximately 0.15 mm y^{-1} to 0.001 mm y^{-1} over approximately 1.5 hr and then to remain constant for the duration of the measurement. At the end of the experiment the electrodes were still metallic in appearance with no visible signs of corrosion.

3.5 Conclusions

Electrochemical and weight-loss methods were used to determine the corrosion rate of 1018 steel in deionised water and brine solutions under aerated, CO_2 and H_2S conditions in the presence and absence of model corrosion inhibitors at 25 °C. 1018 steel corrodes rapidly in all the brine environments tested but corrodes at a slower rate in the absence of

Figure 3.34. Corrosion rate vs [IA] for 1018 steel in deionised water under H_2S conditions at 25 °C, determined by bubble test. Red horizontal line indicates the baseline corrosion rate. Dashed vertical line indicates the cmc of IA.

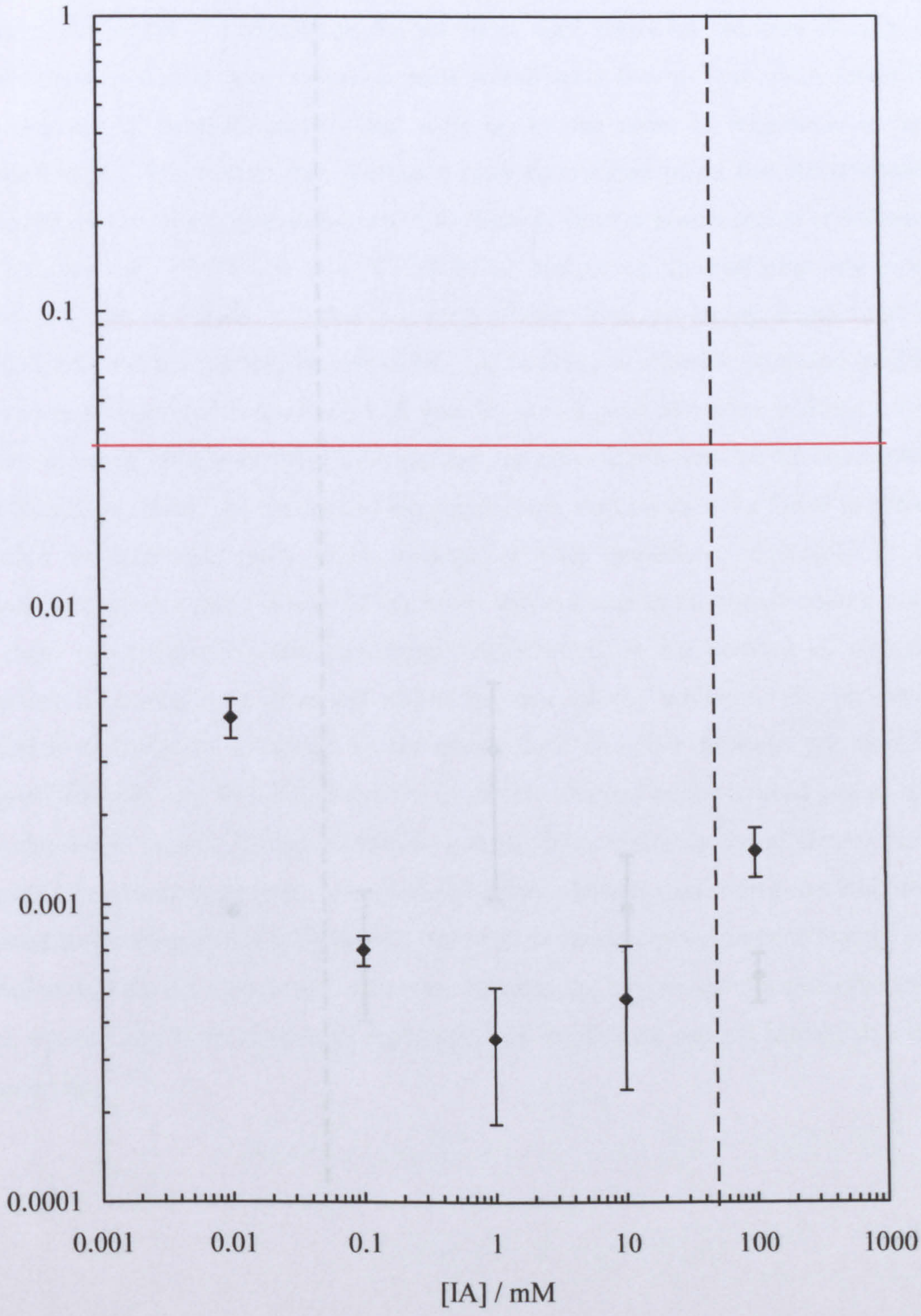

Figure 3.35. Corrosion rate vs [IA] for 1018 steel in 4.7 wt.% brine under H_2S conditions at 25 °C, determined by bubble test. Red horizontal line indicates the baseline corrosion rate. Dashed vertical line indicates the cmc of IA.

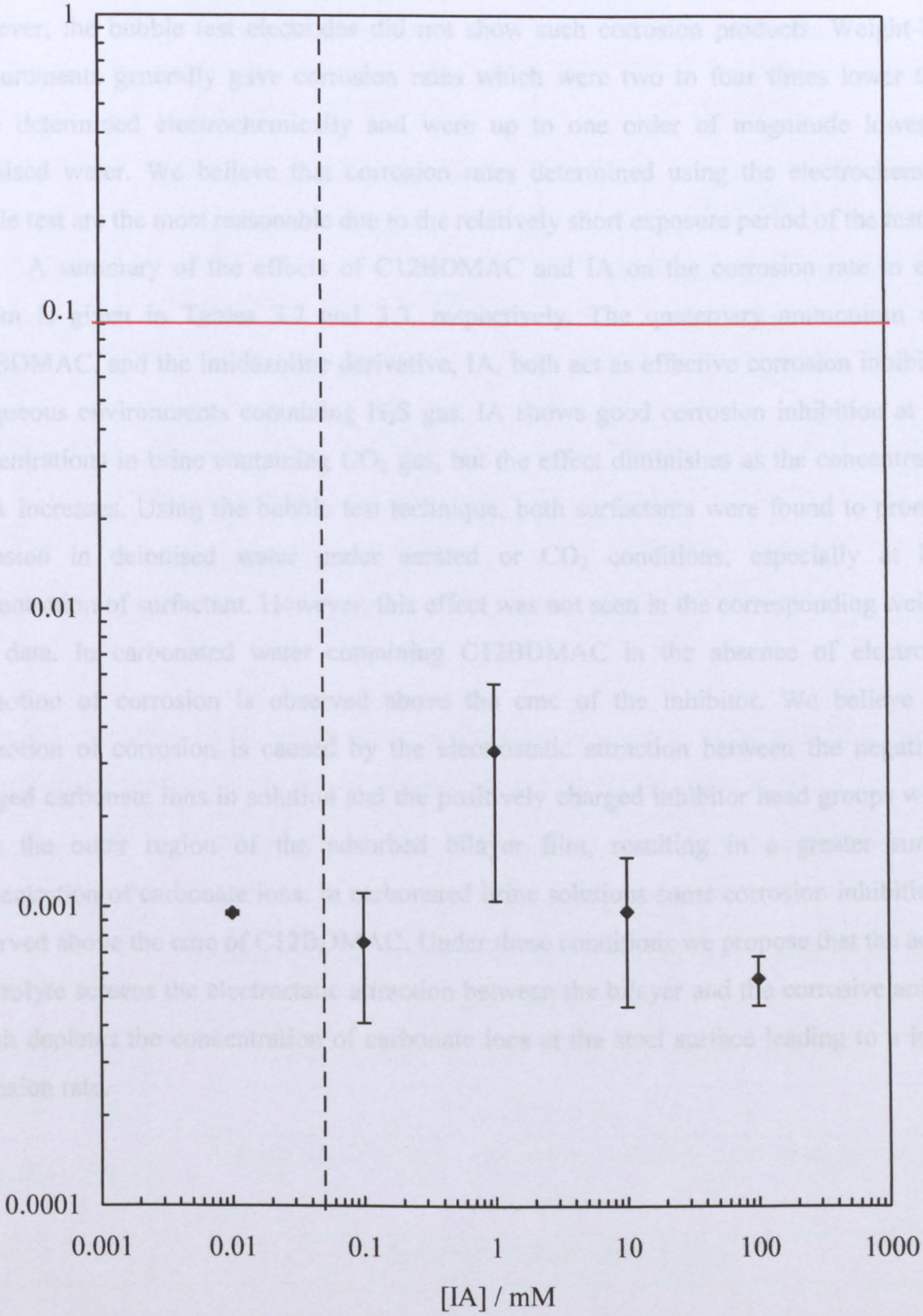

electrolyte due to the lower electrical conductivity of the solution. Steel corroded under aerated conditions exhibited reddish brown iron oxide-hydroxide and black magnetite corrosion products and steel corroded in CO_2-containing environments acquired a grey iron carbonate corrosion product film. Under H_2S conditions, the weight-loss coupons were covered with a black corrosion product film thought to be an iron sulphide compound. However, the bubble test electrodes did not show such corrosion products. Weight-loss measurements generally gave corrosion rates which were two to four times lower than those determined electrochemically and were up to one order of magnitude lower in deionised water. We believe that corrosion rates determined using the electrochemical bubble test are the most reasonable due to the relatively short exposure period of the tests.

A summary of the effects of C12BDMAC and IA on the corrosion rate in each system is given in Tables 3.2 and 3.3, respectively. The quaternary ammonium salt, C12BDMAC, and the imidazoline derivative, IA, both act as effective corrosion inhibitors in aqueous environments containing H_2S gas. IA shows good corrosion inhibition at low concentrations in brine containing CO_2 gas, but the effect diminishes as the concentration of IA increases. Using the bubble test technique, both surfactants were found to promote corrosion in deionised water under aerated or CO_2 conditions, especially at high concentration of surfactant. However, this effect was not seen in the corresponding weight-loss data. In carbonated water containing C12BDMAC in the absence of electrolyte promotion of corrosion is observed above the cmc of the inhibitor. We believe that promotion of corrosion is caused by the electrostatic attraction between the negatively charged carbonate ions in solution and the positively charged inhibitor head groups which form the outer region of the adsorbed bilayer film, resulting in a greater surface concentration of carbonate ions. In carbonated brine solutions some corrosion inhibition is observed above the cmc of C12BDMAC. Under these conditions we propose that the added electrolyte screens the electrostatic attraction between the bilayer and the corrosive anions, which depletes the concentration of carbonate ions at the steel surface leading to a lower corrosion rate.

Table 3.2. Summary of the effect of C12BDMAC on the corrosion rate of 1018 steel in water and brine solutions containing air, CO_2 or H_2S determined by bubble test and wheel box test at 25 °C.

System	Effect of increasing [C12BDMAC] upon corrosion rate (bubble test)	Effect of increasing [C12BDMAC] upon corrosion rate (wheel box test)
Water + Air	Corrosion rate increases	No effect
Water + CO_2	Slight decrease, then increase at high [C12BDMAC]	No effect
Water + H_2S	Decreases then remains constant	Decrease, independent of [C12BDMAC]
Brine + Air	No effect	No effect
Brine + CO_2	No effect at low [C12BDMAC], reduction at high [C12BDMAC]	No effect at low [C12BDMAC], slight decrease above the cmc
Brine + H_2S	Decreases then plateau at cmc	Decrease, independent of [C12BDMAC]

Table 3.3. Summary of the effect of IA on the corrosion rate of 1018 steel in water and brine solutions containing air, CO_2 or H_2S determined by bubble test at 25 °C.

System	Effect of increasing [IA] upon corrosion rate (bubble test)
Water + Air	Corrosion rate increases
Water + CO_2	Increased corrosion rate at low and high [IA] but slight decrease at intermediate [IA]
Water + H_2S	Corrosion rate decreases, effect diminishes above cmc
Brine + Air	No effect
Brine + CO_2	Reduction of corrosion rate at low [IA], effect diminishes with increasing [IA]
Brine + H_2S	Decrease, independent of [IA]

3.6 References

1. *Additional Information and Specification for Gill AC*, http://www.potentiostat.com/literature/spec_gillac.shtml, ACM Instruments (2007).
2. Australian Stainless Steel Development Association, *ASSDA Technical Bulletin No. 2*, 4 (2006).
3. D.A. Jones, *Principles and Prevention of Corrosion, 2nd edition*, Prentice-Hall, New Jersey (1996).
4. P.C.S. Hayfield, *Surf. Sci.*, **56**, 488 (1977).
5. S.D. Cramer, *ASM Handbook Volume 13A: Corrosion: Fundamentals, Testing and Protection, 10th edition*, ASM International, Cleveland (2003).
6. J.P. Broomfield and D.G. Manning, *Transportation in the New Millennium: State of the Art and Future Directions, Perspectives from Transportation Research Board Standing Committees*, Transportation Research Board, USA (2000).
7. S.J. Ahn, H.S. Kwon and D.D. Macdonald, *J. Electrochem. Soc.*, **152**, 482 (2005).
8. R. Ambat, N.N. Aung and W. Zhou, *J. Appl. Electrochem.*, **30**, 865 (2000).
9. F.D. Wall, C.M. Johnson, J.C. Barbour, M.A. Martinez and J.E. Mikkalson, *J. Electrochem. Soc.*, **151**, 77 (2004).
10. L.M. Gourd, *An Introduction to Engineering Materials*, Edward Arnold, London (1982).
11. F.A. Cotton and G. Wilkinson, *Advanced Inorganic Chemistry, 4th edition*, John Wiley & Sons, New York, (1980).
12. W.D. Nesse, *Introduction to Optical Mineralogy*, Oxford University Press, New York (1986).
13. R.A. Higgins, *Engineering Metallurgy, 4th edition*, Hodder & Stoughton, London (1973).
14. D.R. Lide (Ed.), *Handbook of Chemistry and Physics, 79th edition*, CRC Press, Boca Raton (1998).
15. J.L. Mora-Mendoza and S. Turgoose, *Corros. Sci.*, **44**, 1223 (1999).
16. M. Ueda and H. Takabe, *Proceedings of NACE Corrosion/99*, Paper No. 13, NACE International, Houston (1999).
17. T. Hemmingsen and H. Lima, *Electrochim. Acta*, **43**, 35 (1998).
18. A.J. Szyprowski, *Br. Corros. J.*, **35**, 155 (2000).

19. D. Abayarathna, A. Naraghi and N. Obeyesekere, *Proceedings of NACE Corrosion/2003*, Paper No. 03340, NACE International, Houston (2003).

20. A.K. Agrawal, C. Durr and G.H. Koch, *Proceedings of NACE Corrosion/2004*, Paper No. 04736, NACE International, Houston (2004).

21. J. Kvarekval, *Proceedings of EUROCORR '97*, p.27, European Federation of Corrosion, Trondheim (1997).

22. B. Brown, S.R. Reddy and S. Nesic, *Proceedings of NACE Corrosion/2004*, Paper No. 04736, NACE International, Houston (2004).

23. D.J. Shaw, *Introduction to Colloid and Surface Chemistry, 4th edition*, Butterworth-Heinemann, Oxford (1991).

24. J.R. Rodríguez and J. Czapkiewicz, *Colloids Surf., A*, **101**, 107 (1995).

25. *Material Safety Data Sheet for Product PR-9026, version 1.6*, Nalco Ltd., Fawley (2005).

CHAPTER 4

Ellipsometry to monitor corrosion and its inhibition

4.1 Introduction

Chapter 3 showed that the corrosion rate of 1018 steel immersed in aqueous environments was affected by the nature of the dissolved gas present and that under certain gas conditions the corrosion rate can be reduced by the addition of dodecylbenzyldimethylammonium chloride (C12BDMAC). The presence of air, CO_2 and H_2S lead to the formation of iron hydroxide or iron oxide, iron carbonate and iron sulphide corrosion products at the surface of the steel, respectively. This suggests that the effectiveness of surfactants as corrosion inhibitors depends on the nature of the corrosion products present on the steel surface. Electrochemical measurements such as the bubble test measure the electrical current flowing throughout the entire steel electrode; therefore we decided to use ellipsometry to study the adsorption of C12BDMAC at the steel-liquid interface in more detail.

This chapter will show how ellipsometry is used to determine the thickness of surfactant films adsorbed on solid surfaces and how the technique has been employed to study the steel-water interface when steel corrodes in aqueous environments containing air, CO_2 and H_2S gases in the presence and absence of corrosion inhibitors.

4.2 Determining the thickness of adsorbed corrosion inhibitor films

In tackling the problem as to why the inhibitor choice may be different for aerated, CO_2 and H_2S conditions, we set out to use ellipsometry, initially with a view to measuring possible differences in the adsorption isotherms for C12BDMAC on 1018 steel under the different gas conditions. We began by studying the adsorption of C12BDMAC on to 1018 steel from aqueous solution under normal atmospheric conditions in the absence of electrolyte at 25 °C.

The ellipsometric parameters Δ and Ψ were measured for 1018 steel in Milli-Q water under normal atmospheric conditions (Figure 4.1). During this measurement the values of Δ and Ψ do not change with time, suggesting that no changes are occurring at the water-steel interface. The mean values of the final ten Δ and Ψ values were used to calculate the complex refractive index of 1018 steel using the iterative method of McCrackin[1], based on an initial estimate. We began modelling the steel surface as a

Figure 4.1. Δ (black) and Ψ (red) vs time for 1018 steel disc in Milli-Q water at 25°C.

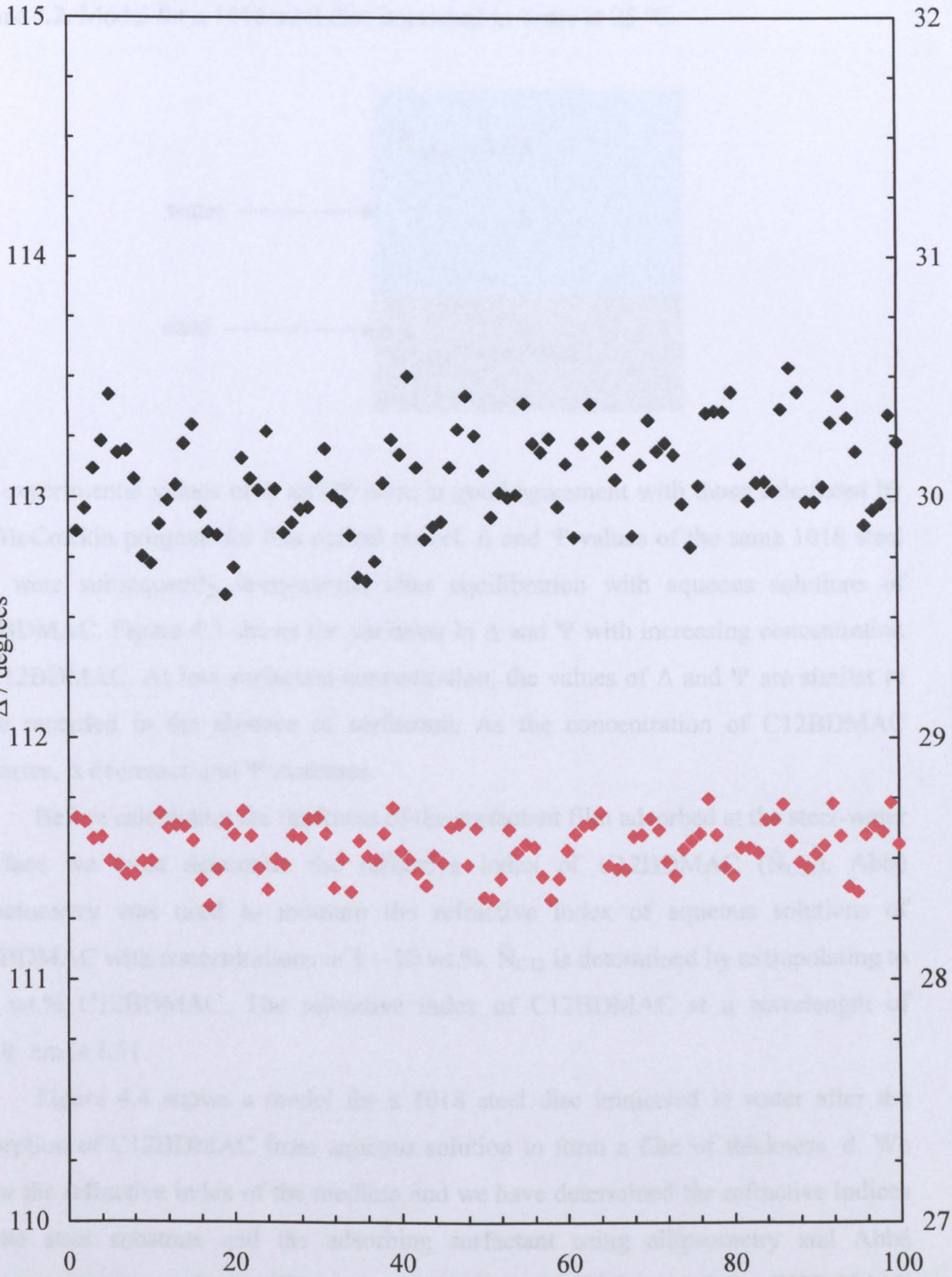

single layer immersed under water with a refractive index of 1.33 (Figure 4.2). The complex refractive index of the steel ($\tilde{N}_{steel}$) was floated whilst keeping the refractive index of the medium ($\tilde{N}_{water}$) fixed, which gave $\tilde{N}_{steel}$ as 2.9 – 3.8i.

Figure 4.2. Model for a 1018 steel disc immersed in water at 25 °C.

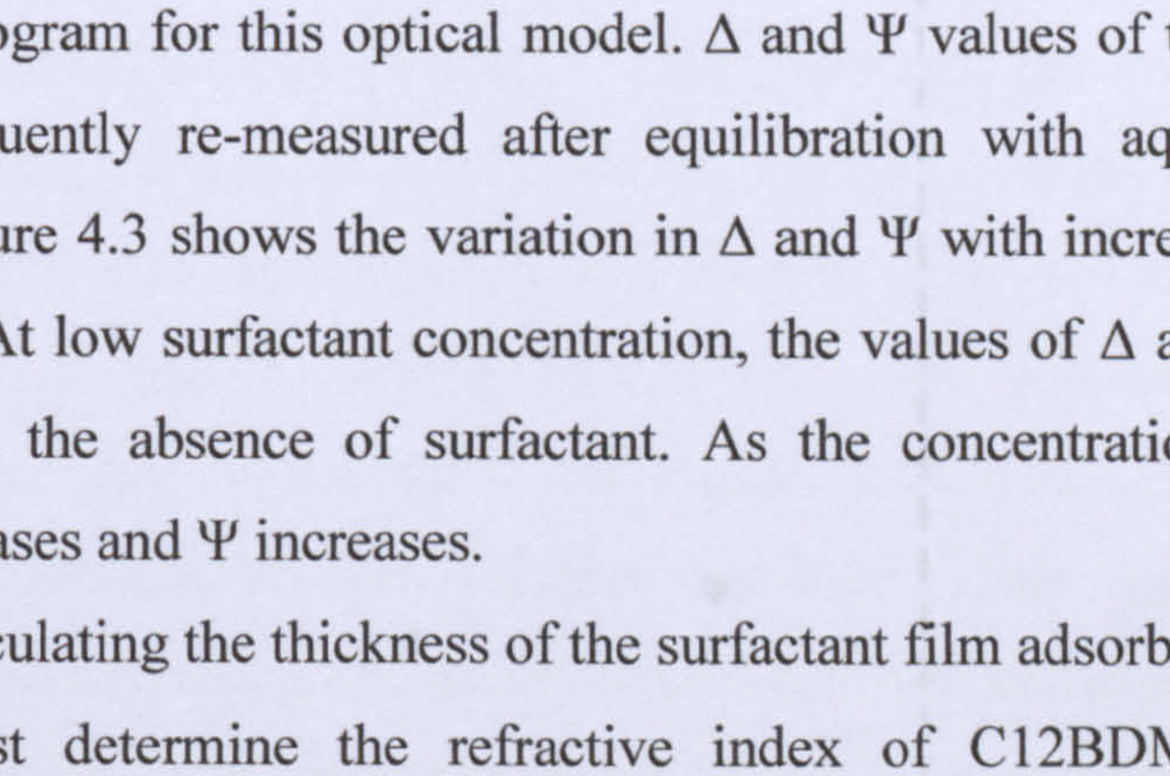

The experimental values of Δ and Ψ were in good agreement with those calculated by the McCrackin program for this optical model. Δ and Ψ values of the same 1018 steel disc were subsequently re-measured after equilibration with aqueous solutions of C12BDMAC. Figure 4.3 shows the variation in Δ and Ψ with increasing concentration of C12BDMAC. At low surfactant concentration, the values of Δ and Ψ are similar to those recorded in the absence of surfactant. As the concentration of C12BDMAC increases, Δ decreases and Ψ increases.

Before calculating the thickness of the surfactant film adsorbed at the steel-water interface we must determine the refractive index of C12BDMAC ($\tilde{N}_{C12}$). Abbé refractometry was used to measure the refractive index of aqueous solutions of C12BDMAC with concentrations of 1 – 10 wt.%. $\tilde{N}_{C12}$ is determined by extrapolating to 100 wt.% C12BDMAC. The refractive index of C12BDMAC at a wavelength of 632.8 nm is 1.51.

Figure 4.4 shows a model for a 1018 steel disc immersed in water after the adsorption of C12BDMAC from aqueous solution to form a film of thickness, d. We know the refractive index of the medium and we have determined the refractive indices of the steel substrate and the adsorbing surfactant using ellipsometry and Abbé refractometry, respectively. We can now calculate the thickness of the C12BDMAC film using the experimental Δ and Ψ values for 1018 steel after the adsorption of C12BDMAC by fixing the refractive indices $\tilde{N}_{water}$, $\tilde{N}_{steel}$ and $\tilde{N}_{C12}$ and floating the thickness based upon an initial guess. Figure 4.5 shows the results expressed as

Figure 4.3. Δ (black) and Ψ (red) vs [C12BDMAC] for 1018 steel disc in aqueous C12BDMAC at 25 °C. Vertical line indicates the cmc of C12BDMAC in Milli-Q water. Horizontal lines shows the mean values of Δ and Ψ in the absence of C12BDMAC.

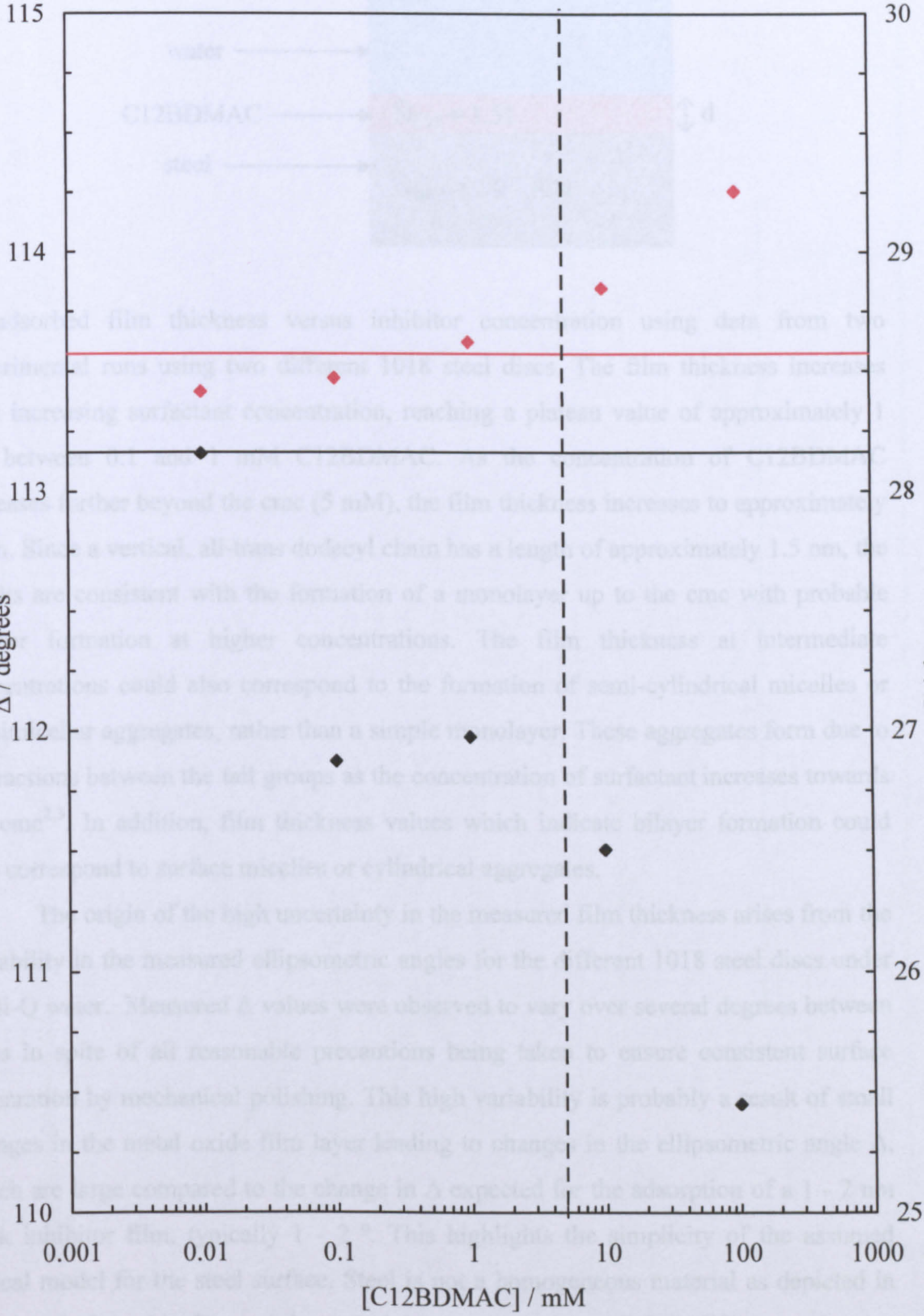

Figure 4.4. Model for a 1018 steel disc immersed in water at 25 °C after the adsorption of C12BDMAC to form a film of thickness, d.

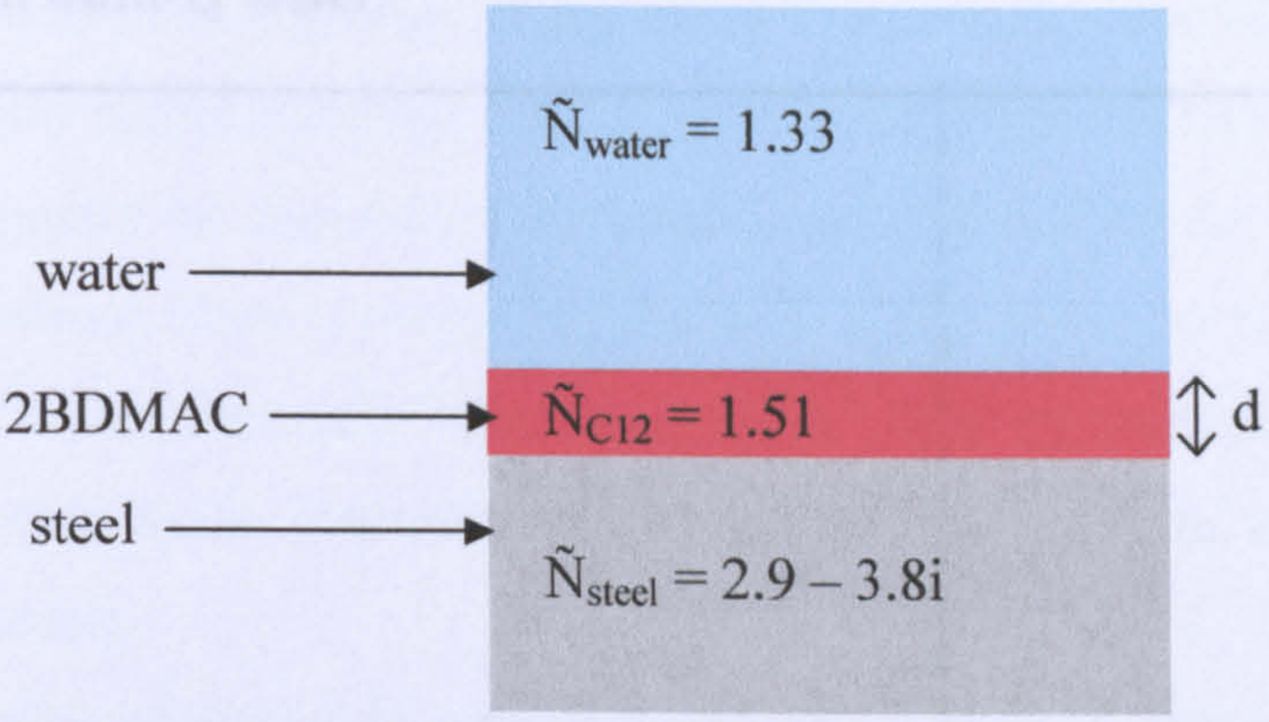

an adsorbed film thickness versus inhibitor concentration using data from two experimental runs using two different 1018 steel discs. The film thickness increases with increasing surfactant concentration, reaching a plateau value of approximately 1 nm between 0.1 and 1 mM C12BDMAC. As the concentration of C12BDMAC increases further beyond the cmc (5 mM), the film thickness increases to approximately 3 nm. Since a vertical, all-trans dodecyl chain has a length of approximately 1.5 nm, the results are consistent with the formation of a monolayer up to the cmc with probable bilayer formation at higher concentrations. The film thickness at intermediate concentrations could also correspond to the formation of semi-cylindrical micelles or hemimicellar aggregates, rather than a simple monolayer. These aggregates form due to interactions between the tail groups as the concentration of surfactant increases towards the cmc[2,3]. In addition, film thickness values which indicate bilayer formation could also correspond to surface micelles or cylindrical aggregates.

The origin of the high uncertainty in the measured film thickness arises from the variability in the measured ellipsometric angles for the different 1018 steel discs under Milli-Q water. Measured Δ values were observed to vary over several degrees between discs in spite of all reasonable precautions being taken to ensure consistent surface preparation by mechanical polishing. This high variability is probably a result of small changes in the metal oxide film layer leading to changes in the ellipsometric angle Δ, which are large compared to the change in Δ expected for the adsorption of a 1 - 2 nm thick inhibitor film, typically 1 - 2 °. This highlights the simplicity of the assumed optical model for the steel surface. Steel is not a homogeneous material as depicted in our model; the oxide film and the underlying steel may have slightly different refractive indices. Therefore our optical model does not accurately represent the true structure and

Figure 4.5. Film thickness vs C12BDMAC for a 1018 steel disc immersed in aqueous C12BDMAC at 25°C. The vertical dashed line indicates the cmc of C12BDMAC in Milli-Q water.

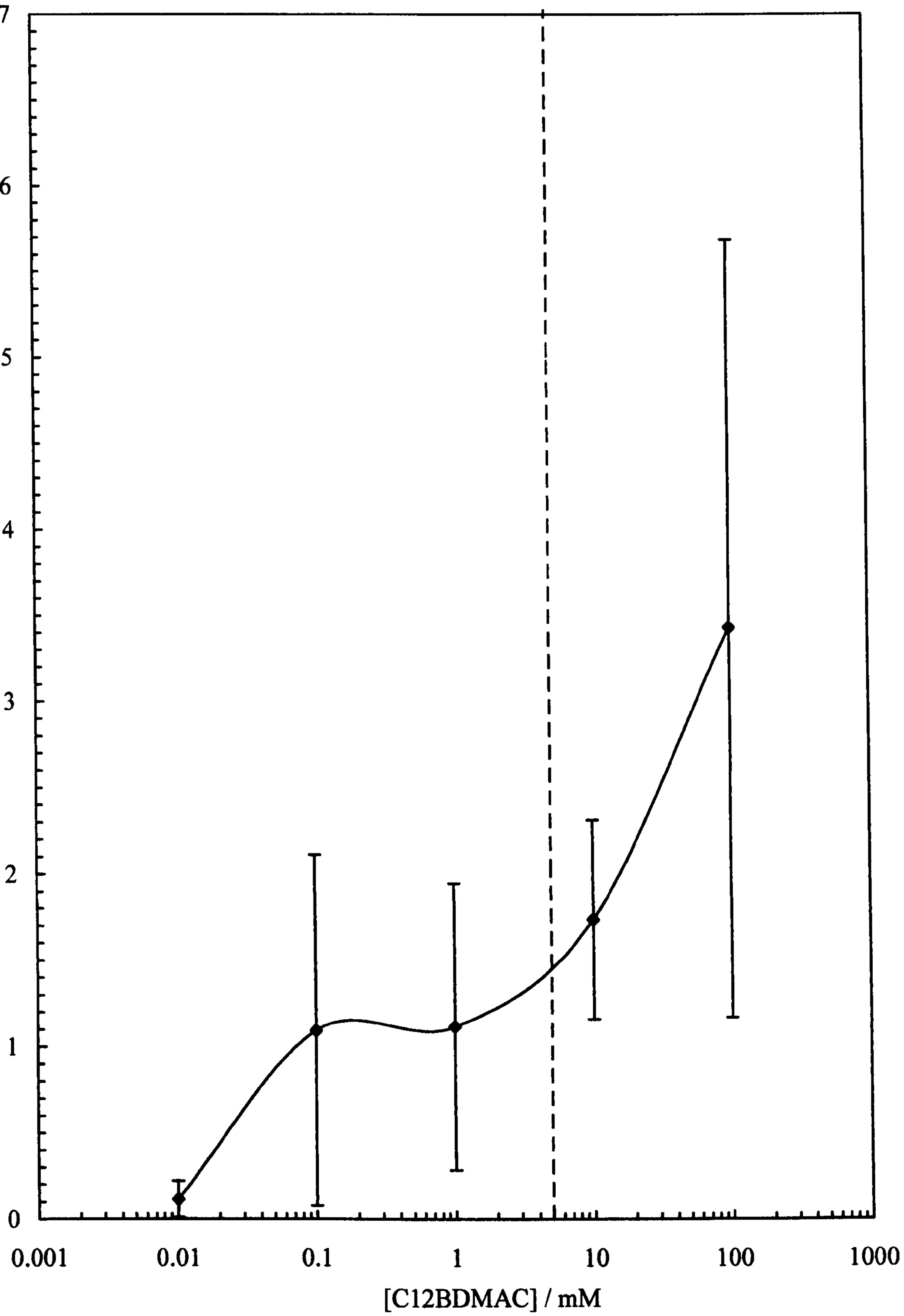

optical properties of 1018 steel, despite achieving good agreement between the calculated and experimental Δ and Ψ values and yielding reasonable adsorbed film thicknesses. The real and imaginary parts of the refractive indices of the oxide film and the underlying steel and the thickness of the oxide film are all unknown, which gives a total of five unknown variables to fit with the McCrackin program. The refractive index of the bulk steel cannot be determined by experiment because of the presence of the oxide film. Most surface films are inhomogeneous in composition, even with the purest of metal samples[4]. The fact that 1018 steel is an alloy of iron suggests that the composition of surface oxide films and other corrosion product films may vary greatly throughout each sample.

The adsorption experiments were repeated using Milli-Q water which had been sparged with CO_2 gas. Under these conditions the Δ and Ψ values for the 1018 steel disc did not remain constant with time, indicating that changes were occurring to the steel surface (Figure 4.6). The higher corrosion rate of 1018 steel in the presence of dissolved CO_2 gas causes rapid dissolution of the steel surface. The corrosion process alters the optical properties of the steel surface, which causes the changes in Δ and Ψ. Δ decreases rapidly once the disc is immersed in the carbonated brine. After 10 min. Δ has decreased by almost 20 °. This change in Δ is very large when compared to the changes seen during the adsorption of C12BDMAC onto steel in Milli-Q water under aerated conditions (Figure 4.3). Despite not achieving steady baseline values of Δ and Ψ we decided to add a small volume of a stock solution of C12BDMAC to see if Δ and Ψ values for the steel disc underwent further changes in the presence of surfactant (Figure 4.6). After the addition of C12BDMAC Δ continues to decrease with time and Ψ increases slightly before continuing to decrease. It appears that any features associated with the adsorption of surfactant are hidden by the greater changes in the optical properties of the steel surface caused by corrosion. The continued corrosion of the surface complicates the modelling procedure and the subsequent calculation of adsorbed surfactant film thickness. This is because the corrosion process and surfactant adsorption are taking place simultaneously, therefore we do not know the exact values of Δ and Ψ after equilibrium adsorption of C12BDMAC.

Similar results were also found with Milli-Q water under H_2S conditions and with 4.7 wt.% brine solutions under aerated, CO_2 and H_2S conditions. Although we were unable to measure the thickness of the corrosion inhibitor films formed under these more corrosive conditions these results indicated that ellipsometry might be a valuable technique for studying steel surfaces during the initial stages of corrosion

Figure 4.6. Δ (black) and Ψ (red) vs time for 1018 steel in Milli-Q water under CO_2 conditions at 25°C, followed by addition of C12BDMAC after 30 min. (vertical line) to give a concentration of 0.1 mM.

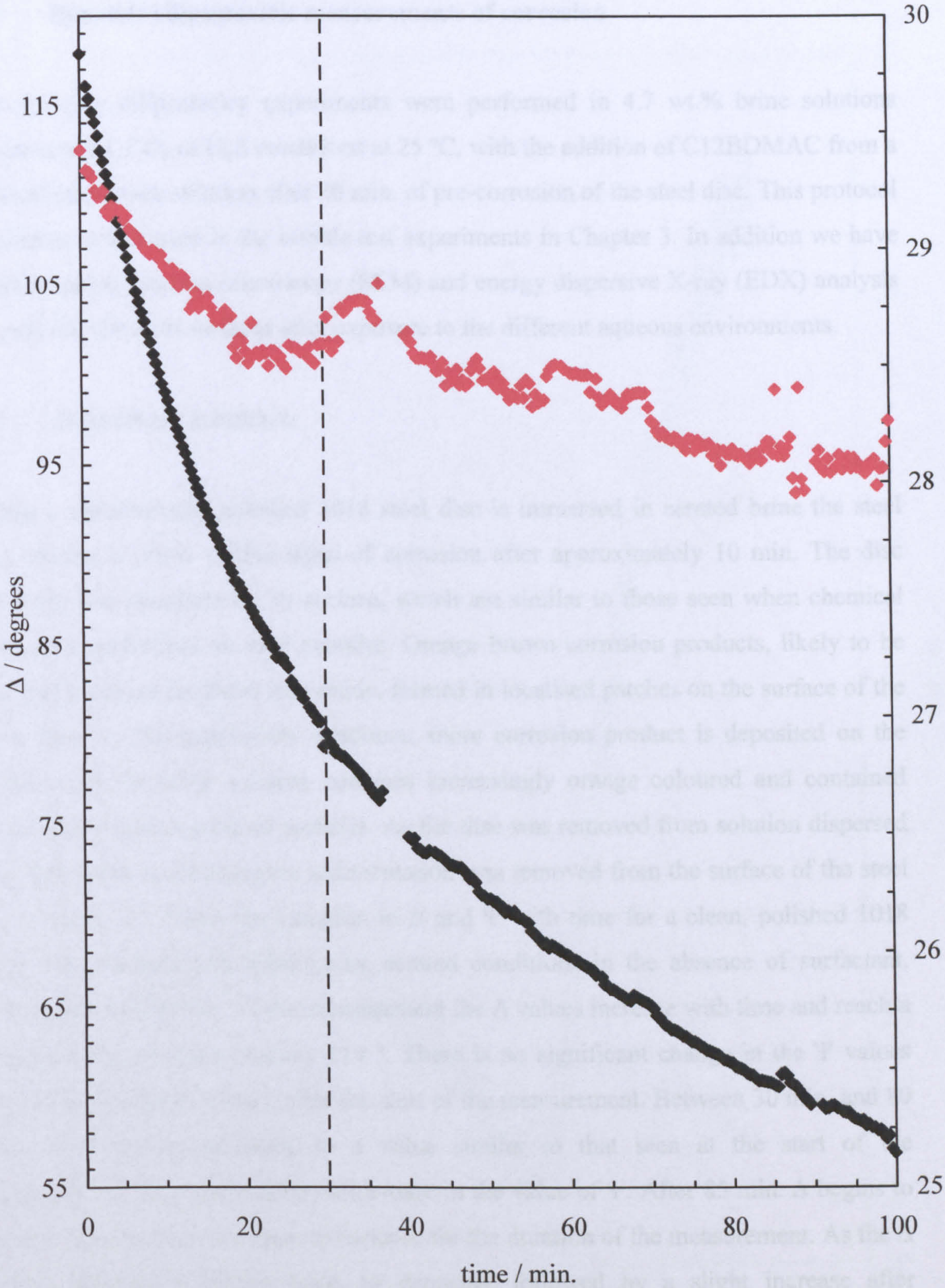

under different gas conditions and could reveal information about the thickness and composition of the corrosion products formed in addition to the thickness of the corrosion inhibitor film.

4.3 Dynamic ellipsometric measurements of corrosion

All dynamic ellipsometry experiments were performed in 4.7 wt.% brine solutions under aerated, CO_2 or H_2S conditions at 25 °C, with the addition of C12BDMAC from a concentrated stock solution after 30 min. of pre-corrosion of the steel disc. This protocol is similar to that used in the bubble test experiments in Chapter 3. In addition we have used scanning electron microscopy (SEM) and energy dispersive X-ray (EDX) analysis to examine the steel surfaces after exposure to the different aqueous environments.

4.3.1 Atmospheric conditions

When a mechanically polished 1018 steel disc is immersed in aerated brine the steel disc begins to show visible signs of corrosion after approximately 10 min. The disc develops fine scratches on its surface, which are similar to those seen when chemical etching is performed on steel samples. Orange brown corrosion products, likely to be iron hydroxide or hydrated iron oxide, formed in localised patches on the surface of the steel disc. As the experiment continues, more corrosion product is deposited on the surface and the brine solution becomes increasingly orange coloured and contained dispersed corrosion product particles. As the disc was removed from solution dispersed material which had undergone sedimentation was removed from the surface of the steel disc. Figure 4.7 shows the variation in Δ and Ψ with time for a clean, polished 1018 steel disc immersed in brine under aerated conditions in the absence of surfactant. During the first 30 min. of the measurement the Δ values increase with time and reach a plateau value of approximately 114 °. There is no significant change in the Ψ values until approximately 20 min. after the start of the measurement. Between 30 min. and 80 min. Δ decreases, returning to a value similar to that seen at the start of the measurement, accompanied by an increase in the value of Ψ. After 85 min. Δ begins to rapidly increase and continues to increase for the duration of the measurement. As the Δ values increase Ψ values begin to decrease, followed by a slight increase after approximately 100 min. These results were fairly reproducible with other samples of 1018 steel, although there were often differences in the absolute values of Δ and Ψ

Figure 4.7. Δ (black) and Ψ (red) vs time for a 1018 steel disc in brine under aerated conditions at 25°C.

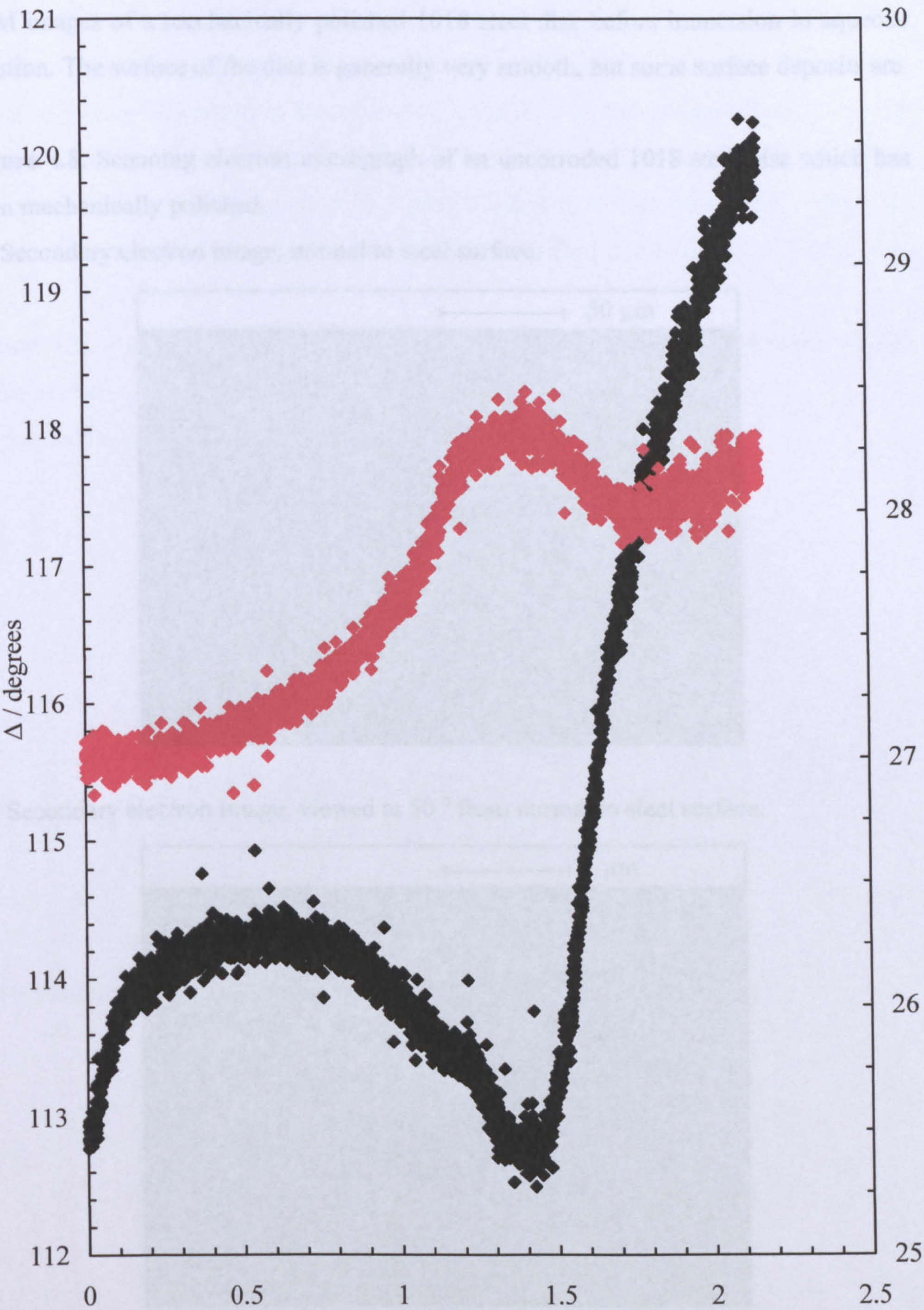

probably arising from differences in the thickness of the native oxide layer. The profile of Δ versus time suggests that at least three consecutive processes are occurring at the surface, resulting in changes in the optical properties of the steel.

In order to identify these processes SEM was used to view steel discs which had been corroded under aerated conditions for increasing periods of time. Figure 4.8 shows SEM images of a mechanically polished 1018 steel disc before immersion in aqueous solution. The surface of the disc is generally very smooth, but some surface deposits are

Figure 4.8. Scanning electron micrograph of an uncorroded 1018 steel disc which has been mechanically polished.

(a) Secondary electron image, normal to steel surface.

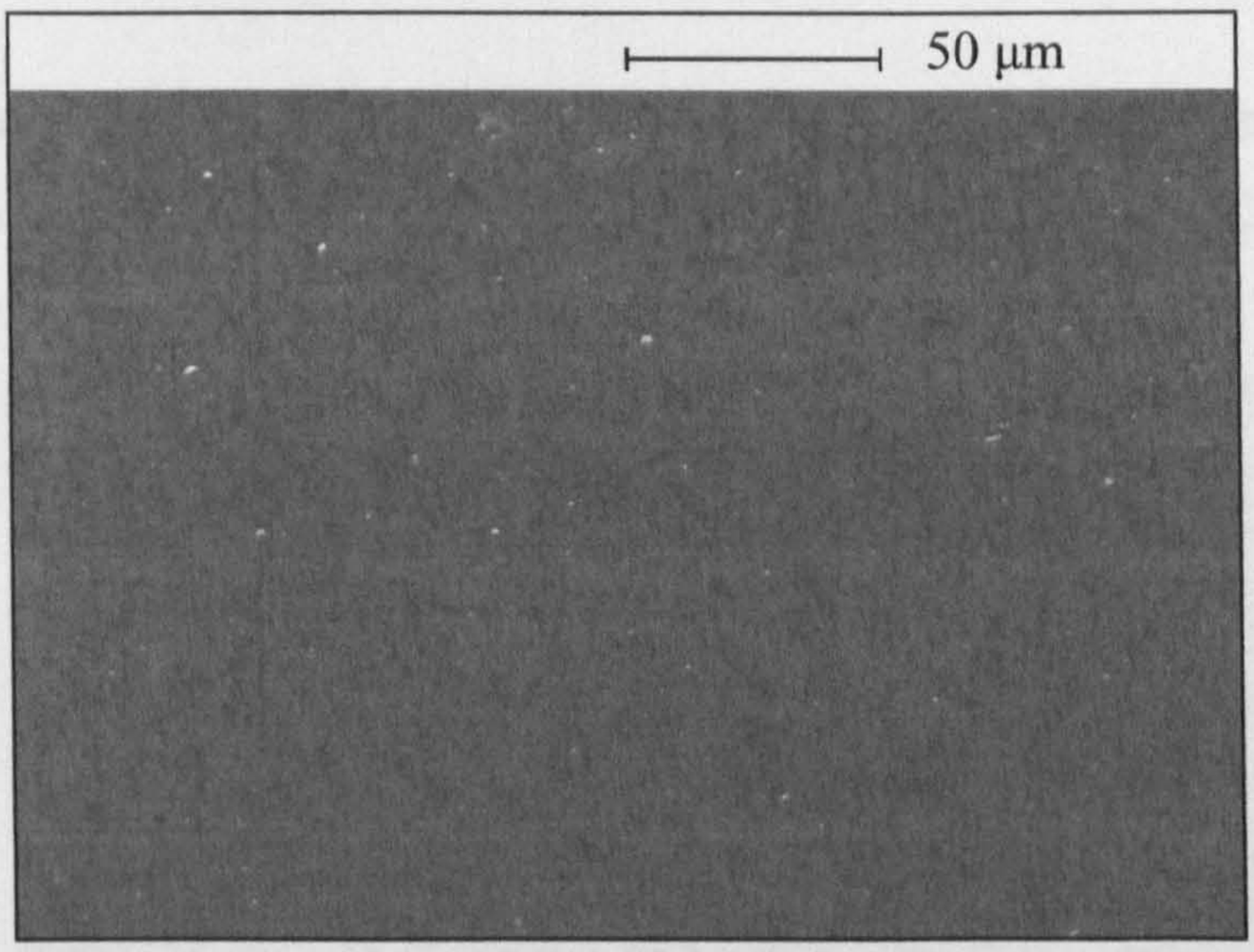

(b) Secondary electron image, viewed at 50 ° from normal to steel surface.

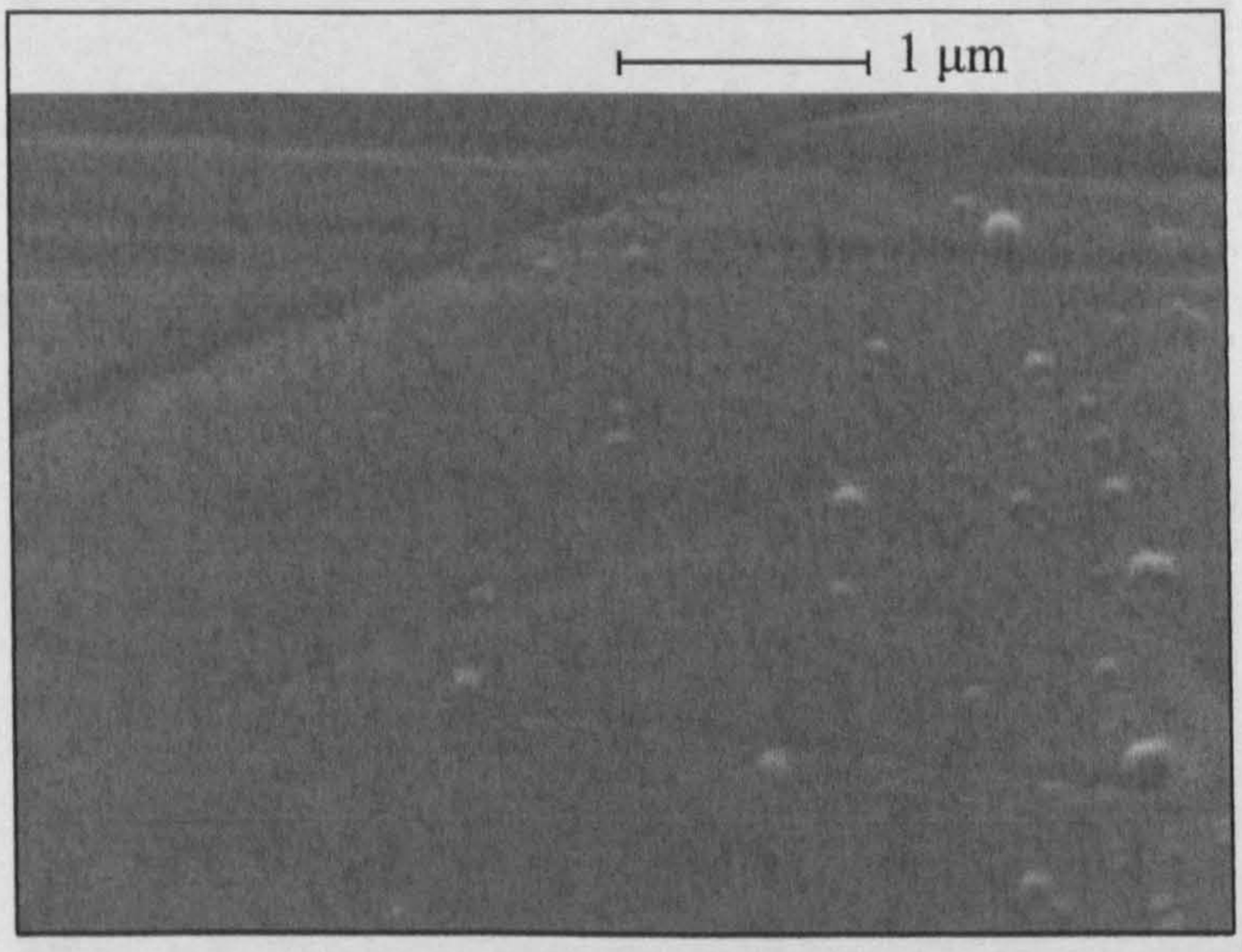

visible. These are likely to be small crystals of iron oxide which formed during or after mechanical polishing. At higher magnification some very fine scratches are visible on the surface of the disc (Figure 4.8b). These scratches are likely to be caused by the final polishing step, which uses 0.25 μm colloidal silica as an abrasive.

Figure 4.9 shows a steel disc which has been corroded for 10 min. in aerated brine. Within this short period of exposure the topography of the steel surface has already changed significantly when compared to the uncorroded disc. The surface shows a criss-cross pattern of fine scratches across the surface (Figure 4.9a). The grain boundaries between the ferrite and pearlite phases of the steel are also becoming visible, indicating that some dissolution of the surface oxide layer has taken place. There are also numerous deposits of corrosion product on the surface of the steel.

Figure 4.9. Scanning electron micrograph of a 1018 steel disc after immersion in brine under aerated conditions for 10 min. in the absence of surfactant at 25 °C.

(a) Secondary electron image, normal to steel surface.

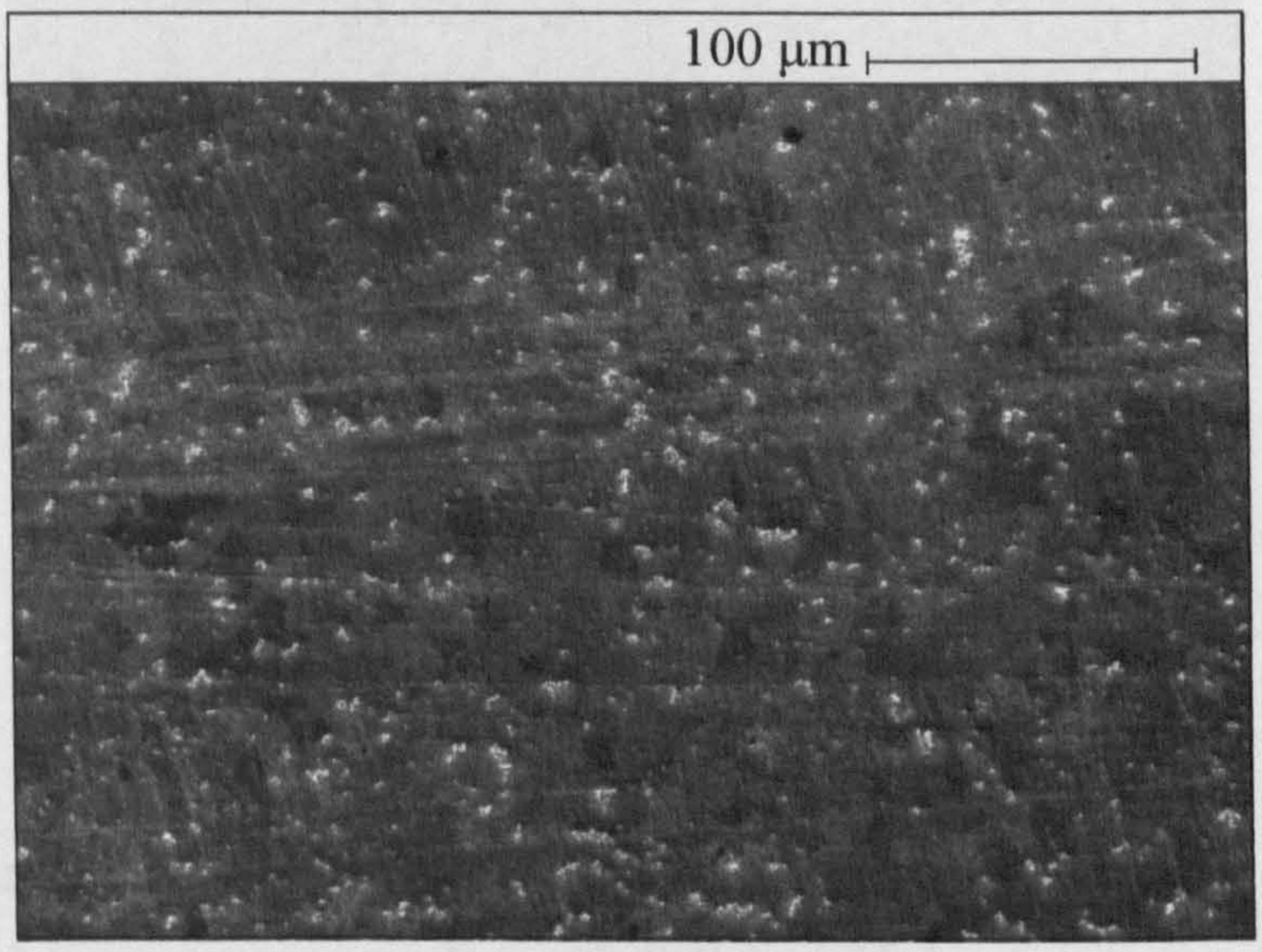

(b) Secondary electron image, normal to steel surface.

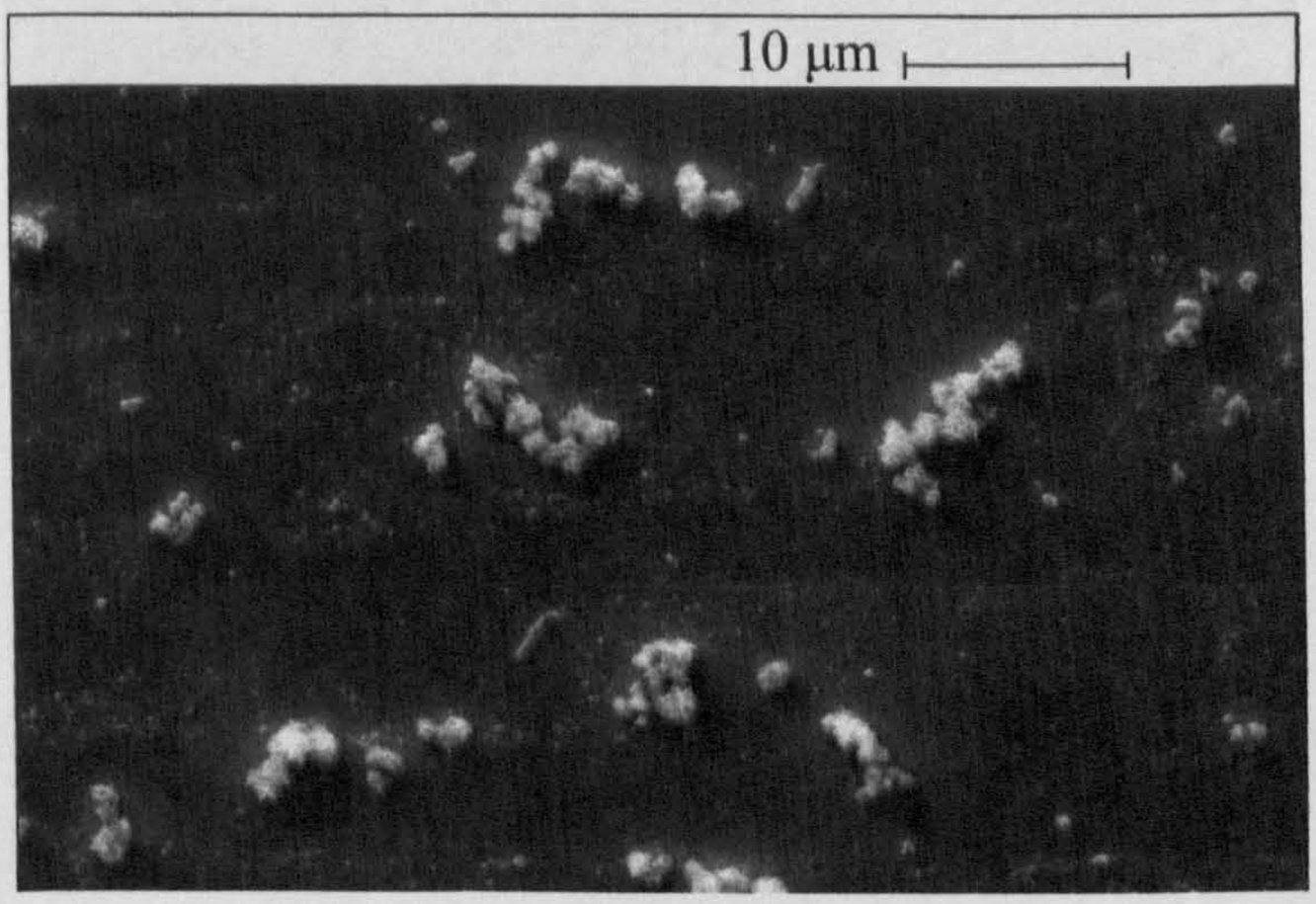

These deposits of corrosion product (Figure 4.9b) are approximately 1 – 2 μm in size and appear to be strongly attached to the surface despite washing the disc with Milli-Q water and drying with compressed air after removal from the brine solution.

Figure 4.10 shows a disc which has been immersed in aerated brine for 30 min. We can see that further metal dissolution has taken place revealing the ferritic-pearlitic microstructure of the steel (Figure 4.10a). The slight difference in the grey-levels of the different domains on the back-scattered electron image (Figure 4.10b) shows that there is only a slight variation in the average atomic number between the different grains of the microstructure.

Figure 4.10. Scanning electron micrograph of a 1018 steel disc after immersion in brine under aerated conditions for 30 min. at 25 ºC.

(a) Secondary electron image, normal to steel surface.

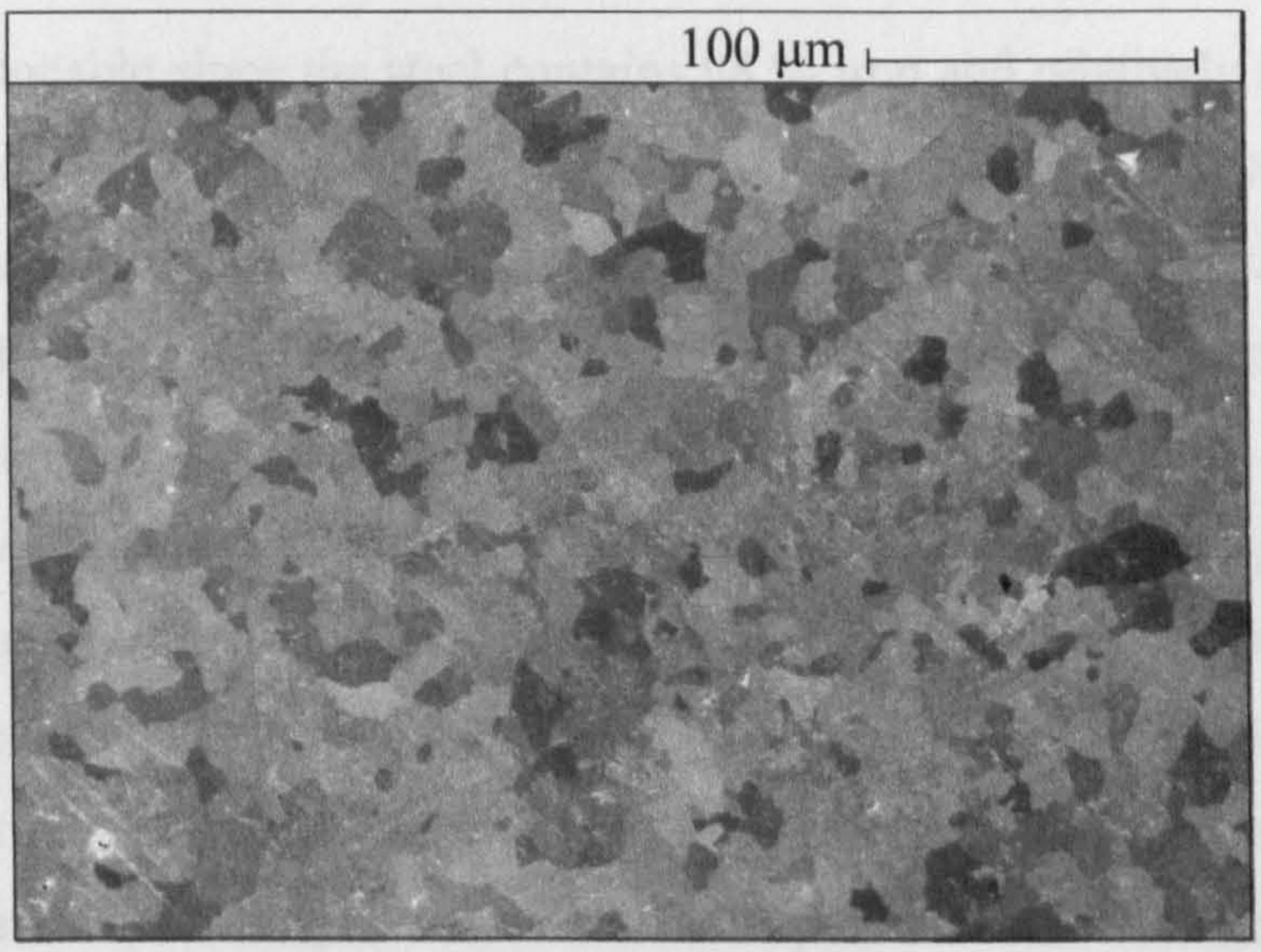

(b) Back-scattered electron image of same area shown in Figure 4.10a, normal to steel surface (dark = lower average atomic number, light = higher average atomic number).

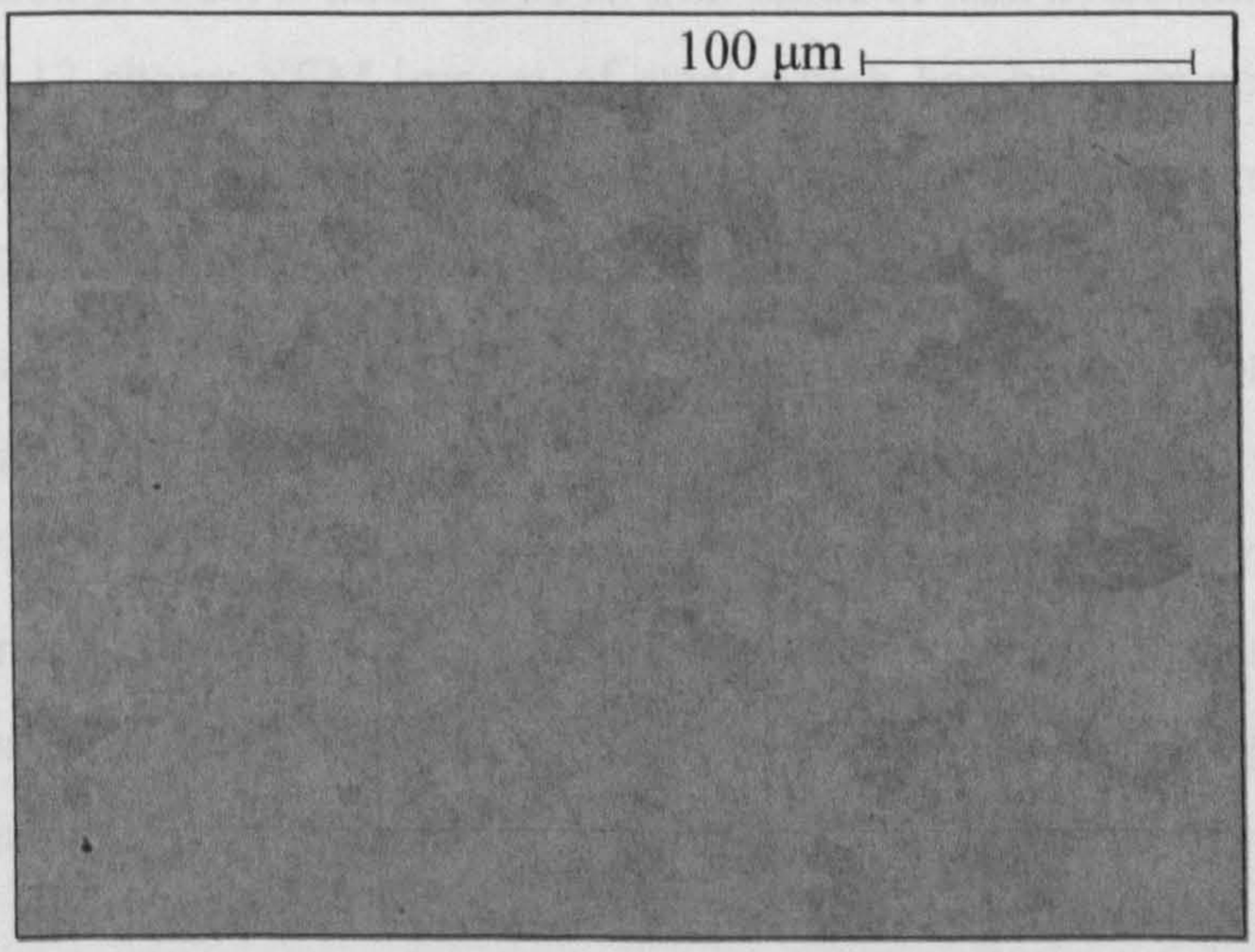

(c) Secondary electron image, normal to steel surface.

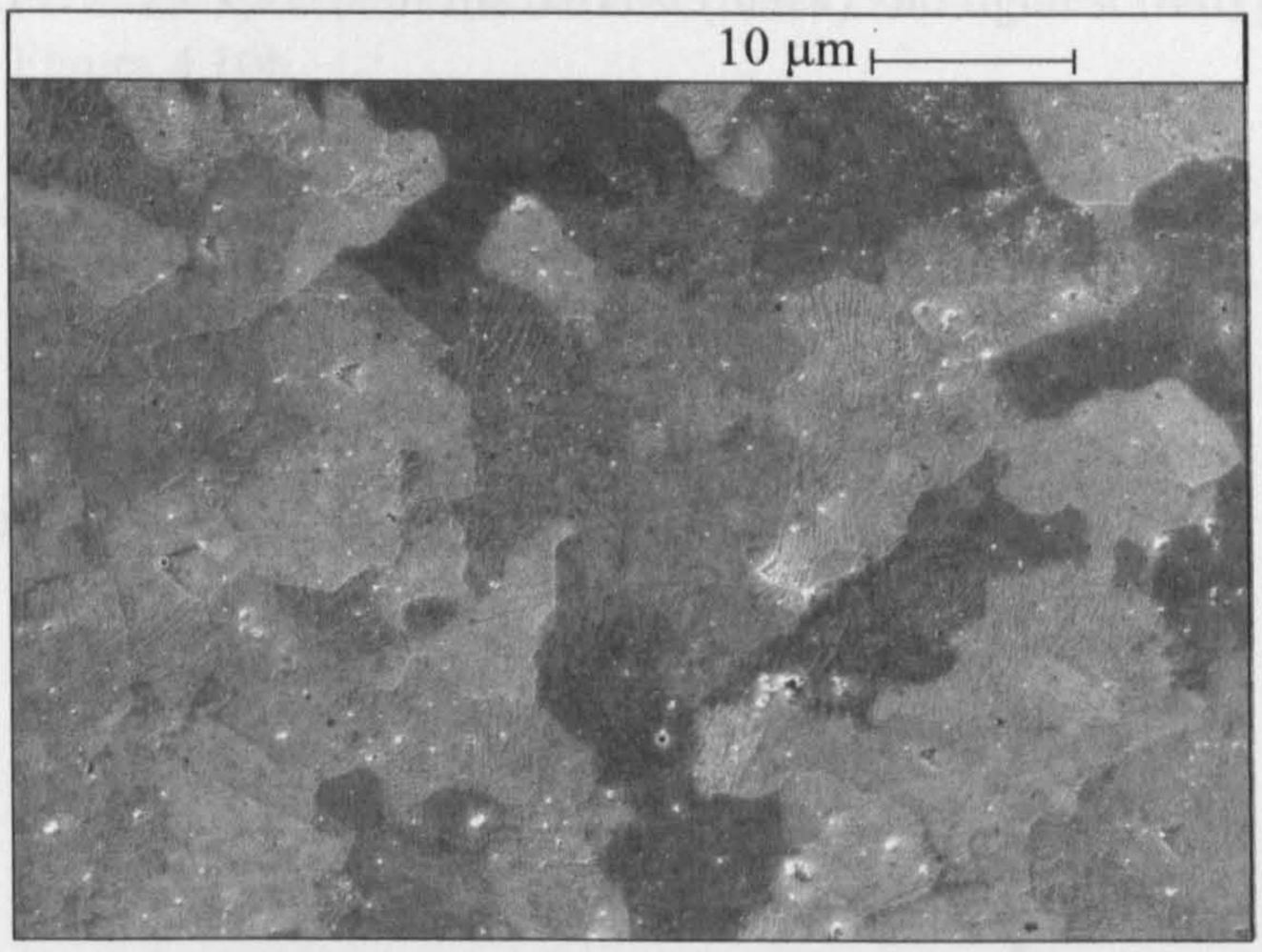

This seems reasonable since the steel contains 98 % iron and relatively low amounts of other elements (C, Mn and Si)[5]. Figure 4.11 compares the EDX analysis spectra for the darkest and lightest grains visible in Figure 4.10a. The spectra are identical showing that the two grains have almost identical elemental composition. Both spectra show intense peaks for Fe ($L_{\alpha 1}$ and $L_{\beta 1}$ at 0.7 keV and $K_{\alpha 1}$ and $K_{\beta 1}$ at 6.40 and 7.06 keV, respectively[6]). At higher magnification we can see more detail of the topography of the irregularly shaped ferrite and pearlite domains (Figure 4.10c). The darker areas appear smooth and are possibly areas of the passive oxide film which have not yet undergone dissolution. Partial dissolution of the oxide film is visible in some grains, revealing the lamellar structure of pearlite grains underneath the passive film. The lighter domains are grains of ferrite which have been revealed after removal of the passive oxide layer. Small clusters of corrosion product are deposited randomly across the surface of the disc. The corrosion product is likely to be an iron oxide or iron hydroxide compound.

Figure 4.12 shows SEM images of steel which has been immersed in aerated brine for 90 min. Figure 4.12a shows a greater coverage of corrosion product deposited across the surface of the steel. Figure 4.12b shows more definition of the ferritic-pearlitic microstructure of the steel due to a greater extent of dissolution of the surface metal. The corrosion product deposits are larger in size compared to those shown in Figure 4.10c. Figure 4.12c is a high magnification image of the corrosion product. The deposits of corrosion product range from approximately 1 – 5 μm in diameter. Some of the larger deposits are composed of two or more small crystallites. Figure 4.13 shows the EDX analysis spectrum of the largest corrosion product deposit

Figure 4.11. EDX spectra of the darkest (black) and lightest (red) grains visible in Figure 4.10b.

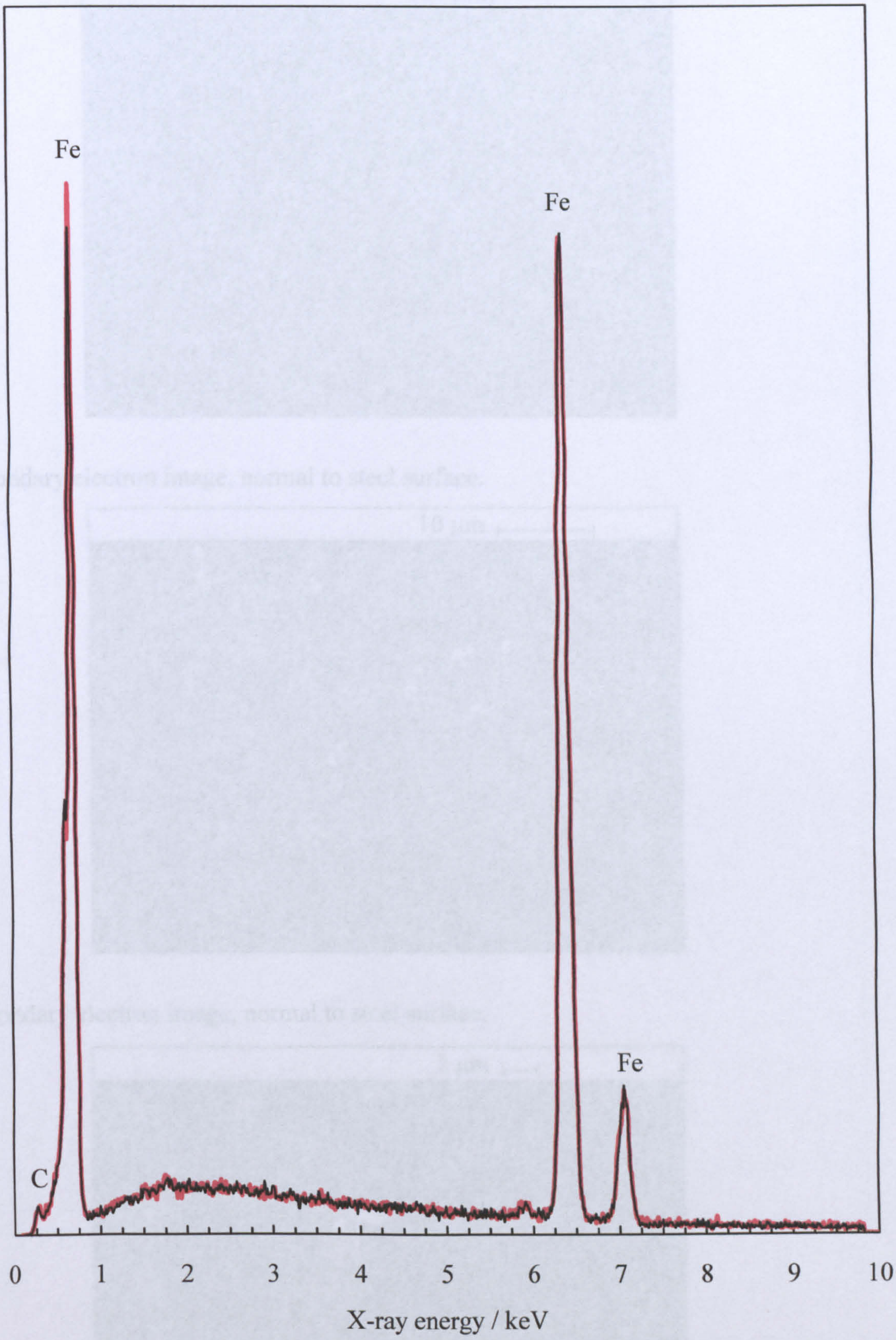

Figure 4.12. Scanning electron micrograph of a 1018 steel disc after immersion in brine under aerated conditions for 90 min. in the absence of surfactant, at 25 °C.

(a) Secondary electron image, normal to steel surface.

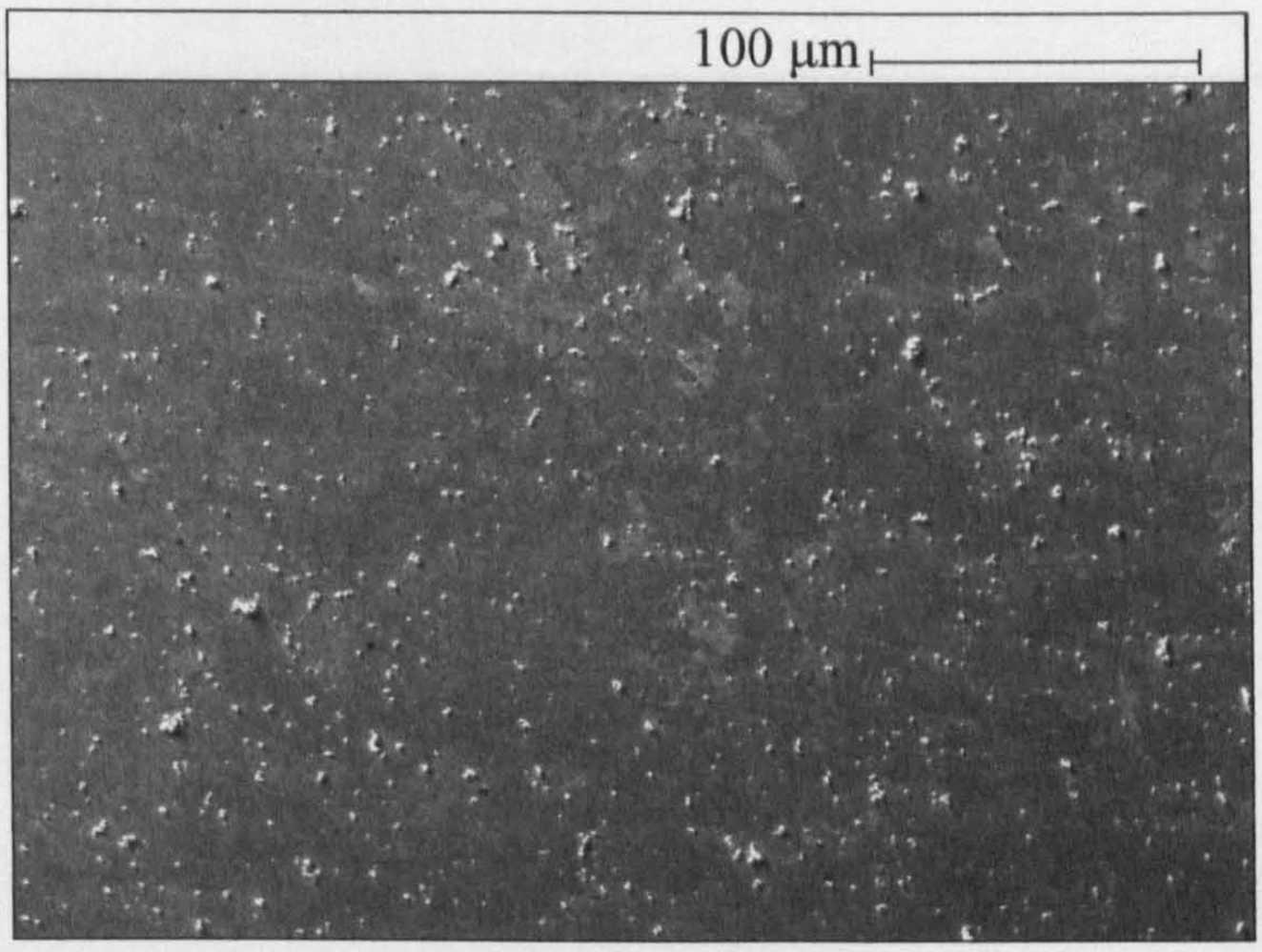

(b) Secondary electron image, normal to steel surface.

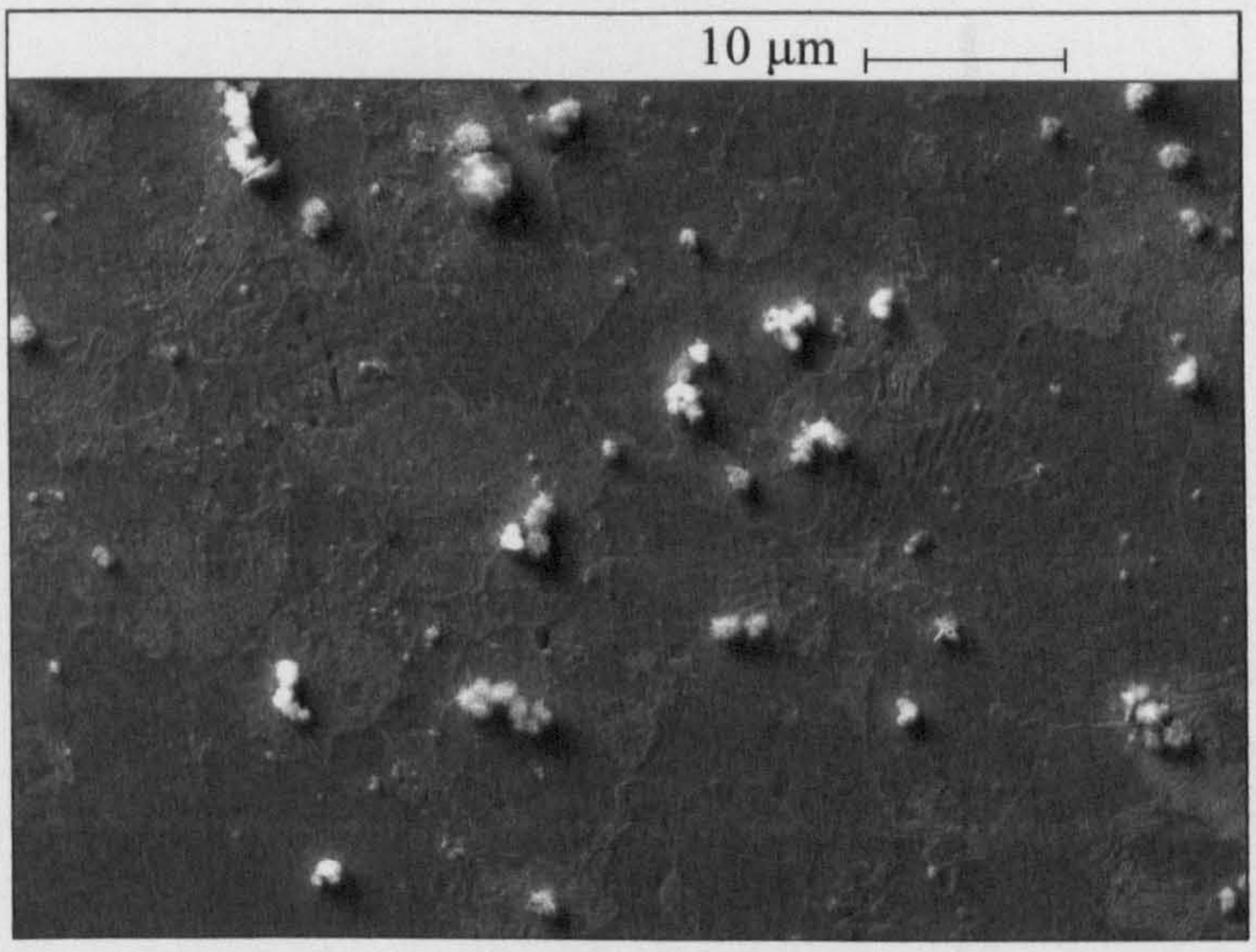

(c) Secondary electron image, normal to steel surface.

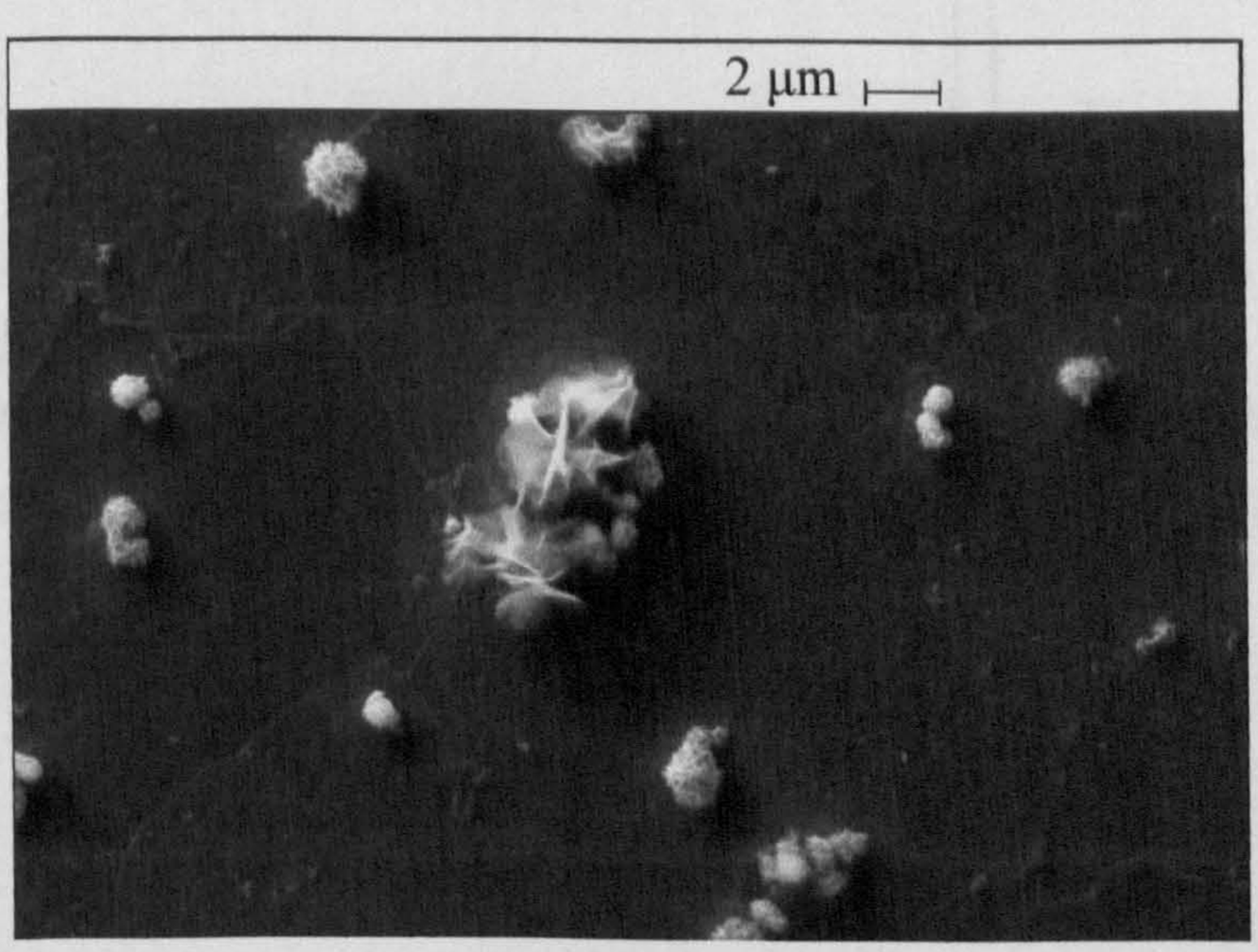

Figure 4.13. EDX analysis spectrum of the corrosion product visible in Figure 4.12c.

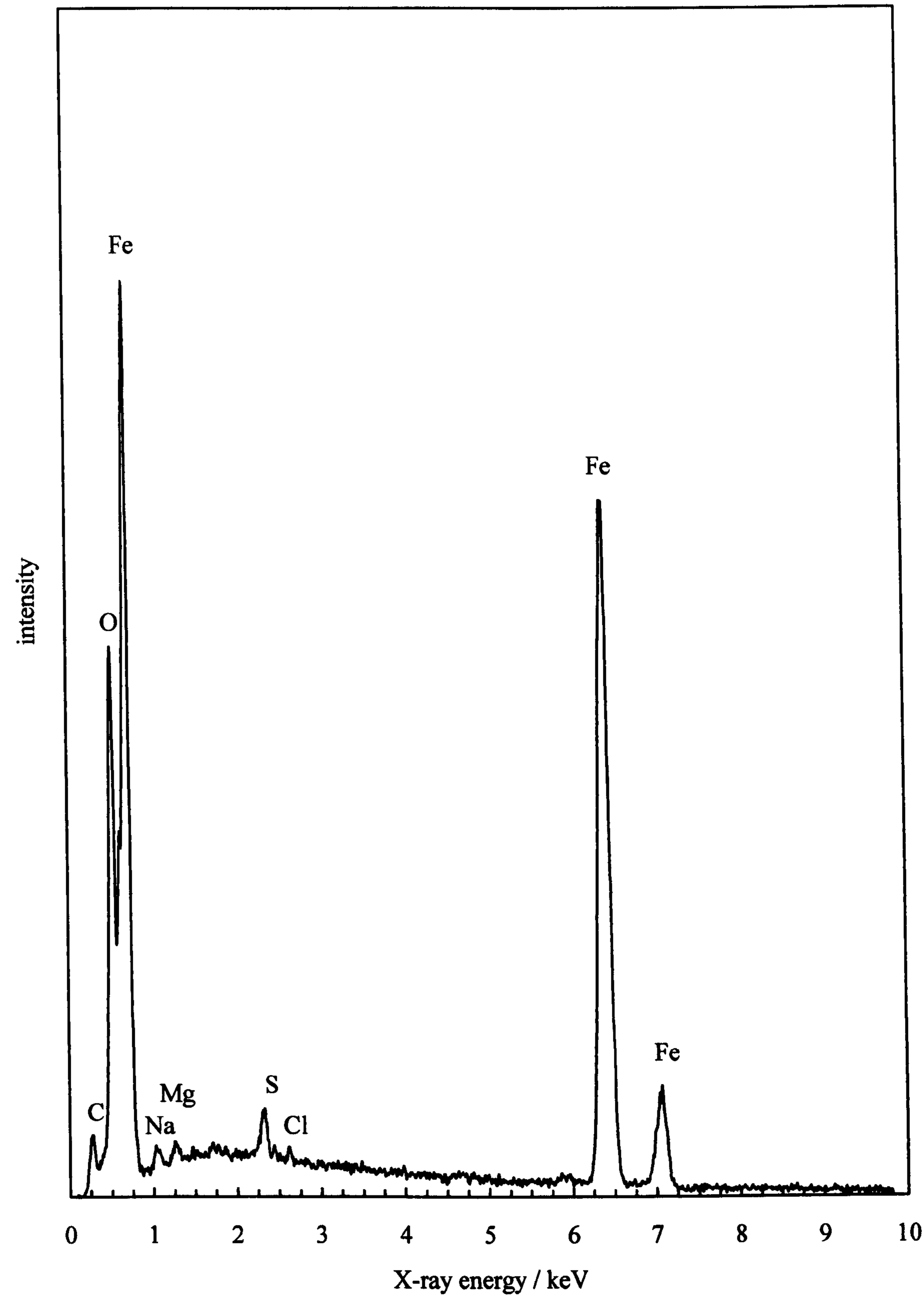

visible in Figure 4.12c which shows the presence of iron and oxygen ($K_{\alpha 1}$ at 0.52 keV) suggesting the presence of iron oxide or iron hydroxide compounds. The spectrum also shows the presence of sodium ($K_{\beta 1}$ at 1.07 keV), magnesium ($K_{\alpha 1}$ and $K_{\alpha 2}$ at 1.25 keV), chlorine ($K_{\alpha 1}$ and $K_{\alpha 2}$ at 2.62 keV) and sulphur ($K_{\alpha 1}$ and $K_{\alpha 2}$ at 2.30 keV). The presence of these elements suggests that constituents of the brine solution (namely NaCl, $MgCl_2$ and Na_2SO_4) could be incorporated into the corrosion product.

SEM images of steel discs exposed to aerated brine for 10 min. (Figure 4.9a) suggest that dissolution of the surface metal and deposition of the corrosion product take place simultaneously. Figure 4.7 shows that the resulting change in the optical properties of the steel surface cause Δ to increase within this period. After 30 min. almost all of the surface metal has been removed, revealing the microstructure of the underlying steel (Figure 4.10a). In Figure 4.7 the Δ value plateaus after approximately 30 min., therefore this event could be related to the complete removal of the steel oxide layer. Longer exposure to the brine solution increases the size and number of corrosion product deposits (Figure 4.12). Over the duration of the experiments the brine solution became orange coloured; therefore the complex refractive index of brine solution is changing with time. The decrease in Δ values between 30 – 80 min. and the rapid increase of Δ after 85 min. in Figure 4.7 possibly reflect these changes in the optical properties of the medium and the surface of the steel as the coverage of the corrosion product increases.

4.3.2 Carbon dioxide conditions

Figure 4.14 shows the variation of Δ and Ψ with time for a 1018 steel disc immersed in brine under CO_2 conditions. Under these conditions metal dissolution occurs rapidly after addition of the brine solution, signified by fine scratches on the surface of the polished disc. After approximately 20 min. the disc begins to develop a grey appearance. Δ and Ψ values rapidly decrease with time immediately after immersion of the steel into carbonated brine solution. The magnitude of change in Δ values is much greater than that seen with Ψ. After approximately 2.5 hr. Δ begins to plateau whilst Ψ continues to decrease.

Figure 4.15 shows a 1018 steel disc which has been exposed to CO_2 sparged brine for 10 min. Figure 4.15a shows the ferritic-pearlitic microstructure of the steel which is visible due to rapid dissolution of the native oxide layer. Corrosion product

Figure 4.14. Δ (black) and Ψ (red) vs time for a 1018 steel disc in brine under CO_2 conditions at 25 °C.

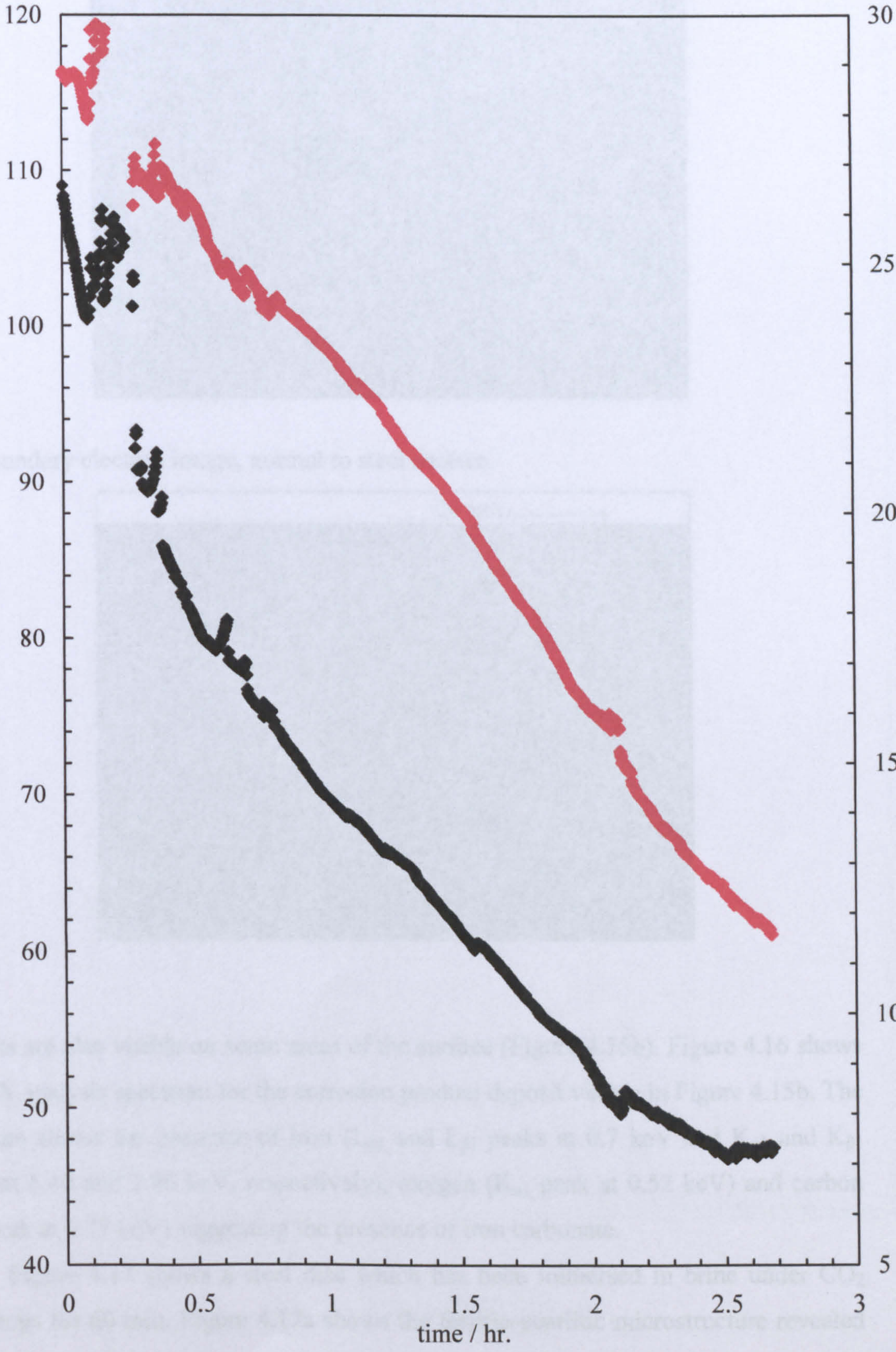

Figure 4.15. Scanning electron micrograph of a 1018 steel disc after immersion in brine under CO_2 conditions for 10 min. at 25 °C.

(a) Secondary electron image, normal to steel surface.

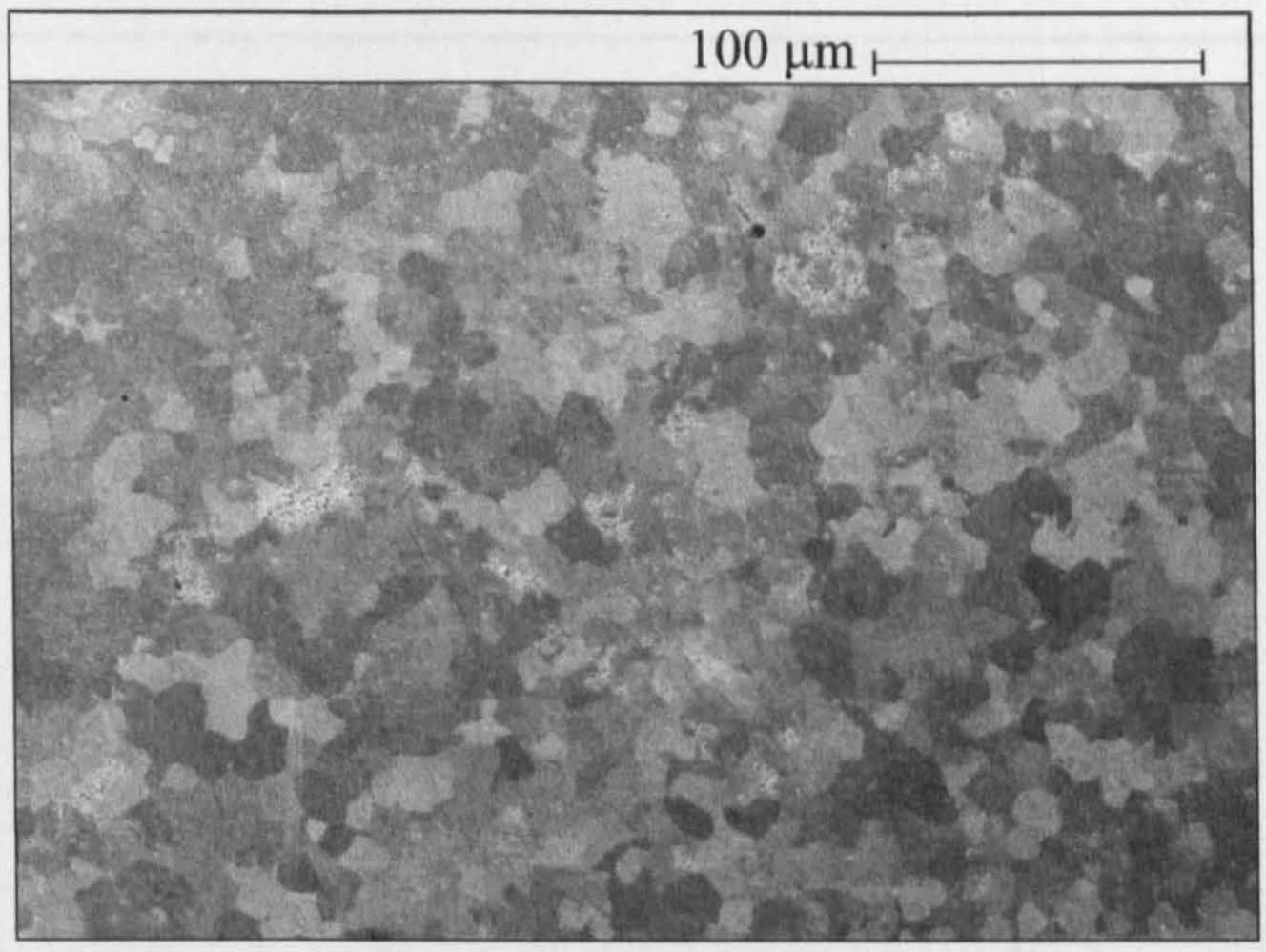

(b) Secondary electron image, normal to steel surface.

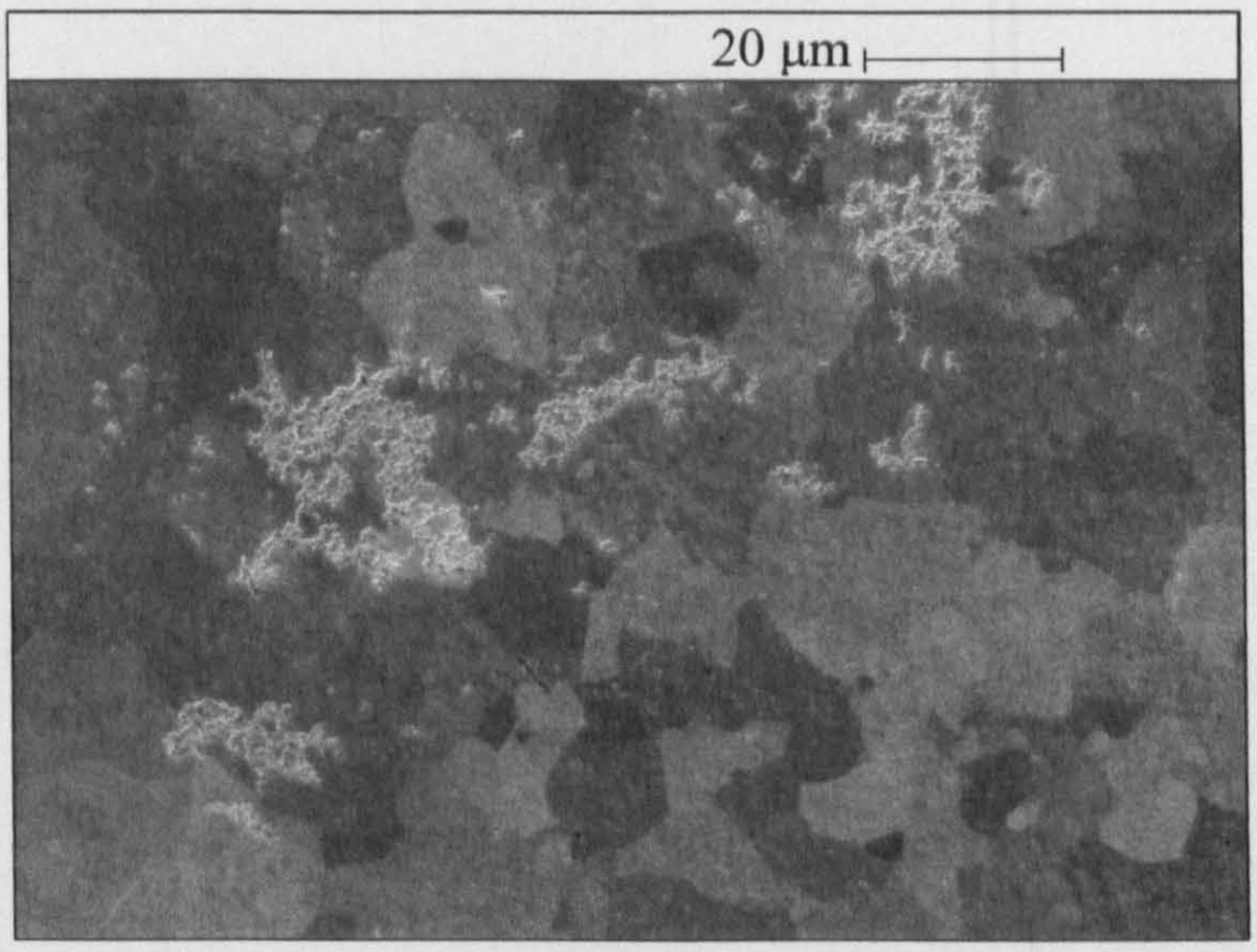

deposits are also visible on some areas of the surface (Figure 4.15b). Figure 4.16 shows an EDX analysis spectrum for the corrosion product deposit visible in Figure 4.15b. The spectrum shows the presence of iron ($L_{\alpha 1}$ and $L_{\beta 1}$ peaks at 0.7 keV and $K_{\alpha 1}$ and $K_{\beta 1}$ peaks at 6.40 and 7.06 keV, respectively), oxygen ($K_{\alpha 1}$ peak at 0.52 keV) and carbon ($K_{\alpha 1}$ peak at 0.27 keV) suggesting the presence of iron carbonate.

Figure 4.17 shows a steel disc which has been immersed in brine under CO_2 conditions for 60 min. Figure 4.17a shows the ferritic-pearlitic microstructure revealed by dissolution of the surface metal. When compared to Figure 4.15 there appears to be

Figure 4.16. EDX analysis spectrum of corrosion product visible in Figure 4.15b.

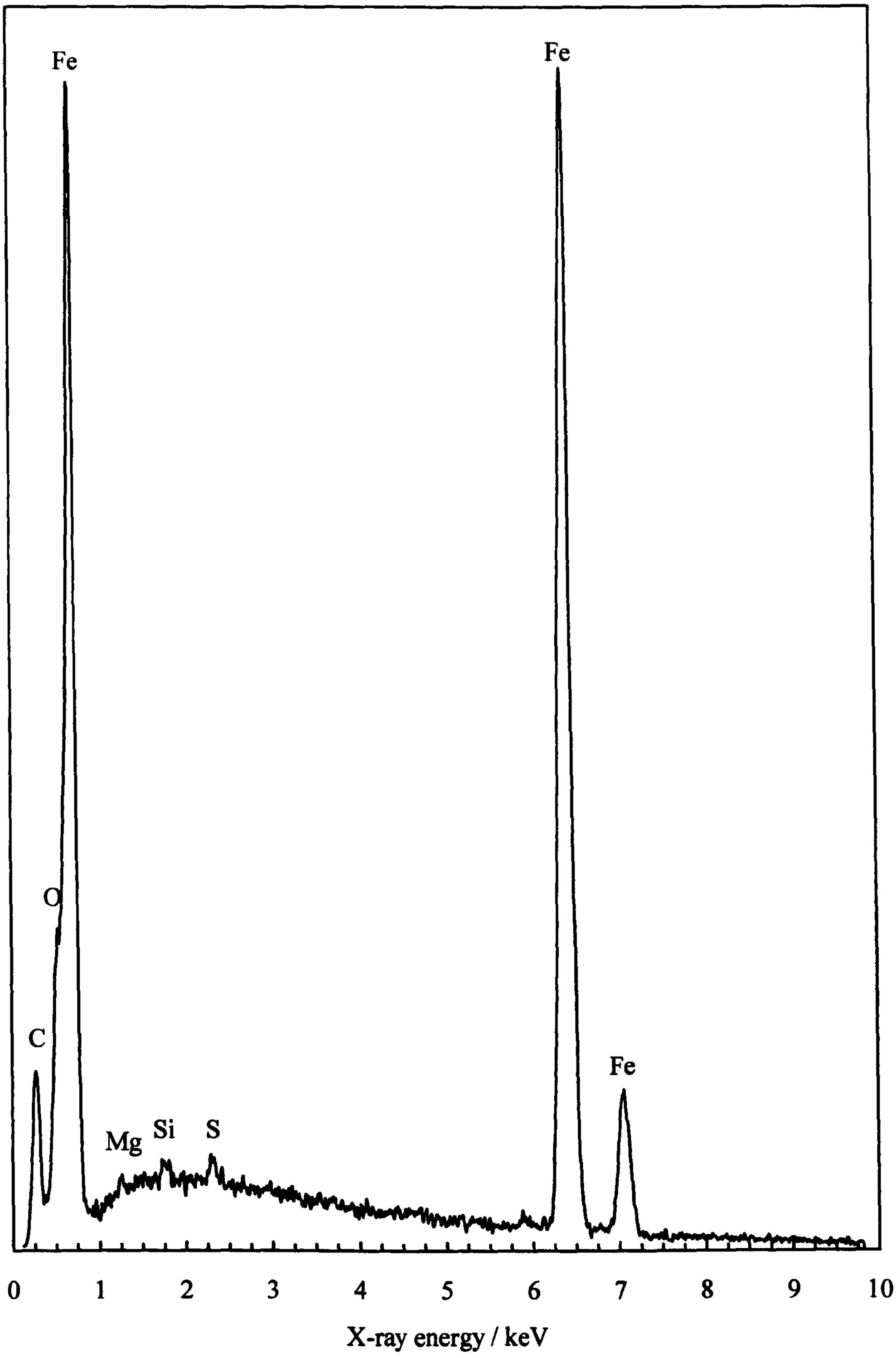

no presence of corrosion product deposits despite a longer period of exposure to the carbonated brine solution. Figure 4.17b shows the microstructure of the steel at high magnification. The grain in the centre of the image shows signs of partial dissolution revealing patches of the underlying steel.

Figure 4.17. Scanning electron micrograph of a 1018 steel disc after immersion in brine under CO_2 conditions for 60 min. at 25 ºC.

(a) Secondary electron image, normal to sample surface.

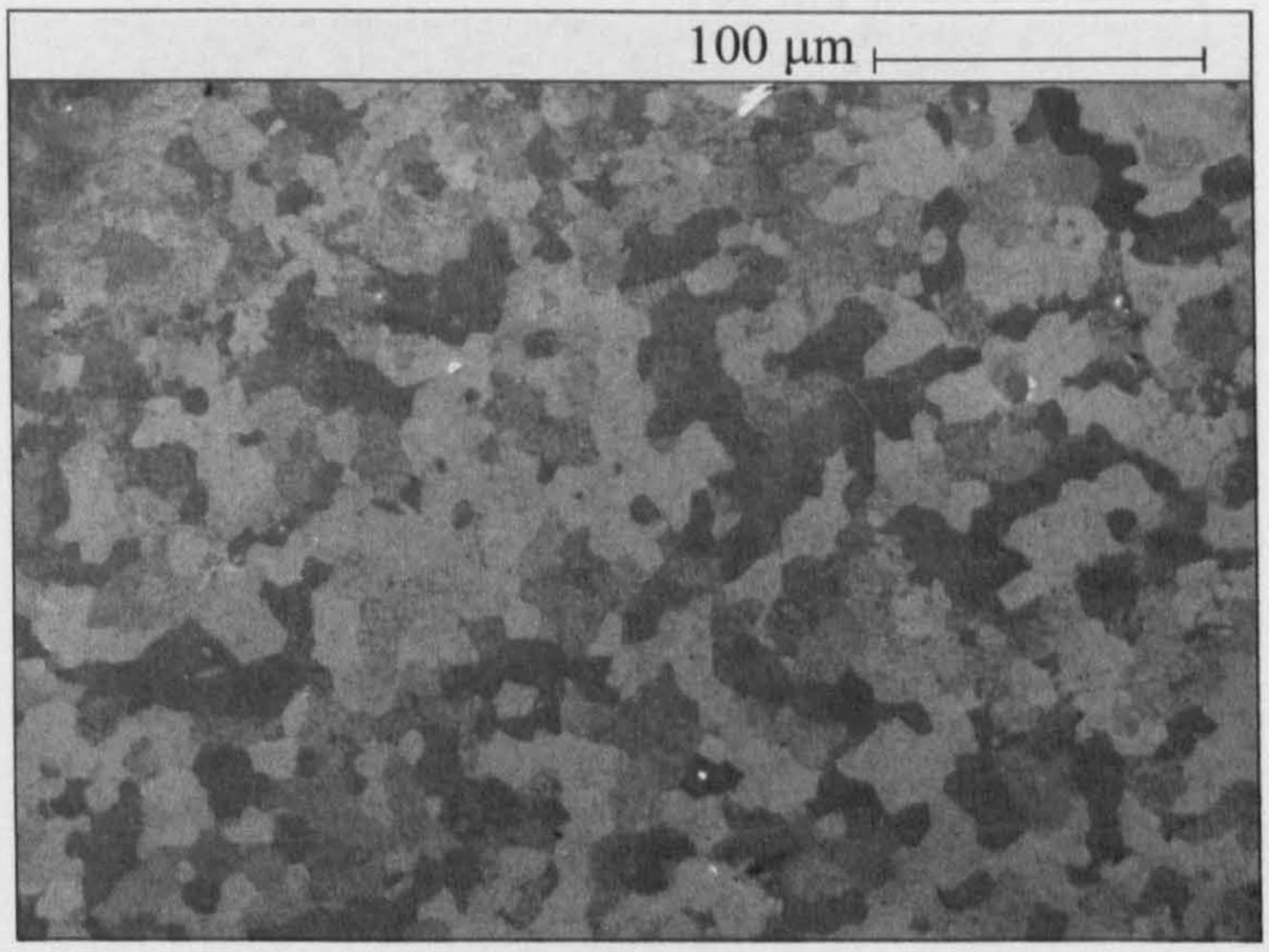

(b) Secondary electron image, normal to sample surface.

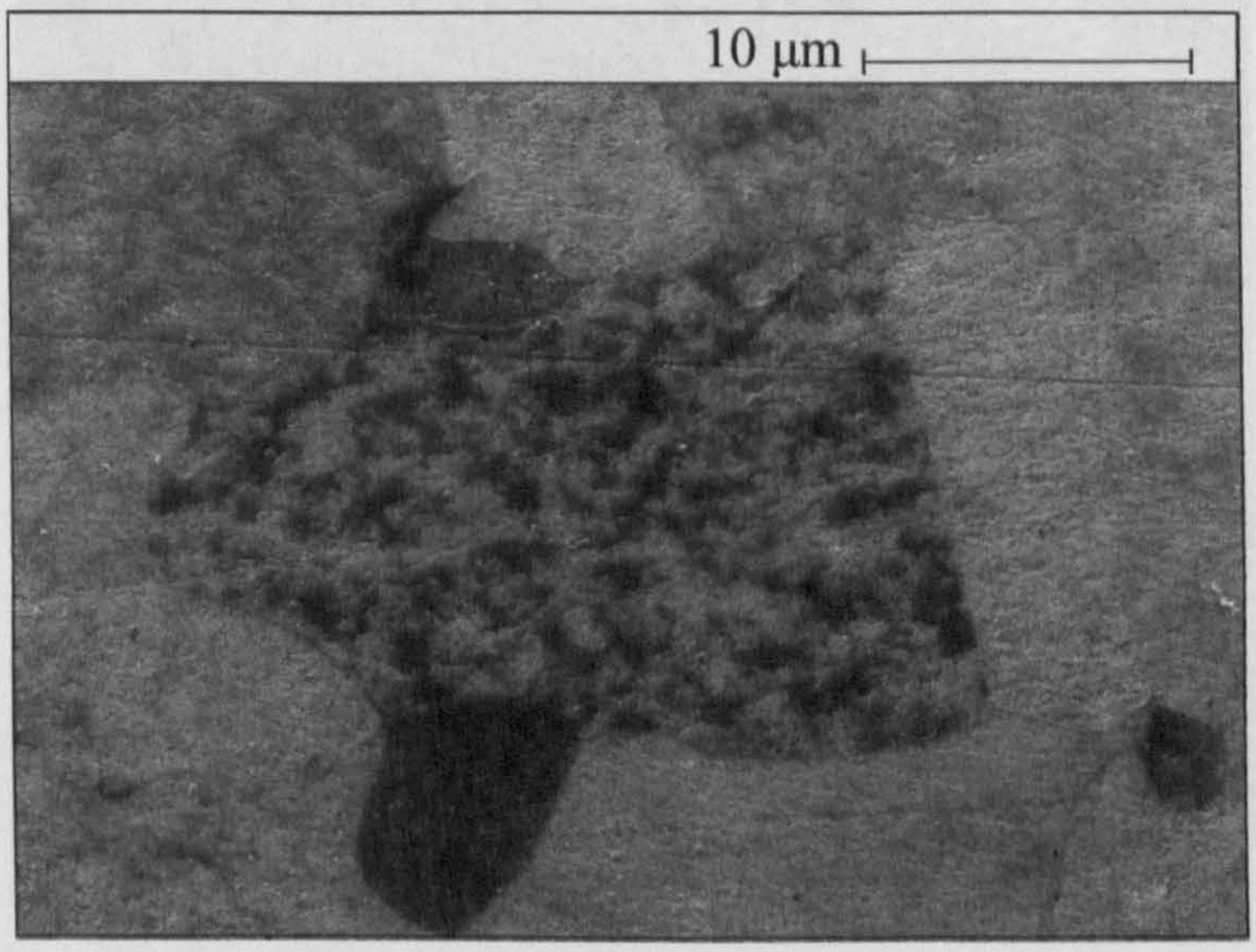

Figure 4.18 shows a steel disc which has been exposed to CO_2 brine for 90 min. Figure 4.18a looks similar to Figure 4.17a showing exposed ferrite and pearlite grains and dark

grey areas where the surface of the steel has not been corroded. Figure 14.8a contains fewer of these darker grains showing a greater extent of metal dissolution has taken place.

Figure 4.18. Scanning electron micrograph of a 1018 steel disc after immersion in brine under CO_2 conditions for 90 min. at 25 ºC.

(a) Secondary electron image, normal to sample surface.

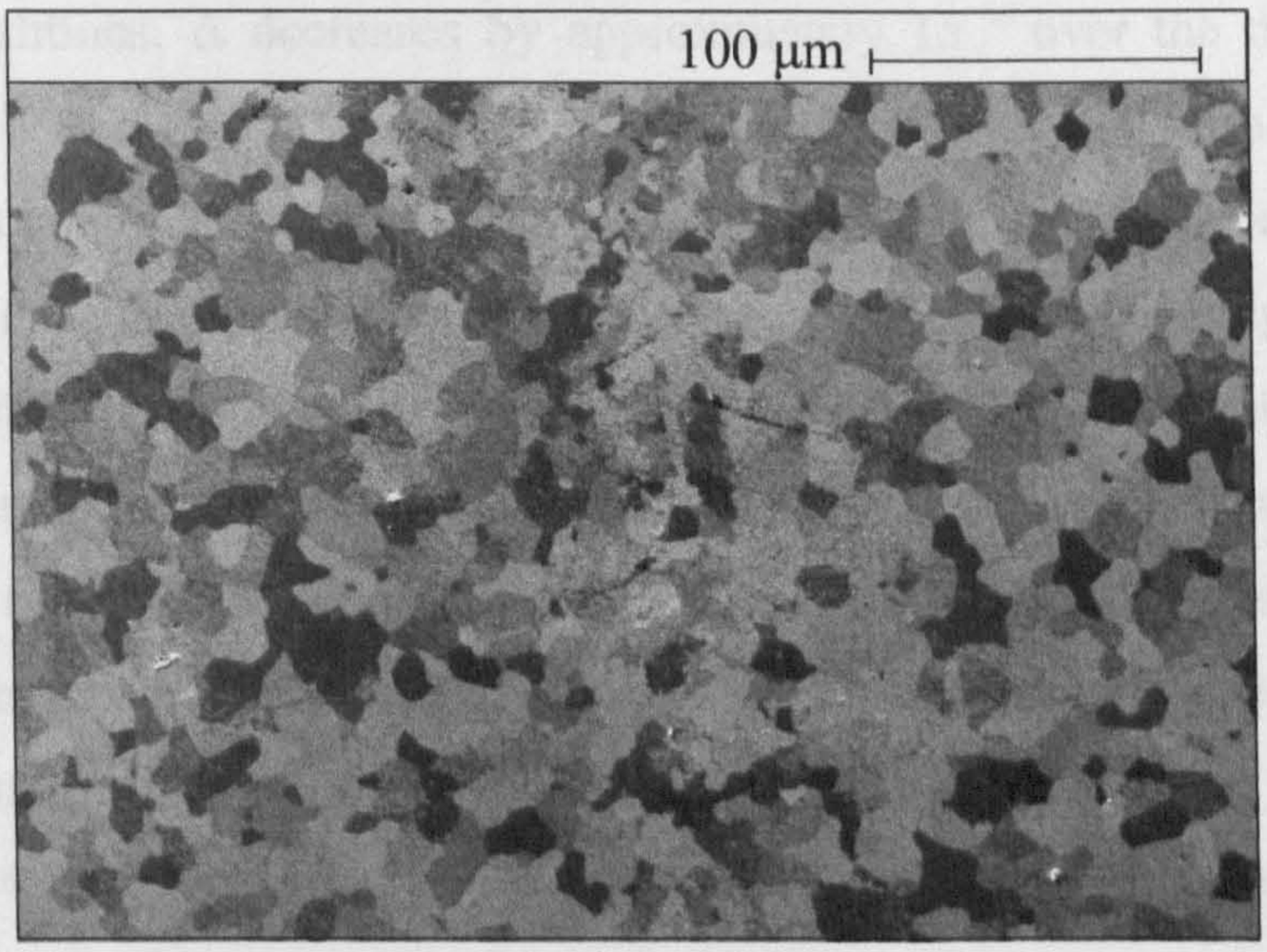

(c) Secondary electron image, normal to sample surface.

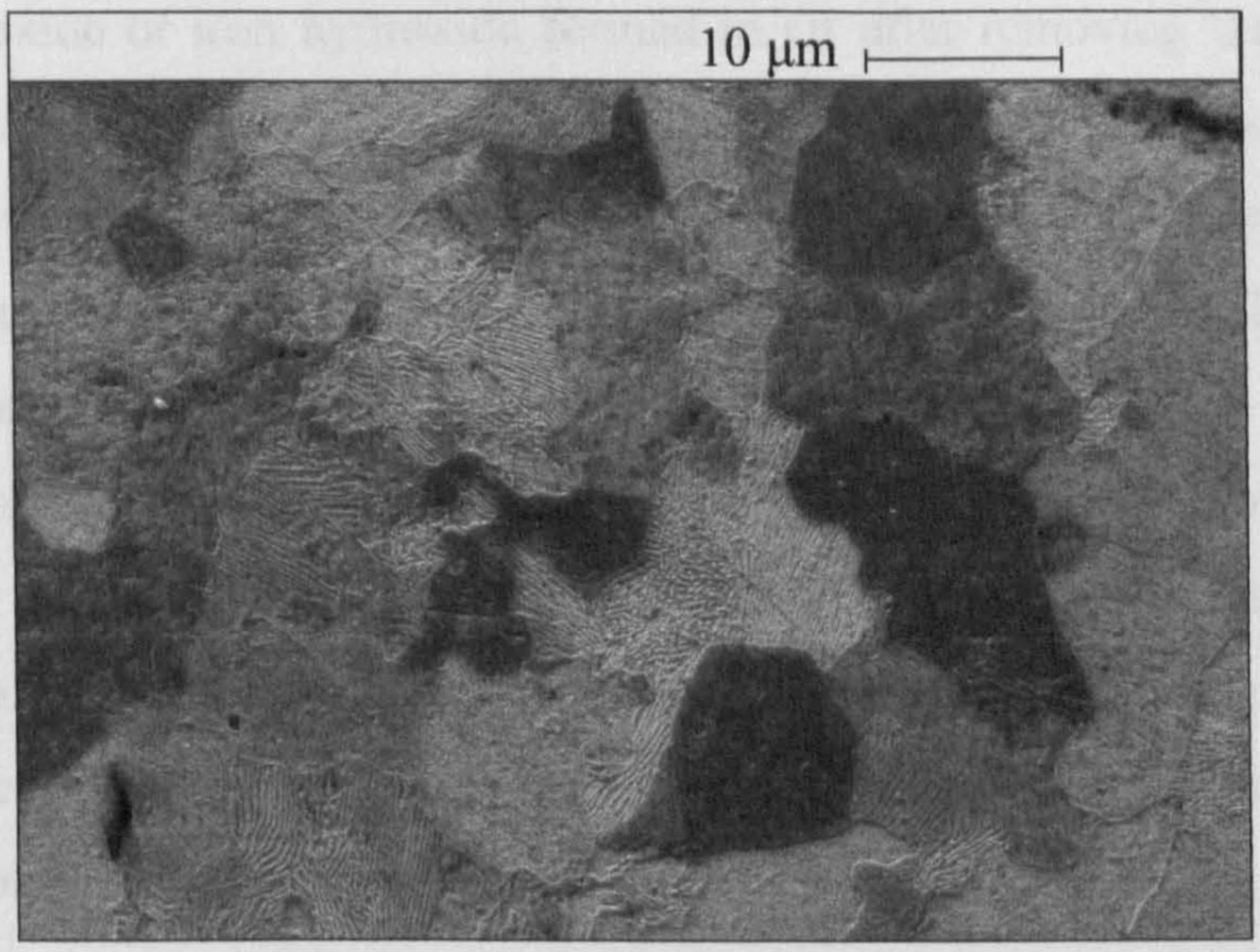

The SEM images generally show increased dissolution of the surface oxide film as the length of exposure to CO_2 brine increases from 10 – 90 min. Figure 4.14 shows that Δ decreases with time suggesting that only one process is affecting the optical

properties of the steel surface, which seems consistent with the general trend of the SEM images. The absence of corrosion product deposits in Figures 4.17 and 4.18 suggest that the corrosion product visible after 10 min. (Figure 4.15b) could be anomalous.

4.3.3 Hydrogen sulphide conditions

Figure 4.19 shows the variation of Δ and Ψ with time for a 1018 steel disc in brine under H_2S conditions. Δ decreases by approximately 15 ° over the duration of this measurement. Ψ also decreases, but at a much slower rate. The surface of the discs retained their metallic appearance throughout the experiment, but some fine scratches were present signifying dissolution of the surface metal. Black iron sulphide corrosion products, which are commonly formed in the presence of H_2S, were not seen in any of the experiments performed under these conditions. Steel discs which were exposed to H_2S brine was rapidly oxidised in the atmosphere once removed from solution. Brown rust spots became visible to the naked eye as the discs were quickly rinsed with Milli-Q water and transferred to a vacuum desiccator.

Figure 4.20 shows a steel disc which has been immersed in brine under H_2S conditions for 5 hr. Figure 4.20a shows the corrosion product deposits which were formed after removing the disc from the brine solution. These corrosion products are probably iron oxide or iron hydroxide formed in air after removing the disc from the aqueous environment. Figure 4.20b shows the presence of pits at the centre of the roughly circular corrosion product deposits. Pitting corrosion is localized corrosion of the metal surface resulting in relatively rapid corrosion rates in small areas[7]. Pitting corrosion is commonly observed in systems containing H_2S[8,9]. Figure 4.20c shows a high magnification view of a single pit. The surface oxide film has been broken allowing the corrosive brine solution to penetrate the underlying steel. The accumulation of the oxide or hydroxide corrosion products around the pits suggests that the pitting process has in some way compromised the passive film surrounding the pit resulting in rapid corrosion when exposed to the air. Other areas of the surface showed more uniform corrosion of the surface metal revealing the ferrite and pearlite microstructure underneath (Figure 4.20d), however the extent of uniform corrosion appears to be less than that seen under aerated and CO_2 conditions. The direction of the changes in Δ and Ψ are the same as those seen under CO_2 conditions, but the magnitudes of the changes are smaller. This may reflect the lower extent of uniform

Figure 4.19. Δ (black) and Ψ (red) vs time for 1018 steel disc in brine under H_2S conditions at 25 °C.

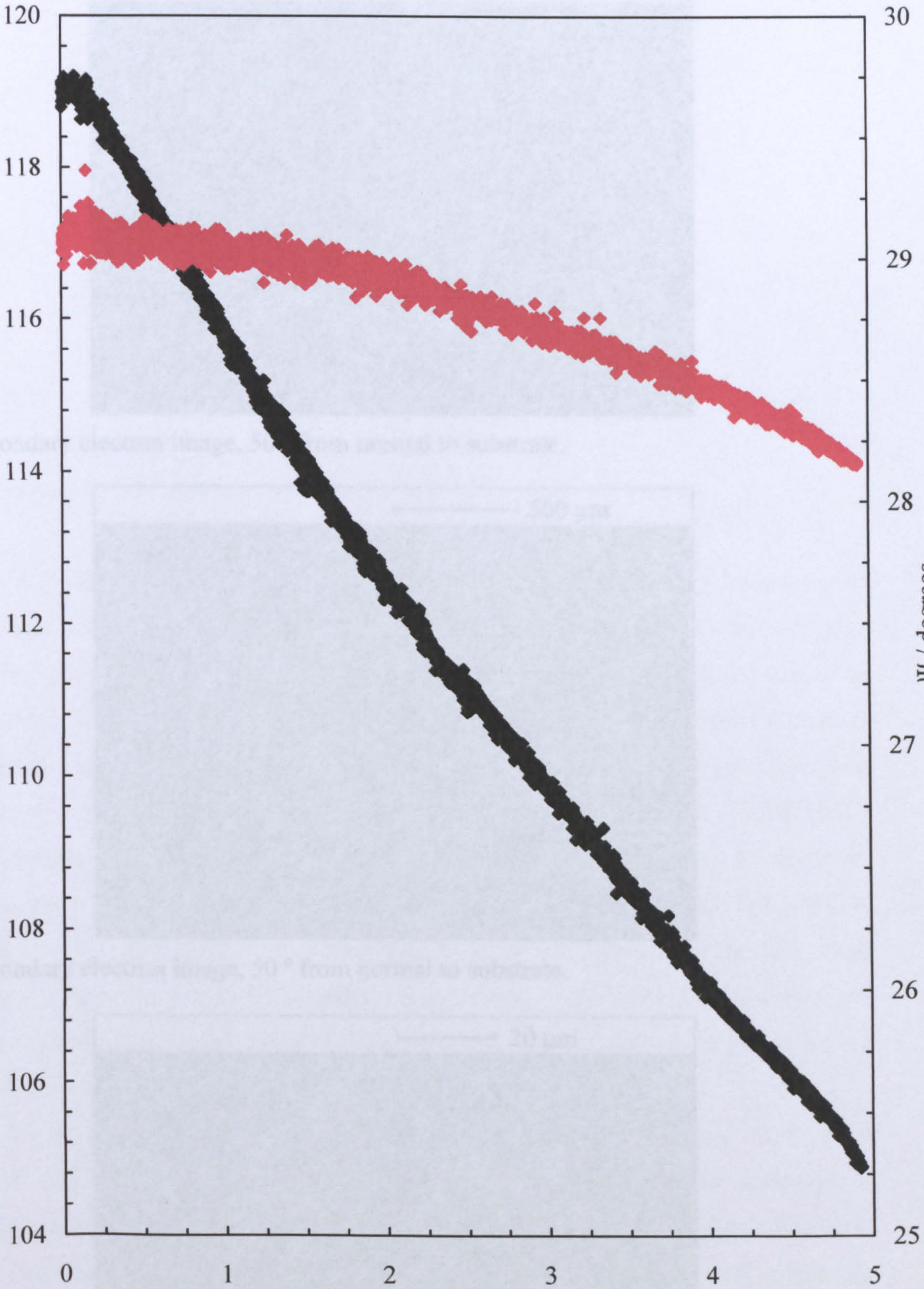

Figure 4.20. Scanning electron micrograph of a 1018 steel disc after immersion in brine under H_2S conditions for 5hr. at 25 °C.

(a) Secondary electron image, 50 ° from normal to substrate.

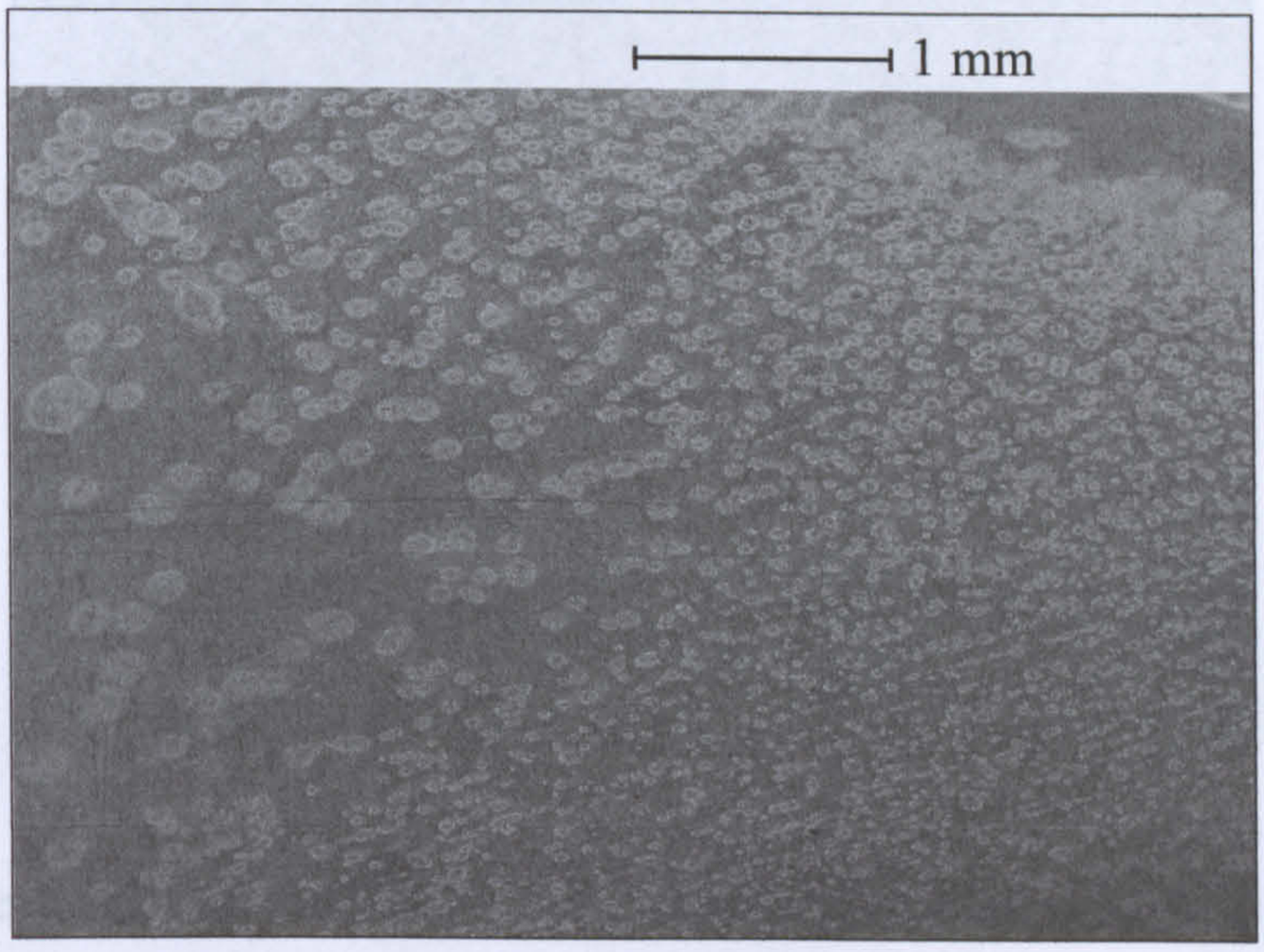

(b) Secondary electron image, 50 ° from normal to substrate.

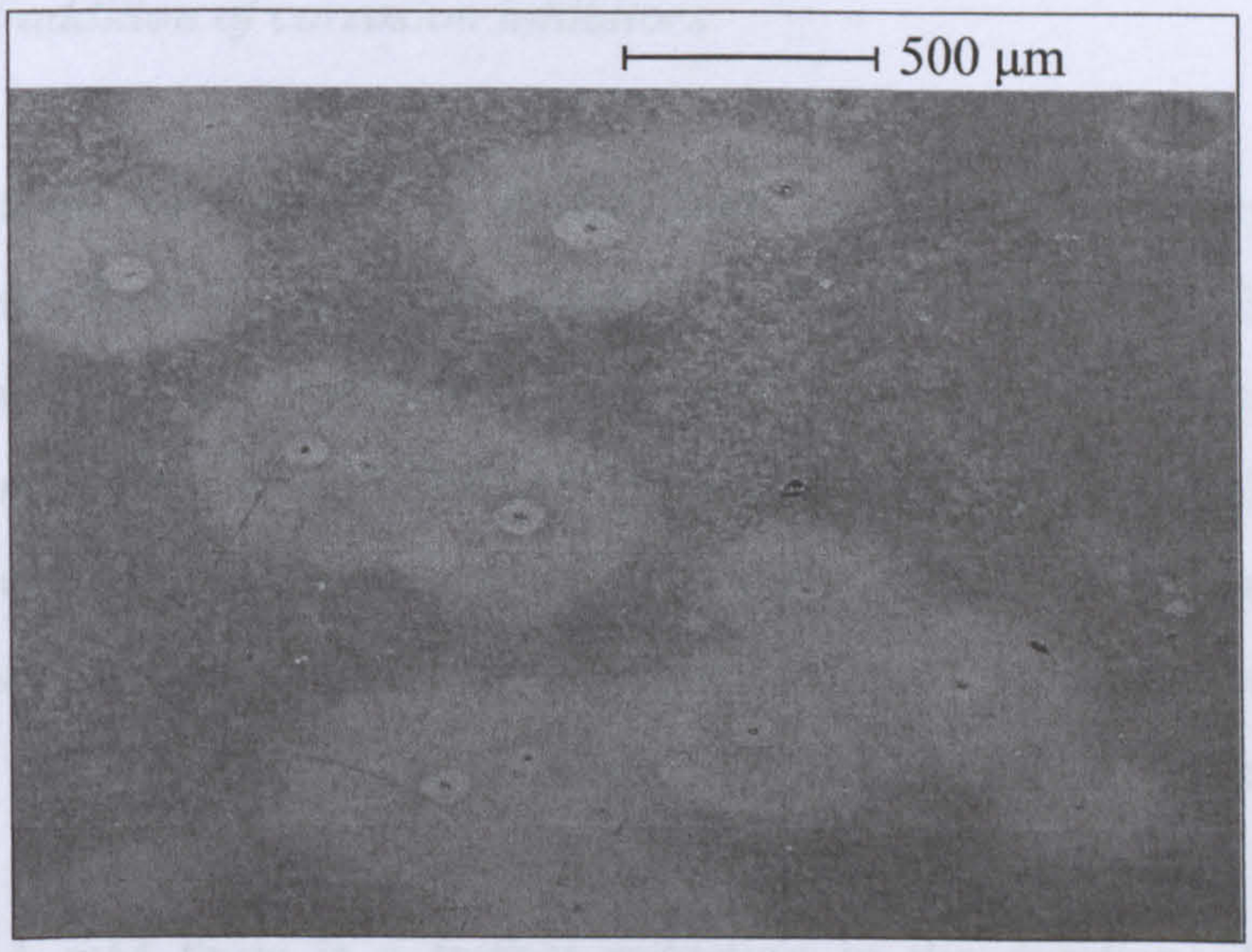

(c) Secondary electron image, 50 ° from normal to substrate.

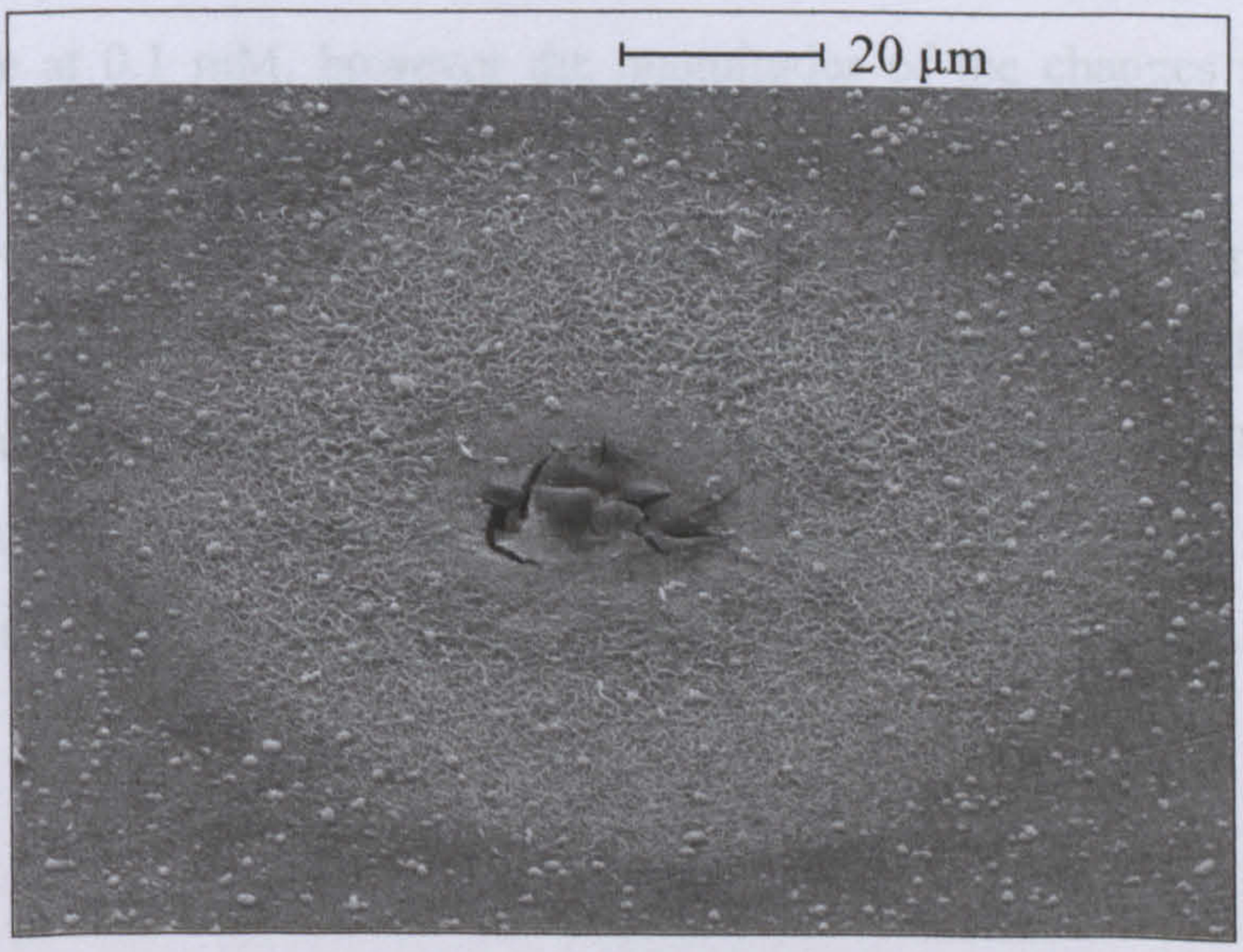

(d) Secondary electron image, 50 ° from normal to substrate.

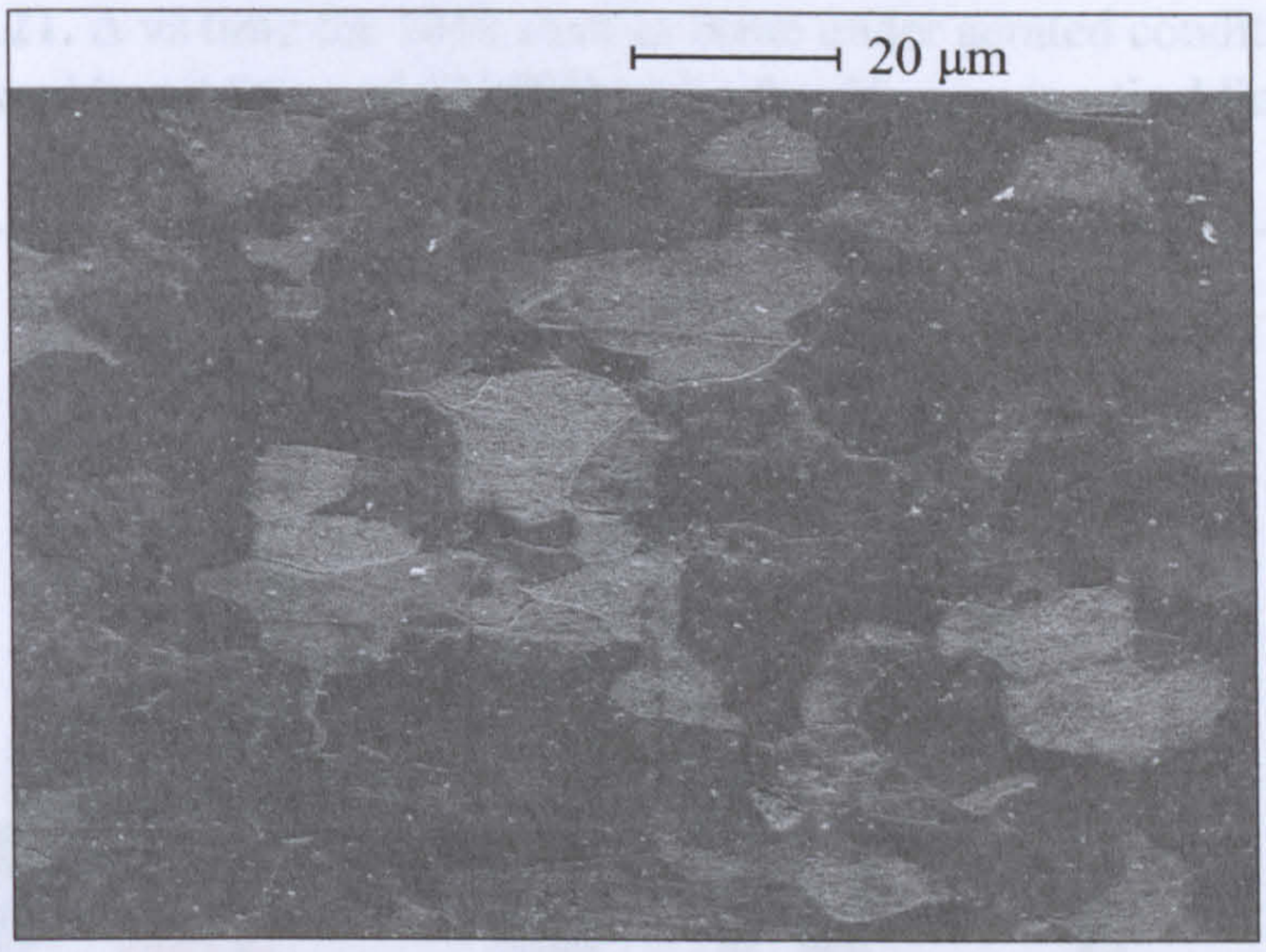

corrosion of the surface seen in the SEM images.

4.3.4 Effect of addition of corrosion inhibitors

Figures 4.21 shows the variation of Δ with time for steel discs during immersion in brine under aerated conditions with addition of C12BDMAC after 30 min. of pre-corrosion. In each case the profile of Δ versus time shows features which are similar to those seen in the absence of C12BDMAC (Figure 4.7) indicating that similar corrosion processes are occurring. In the presence of 0.01 mM C12BDMAC these processes take place over a shorter period of time compared to in the absence of C12BDMAC. Approximately 30 min. after the addition of C12BDMAC Δ begins to decrease, showing that a fourth process is beginning. When the concentration of C12BDMAC is increased to 0.1 mM there is a further reduction in the duration of the first three processes. Finally, at 1 mM C12BDMAC the duration of the corrosion processes are similar to those at 0.1 mM, however the magnitudes of the changes in Δ values are different from those at lower concentrations of C12BDMAC.

Figure 4.22 shows SEM images of steel discs exposed to aerated brine in the presence and absence of C12BDMAC for approximately 2 hr. The coverage of corrosion product generally increases as the concentration of C12BDMAC increases, which may explain the compression of the Δ versus time graphs with increasing concentration of C12BDMAC. These results indicate that changes in the optical

Figure 4.21. Δ vs time for 1018 steel in brine under aerated conditions at 25 °C, followed by addition of C12BDMAC after 30 min. (vertical line).

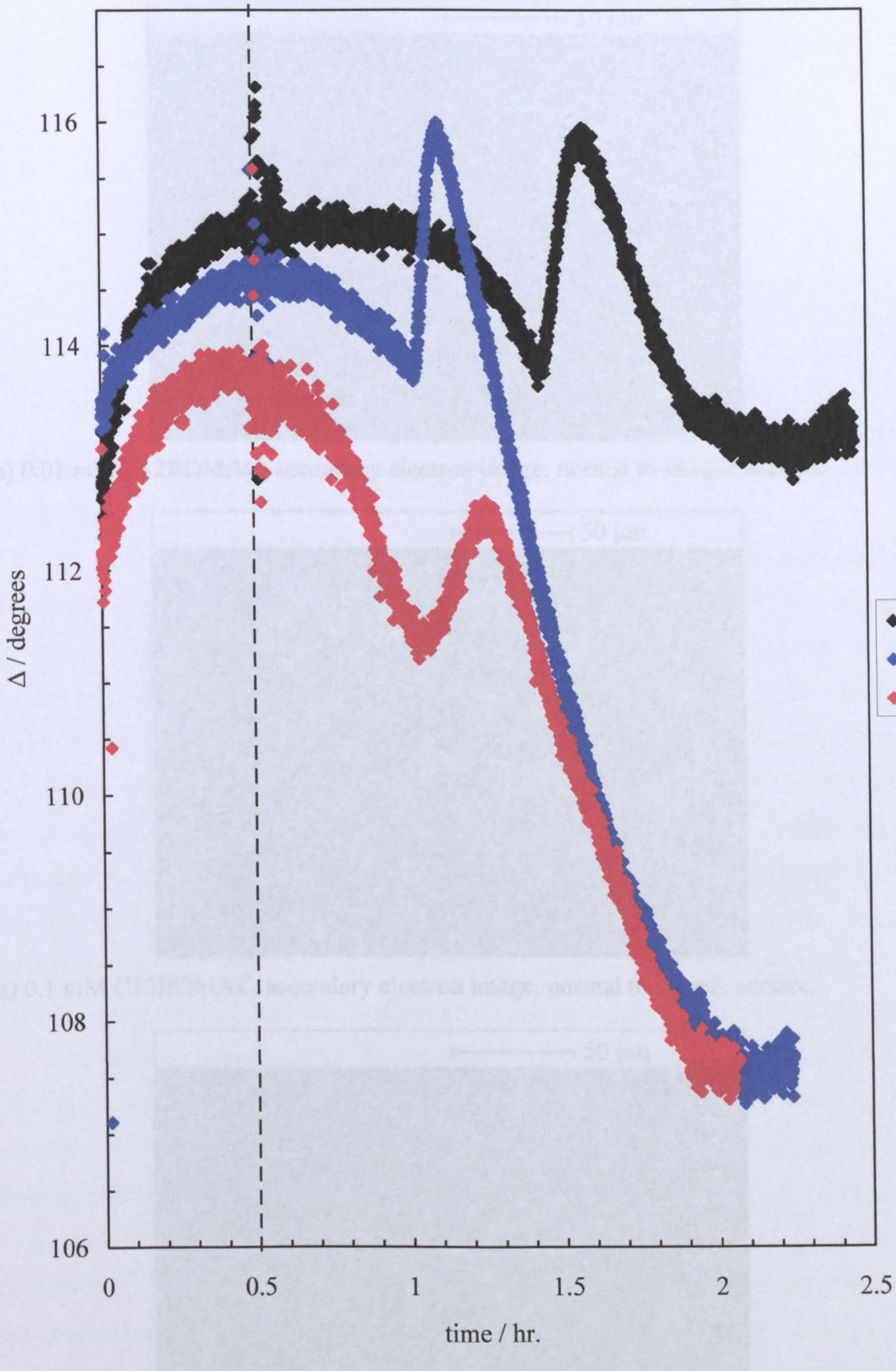

Figure 4.22. Scanning electron micrograph of 1018 steel discs after immersion in brine under aerated conditions in the presence and absence of C12BDMAC for 2 hr. at 25 ºC. (a) Absence of C12BDMAC, secondary electron image, normal to sample surface.

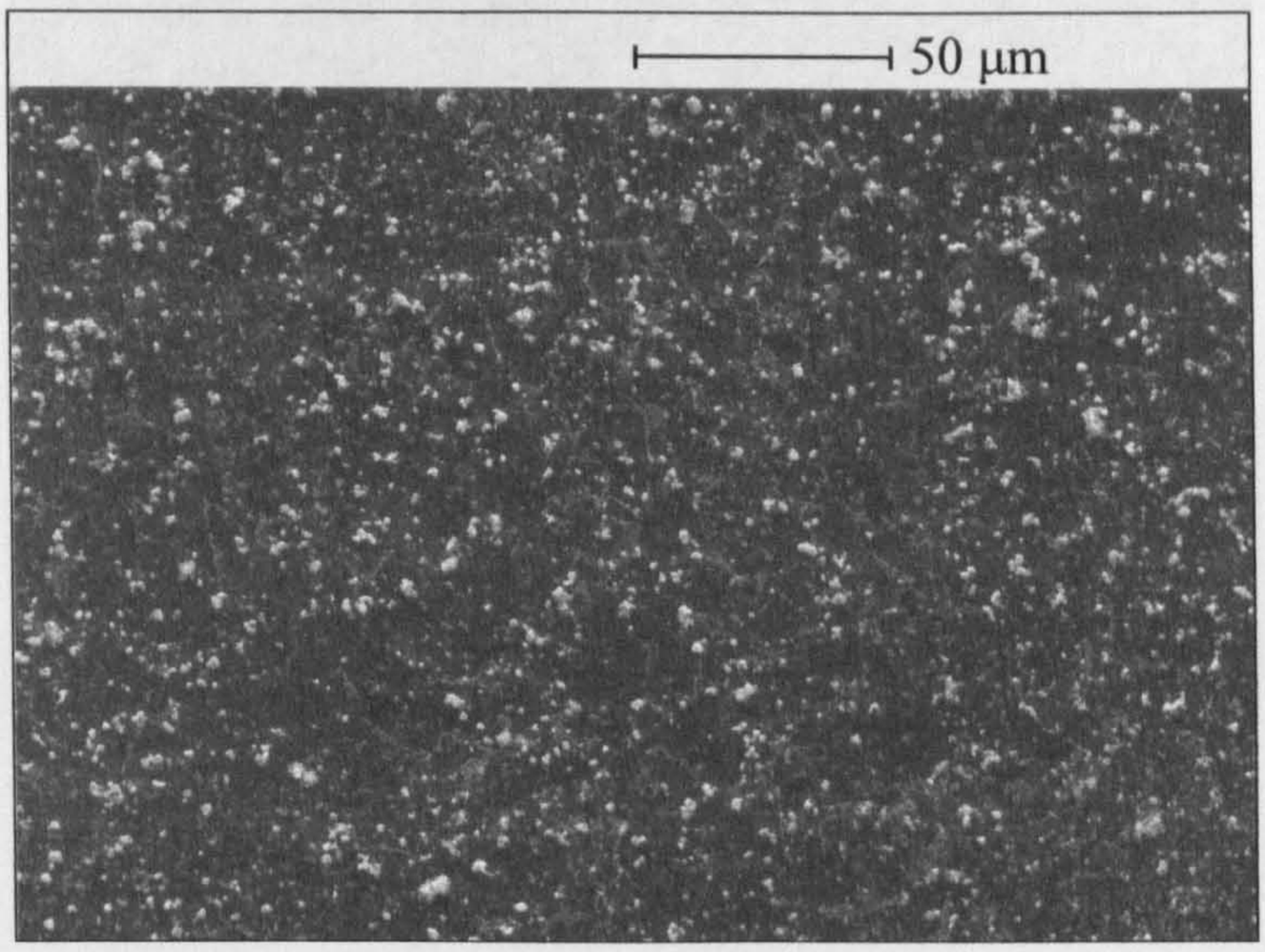

(b) 0.01 mM C12BDMAC, secondary electron image, normal to sample surface.

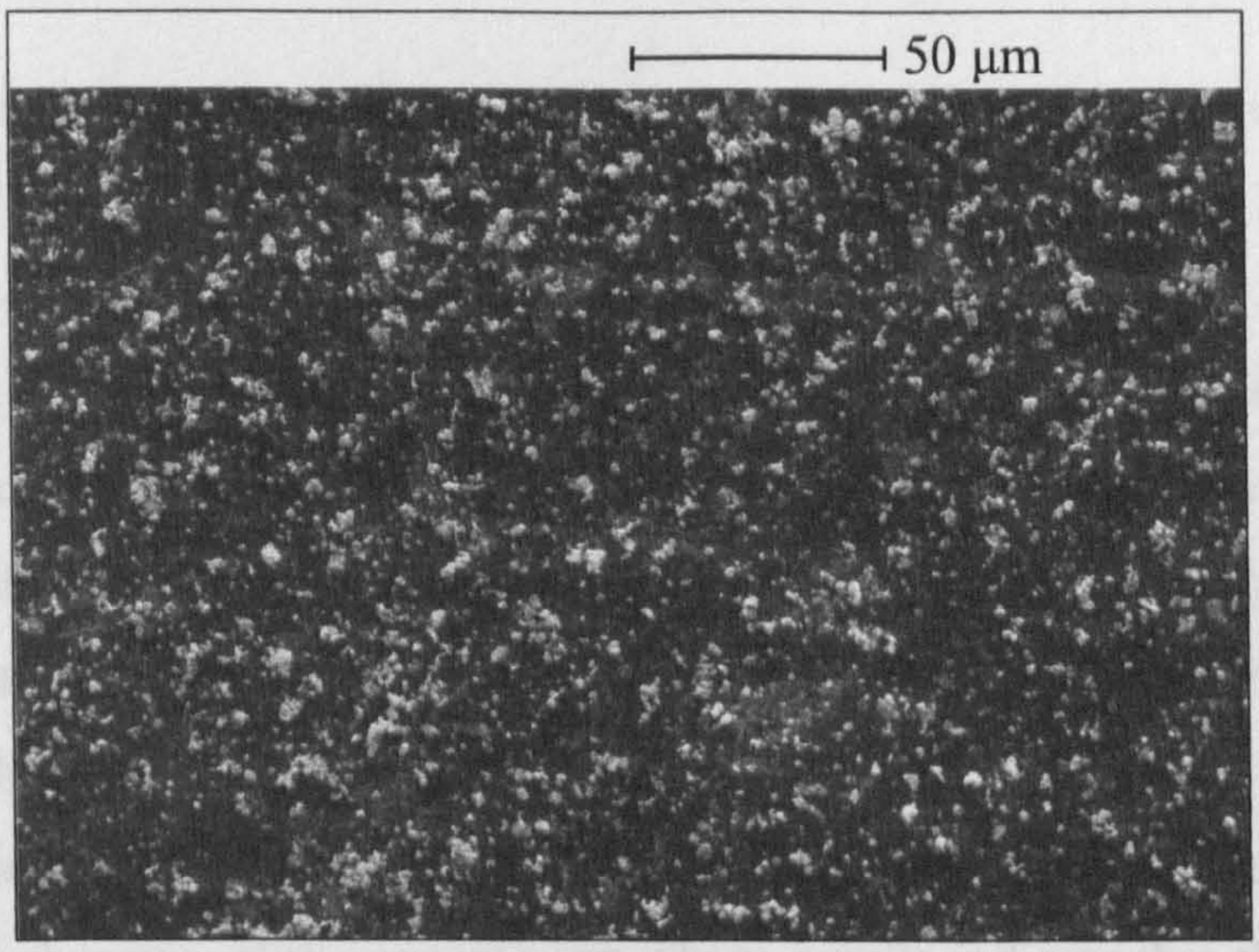

(c) 0.1 mM C12BDMAC, secondary electron image, normal to sample surface.

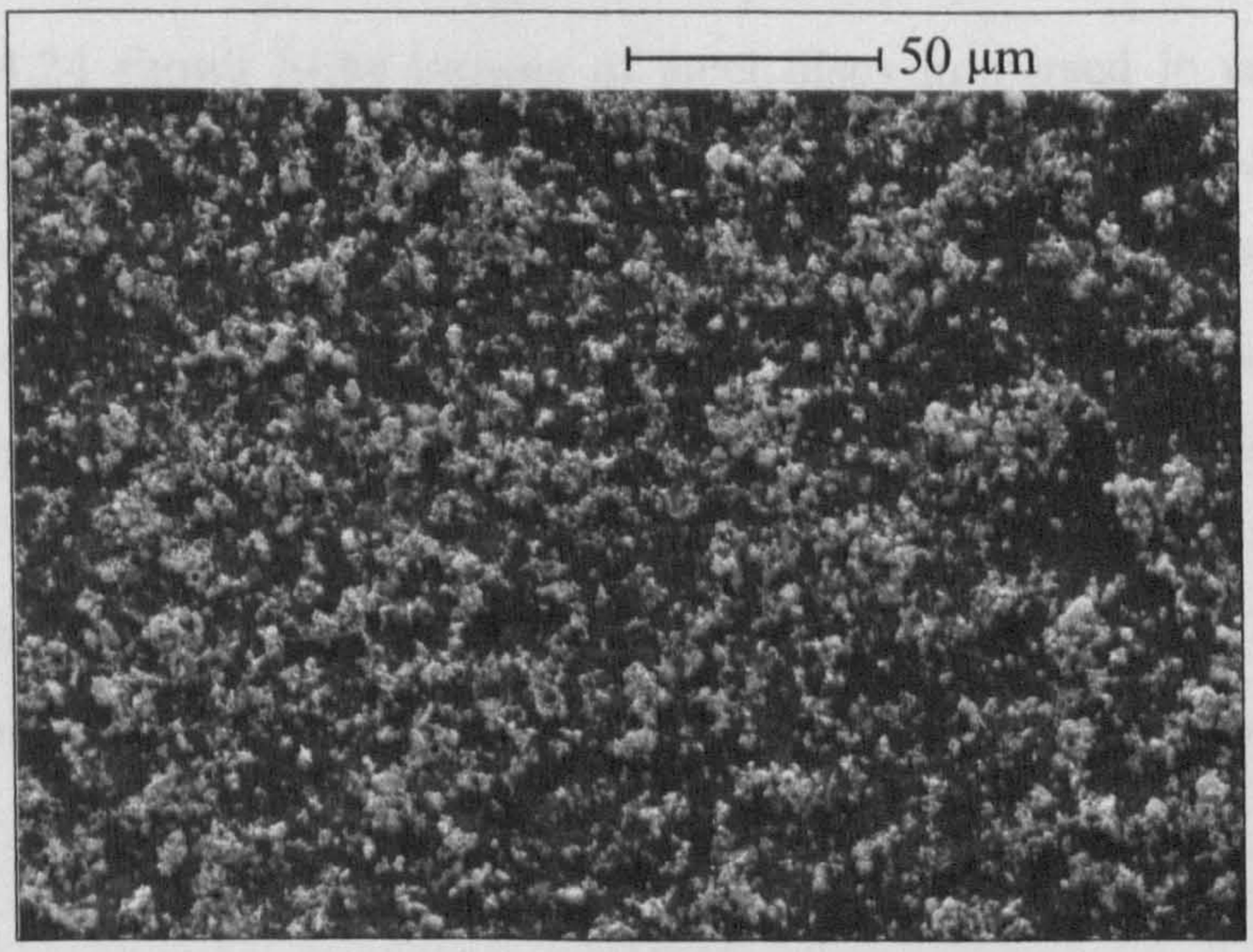

(d) 1 mM C12BDMAC, secondary electron image, normal to sample surface.

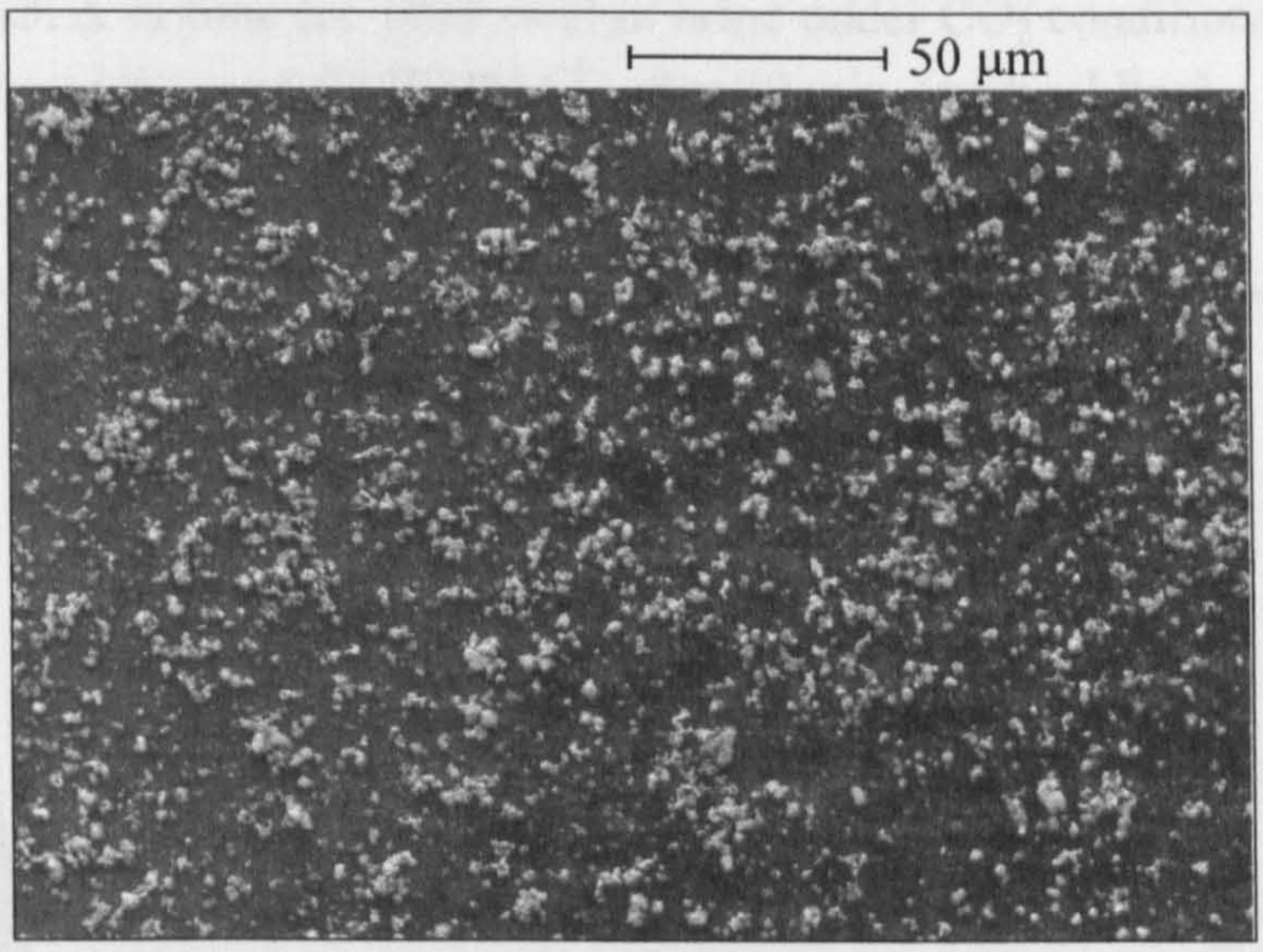

properties of the steel surface, caused by corrosion, occur faster in the presence of C12BDMAC.

Figure 4.23 shows the variation of Δ with time after immersion of steel discs in brine under CO_2 conditions in the presence of C12BDMAC. In the first 30 min. of each experiment, the steel disc is pre-corroded in the CO_2 sparged brine solution in the absence of C12BDMAC. During the pre-corrosion period, Δ values decrease with time. Ψ also decreases with time but the magnitude of the change is much smaller compared to that seen with Δ. Although the absolute values of Δ and Ψ are different for each disc, the magnitudes of the changes in these angles are approximately the same which indicates that the optical changes are occurring at the same rate. Approximately 5 min. after the addition of C12BDMAC the Δ and Ψ values both plateau and then remain constant for the duration of the experiment. These results indicate that the adsorption of C12BDMAC onto steel stops all changes in the optical properties of the steel surface.

Figure 4.24 shows SEM images of steel discs immersed in carbonated brine solutions in the absence and presence of C12BDMAC for approximately 2.5 hr. In the absence of C12BDMAC (Figure 4.24a) significant dissolution of the metal surface has taken place, revealing the ferritic-pearlitic microstructure of the steel. Figures 4.24b and 4.24c show significantly less dissolution of the metal surface in the presence of C12BDMAC. These images seem consistent with the dynamic ellipsometry results, showing that the presence of C12BDMAC stops the corrosion process occurring at the metal surface and that in the absence of C12BDMAC the corrosion process continues.

Figure 4.23. Δ vs time for 1018 steel in brine under CO_2 conditions at 25 °C, followed by addition of C12BDMAC after 30 min. (vertical line).

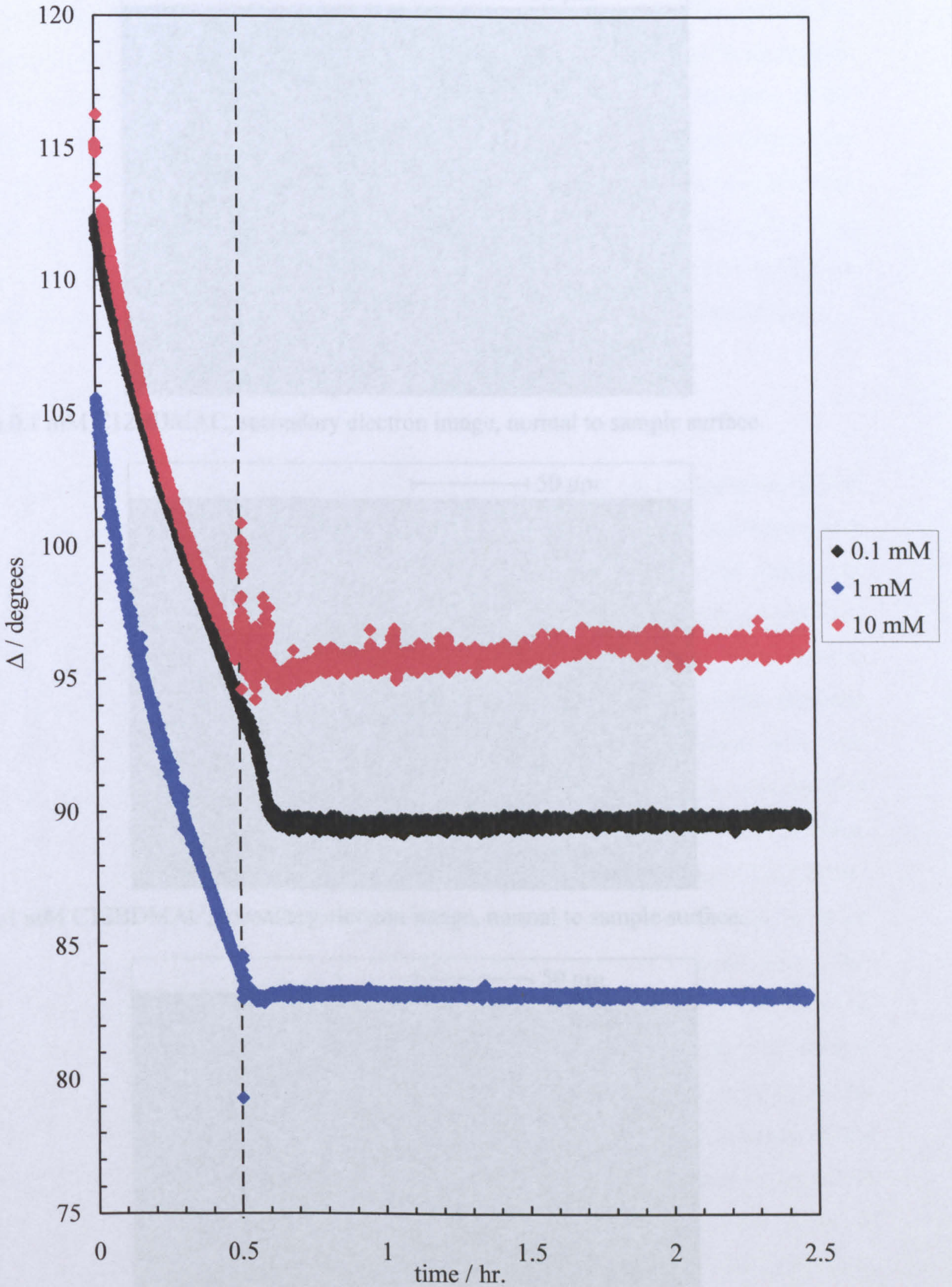

Figure 4.24. Scanning electron micrograph of 1018 steel discs after immersion in brine under CO_2 conditions in the presence and absence of C12BDMAC for 2.5 hr. at 25 °C.

(a) Absence of C12BDMAC, secondary electron image, normal to sample surface.

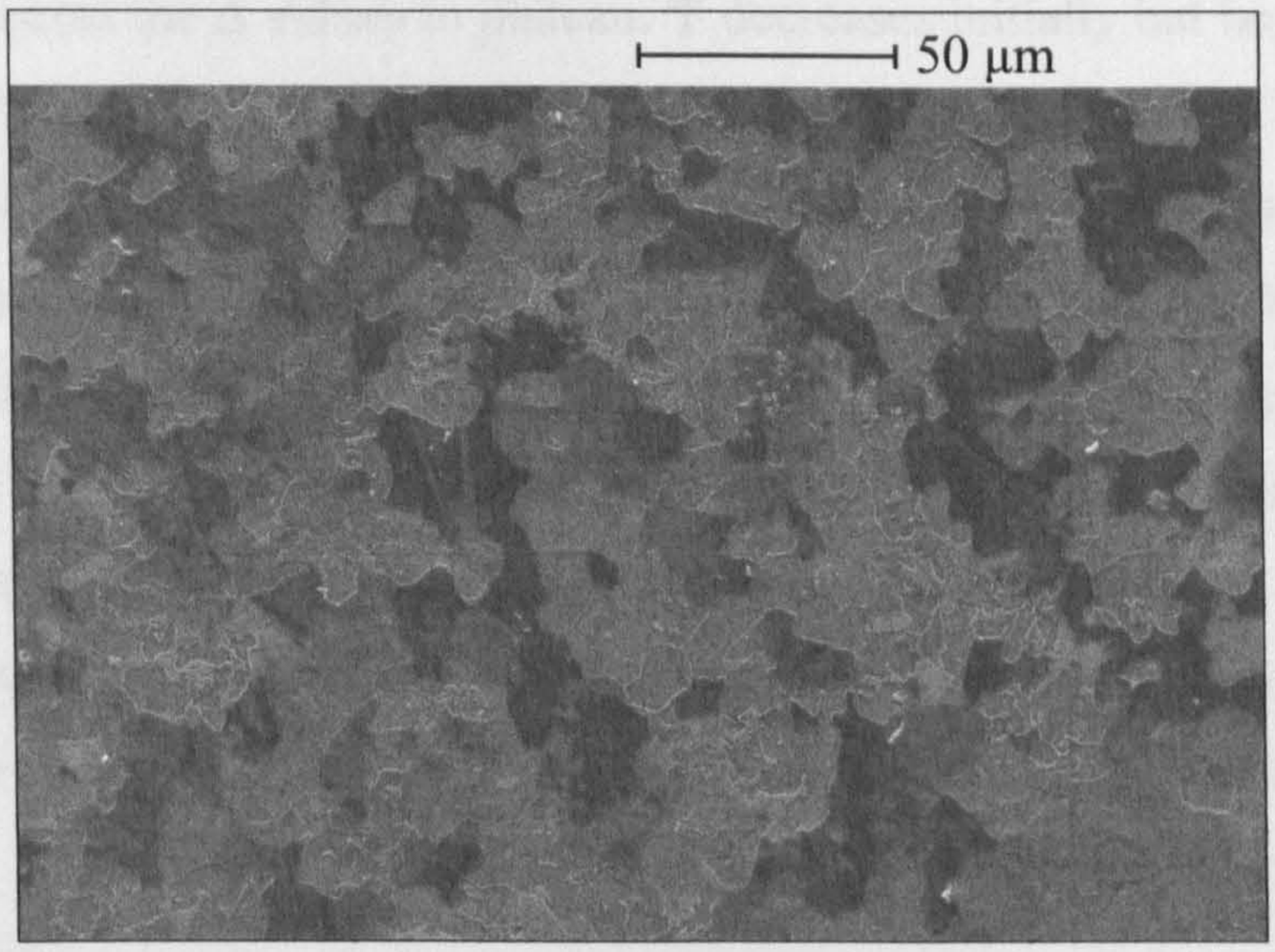

(b) 0.1 mM C12BDMAC, secondary electron image, normal to sample surface.

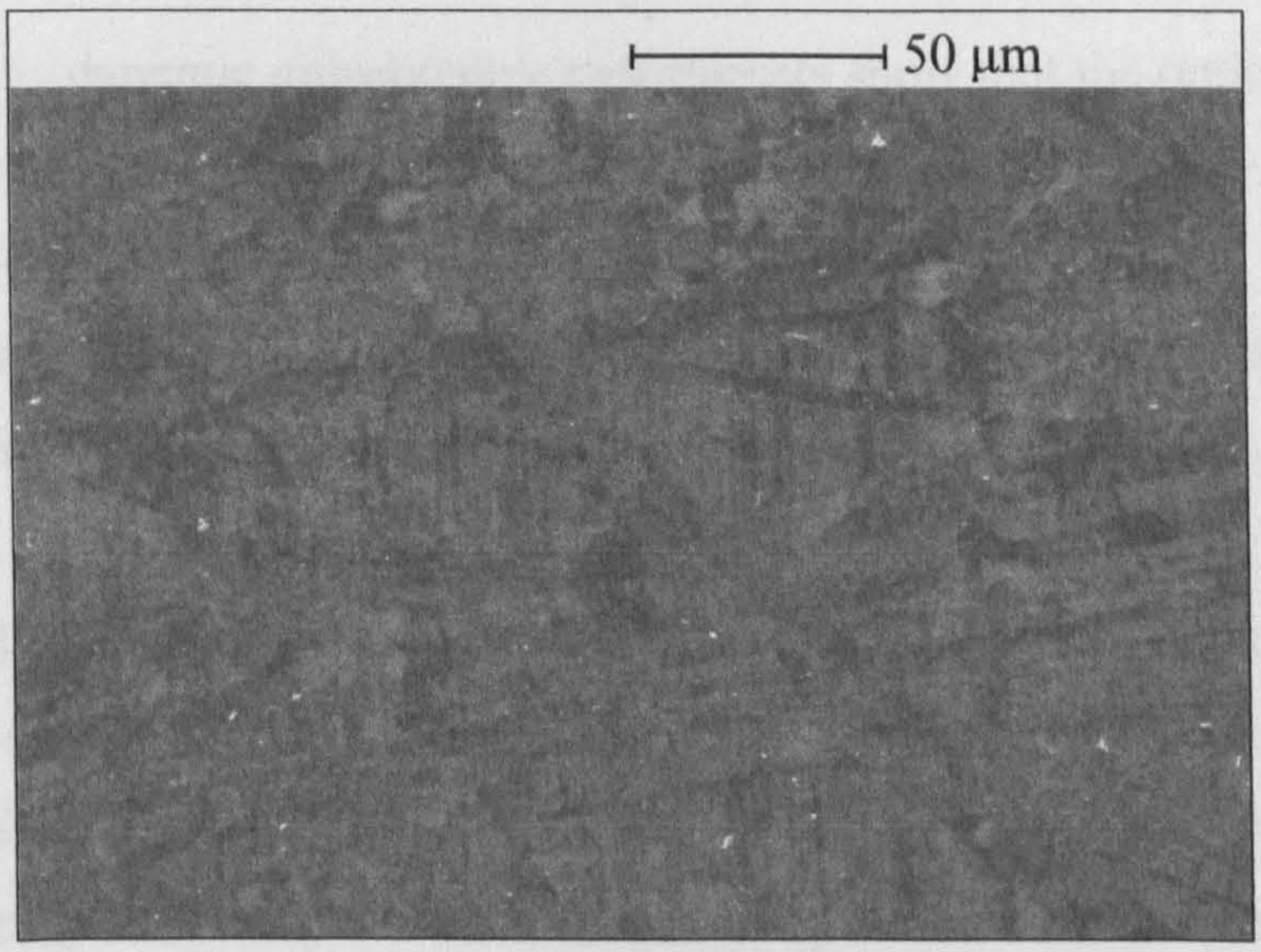

(c) 1 mM C12BDMAC, secondary electron image, normal to sample surface.

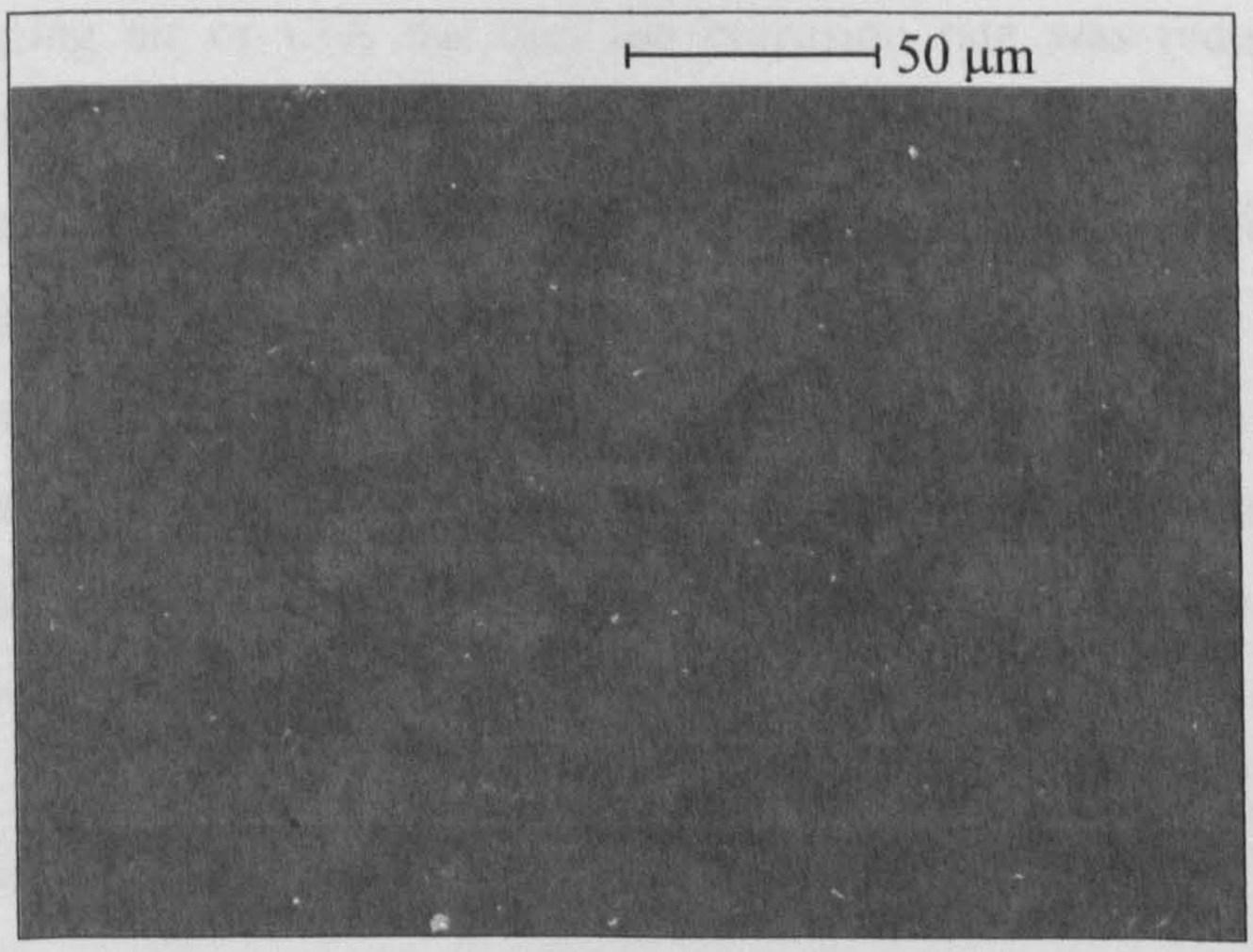

Figure 4.25 shows the variation of Δ with time after immersion of steel in brine under H_2S conditions with addition of C12BDMAC after 30 min. of pre-corrosion. Δ and Ψ decrease with time during the pre-corrosion period. Addition of 0.01 mM C12BDMAC causes the Δ values to plateau. Ψ decreases initially but begins to increase slightly after the addition of the surfactant. Approximately 2hr. after the start of the measurement Δ begins to decrease slightly. Further fluctuations of Δ and Ψ occur after 4.5 hr. and between 6 – 8 hrs. which were caused by slight lateral movements of the steel disc. In the presence of 0.1 mM C12BDMAC both Δ and Ψ plateau shortly after the addition of the surfactant and remain constant for the duration of the measurement. The steel retained its metallic appearance throughout the experiment. When the steel discs were removed from aqueous solution they were rapidly oxidised in the atmosphere resulting in the formation of brown rust spots which were visible with the naked eye.

4.3.5 Discussion

The results of the dynamic ellipsometry experiments show that the optical properties of the steel surface begin to change immediately upon exposure to brine solutions under atmospheric, CO_2 and H_2S conditions in the absence of C12BDMAC. The changes in optical properties cause large changes in the Δ parameter. Under atmospheric conditions Δ increases and decreases as corrosion of the steel progresses suggesting that a number of consecutive processes are taking place. These processes occur faster in the presence of C12BDMAC. Under CO_2 and H_2S conditions Δ continually decreases with time indicating that only one process is occurring at the surface. In both systems the addition of C12BDMAC suppresses the changes of the optical properties of the steel surface, resulting in plateaus of the Δ and Ψ values. In Chapter 3 we showed that C12BDMAC does not have a significant effect upon the electrochemical corrosion rate in brine systems containing air or CO_2 but that the corrosion rate was reduced under H_2S conditions. Although the timescales of the two techniques are different, the dynamic ellipsometry data suggest that the surfactant promotes corrosion of the steel surface under aerated conditions but inhibits it under CO_2 and H_2S conditions. In addition, the SEM images of the corroded steel are consistent with the general features of the ellipsometry data. This hypothesis could be tested further by conducting ellipsometric and electrochemical measurements simultaneously, using a polished steel disc as part of the three-electrode arrangement. Under conditions where the addition of C12BDMAC

Figure 4.25. Δ vs time for 1018 steel in brine under H_2S conditions at 25 °C, followed by addition of C12BDMAC after 30 min. (vertical line).

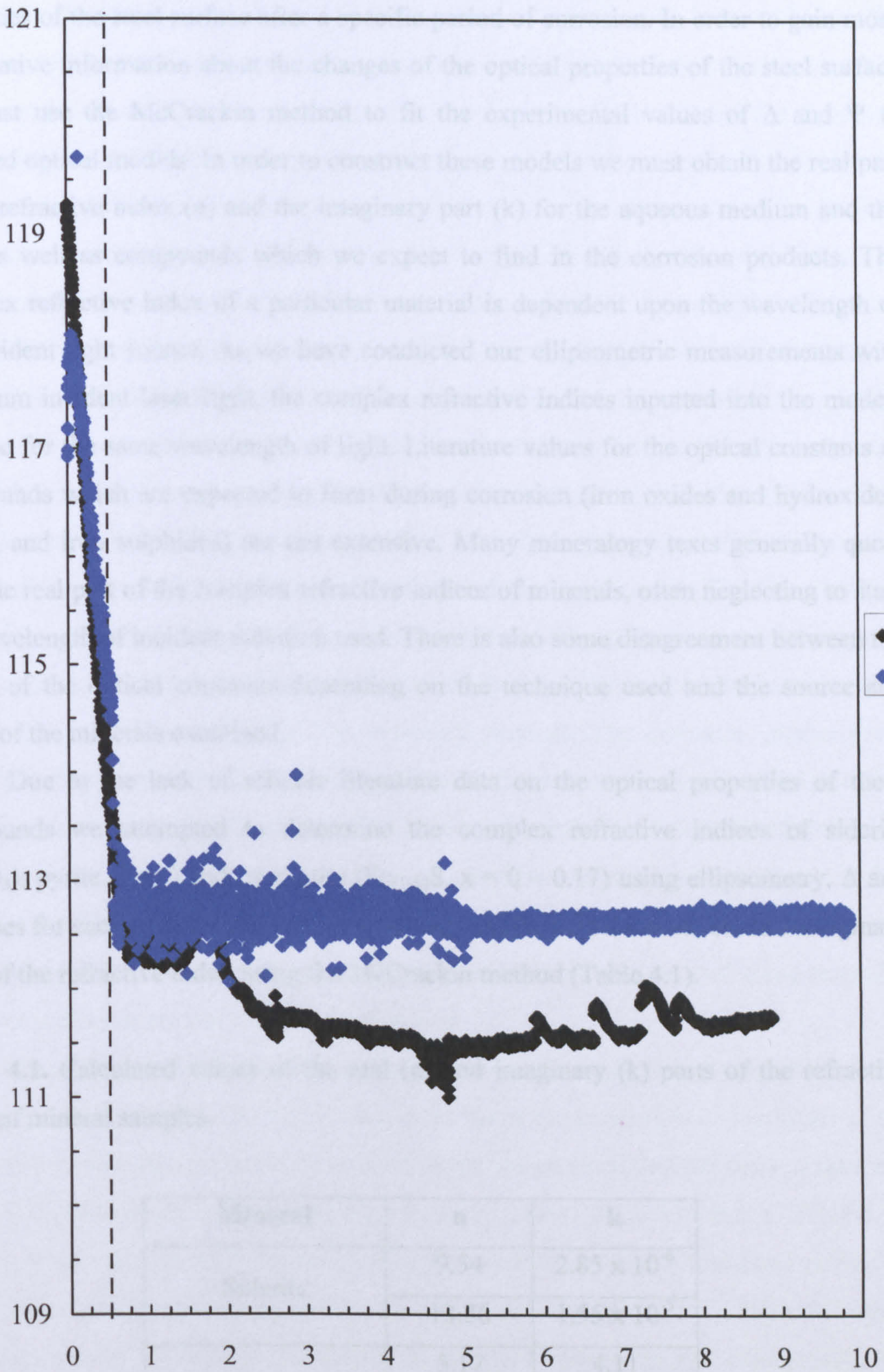

appears to stop all changes in the optical properties of the steel surface, spectroscopic ellipsometry, using incident laser light of different wavelengths, could be used to confirm whether the surface corrosion process is completely suppressed.

The values of Δ and Ψ do not give us directly information about the optical properties of the steel surface after a specific period of corrosion. In order to gain more quantitative information about the changes of the optical properties of the steel surface we must use the McCrackin method to fit the experimental values of Δ and Ψ to assumed optical models. In order to construct these models we must obtain the real part of the refractive index (n) and the imaginary part (k) for the aqueous medium and the steel as well as compounds which we expect to find in the corrosion products. The complex refractive index of a particular material is dependent upon the wavelength of the incident light source. As we have conducted our ellipsometric measurements with 632.8 nm incident laser light, the complex refractive indices inputted into the models must be for the same wavelength of light. Literature values for the optical constants of compounds which are expected to form during corrosion (iron oxides and hydroxides, $FeCO_3$ and iron sulphides) are not extensive. Many mineralogy texts generally quote only the real part of the complex refractive indices of minerals, often neglecting to state the wavelength of incident radiation used. There is also some disagreement between the values of the optical constants depending on the technique used and the source and purity of the minerals examined.

Due to the lack of reliable literature data on the optical properties of these compounds we attempted to determine the complex refractive indices of siderite ($FeCO_3$), pyrite (FeS_2) and pyrrhotite ($Fe_{(1-x)}S$, $x = 0 - 0.17$) using ellipsometry. Δ and Ψ values for each polished mineral sample were used to calculate the real and imaginary parts of the refractive index using the McCrackin method (Table 4.1).

Table 4.1. Calculated values of the real (n) and imaginary (k) parts of the refractive index of mineral samples.

Mineral	n	k
Siderite	9.54	2.85×10^{-6}
	13.86	1.55×10^{-5}
Pyrite	5.17	4.11
	1.13	0.45
Pyrrhotite	2.31	2.38

The values of Δ and Ψ gave multiple solutions for the complex refractive indices for siderite and pyrite, depending upon the initial estimates of n and k. For siderite, the calculated values of Δ and Ψ did not agree with the experimental values for any of the solutions, indicating that these calculated values of n and k were not realistic. The calculated n values are too high and the k values are extremely low. Although the mineral sample was of relatively high purity, it is likely that the defects in the structure of the sample or mechanical polishing of the surface may have affected the measured values of Δ and Ψ which were used to calculate these optical constants. For pyrite, the experimental and calculated values of Δ and Ψ were in good agreement for the two solutions to the complex refractive index; however there is a significant difference in the magnitudes of the real and imaginary part of the refractive index. Without knowing a rough estimate of the optical constants at 632.8 nm wavelength incident radiation it is difficult to decide whether or not any of the calculated values are reasonable.

Further complications in modelling the formation of corrosion products may arise if the optical properties of the corrosion product compound differ from those of the mineral form[10]. SEM images of the corroded steel discs show that coherent corrosion product films do not form within the timescale of the experiments. The iron oxide or hydroxide corrosion products formed under aerated conditions also showed the presence of other elements, possibly originating from the brine solution. Such inclusions could change the optical properties of the corrosion product. The corrosion products are deposited in patches and the size and coverage of the deposits increases with time. The size of the increasing size of the corrosion product deposits could also alter their optical properties. Iron oxide particles, which are used in pigments, are known to have varying optical properties depending upon the size and shape of the particles[11]. The complex refractive index of the deposits of corrosion product formed in aerated brine may also alter in a similar fashion as they increase in size.

The changes in the Δ and Ψ values with time for steel discs immersed in brine solutions cannot be fully understood unless we know the exact optical properties of the steel before it has begun to corrode. In section 4.2 we assumed that the steel surface was a single infinite layer with a complex refractive index, $\tilde{N}_{steel}$ and that C12BDMAC adsorbs from aqueous solution to form a film with uniform thickness and refractive index. This model appears adequate for modelling the adsorption of C12BDMAC under conditions where the optical properties of the steel surface do not change over the course of adsorption. However, we know that this model for the steel surface is not a

Figure 4.26. Models for 1018 steel possessing a layer of oxide film immersed in brine solution.

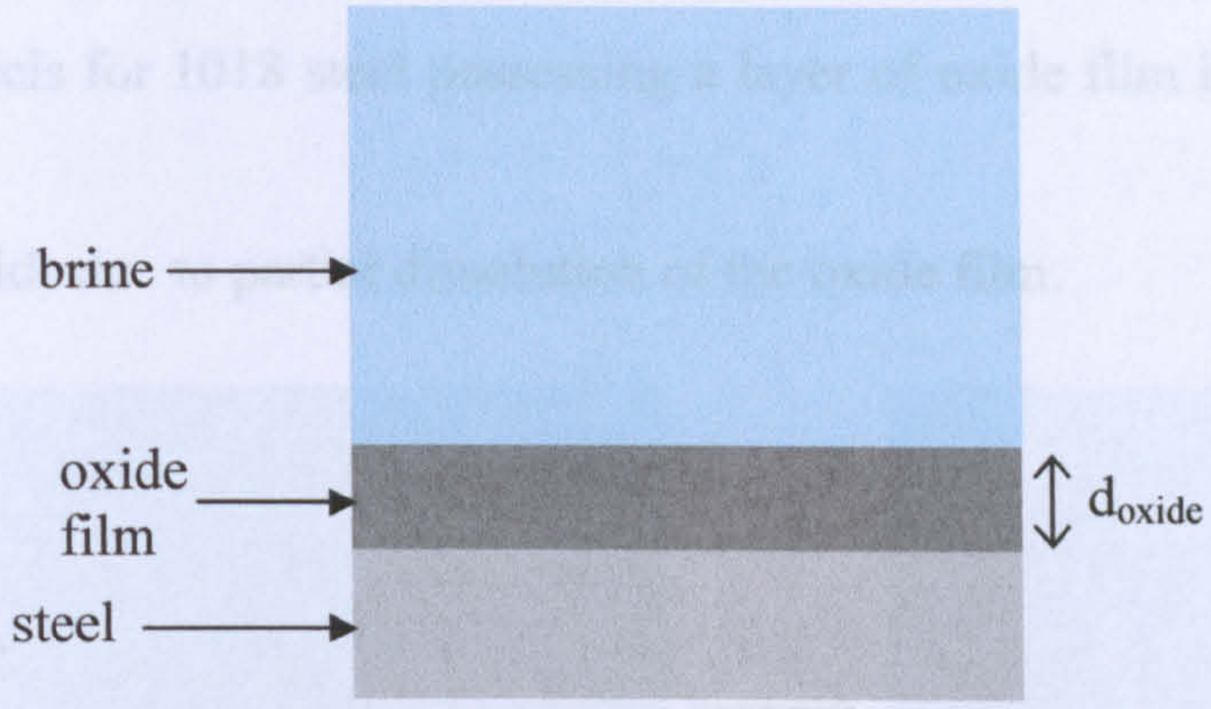

true representation of the structure and optical properties of 1018 steel. The steel has a native oxide layer, composed of Fe_2O_3 and Fe_3O_4[10], on top of the bulk steel (Figure 4.26). The complex refractive indices of the oxide layer ($\tilde{N}_{oxide}$) and the bulk steel ($\tilde{N}_{steel}$) and the thickness of the oxide layer (d_{oxide}) are unknown. It would be unwise to use the McCrackin method to calculate $\tilde{N}_{oxide}$, $\tilde{N}_{steel}$ and d_{oxide} simultaneously, since we would be trying to fit five unknown variables using only two experimental values, Δ and Ψ. Further experiments could be used to gain more information about the optical properties of the oxide film and the bulk steel. The oxide film-free values of Δ and Ψ could be measured for a steel disc which has been chemically etched in order to determine $\tilde{N}_{steel}$. Etchants such as Nital solution (2 % NHO_3 in ethanol) can completely remove the surface oxide film from carbon steel to reveal the underlying ferritic-pearlitic structure[12]. $\tilde{N}_{oxide}$ and d_{oxide} could be determined subsequently for a steel disc possessing its native oxide film.

The SEM images of steel corroded in aerated and carbonated brine solutions show that dissolution of the oxide film begins immediately upon exposure to each brine solution. The images also show that the dissolution of the oxide film occurs in localised patches. An accurate model for uncorroded steel must include the thickness and complex refractive index of the oxide film. Localised dissolution of the oxide film will create voids which are occupied by the aqueous medium (Figure 4.27a). The laser beam reflecting from the surface probes an area of approximately 2 mm^2 and the voids created by dissolution of patches of the oxide have an area of approximately 100 μm^2. The area probed by the laser beam can be assumed to be covered with a discrete layer of uniform thickness and homogeneous optical properties (Figure 4.27b). The effective refractive index of this layer ($\tilde{N}_{oxide + brine}$) will lie somewhere between that of the oxide film and

the medium, depending on the fraction of the oxide film which has been removed from the surface. $\tilde{N}_{oxide + brine}$ can be calculated using an effective medium approximation

Figure 4.27. Models for 1018 steel possessing a layer of oxide film immersed in brine solution.

(a) Creation of voids due to partial dissolution of the oxide film.

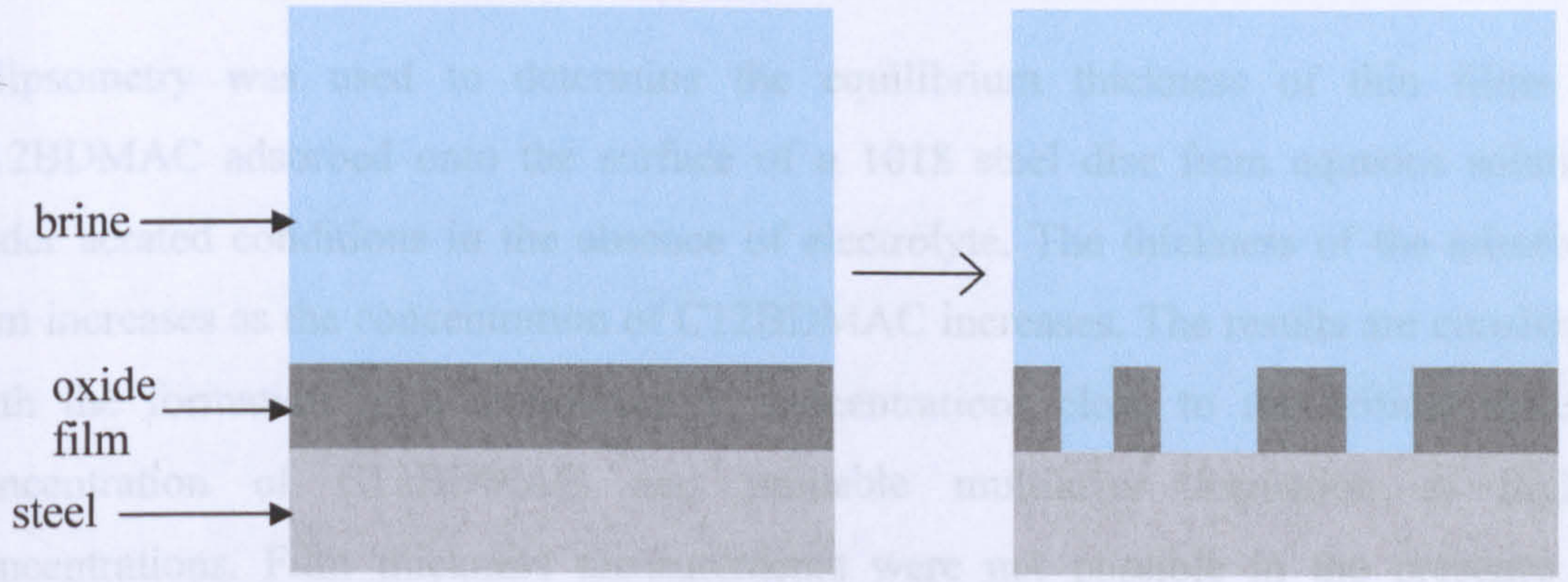

(b) Equivalent model with an effective surface film composed of oxide and the brine medium.

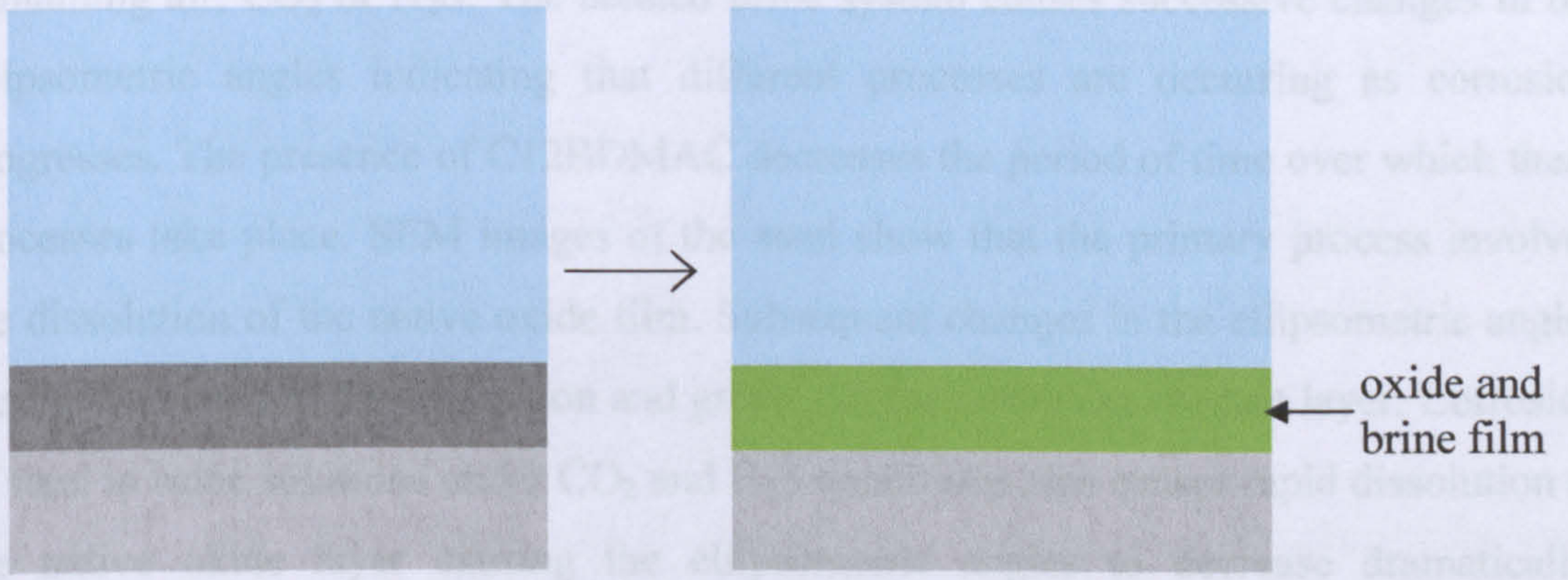

if the complex refractive indices of the oxide film and the medium are known. Since we do not know the complex refractive indices of the oxide film or the underlying steel and we do not know the exact thickness of the oxide film at the start of each measurement it is virtually impossible to accurately model the initial dissolution of the steel.

Other studies investigating the breakdown and growth of oxide films on iron specimens using ellipsometry[13] suggest that quantitative characterization of the thickness and optical properties of surface oxide films is problematic, due to the likelihood of continually varying optical properties of the film and medium. A more recent surface enhanced Raman spectroscopy study[14] proposes a bilayer passive film

consisting of an inner layer of Fe_3O_4 covered by an outer layer containing Fe_2O_3 and other Fe (III) species. Given that steel is an alloy of iron, the presence of other elements (such as carbon) may significantly alter the structure and composition of the passive film.

4.4 Conclusions

Ellipsometry was used to determine the equilibrium thickness of thin films of C12BDMAC adsorbed onto the surface of a 1018 steel disc from aqueous solution under aerated conditions in the absence of electrolyte. The thickness of the adsorbed film increases as the concentration of C12BDMAC increases. The results are consistent with the formation of a monolayer at concentrations close to the critical micelle concentration of C12BDMAC and probable multilayer formation at higher concentrations. Film thickness measurements were not possible in the presence of electrolyte and dissolved gases such as CO_2 due to rapid corrosion of the steel substrate.

Dynamic ellipsometric measurements show that the optical properties of the steel surface begin to change immediately upon immersion into brine solutions containing air, CO_2 or H_2S. The aerated brine system causes successive changes in the ellipsometric angles indicating that different processes are occurring as corrosion progresses. The presence of C12BDMAC decreases the period of time over which these processes take place. SEM images of the steel show that the primary process involves the dissolution of the native oxide film. Subsequent changes in the ellipsometric angles are likely related to the deposition and growth of the corrosion product layer. Corrosion of steel in brine solutions under CO_2 and H_2S conditions also causes rapid dissolution of the native oxide layer causing the ellipsometric angles to decrease dramatically. Addition of C12BDMAC virtually suppresses the changes in the optical properties of the steel surface. SEM images of steel surfaces corroded under CO_2 conditions show significantly less dissolution of the oxide film after corrosion in the presence of C12BDMAC.

Quantitative information about the corrosion processes and adsorption of the corrosion inhibitor on to the steel surface are extremely difficult to obtain using the current technique. We have not been able to determine the exact composition and the variation in thickness of the corrosion product layers which form under different dissolved gas conditions. SEM images show that in all cases the corrosion products formed in localised areas rather than coherent surface films. The modelling procedure is

complicated further by lack of reliable optical data for 1018 steel and iron compounds found in corrosion products. The optical properties and structure of the steel and the native oxide film must be known in order to model the structure of the initial dissolution of the steel surface. In addition, characterisation of the precise composition of the corrosion products and their optical properties must be obtained to allow further interpretation of the dynamic ellipsometry data.

4.5 References

1. F.L. McCrackin, *Natl. Bur. Stand. (U.S.) Tech Note*, 479 (1969).
2. S. Manne and H.E. Gaub, *Science*, **270**, 1480 (1995).
3. R. Atkin, V.S.J. Craig, E.J. Wanless and S. Biggs, *Adv. Colloid Interface Sci.*, **103**, 219 (2003).
4. P.C.S. Hayfield, *Surf. Sci.*, **56**, 488 (1976).
5. *Certificate of Compliance for Material: Mild Steel C1018, Specification AISI / SAE C1018*, European Corrosion Supplies Ltd., Kidderminster, UK.
6. J.A. Bearden, *Rev. Mod. Phys.*, **39**, 86 (1967).
7. D.A. Jones, *Corrosion, 2nd edition*, Prentice-Hall, New Jersey (1996).
8. K. Videm and J. Kvarekvel, *Proceedings of NACE Corrosion/96*, Paper No.12, NACE International, Houston (1996).
9. D. Abayarathna, A. Naraghi and N. Obeyesekere, *Proceedings of NACE Corrosion/2003*, Paper No.03340, NACE International, Houston (2003).
10. C.L. McBee and J. Kruger, *Surf. Sci.*, **16**, 340 (1969).
11. V. Buttignol, *J. Paint Technol.*, **40**, 480 (1968).
12. G.F. van der Voort, *ASM Handbook Volume 9: Metallography and Microstructures*, ASM International, Cleveland (2004).
13. J. Kruger and J.R. Ambrose, *Surf. Sci.*, **56**, 394 (1976).
14. V. Schroeder and T.M. Devine, *J. Electrochem. Soc.*, **146**, 4061 (1999).

CHAPTER 5

Phase behaviour of corrosion inhibitors in oil and water systems

5.1 Introduction

The oil to water volume ratio of produced fluids in oil pipelines varies with location, but in all cases corrosion will occur wherever water is in contact with the pipeline surface and corrosion inhibitors must be applied to reduce the corrosion rate. Parasitic consumption of corrosion inhibitors occurs due adsorption of the surfactant onto surfaces other than the steel pipe (such as dispersed solids and emulsion droplets[1]) and through partitioning to the oil phase[2]. A corrosion inhibitor will be most effective if all the surfactant remains in the water phase, where corrosion is most rapid. However, it is not uncommon for water-soluble soluble surfactants to partition almost exclusively to oil phases, given favourable conditions such as temperature and electrolyte concentration. Due to the lack of recognition of corrosion inhibitors as classical surfactants, their phase behaviour in oil-water systems is one aspect of the field which has not been studied extensively. This chapter will show how common oil field variables (temperature, electrolyte concentration and oil type) and the inhibitor's molecular structure can affect the phase behaviour of corrosion inhibitors in oil-water systems.

5.2 Emulsion type and partitioning of corrosion inhibitors in mixtures of oil and water

Equilibrium partitioning studies were carried out using a series of alkyl-BDMAC surfactants (C12, C14 and C16) to determine their partition coefficient, P (equation (5.1)), in the presence and absence of electrolyte at different volume ratios of heptol and water[3]. In all cases, the surfactant was initially present in the aqueous phase. The cmc values of C12BDMAC, C14BDMAC, C16BDMAC and IA in pure water and 4.7 wt.% brine solution are given in Table 5.1. The concentration of surfactant present in each phase after equilibration was determined using the Epton titration.

$$P = \frac{[\text{surfactant}]_{oil}}{[\text{surfactant}]_{water}} \qquad (5.1)$$

Further experiments used the phenomenon of transitional emulsion phase

inversion to study the phase behaviour of aggregated corrosion inhibitors[3]. Aqueous solutions of C12BDMAC, C16BDMAC or IA containing increasing concentrations of brine mixture were emulsified with equal volumes of heptane in a batch method. In each case the concentration of surfactant was in excess of the cmc in the absence of electrolyte. The experiments were repeated using toluene, heptol and Prudhoe Bay

Table 5.1 Critical micelle concentration (cmc) values of inhibitors in aqueous solution in the absence of electrolyte and 4.7 wt.% brine solution.

Inhibitor	**cmc in the absence of electrolyte / mM**	**cmc in 4.7 wt.% brine solution / mM**
C12BDMAC	5	0.1
C14BDMAC	1.25	0.03
C16BDMAC	0.3	0.005
IA	50	0.005

crude oil. Conductivity measurements and drop-tests were performed to characterise the type of emulsion produced. Since water continuous emulsions are generally of high electrical conductivity and oil continuous emulsions are of low conductivity, phase inversion of an emulsion system from o/w to w/o is signified by an abrupt decrease in conductivity. The type of emulsion formed is generally the same as the equilibrium microemulsion type[4,5]. At surfactant concentrations in excess of the cmc, emulsion phase inversion will occur at an electrolyte concentration close to that seen in the equilibrium microemulsion system. For ionic surfactants the continuous phase of the emulsion tends to be the phase containing the greatest amount of surfactant, whether it is in its monomeric or aggregated form, in agreement with Bancroft's rule[6,7]. However, with non-ionic surfactants at low concentrations, the continuous phase is not necessarily the phase containing the greatest surfactant concentration[8].

5.2.1 Dodecylbenzyldimethylammonium chloride (C12BDMAC)

Equilibrium partitioning experiments were carried out at 1:1 and 10:1 heptol to water volume ratios in the presence and absence of 4.7 wt.% brine mixture at 25 °C. Tables 5.2 - 5.5 show the concentration of C12BDMAC in the aqueous phase before and after equilibration with heptol. When the surfactant remains in the aqueous phase after equilibration with oil the percentage error in the equilibrium surfactant concentration,

which is the relative error multiplied by one hundred, was calculated using equation (5.2).

$$\text{Error} = \left(\frac{[\text{surfactant}]_{\text{water(initial)}}}{[\text{surfactant}]_{\text{water(equilibrium)}}} - 1 \right) * 100 \qquad (5.2)$$

These results indicate that virtually all of the surfactant, which is initially present in the aqueous phase, remains in the aqueous phase after equilibration with heptol. Surfactant concentrations determined using the Epton titration have an error of approximately 2 %, therefore we can only establish that the partition coefficient of the surfactant has a value less than 0.02 at 1:1 heptol to water volume ratio and 0.002 at 10:1 volume ratio. At concentrations greater than the cmc, the C12BDMAC will aggregate into micelles which remain in the aqueous phase.

Table 5.2. Initial and equilibrium concentrations of C12BDMAC in aqueous phases for 1:1 heptol/water volume ratio in the absence of electrolyte at 25 °C.

$[\text{C12BDMAC}]_{\text{water}}$ (initial) / mM	$[\text{C12BDMAC}]_{\text{water}}$ (equilibrium) / mM	Error / %
0.0106	0.011	3.6
0.1020	0.103	0.9
1.0340	1.041	0.7
10.0200	10.043	0.2

Table 5.3. Initial and equilibrium concentrations of C12BDMAC in aqueous phases for 1:1 heptol/water volume ratio in the presence of electrolyte (4.7 wt.% brine) at 25 °C.

$[\text{C12BDMAC}]_{\text{water}}$ (initial) / mM	$[\text{C12BDMAC}]_{\text{water}}$ (equilibrium) / mM	Error / %
0.0108	0.011	1.8
0.1060	0.107	0.9
1.0500	1.059	0.8
10.0800	10.104	0.2

Table 5.4. Initial and equilibrium concentrations of C12BDMAC in aqueous phases for 10:1 heptol/water volume ratio in the absence of electrolyte at 25 °C.

$[C12BDMAC]_{water}$ (initial) / mM	$[C12BDMAC]_{water}$ (equilibrium) / mM	Error / %
0.0102	0.010	2.0
0.1140	0.116	1.7
1.0260	1.020	0.6
10.0400	10.060	0.2

Table 5.5. Initial and equilibrium concentrations of C12BDMAC in aqueous phases for 10:1 heptol/water volume ratio in the presence of electrolyte (4.7 wt.% brine) at 25 °C.

$[C12BDMAC]_{water}$ (initial) / mM	$[C12BDMAC]_{water}$ (equilibrium) / mM	Error / %
0.0112	0.011	1.8
0.1140	0.116	1.7
1.0460	1.050	0.4
10.2000	10.160	0.4

Figure 5.1 shows the conductivity of emulsions prepared from equal volumes of 10 mM aqueous C12BDMAC and four different oil phases as a function of aqueous phase electrolyte concentration. All emulsions containing C12BDMAC were of high conductivity suggesting o/w emulsions had been produced. Drop tests confirmed that all emulsions were water continuous. Therefore, the corresponding equilibrium two phase systems are also water continuous at all electrolyte concentrations within this range, with all aggregated surfactant present in the aqueous phase as dry micelles. Figure 5.2 shows the appearance of emulsions prepared using crude oil after 24 hr. Emulsions with aqueous phase brine concentrations between 0.1 and 1 wt.% phase separate, however, the aqueous phases remain opaque. At 3 wt.% brine the emulsion phase separates; the aqueous phase is slightly turbid and light brown coloured. Emulsions with aqueous phase brine concentrations between 5 and 10 wt.% rapidly phase separate. The lower aqueous phases are clear and colourless.

Figure 5.1. Conductivity vs [brine] for emulsions produced from 10 mM aqueous C12BDMAC and different oils (1:1 volume ratio) after homogenisation for 2 min. at 13000 rpm.

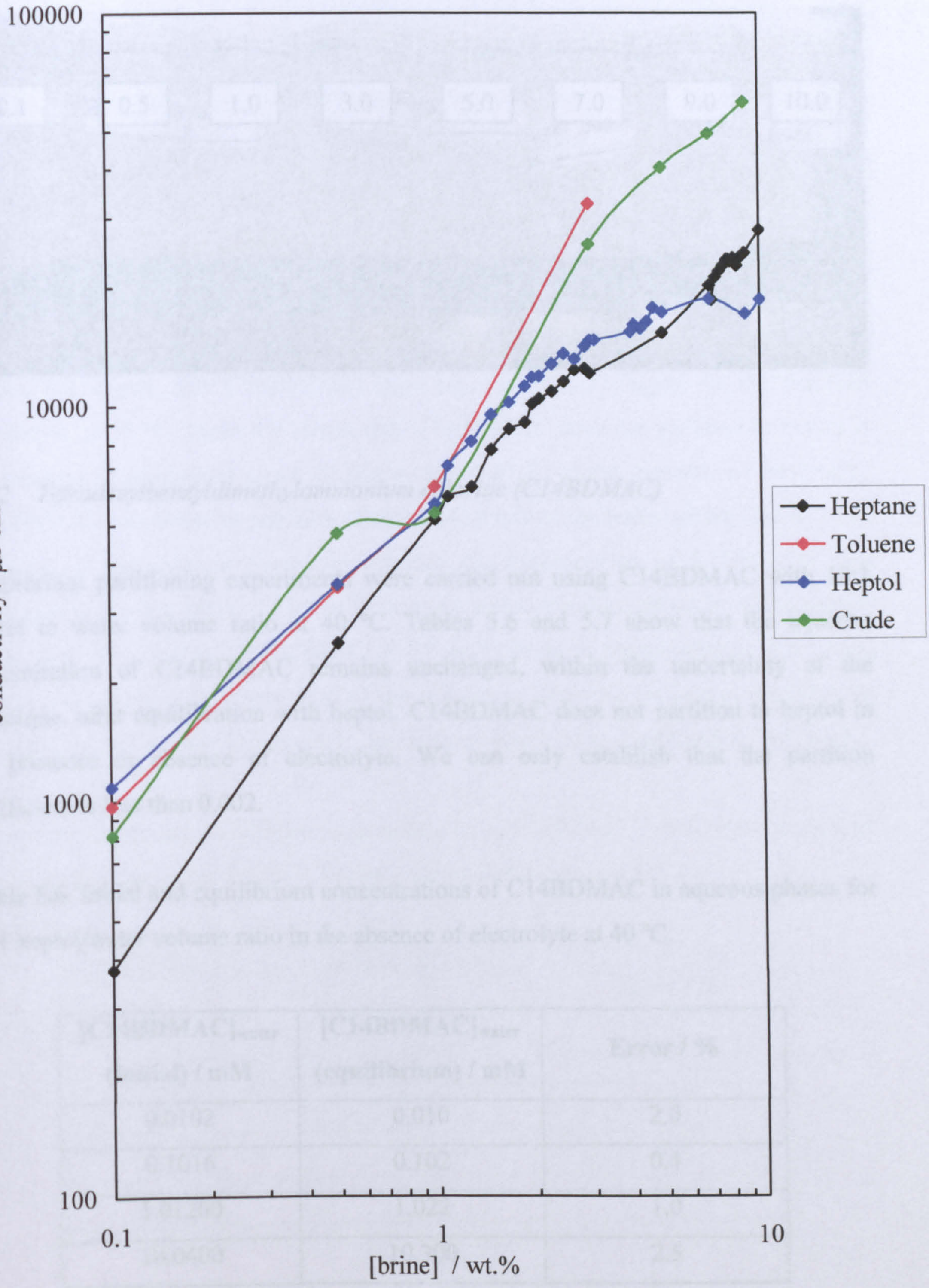

Figure 5.2. Appearance of emulsions produced from equal volumes of 10 mM aqueous C12BDMAC solutions and Prudhoe Bay crude oil after 24 hr. at 25 °C. Labels indicate the initial concentration of electrolyte (wt.%) in the aqueous phase. Drop tests confirmed that all emulsions were water continuous.

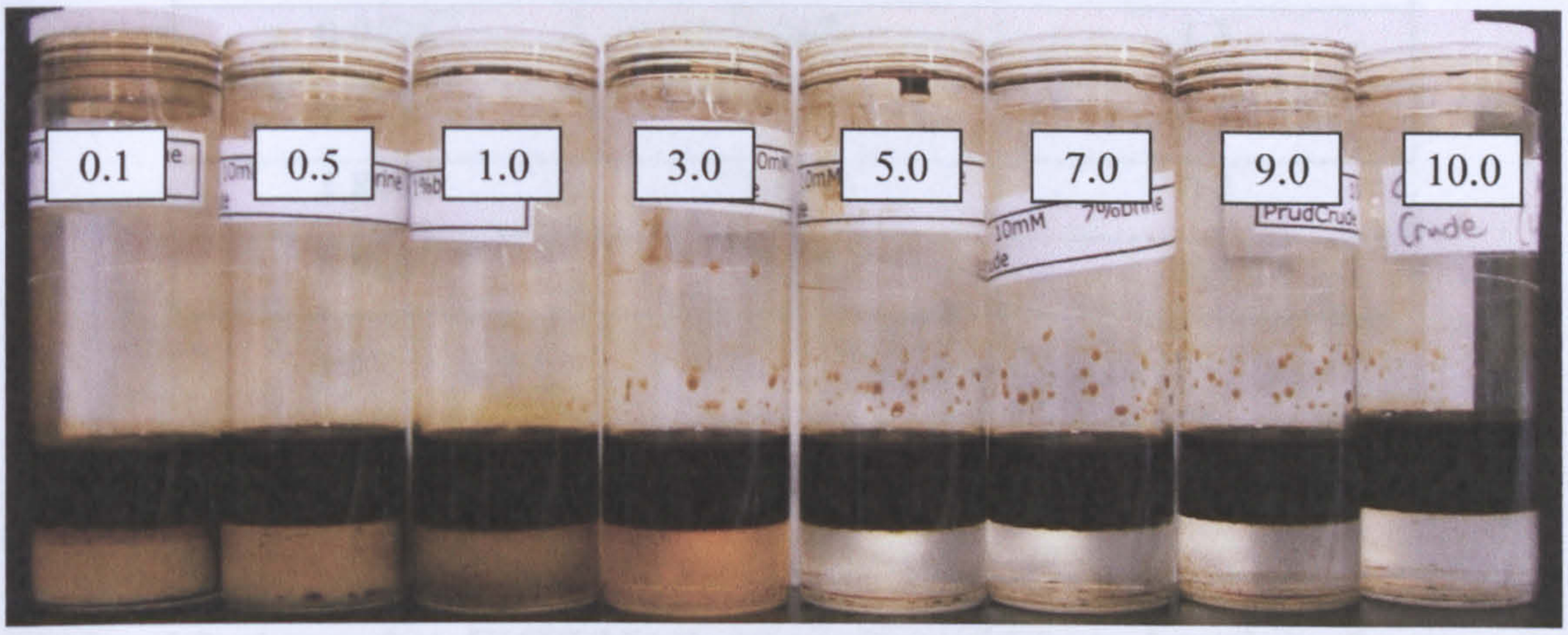

5.2.2 Tetradecylbenzyldimethylammonium chloride (C14BDMAC)

Equilibrium partitioning experiments were carried out using C14BDMAC with 10:1 heptol to water volume ratio at 40 °C. Tables 5.6 and 5.7 show that the aqueous concentration of C14BDMAC remains unchanged, within the uncertainty of the technique, after equilibration with heptol. C14BDMAC does not partition to heptol in the presence or absence of electrolyte. We can only establish that the partition coefficient is less than 0.002.

Table 5.6. Initial and equilibrium concentrations of C14BDMAC in aqueous phases for 10:1 heptol/water volume ratio in the absence of electrolyte at 40 °C.

$[C14BDMAC]_{water}$ (initial) / mM	$[C14BDMAC]_{water}$ (equilibrium) / mM	Error / %
0.0102	0.010	2.0
0.1016	0.102	0.4
1.01200	1.022	1.0
10.0400	10.300	2.5

Table 5.7. Initial and equilibrium concentrations of C12BDMAC in aqueous phases for 10:1 heptol/water volume ratio in the presence of electrolyte (4.7 wt.% brine) at 40 °C.

$[C14BDMAC]_{water}$ (initial) / mM	$[C14BDMAC]_{water}$ (equilibrium) / mM	Error / %
0.0476	0.047	1.3
0.1320	0.134	1.5
1.8420	1.838	0.2
8.9800	9.020	0.4

5.2.3 Hexadecylbenzyldimethylammonium chloride (C16BDMAC)

Tables 5.8 shows that C16BDMAC does not partition to heptol in the presence electrolyte at 25 °C. Table 5.9 shows that C16BDMAC does not partition to heptol in the absence of electrolyte at 40 °C. However, at 40 °C in the presence of electrolyte, C16BDMAC was found to partition almost exclusively to the heptol phase (Table 5.10). Analysis of the aqueous phase showed that the concentration of C16BDMAC had decreased to a value below the lower limit of the Epton titration, which is approximately 0.008 mM. The cmc of C16BDMAC in 4.7 wt.% brine is approximately 0.005 mM, which is also below the lower limit of the technique; therefore we cannot establish the concentration of monomer present in the aqueous phase after equilibration with heptol.

Table 5.8. Initial and equilibrium concentrations of C16BDMAC in aqueous phases for 10:1 heptol/water volume ratio in the absence of electrolyte at 40 °C.

$[C16BDMAC]_{water}$ (initial) / mM	$[C16BDMAC]_{water}$ (equilibrium) / mM	Error / %
0.0104	0.010	2.0
0.1080	0.110	1.8
1.0660	1.070	0.4
10.0400	10.080	0.4

Table 5.9. Equilibrium concentrations of C16BDMAC in aqueous phases and heptol phases for 10:1 heptol/water volume ratio in the presence of electrolyte (4.7 wt.% brine) at 25 °C.

$[C16BDMAC]_{water}$ (initial) / mM	**$[C16BDMAC]_{water}$ (equilibrium) / mM**	**Error / %**
0.00968	0.00962	0.6
0.1110	0.114	2.4
1.0380	1.048	1.0
9.990	10.010	0.2

Table 5.10. Equilibrium concentrations of C16BDMAC in aqueous phases and heptol phases for 10:1 heptol/water volume ratio in the presence of electrolyte (4.7 wt.% brine) at 40 °C.

$[C16BDMAC]_{water}$ (initial) / mM	**$[C16BDMAC]_{water}$ (equilibrium) / mM**	**$[C16BDMAC]_{heptol}$ (equilibrium) / mM**
0.0098	< 0.01	< 0.01
0.9970	< 0.01	0.01
1.0130	< 0.01	0.10
10.4400	< 0.01	1.05

At concentrations in excess of the cmc, C16BDMAC will form micelles which partition to the heptol phase. The micelles can solubilise water into their cores, which leads to formation of a w/o (Winsor II) microemulsion phase.

In the presence of 10 mM C16BDMAC, all emulsions containing heptane or heptol were of high conductivity indicating the formation of o/w emulsions (Figure 5.3). Oil continuous emulsions were produced using toluene or crude oil as the hydrocarbon phase when the concentration of electrolyte in the aqueous phase was greater than 1 wt.%. The abrupt decrease in the conductivity of the emulsions signifies the phase inversion point, which was confirmed using the drop test. Figure 5.4 shows the appearance of the emulsions containing crude oil after 24 hr.

Figure 5.3. Conductivity vs [brine] for emulsions produced from 10 mM aqueous C16BDMAC and different oils (1:1 volume ratio) after homogenisation for 2 min. at 13000 rpm. Vertical lines show phase inversion points which were confirmed by drop tests.

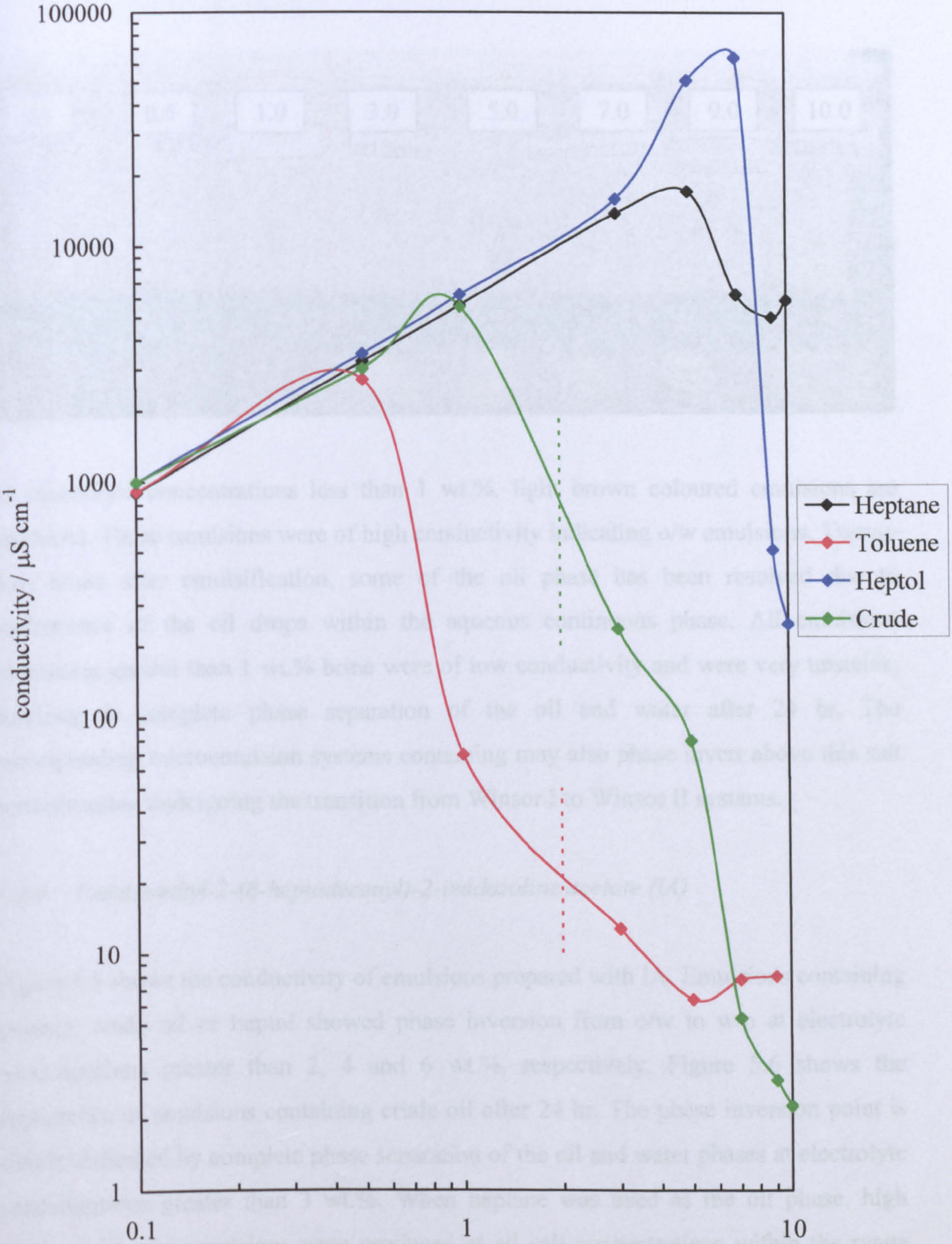

Figure 5.4. Appearance of emulsions produced from equal volumes of 10 mM aqueous C16BDMAC solutions and Prudhoe Bay crude oil after 24 hr. at 40 °C. Labels indicate the initial concentration of electrolyte (wt.%) in the aqueous phase. Red vertical line indicates the transition from o/w (high conductivity) to w/o (low conductivity) emulsions, which was confirmed using the drop test.

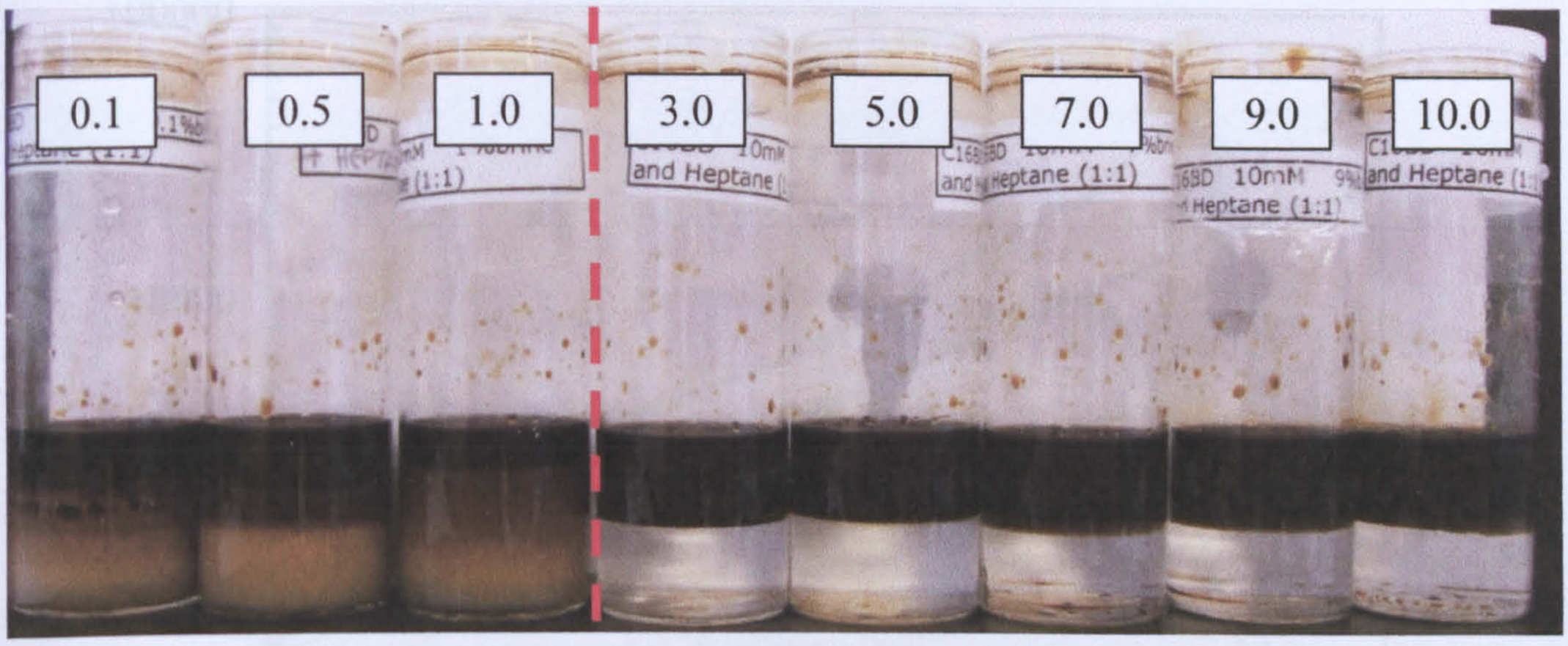

At electrolyte concentrations less than 1 wt.%, light brown coloured emulsions are produced. These emulsions were of high conductivity indicating o/w emulsions. Twenty four hours after emulsification, some of the oil phase has been resolved due to coalescence of the oil drops within the aqueous continuous phase. All emulsions containing greater than 1 wt.% brine were of low conductivity and were very unstable, resulting in complete phase separation of the oil and water after 24 hr. The corresponding microemulsion systems containing may also phase invert above this salt concentration, undergoing the transition from Winsor I to Winsor II systems.

5.2.4 1-aminoethyl-2-(8-heptadecenyl)-2-imidazoline acetate (IA)

Figure 5.5 shows the conductivity of emulsions prepared with IA. Emulsions containing toluene, crude oil or heptol showed phase inversion from o/w to w/o at electrolyte concentrations greater than 2, 4 and 6 wt.%, respectively. Figure 5.6 shows the appearance of emulsions containing crude oil after 24 hr. The phase inversion point is clearly indicated by complete phase separation of the oil and water phases at electrolyte concentrations greater than 3 wt.%. When heptane was used as the oil phase, high conductivity o/w emulsions were produced at all salt concentrations within the range tested, indicating that phase inversion of the microemulsion system does not occur.

Figure 5.5. Conductivity vs [brine] for emulsions produced from 100 mM aqueous IA and different oils (1:1 volume ratio) after homogenisation for 2 min. at 13000 rpm. Vertical lines show phase inversion points which were confirmed by drop tests.

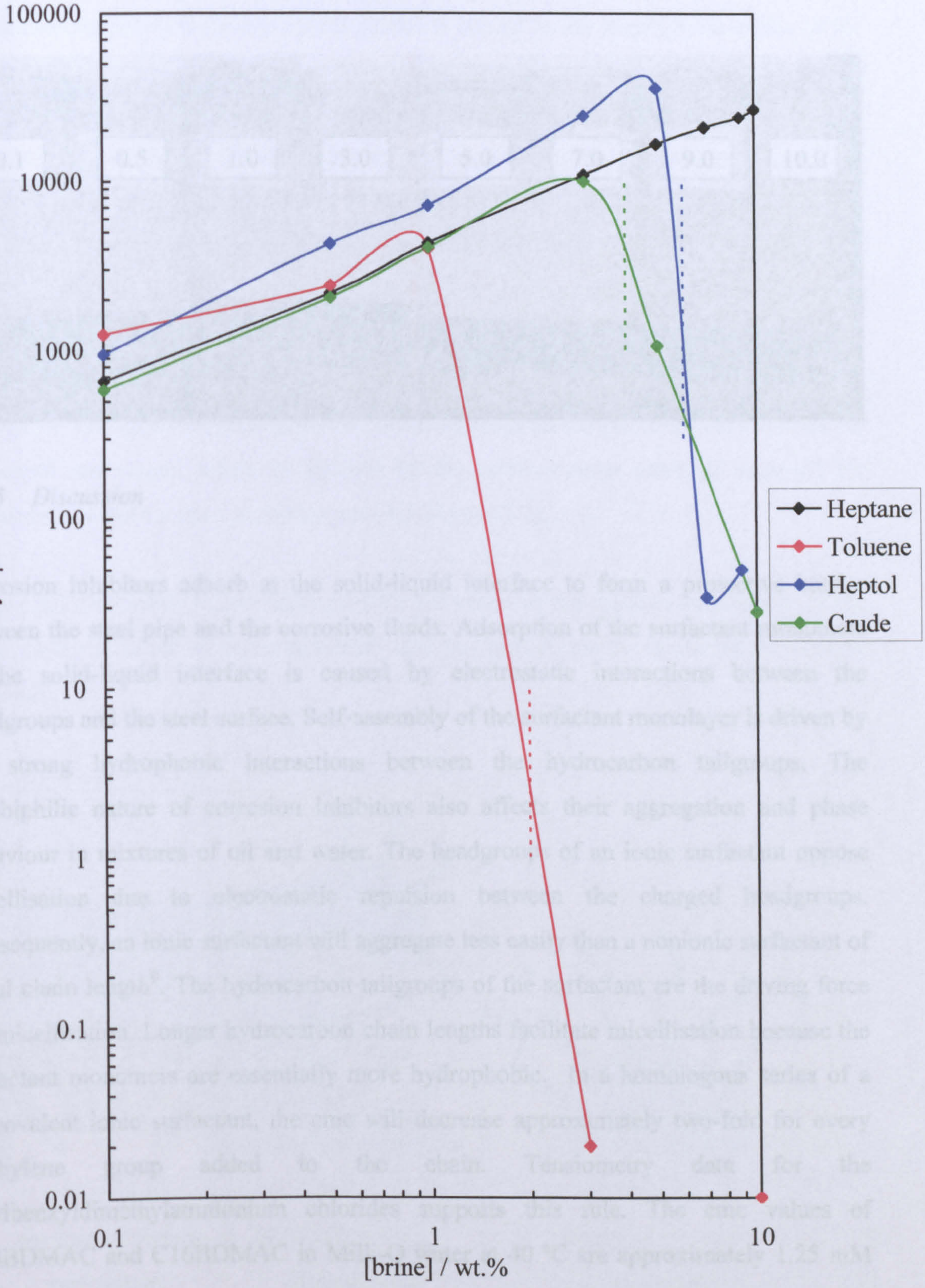

Figure 5.6. Appearance of emulsions produced from equal volumes of 100 mM aqueous IA solutions and Prudhoe Bay crude oil after 24 hr. at 25 °C. Labels indicate the initial concentration of electrolyte (wt.%) in the aqueous phase. Red vertical line indicates the transition from o/w to w/o emulsions. Red vertical line indicates the transition from o/w (high conductivity) to w/o (low conductivity) emulsions, which was confirmed using the drop test.

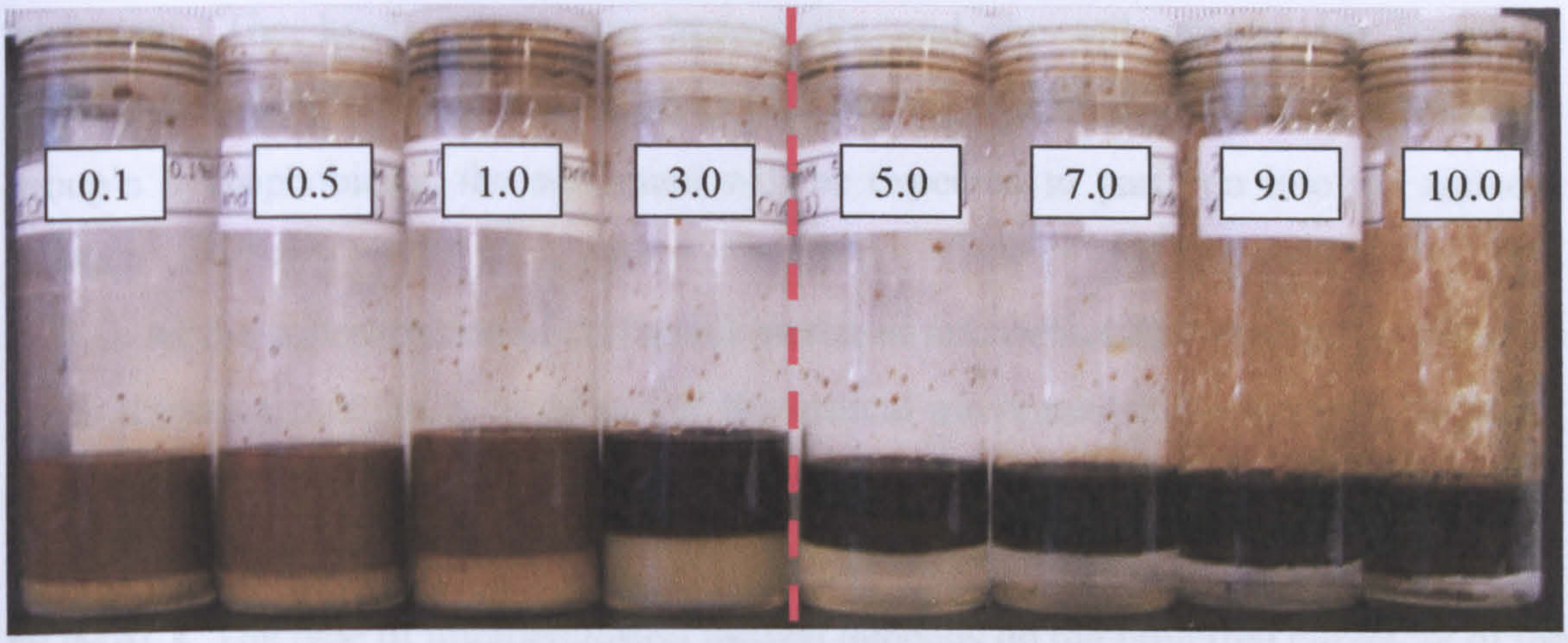

5.2.5 Discussion

Corrosion inhibitors adsorb at the solid-liquid interface to form a protective barrier between the steel pipe and the corrosive fluids. Adsorption of the surfactant monomers at the solid-liquid interface is caused by electrostatic interactions between the headgroups and the steel surface. Self-assembly of the surfactant monolayer is driven by the strong hydrophobic interactions between the hydrocarbon tailgroups. The amphiphilic nature of corrosion inhibitors also affects their aggregation and phase behaviour in mixtures of oil and water. The headgroups of an ionic surfactant oppose micellisation due to electrostatic repulsion between the charged headgroups. Consequently, an ionic surfactant will aggregate less easily than a nonionic surfactant of equal chain length[9]. The hydrocarbon tailgroups of the surfactant are the driving force for micellisation. Longer hydrocarbon chain lengths facilitate micellisation because the surfactant monomers are essentially more hydrophobic. In a homologous series of a monovalent ionic surfactant, the cmc will decrease approximately two-fold for every methylene group added to the chain. Tensiometry data for the alkylbenzyldimethylammonium chlorides supports this rule. The cmc values of C14BDMAC and C16BDMAC in Milli-Q water at 40 °C are approximately 1.25 mM

and 0.3 mM, respectively. The alkylbenzyldimethylammonium chlorides have lower cmc values than their analogous alkyltrimethylammonium chlorides[10]. The benzyl group is believed to act as a second hydrophobic substituent.

When a low concentration of surfactant is added to equal volumes of oil and water the surfactant will be present only as monomers and these may distribute themselves between the two phases and also adsorb at the oil-water interface. The extent of partitioning between the two liquid phases is related to the amphiphilic nature of the surfactant. The head groups are hydrophilic and the tail groups are lipophilic (hydrophobic). When the relative hydrophilicity of the head group exceeds the tail group's hydrophobicity, the surfactant will be expected to partition into the aqueous phase.

As the concentration of surfactant increases microemulsion aggregates will form when the concentration is in excess of the critical microemulsion concentration (cμc). The cμc in the aqueous phase is approximately equal to the cmc in the absence of oil. The cμc in the oil phase will be very low for ionic surfactants such as the alkyl-BDMACs. The type of microemulsion formed depends on the preferred curvature of the surfactant monolayer, which is dictated by the relative cross sectional areas of the surfactant headgroup (A_h) and tailgroup (A_t) (Figure 5.7).

Figure 5.7 Schematic representation of the influence of the relative magnitudes of the cross sectional areas of surfactant head and tail groups on the preferred monolayer curvature.

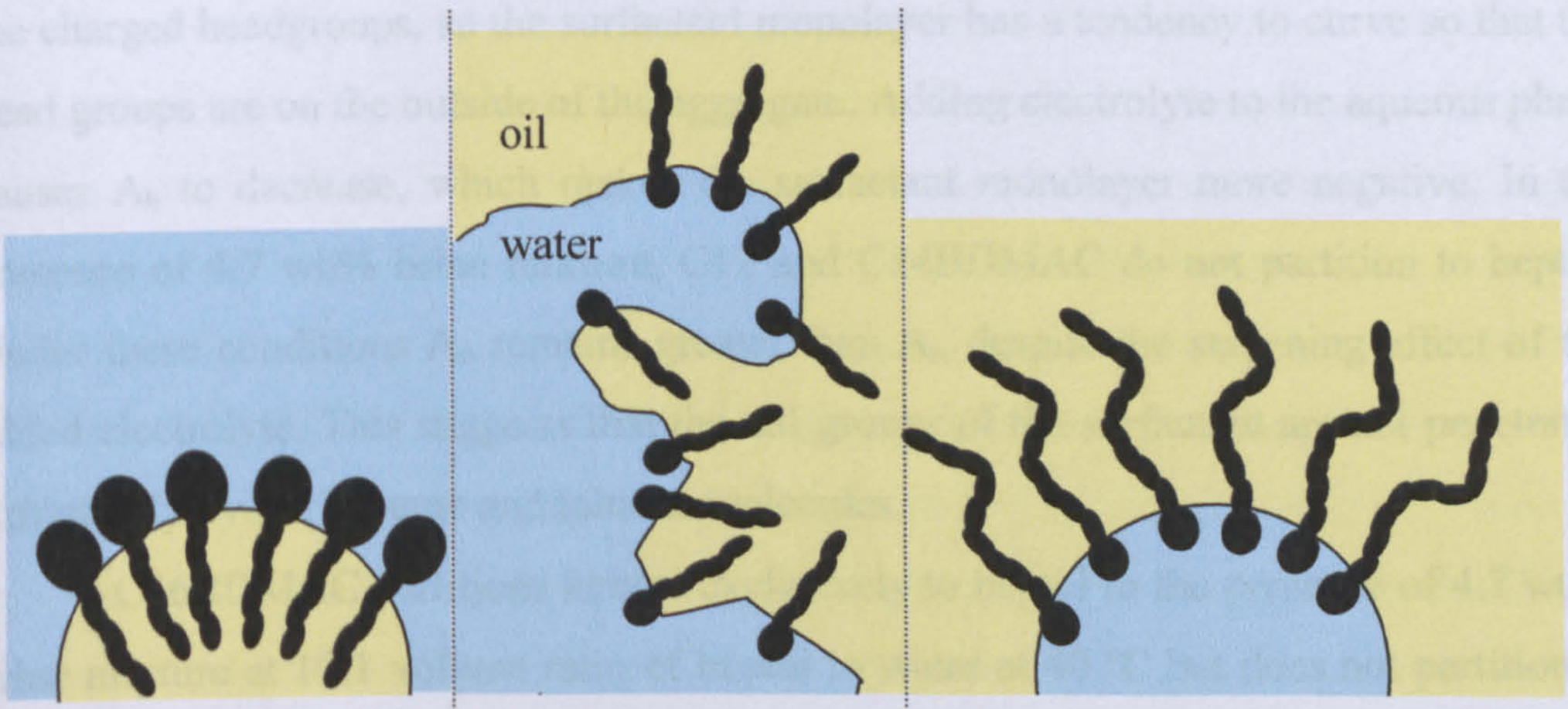

Larger headgroups will promote more positive curvature, whereas longer or branched hydrocarbon tailgroups promote more negative curvature. However, the preferred curvature is not determined solely by the chemical structure of the surfactant[11]. Microemulsion systems can phase invert due to changes in conditions of temperature, salt concentration and oil type. These variables affect the effective geometry of the surfactant molecules in the curved monolayer, which leads to changes in the preferred curvature of the surfactant monolayer.

The charged headgroups of an ionic surfactant will oppose micellisation in aqueous solution. Addition of electrolyte to an aqueous ionic surfactant solution screens the electrostatic repulsion between neighbouring headgroups, which decreases the effective area of the headgroup. This promotes micellisation and leads to a reduction in the cmc. For example, the cmc of C14BDMAC is 1.25 mM in Milli-Q water at 40 °C. In the presence of 4.7 wt.% synthetic brine mixture, the cmc of the C14BDMAC decreases to 0.03 mM. Since the aqueous cμc of an ionic surfactant is approximately equal to the cmc in the absence of oil, increasing electrolyte concentration also decreases the value of the cμc in water.

The cross-sectional area of the tailgroup can be enlarged through solvation by oils. The extent of tailgroup swelling depends on the type of oil present in the system. Short chain oils generally penetrate and swell the tailgroups more than longer chain oils. In the equilibrium partitioning studies of the alkylbenzyldimethylammonium chlorides, neither the micelles nor the monomers partition to the heptol phase in the absence of added electrolyte. The aggregated form of the surfactant exists in the aqueous phase as normal micelles. Under these conditions, A_h is greater than A_t due to repulsion between the charged headgroups, so the surfactant monolayer has a tendency to curve so that the head groups are on the outside of the aggregate. Adding electrolyte to the aqueous phase causes A_h to decrease, which makes the surfactant monolayer more negative. In the presence of 4.7 wt.% brine mixture, C12 and C14BDMAC do not partition to heptol. Under these conditions A_h remains greater than A_t, despite the screening effect of the added electrolyte. This suggests that the tail groups of the surfactant are not penetrated sufficiently by the heptane and toluene molecules.

C16BDMAC partitions almost exclusively to heptol in the presence of 4.7 wt.% brine mixture at 10:1 volume ratio of heptol to water at 40 °C but does not partition at 25 °C. Although the electrolyte concentration, oil type and volume ratio of oil and water are the same, elevated temperature causes the surfactant monolayer curvature to be negative. With ionic surfactants, the degree of counter-ion binding decreases with

increasing temperature, causing A_h to increase (making the monolayer curvature more positive) due to increased repulsion between neighbouring head groups. In this case we have more negative curvature of the monolayer at high temperature which suggests that penetration of the tail groups by oil, which increases A_t, is more prevalent at higher temperatures and drives the change in monolayer curvature. Higher temperatures also induce more gauche conformations into the hydrocarbon chains resulting in coiling of the tail group which will make the curvature more negative.

The effect of the nature of the oil phase can be seen in the results of the emulsification experiments. All emulsions of equal volumes of oil and water containing C12BDMAC were o/w emulsions at all electrolyte concentrations with the range tested. The corresponding microemulsion systems may also be water continuous (Winsor I) systems. At low concentrations of salt A_h is greater than A_t due to electrostatic repulsion between the head groups. As the salt concentration increases A_h decreases. The absence of phase inversion shows that the curvature of the surfactant monolayer remains positive at higher salt concentrations despite A_h decreasing. This shows that the tail groups of C12BDMAC are not penetrated and swollen sufficiently by these oils.

The phase behaviour of C16BDMAC shows a greater dependence upon the oil type. All emulsions prepared with heptane were o/w emulsions, indicating poor penetration of the tail groups by the aliphatic hydrocarbon. Phase inversion of the emulsions was observed in systems containing either toluene or crude oil. Toluene is an aromatic hydrocarbon and crude oil is a complex mixture of aromatic and aliphatic hydrocarbons. The corresponding microemulsion systems will be expected to undergo phase inversion at electrolyte concentrations close to those of the emulsion systems. The transition from Winsor I to Winsor II systems is induced by the change in the preferred curvature of the surfactant monolayer as the electrolyte concentration increases. Swelling of the C16BDMAC tail groups by toluene or crude oil increases A_t such that it is greater than A_h at high salt concentrations. These results show that the tail groups of C16BDMAC can be penetrated more by the presence of aromatic hydrocarbons and indicates that the benzyl substituent of C16BDMAC also contributes to the effective geometry of the tail group. Emulsions prepared with heptol, which is a 7:3 volume ratio mixture of heptane and toluene, remained water continuous as the concentration of electrolyte increased. Phase inversion was not observed in emulsions containing heptane, but was observed with toluene. This suggests that the higher volume fraction of heptane in heptol prevents swelling of the surfactant tail groups, which results in positive curvature of the surfactant monolayer at low and high salt concentrations.

Heptol and crude oil are both mixtures of aliphatic and aromatic oils; however phase inversion is only seen in the crude oil system. The presence of aliphatic oil chains shorter than heptane means that crude oil will swell the hydrocarbon chain of C16BDMAC more effectively than heptane or heptol alone.

Emulsions containing the commercial product IA phase invert to w/o emulsions at high salt concentrations when the oil is toluene, heptol or crude oil. The corresponding microemulsion systems will also phase invert. Toluene and the aromatic fractions of heptol and crude oil interact with the aromatic heterocyclic ring system of the IA molecule, leading to swelling of the tail groups, such that A_t is greater than A_h at high salt concentrations, resulting in negative preferred curvature of the surfactant monolayer. Emulsions prepared with heptane are water continuous at high and low salt concentrations, indicating poor penetration of the surfactant tail groups by the aliphatic hydrocarbon.

These results show that environmental factors such as salt concentration, temperature and oil composition affect the phase behaviour of corrosion inhibitors in systems containing oil and water phases. These factors can differ greatly between oil fields. Slight differences in these factors can change the preferred phase in which the majority of the corrosion inhibitor will exist. If the corrosion inhibitor prefers the oil phase, it will not be available to act as a corrosion inhibitor in the aqueous phase, where corrosion occurs most rapidly when in contact with the steel surface.

5.3 Effect of the presence of oil on corrosion inhibition

In Chapter 3 electrochemical measurements were used to investigate whether C12BDMAC and IA act as corrosion inhibitors in aqueous environments under different oil field gas conditions. Both surfactants were found to act as corrosion inhibitors in deionised water and brine solutions under H_2S gas conditions. Results from the emulsion phase inversion experiments show that, at concentrations in excess of the cmc, the aggregated forms of C16BDMAC and IA both partition from water to toluene at high concentrations of electrolyte and that C12BDMAC does not partition from water to toluene. Partitioning of these water-soluble surfactants involves the migration of surfactant from water (where corrosion occurs most rapidly) to oil; therefore we decided to use the bubble test technique to investigate whether partitioning of corrosion inhibitor micelles to oil at high salt concentrations affects corrosion inhibition in the aqueous phase. All experiments were carried out in brine solutions containing H_2S, where

C12BDMAC, C16BDMAC and IA are expected to exhibit good corrosion inhibition. The corrosion rate of 1018 steel electrodes was measured in the relevant aqueous solution in the presence of surfactant for 24 hr. before adding an equal volume of toluene on top of the aqueous solution. The corrosion rate of the steel electrodes was measured continuously for approximately 56 hr. whilst the two phases were stirred gently. If partitioning of the corrosion inhibitor micelles to toluene drastically affects corrosion inhibition we should expect to see an increase in the corrosion of the steel with time after the addition of the oil layer.

The bubble test was used to measure the corrosion rate of 1018 steel in 10 wt.% brine solution under H_2S conditions containing 10 mM C12BDMAC with addition of an equal volume layer of toluene after 24 hr. (Figure 5.8). During the first 30 min. of the experiment the steel electrodes are allowed to corrode in the absence of surfactant; the corrosion rate is approximately 0.2 mm y^{-1}. Addition of C12BDMAC causes the corrosion rate to decrease rapidly to 0.003 mm y^{-1} which shows that the surfactant is a good corrosion inhibitor under these conditions. The corrosion rate begins to decrease after the addition of the toluene layer before reaching a plateau value of 0.0007 mm y^{-1}. Despite the high salt concentration, C12BDMAC remains in the aqueous phase throughout the experiment. Poor penetration of the inhibitor's tail group by toluene leaves A_t less than A_h, causing the curvature of the monolayer of the micelles to remain positive.

Using the emulsification method, phase inversion was observed with aqueous C16BDMAC at high salt concentrations with toluene at 40 °C. In total, four bubble test experiments were conducted using C16BDMAC in brine solutions under H_2S conditions with equal volume layers of toluene added after 24hr. Corrosion rate measurements were conducted at 25 and 40 °C with 1 and 10 wt.% brine solutions, with addition of 10 mM C16BDMAC after 30 min. of pre-corrosion. Figure 5.9 shows the corrosion rate versus time for 1018 steel in 1 wt.% brine solution under H_2S conditions at 25 °C with addition of 10 mM C16BDMAC to the aqueous phase. The corrosion rate during the pre-corrosion is 0.15 mm y^{-1} and quickly decreases to approximately 0.002 mm y^{-1} on addition of the surfactant before slowly increasing to 0.008 mm y^{-1} after 24 hr. After addition of the toluene layer the corrosion rate decreases steadily to approximately 0.0025 mm y^{-1} which shows that the presence of a layer of toluene does not adversely affect corrosion inhibition. Figure 5.10 shows the corrosion rate versus time for 1018 steel electrodes immersed in 10 wt.% brine solution under H_2S conditions at 25 °C, with addition of 10 mM C16BDMAC after 30 min. pre-corrosion. The

Figure 5.8. Corrosion rate vs time for 1018 steel in 10 wt.% brine under H_2S conditions at 25 °C. Addition of C12BDMAC after 0.5 hr. to give aqueous concentration of 10 mM and addition of equal volume layer of toluene after 24 hr.

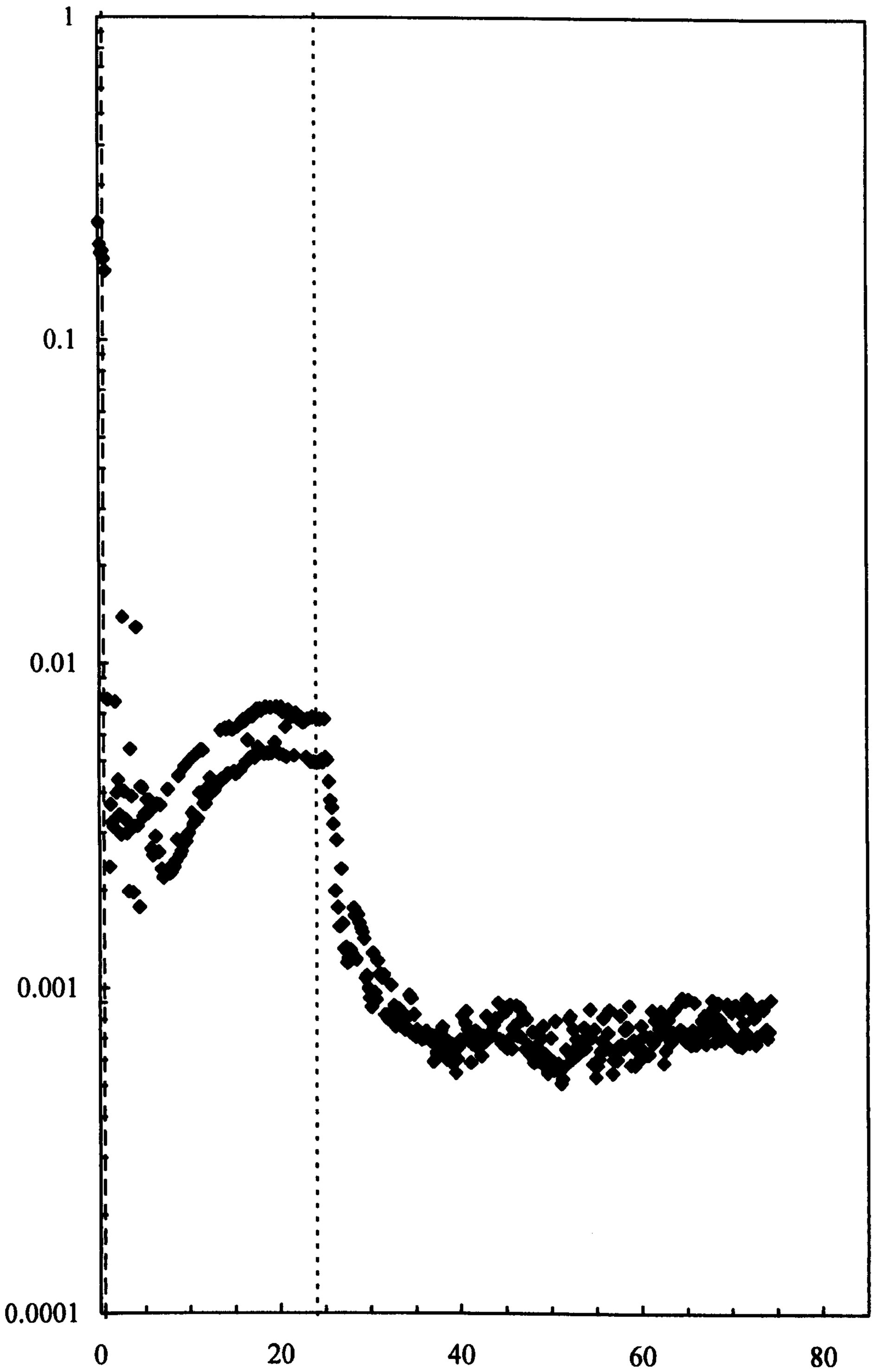

Figure 5.9. Corrosion rate vs time for 1018 steel electrodes in 1 wt.% brine under H_2S conditions at 25 °C. Addition of C16BDMAC after 0.5 hr. to give aqueous concentration of 10 mM and addition of equal volume layer of toluene after 24 hr.

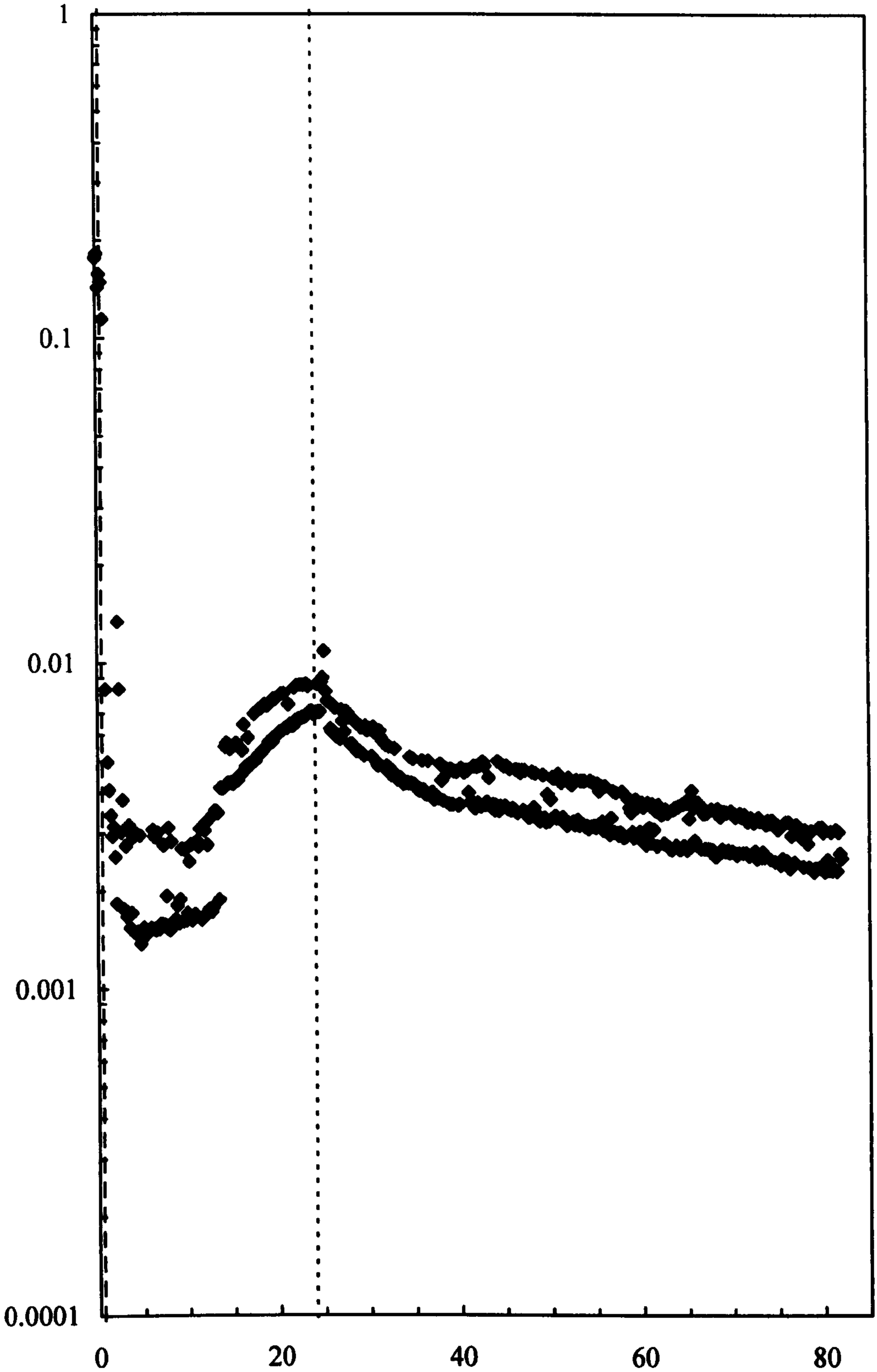

Figure 5.10. Corrosion rate vs time for 1018 steel electrodes in 10 wt.% brine under H_2S conditions at 25 °C. Addition of C16BDMAC after 0.5 hr. to give aqueous concentration of 10 mM and addition of equal volume layer of toluene after 24 hr.

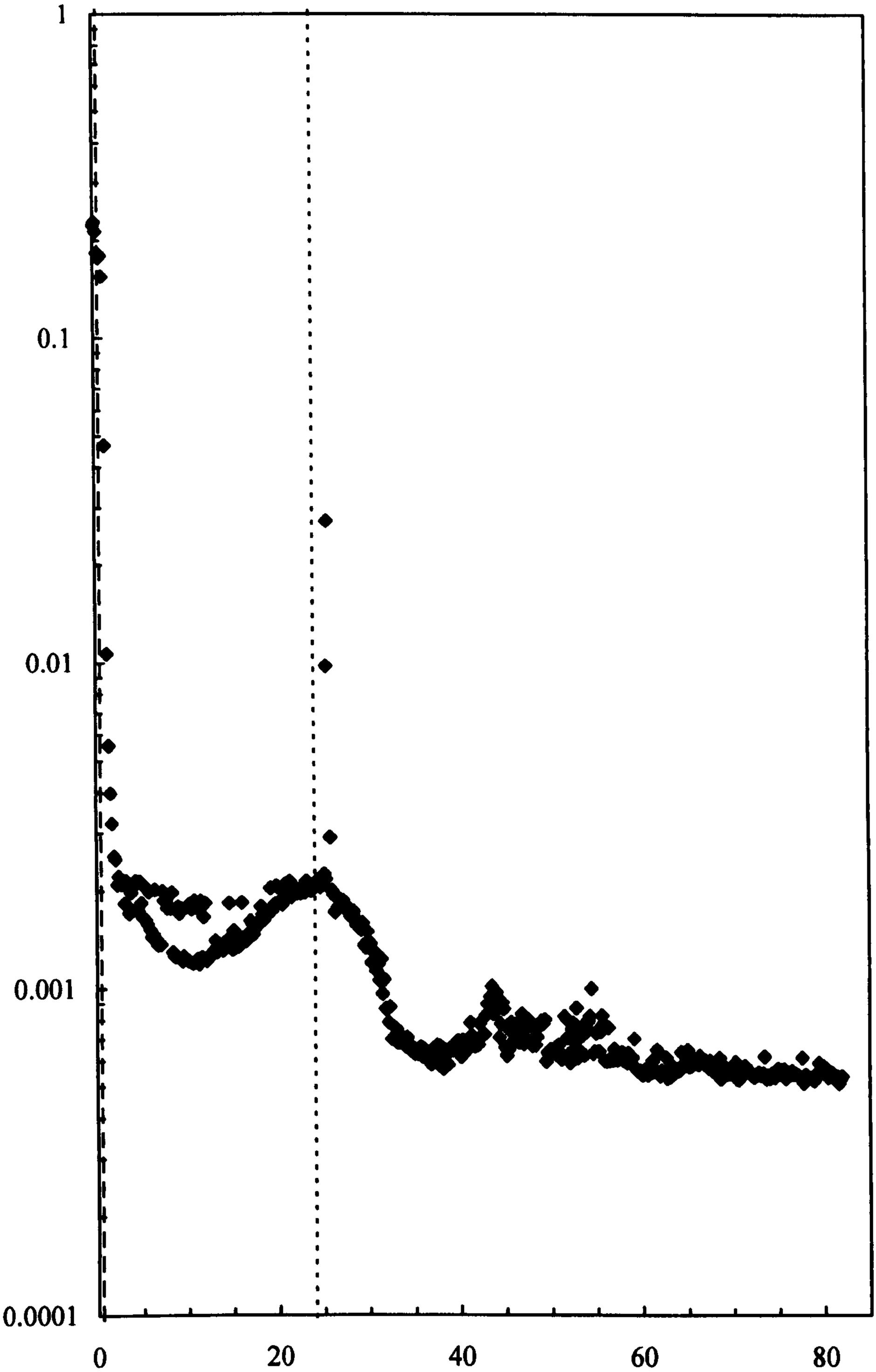

corrosion rate during the pre-corrosion period is approximately 0.2 mm y^{-1} and quickly decreases to approximately 0.002 mm y^{-1} after the addition of the surfactant. The presence of an equal volume layer of toluene causes the corrosion rate to decrease to a plateau value of approximately 0.0006 mm y^{-1}.

Figure 5.11 shows the corrosion rate versus time for 1018 steel electrodes immersed in 1 wt.% brine solution under H_2S conditions at 40 °C, with addition of 10 mM C16BDMAC after 30 min. pre-corrosion. In the absence of surfactant the corrosion rate of the 1018 steel electrodes is approximately 1 mm y^{-1}. Addition of C16BDMAC causes the corrosion rate to decrease to approximately 0.05 mm y^{-1}. After addition of the toluene layer the corrosion rate begins to decrease slowly to 0.003 mm y^{-1} over the duration of the measurement. At this low concentration of electrolyte C16BDMAC does not partition to the toluene phase. Finally, Figure 5.12 shows the corrosion rate versus time for 1018 steel in 10 wt.% brine solution under H_2S conditions at 40 °C with addition of 10 mM C16BDMAC to the aqueous phase and addition of an equal volume layer of toluene after 24 hr. At this temperature and high salt concentration the C16BDMAC micelles are expected to partition to the toluene phase. During the pre-corrosion period the corrosion rate is approximately 0.5 mm y^{-1} and rapidly decreases to 0.003 mm y^{-1} after addition of the surfactant. Over the next 24 hr. the corrosion rate steadily decreases to approximately 0.007 mm y^{-1}; addition of the toluene layer causes a further decrease in the corrosion rate, which reaches a plateau value of approximately 0.001 mm y^{-1} 10 hr. after adding the toluene phase. The system is expected to phase invert to a water-in-oil microemulsion under these conditions due to a change in the preferred curvature of the surfactant monolayer caused by the high electrolyte concentration and penetration of the hydrocarbon tails by toluene. However, the corrosion rate in the presence of the toluene phase is actually slightly lower than the corrosion rate in the absence of toluene. If the aggregated form of C16BDMAC contributes towards corrosion inhibition in the aqueous phase we might expect to see an increase in the corrosion rate of the steel after addition of the oil, since the high salt concentration and temperature would favour the formation of a water-in-oil microemulsion. As we do not see an increase in corrosion rate this suggests that either the aggregated form of the inhibitor does not participate in corrosion inhibition, or that enough monomeric surfactant remains in the aqueous phase to provide good corrosion inhibition after partitioning of the aggregates.

Figure 5.13 shows the corrosion rate versus time for 1018 steel in 1 wt.% brine solution under H_2S conditions at 40 °C with addition of 1 mM IA to the aqueous

Figure 5.11. Corrosion rate vs time for 1018 steel electrodes in 1 wt.% brine under H_2S conditions at 40 °C. Addition of C16BDMAC after 0.5 hr. to give aqueous concentration of 10 mM and addition of equal volume layer of toluene after 24 hr.

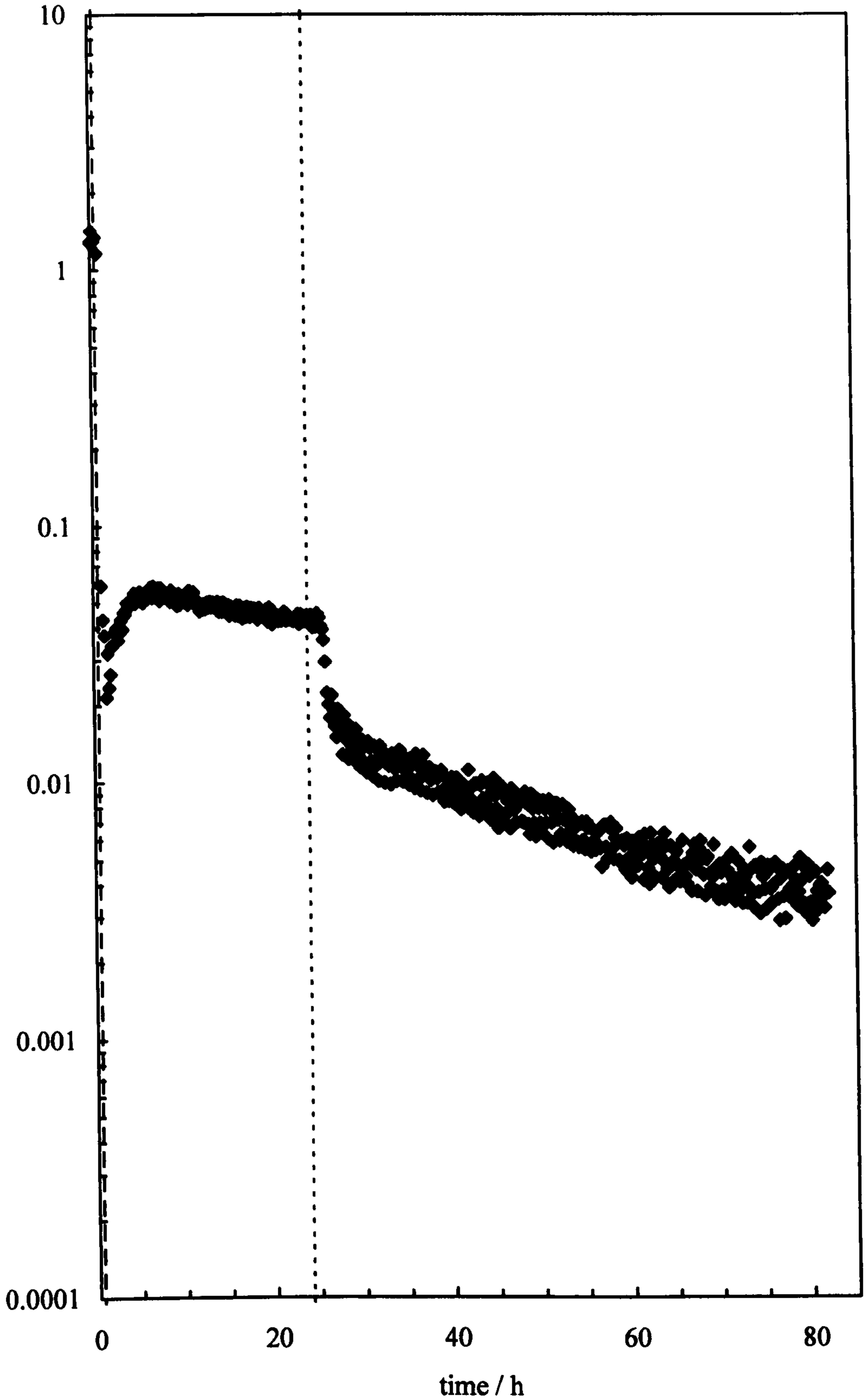

Figure 5.12. Corrosion rate vs time for 1018 steel electrodes in 10 wt.% brine under H_2S conditions at 40 °C. Addition of C16BDMAC after 0.5 hr. to give aqueous concentration of 10 mM and addition of equal volume layer of toluene after 24 hr.

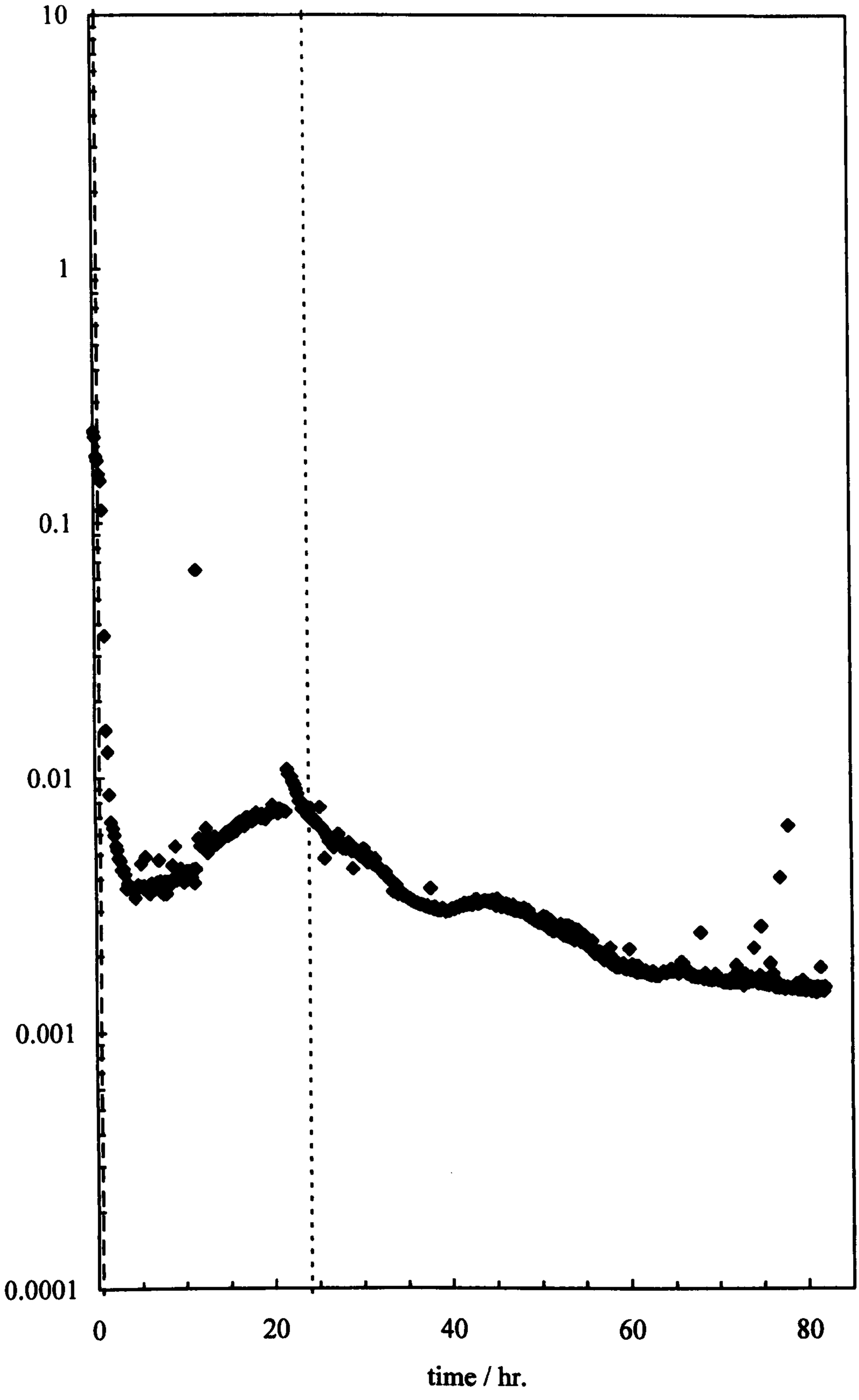

phase and addition of an equal volume layer of toluene after 24 hr. At this salt concentration the micelles are expected to remain in the aqueous phase in the presence of the oil layer. During the pre-corrosion, the corrosion rate of the steel electrodes is 0.44 mm y^{-1} and decreases rapidly to approximately 0.005 mm y^{-1} after addition of the surfactant. Over the next 24 hr. the corrosion rate increases to approximately 0.01 mm y^{-1}. Two hours after addition of the toluene layer the corrosion rate decreases to approximately 0.004 mm y^{-1} and then steadily decreases to 0.001 mm y^{-1} over the duration of the measurement. Figure 5.14 shows the corrosion rate versus time for steel electrodes immersed in 10 wt.% brine solution under H_2S conditions at 40 °C, with addition of 1 mM IA after 30 min. pre-corrosion. In the absence of surfactant the corrosion rate is approximately 0.2 mm y^{-1}. Addition of IA causes the corrosion rate to decrease to approximately 0.004 mm y^{-1}. During the addition of the oil some emulsification occurred, leaving a thin layer (2 – 4 mm thick) of emulsion between the two bulk phases and increased the turbidity of the toluene phase. Three hours after the addition of the toluene layer, the corrosion rate decreases rapidly to approximately 0.0001 mm y^{-1}. Over the duration of the measurement the corrosion rate increases slightly with abrupt increases in corrosion rate at 20 and 40 hr. after addition of the toluene phase which may be caused by the accumulation of emulsion drops around the electrode as shown in Figure 5.15.

Table 5.11 summarises the corrosion rates in the presence of each surfactant before and after the addition of the oil phase. These results suggest that partitioning of the aggregated form of water-soluble corrosion inhibitors to oil does not adversely affect corrosion inhibition in the aqueous phase. Regardless of whether partitioning of the inhibitor occurs, the presence of the oil phase generally decreases the corrosion rate by up to one order of magnitude. This may be due to partitioning of the sulphide species from water to oil which decreases the corrosivity of the solution. When phase inversion is expected at high electrolyte concentrations, virtually all of the surfactant exists in its aggregated form in the oil phase. This suggests that the amount of monomeric surfactant remaining in the aqueous phase seems sufficient to maintain a good degree of corrosion inhibition throughout the duration of the experiment.

5.4 Conclusions

Surface-active corrosion inhibitors can partition between the aqueous and oil phases of the produced fluid. At concentrations in excess of the cmc corrosion inhibitors form

Figure 5.13. Corrosion rate vs time for 1018 steel electrodes in 1 wt.% brine under H_2S conditions at 40 °C. Addition of IA after 0.5 hr. to give aqueous concentration of 1 mM and addition of equal volume layer of toluene after 24 hr.

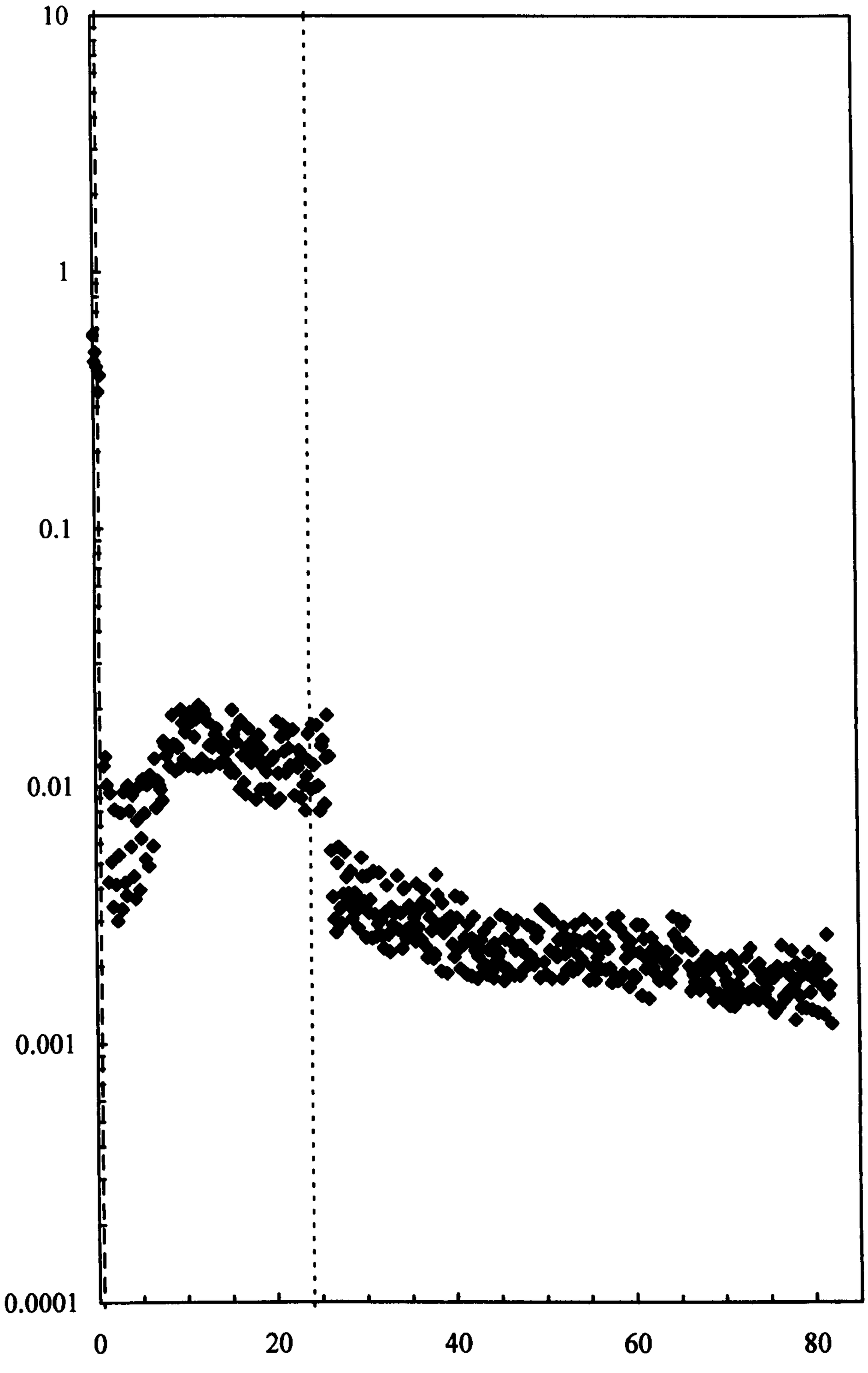

Figure 5.14. Corrosion rate vs time for 1018 steel electrodes in 10 wt.% brine under H_2S conditions at 40 °C. Addition of IA after 0.5 hr. to give aqueous concentration of 1 mM and addition of equal volume layer of toluene after 24 hr.

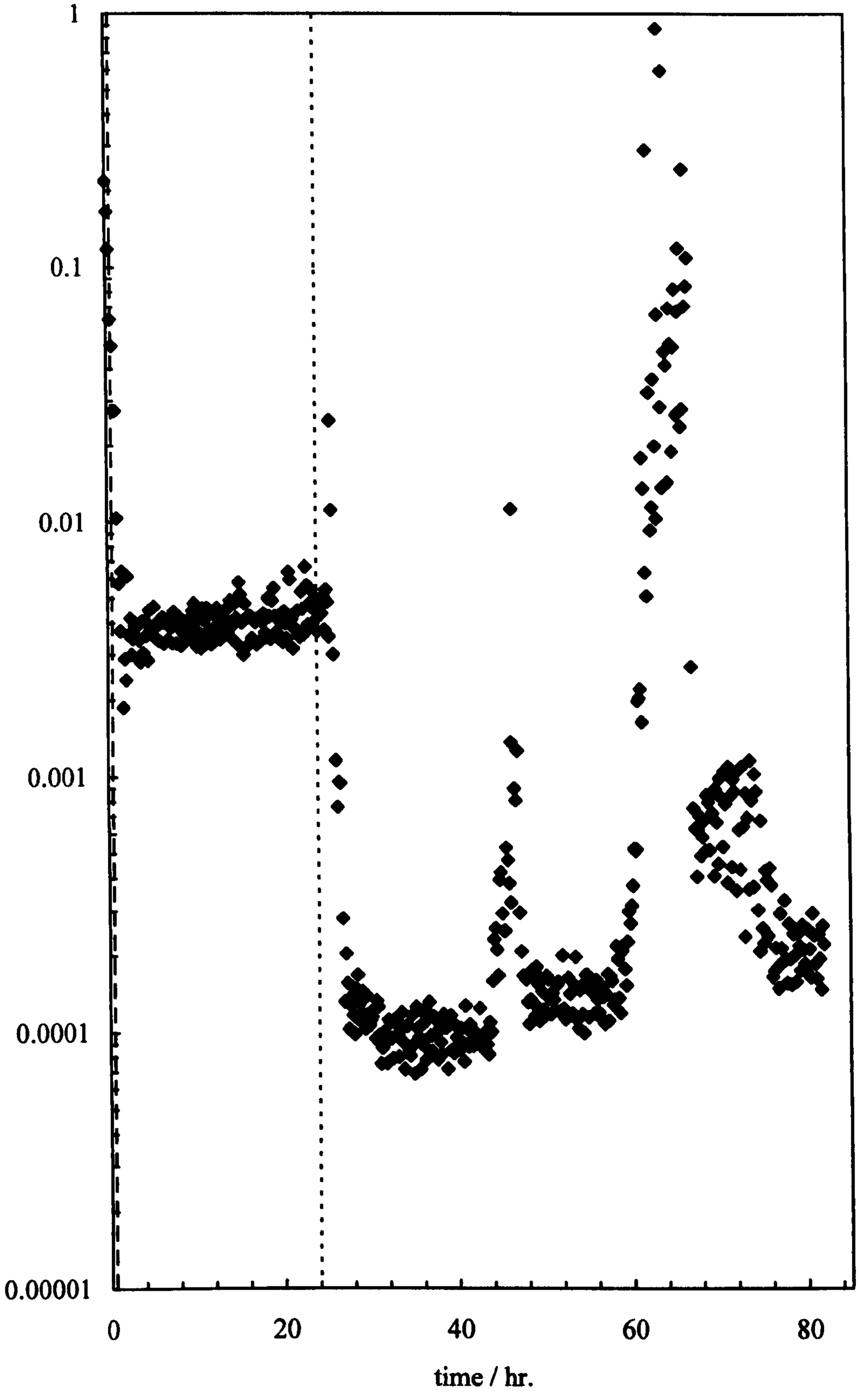

Figure 5.15. Photograph of bubble test cell containing 10 wt.% brine with 1 mM IA under H_2S conditions after the addition of an equal volume layer of toluene at 40 °C. Magnetic stirring has caused emulsion drops to disperse in the aqueous phase and accumulate at the base of the stainless steel probe.

Table 5.11. Summary of corrosion rates of 1018 steel in brine solutions under H_2S gas conditions in the presence of C12BDMAC, C16BDMAC and IA before and after the addition of an equal volume layer of toluene.

		1 wt.% brine		*10 wt.% brine*		
		Corrosion Rate / mm y^{-1}		**Phase Inversion Expected?**	**Corrosion Rate / mm y^{-1}**	
Surfactant	**Temp. / °C**	**Absence of oil**	**Presence of oil**		**Absence of oil**	**Presence of oil**
C12BDMAC	25	-	-	NO	0.003	0.0007
C16BDMAC	25	0.008	0.0025	NO	0.002	0.0006
C16BDMAC	40	0.05	0.003	YES	0.007	0.001
IA	40	0.01	0.0015	YES	0.004	0.0001

aggregates in solution. The micelles or microemulsion droplets act as a reservoir for the active monomer, which adsorbs onto the steel surface to inhibit the corrosion rate. The level of the reservoir is dictated by the cmc. When the monomers adsorb at the steel surface the concentration of active monomer decreases slightly. If the reservoir of aggregated inhibitor exists in the oil phase then it may be unable to replenish the required amount of monomers in the aqueous phase. The aggregated form of the corrosion inhibitor will exist in the oil or water phase depending on the preferred curvature of the surfactant monolayer which is determined by the effective molecular geometry. The effective geometry of the surfactant head and tail groups can be altered by conditions such as electrolyte concentration, temperature and the nature of the oil. As these factors differ between oil fields, the concentration of corrosion inhibitor available for inhibition may vary similarly. Corrosion rate measurements conducted in the presence of oil phases show that partitioning of corrosion inhibitor aggregates from water to oil does not lead to an increase in the corrosion rate of steel in contact with the aqueous phase. However, it remains to be seen whether these results will be replicated in actual oil pipeline systems.

5.5 References

1. M. Knag, J. Sjöblom and E. Gulbrandsen, *J. Disp. Sci. Technol.*, **27**, 65 (2006).
2. E. Gulbrandsen, J. Kvarekval and A. Dugstad, *Proceedings of EUROCORR 2003*, European Federation of Corrosion, Budapest (2003).
3. D.I. Horsup, J. Caleb Clark, B.P. Binks, P.D.I. Fletcher and J.T. Hicks, *Proceedings of NACE Corrosion/2007*, Paper No. 07617, NACE International, Houston (2007).
4. H. Kunieda and K. Shinoda, *J. Colloid Interface Sci.*, **106**, 107 (1985).
5. R. Aveyard, B.P. Binks, P.D.I. Fletcher, A.J. Kirk and P. Swansbury, *Langmuir*, **9**, 523 (1993).
6. W.D. Bancroft, *J. Phys. Chem.*, **17**, 501 (1913).
7. B.P. Binks, *Colloids Surf. A*, **71**, 167 (1993).
8. B.P. Binks, *Langmuir*, **9**, 25 (1993).
9. Y. Moroi, *Micelles: Theoretical and Applied Aspects*, Plenum Press, New York (1992).
10. J.R. Rodríguez and J. Czapkiewicz, *Colloids Surf. A*, **101**, 107 (1995).

11. R. Aveyard, B.P. Binks and P.D.I. Fletcher, *in The Structure, Dynamics and Equilibrium Properties of Colloidal Systems*, eds. D.M. Bloor and E. Wyn-Jones, Kluwer Academic, Amsterdam, p.557 (1990).

CHAPTER 6

Summary of conclusions and future work

6.1 Summary of conclusions

In this study we have aimed to investigate the surfactant aspects of corrosion inhibition. A combination of electrochemical and weight-loss measurements was employed to assess the performance of two model inhibitors for the corrosion of a carbon steel in aqueous systems in the presence and absence of electrolyte under different dissolved gas conditions. The inhibitors were the quaternary ammonium salt dodecylbenzyldimethylammonium chloride (C12BDMAC) and an imidazoline salt, 1-aminoethyl-2-(8-heptadecenyl)-2-imidazoline acetate (IA). Using the electrochemical bubble test method, in the absence of inhibitors 1018 steel corrodes rapidly (0.1 – 1 mm y^{-1}) in brine environments under atmospheric, CO_2 and H_2S gas conditions but corrodes at a slower rate in the absence of electrolyte (0.001 – 0.05 mm y^{-1}) due to the lower electrical conductivity of the solution. Weight-loss measurements generally gave corrosion rates which were two to four times lower than those determined electrochemically and were up to one order of magnitude lower in deionised water. We believe that corrosion rates determined using the electrochemical bubble test are the most plausible due to the relatively short exposure period of the wheel box tests.

Under atmospheric conditions reddish brown iron oxide-hydroxide corrosion products form at the surface of the steel in the absence and presence of electrolyte. Magnetite corrosion products were also observed on the bubble test electrodes under atmospheric conditions in the absence of electrolyte. Steel corroded in CO_2-containing environments acquired a grey corrosion product film, which is probably iron carbonate. Under H_2S conditions, the weight-loss coupons were covered with a black corrosion product film thought to be an iron sulphide compound. However, black corrosion products were not observed on the bubble test electrodes under the same conditions.

C12BDMAC and IA both act as effective corrosion inhibitors in aqueous environments containing H_2S gas, reducing the corrosion rate of the steel by up to two orders of magnitude. Corrosion inhibition increases with increasing concentration of inhibitor up to the cmc and remains constant. IA shows good corrosion inhibition at low concentrations in brine containing CO_2 gas, but the effect diminishes as the concentration of IA increases. Using the bubble test technique, both surfactants were found to promote corrosion in deionised water under aerated or CO_2 conditions, especially at high concentration of surfactant. In carbonated water in the absence of

electrolyte promotion of corrosion is observed above the cmc of C12BDMAC, where a bilayer adsorbed film may be expected to form. We believe that under these conditions promotion of corrosion is caused by the electrostatic attraction between the negatively charged carbonate ions in solution and the positively charged inhibitor head groups which form the outer surface of the adsorbed bilayer film resulting in a greater surface concentration of carbonate ions. In the presence of electrolyte corrosion inhibition is observed above the cmc of C12BDMAC. We propose that under these conditions the added electrolyte screens the electrostatic attraction between the bilayer head groups and the corrosive anions, which depletes the concentration of carbonate ions at the steel surface leading to a lower corrosion rate. Overall, these results show that the performance of surfactants as corrosion inhibitors depends upon the nature of the corrosion products formed at the steel surface, the concentration of electrolyte and the concentration of inhibitor applied.

Ellipsometry has been used to examine the adsorption of C12BDMAC at the steel-water interface. Under aerated conditions in the absence of electrolyte the thickness of the inhibitor film increases as the concentration of surfactant increases. The results are consistent with the formation of a monolayer at concentrations close to the critical micelle concentration of C12BDMAC and probable multilayer formation at higher concentrations. The film thicknesses values for monolayer and bilayer coverage may also be caused by the formation of surface aggregates such as semi-cylindrical micelles or hemimicelles and spherical micelles and cylindrical aggregates, respectively. Film thickness measurements were not possible in systems which cause rapid corrosion of the steel surface due to large changes in the optical properties of the surface caused by the dissolution of the steel and the formation of corrosion products on the surface. In subsequent dynamic ellipsometric measurements, the changes in Δ and Ψ during corrosion were monitored with time in the absence and presence of C12BDMAC. In aerated brine corrosion causes successive changes in the ellipsometric angles indicating that multiple processes are occurring as corrosion progresses. The presence of increasing concentrations of C12BDMAC generally decreases the period of time over which these processes take place. Under CO_2 and H_2S conditions rapid dissolution of the native oxide layer causes the ellipsometric angles to decrease dramatically. Addition of C12BDMAC virtually suppresses the changes in the optical properties of the steel surface at all concentrations. SEM images of corroded steels discs show that the corrosion products were deposited in localised areas rather than coherent films. The images were also consistent with features of the Δ versus time profiles of

each system. Under aerated conditions the coverage of corrosion product crystals was observed to increase with increasing concentration of C12BDMAC over a 2 hr. exposure period, which is consistent with the compression of the Δ versus time profiles which suggest that increasing concentrations of surfactant increase the rate of the surface corrosion processes. Under carbonated conditions the SEM images show that corrosion of the steel surface is reduced with increasing concentrations of C12BDMAC, signified by a lesser degree of metal dissolution in the presence of the inhibitor. These observations support the corresponding dynamic ellipsometry data. Quantitative information on the composition and thickness of the corrosion product films and the thickness of adsorbed inhibitor films is extremely difficult to determine using this technique. We have not been able to determine the variation in optical properties and thickness of the corrosion product deposits which form on the surface of steel as it corrodes under different gas conditions. This is mainly due to the complex structure of the steel surface as it corrodes and the lack of optical data for steel and iron compounds which are present in corrosion product deposits.

The equilibrium partition coefficient of alkyl-BDMACs (C12 – C16) in mixtures of heptol and water (equal volumes and 10:1 volume ratio in favour of oil) has been determined in the presence and absence of electrolyte at 25 and 40 °C. For C12 and C14BDMAC, virtually all the surfactant remains the aqueous phase under all conditions. At concentrations greater than the cmc in the water phase, the alkyl-BDMAC will aggregate into micelles which remain in the aqueous phase. Only C16BDMAC partitions to the heptol phase at 10:1 heptol to water volume ratio in the presence of electrolyte at 40 °C. At concentrations in excess of the cmc, C16BDMAC forms micelles which partition to the heptol phase, which leads to formation of a Winsor II microemulsion system. The effect of oil type on the phase behaviour of C12 and C16BDMAC and IA was studied using an emulsion phase inversion technique. Emulsions containing C12BDMAC remain water continuous at high and low [salt] with heptane, toluene, heptol and crude oil which indicates that the corresponding microemulsion systems are also water continuous at high and low [salt]. Emulsions containing C16BDMAC or IA phase invert from o/w to w/o as the concentration of electrolyte is increased with toluene and crude oil as the oil phase. This indicates that the effective geometry of the inhibitor within the monolayer is altered as [salt] increases with oils which can penetrate and swell the hydrocarbon tail groups of the inhibitors. The corresponding microemulsion systems should invert from Winsor I to Winsor II systems at a similar [salt] due to the change in the curvature of the surfactant

monolayer. These results show that water-soluble corrosion inhibitors can transfer between the aqueous and hydrocarbon phases of an oil pipeline depending upon the prevailing conditions. The micellar aggregates act as a reservoir for the active monomeric form of the inhibitor, which adsorbs onto steel surfaces to inhibit corrosion in aqueous solution. At low concentrations of electrolyte the aggregates are present in the aqueous phase and may supply more active monomer to inhibit corrosion. At high [salt] conditions all of the aggregated corrosion inhibitor exists in the oil phase and may be unable to replenish the required amount of monomers to provide corrosion inhibition in the aqueous phase. By combining the equilibrium partitioning method with the bubble test method we were able to examine whether partitioning of the aggregated form of C16BDMAC or IA from water to oil affects corrosion inhibition in the aqueous phase. The results indicate that partitioning of the aggregated corrosion inhibitor from water to oil, caused by system conditions which change the effective geometry of the inhibitor molecules within the monolayer of the aggregates, does not have a detrimental effect upon corrosion inhibition in the aqueous phase. Although the aggregated corrosion inhibitor is transferred to the oil phase in the presence of high concentrations of electrolyte the amount of monomeric surfactant remaining in the aqueous phase seems sufficient to maintain a good degree of corrosion inhibition.

6.2 Possibilities for future work

We have approached this study by systematically investigating the performance, adsorption and phase behaviour of alkyl-BDMACs and IA under different conditions. Although the dynamic ellipsometry experiments, in conjunction with SEM and EDX analysis, have yielded interesting qualitative information about the corrosion processes which occur under different dissolved gas conditions, we must know much more about the structure and optical properties of the steel surface and the composition and optical properties of the corrosion products in order to determine the thickness of the adsorbed inhibitor film. Undoubtedly, knowledge of the film thickness under different dissolved gas conditions would be valuable; however, we feel that the experiments required to gather the necessary optical data are beyond the scope of the current study. Other techniques such as the quartz-crystal microbalance may provide an easier method for examining possible differences in the adsorption isotherms for inhibitors adsorbing onto different corrosion product surfaces.

The investigation into the phase behaviour of corrosion inhibitors offers the most possibilities for further study. The equilibrium partitioning and emulsion phase inversion experiments can be extended to study other corrosion inhibitor types, such as alkylamines, alkylpyridinium salts and other imidazoline derivatives. The range of system conditions can also be widened. The effects of high temperatures, brine composition, the oil to water volume ratio and the nature of the oil phase (particularly the relative volumes of aliphatic and aromatic hydrocarbons) can be studied in greater detail. We hope that by examining a wide range of inhibitor types and environmental conditions it will be easier to predict the phase behaviour of an inhibitor when applied to a particular oil field.

Our studies into the effect of partitioning of corrosion inhibitors from water to oil upon corrosion inhibition in the aqueous phase can also be expanded. From our results for the alkyl-BDMACs and IA it is evident that partitioning of the aggregated form of the inhibitor does not affect corrosion inhibition in the aqueous phase under dissolved gas conditions where the inhibitors show good corrosion inhibition. These findings could be verified by repeating the experiments with other types of corrosion inhibitor which show good performance under CO_2 gas conditions. Partitioning from water to oil is one possible means by which parasitic consumption of inhibitors can occur. There is a need for more detailed investigation into the effects of variables such as inhibitor type, temperature, concentration and electrolyte and oil type on the loss of inhibitors by adsorption onto unwanted surfaces such as emulsion drops, dispersed corrosion product debris and sand particles. Such information could also lead to improvements in the optimisation of inhibitor formulations for application in the field.